ON THE PROCESSING OF HIGHLY NONLINEAR SOLITARY WAVES AND GUIDED ULTRASONIC WAVES FOR STRUCTURAL HEALTH MONITORING AND NONDESTRUCTIVE EVALUATION

by

Abdollah Bagheri

Master of Science in Civil Engineering, Iran University of Science and Technology, 2005

Submitted to the Graduate Faculty of

Swanson School of Engineering in partial fulfillment

of the requirements for the degree of

Doctor of Philosophy in Civil Engineering

University of Pittsburgh

2015

UNIVERSITY OF PITTSBURGH

SWANSON SCHOOL OF ENGINEERING

This dissertation was presented

by

Abdollah Bagheri

It was defended on

June 2, 2015

and approved by

John C. Brigham, Ph.D., Assistant Professor, Department of Civil and Environmental Engineering

Jelena Kovačević, Ph.D., Professor, Department of Electrical and Computer Engineering, Carnegie Mellon University

Albert C.F. To, Ph.D., Associate Professor, Department of Mechanical Engineering and Materials Science

Qiang Yu, Ph.D., Assistant Professor, Department of Civil and Environmental Engineering

Dissertation Director: Piervincenzo Rizzo, Ph.D., Associate Professor, Department of Civil and Environmental Engineering

ON THE PROCESSING OF HIGHLY NONLINEAR SOLITARY WAVES AND GUIDED ULTRASONIC WAVES FOR STRUCTURAL HEALTH MONITORING AND NONDESTRUCTIVE EVALUATION

Abdollah Bagheri, Ph.D.

University of Pittsburgh, 2015

The *in-situ* measurement of thermal stress in civil and mechanical structures may prevent structural anomalies such as unexpected buckling. In the first half of the dissertation, we present a study where highly nonlinear solitary waves (HNSWs) were utilized to measure axial stress in slender beams. HNSWs are compact non-dispersive waves that can form and travel in nonlinear systems such as one-dimensional chains of particles. The effect of the axial stress acting in a beam on the propagation of HNSWs was studied. We found that certain features of the solitary waves enable the measurement of the stress.

In general, most guided ultrasonic waves (GUWs)-based health monitoring approaches for structural waveguides are based on the comparison of testing data to baseline data. In the second half of the dissertation, we present a study where some baseline-free signal processing algorithms were presented and applied to numerical and experimental data for the structural health monitoring (SHM) of underwater or dry structures. The algorithms are based on one or more of the following: continuous wavelet transform, empirical mode decomposition, Hilbert transform, competitive optimization algorithm, probabilistic methods. Moreover, experimental data were also processed to extract some features from the time, frequency, and joint time-frequency domains. These features were then fed to a supervised learning algorithm based on

artificial neural networks to classify the types of defect. The methods were validated using the numerical model of a plate and a pipe, and the experimental study of a plate in water. In experiment, the propagation of ultrasonic waves was induced by means of laser pulses or transducer and detected with an array of immersion transducers. The results demonstrated that the algorithms are effective, robust against noise, and able to localize and classify the damage.

TABLE OF CONTENTS

LIST OF TABLES

LIST OF FIGURES

PREFACE

First of all, I wish to acknowledge God almighty who has been giving me everything to accomplish this dissertation: wisdom, health, patience, and blessing. Without all these things, I could not have accomplished this study.

I would like to express my sincere gratitude to my advisor, Prof. Piervincenzo Rizzo, for his valuable supports, advices, and supervision during my Ph.D. studies. He gave me the opportunity to study some of the most recent advancements in the field of nondestructive evaluation and structural health monitoring.

I owe my sincere thanks to the members of my defense committee, Prof. John C. Brigham, Prof. Jelena Kovačević, Prof. Albert C. F. To, and Prof. Qiang Yu, for reading the manuscript, and for all the suggestions and insightful discussions.

I sincerely acknowledge the support of the U.S. Federal Railroad Administration under contract DTFR53-12-C-00014, the Center for Energy at the University of Pittsburgh's Swanson School of Engineering, the U.S. National Science Foundation, grants CMMI–1029457 and CMMI–1200259, and the Teaching Assistantships provided by the Civil and Environmental Department of the Swanson School of Engineering to support my Ph.D. studies.

I sincerely appreciated the time spent with the colleagues of the Laboratory for Nondestructive Evaluation and Structural Health Monitoring studies. Experimental part of this study in Chapters 5, 7, and 8 was conducted with the contribution of Dr. Elisabetta Pistone and

Miss Emma La Malfa Ribolla at the University of Pittsburgh's Laboratory for Nondestructive Evaluation and Structural Health Monitoring studies. Also, the finite element model of a plate in Chapter 6 and the initial model of a pipe in Chapter 10 were simulated by Mr. Kaiyuan Li.

For this study, we used test equipment at the University of Pittsburgh's Laboratory for Nondestructive Evaluation and Structural Health Monitoring studies and the Watkins-Haggart Structural Engineering Laboratory (WHSEL).

The contribution of Mr. Charles Hager, full-time staff member at the University of Pittsburgh's Department of Civil and Environmental Engineering, in the preparation and execution of some experiments is greatly appreciated.

I would like to thank my parents and elder brother for their unconditional love and support. Without their support, I could not have finished my graduate study. Lastly but not least, I am deeply thankful to my devoted wife, Hajar, for her endless love, patience, and encouragement.

1.0 INTRODUCTION

Existing structures are aging and constantly novel materials and technology of constructions are employed for new engineering systems. Even though innovation is what potentially improves our daily life, methods to properly assess the damage-state and, therefore, the level of safety of the systems we are developing are needed. Nondestructive evaluation (NDE) are becoming more and more attractive due to their enormous potential. NDE methods can potentially investigate the damage state of a structure without further damaging. In literature, as well as in the industrial development side, various methods have been studied and implemented and their use and effectiveness is based upon the application. Nonetheless, their potential resides in the aim of detecting damage and, as a consequence, preventing failure at a very early stage. Thus, safety is increased and costs associated to unexpected failures are decreased. In fact, ideally, a constant or well-appointed monitoring allows the detection of flaws at an early stage, thus leading to expenses related more to maintenance and service rather than extensive repair. The structural health monitoring (SHM) approach is based on the process of implementing a damage detection strategy (with the aim of real time monitoring) for engineering structures. SHM techniques very often make use of NDE methods. In general, effective NDE and SHM techniques should reach a level where they are capable of detecting and quantifying damage at the very beginning, thus increasing the level of safety of our engineering system.

In this study, highly nonlinear solitary waves (HNSWs) and guided ultrasonic waves (GUWs) are used for the SHM and NDE of some engineering structures. First, we use the propagation of HNSWs to estimate axial stress indirectly in slender structures. Then, we present some signal processing algorithms for damage identification and localization in pipes, plates, and underwater structures based on GUWs. Figure 1.1 shows the box diagram of the dissertation. The motivations for these studies are detailed Sections 1.1 and 1.2.

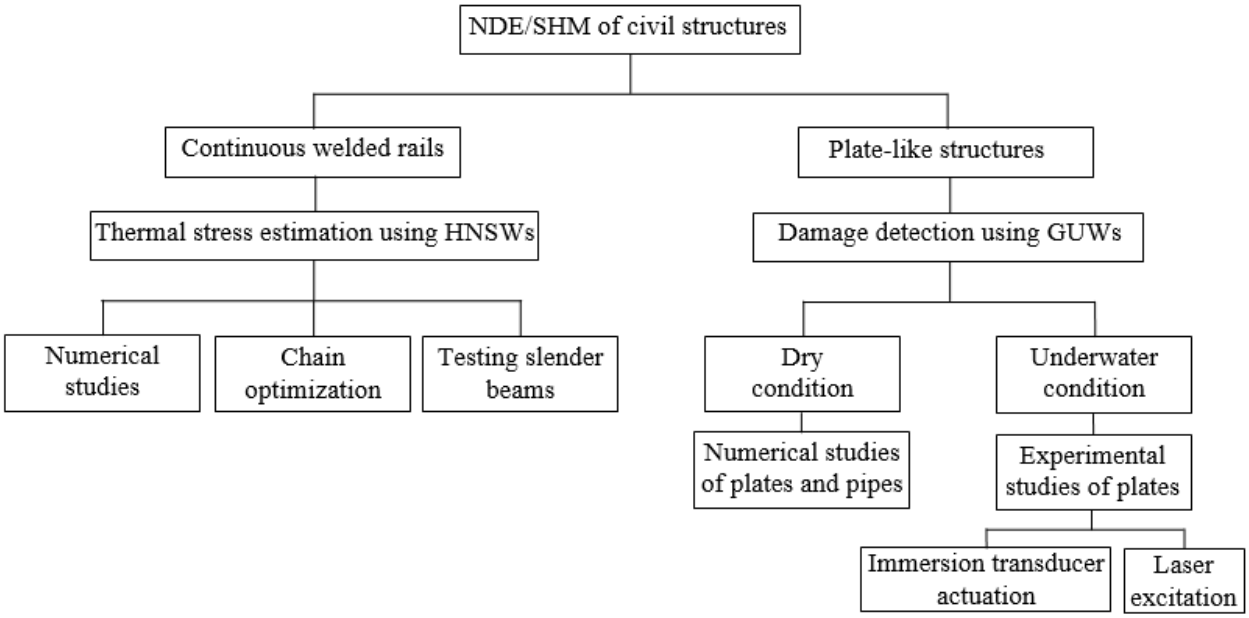

Figure 1.1. Box diagram of the dissertation.

The *in-situ* measurement of axial stress in beams may prevent structural anomalies such as unexpected buckling. For example, continuous welded rails (CWR), which are typically hundreds of meters long, are prone to buckling in hot weather and to breakage or pulling apart in cold weather. In this study, we propose the coupling mechanism between HNSWs propagating along a granular system and a beam in contact with the granular medium to assess the ability of

HNSWs at measuring axial stress. HNSWs are compact non-dispersive waves that can form and travel in nonlinear systems such as one-dimensional chains of particles.

Studies conducted in the last two decades have demonstrated the effectiveness of GUWs for the NDE and SHM of waveguides, such as pipes, plates, and rails. Owing to the ability of travelling relatively large distances in dry structures with little attenuation, GUWs allows for the inspection of long waveguides, locating cracks and notches from few monitoring points, while providing full coverage of the cross section. In this dissertation, we propose some algorithms to process GUWs for SHM and NDE of plates, pipes, and underwater structures.

1.1 HNSWS FOR EVALUATION OF SLENDER STRUCTURES

Columns, beam-like structures, and CWRs all subjected to thermal stress are common in civil engineering. For example, the several hundred meters long CWRs are prone to buckling in hot weather and breakage or pulling apart in cold weather. Buckling is usually caused by the simultaneous occurrence of one or more of the following: high compressive stress due to thermal load, weak track conditions, and vehicle loads. A typical rail buckling is shown in Fig. 1.2. To prevent these accidents, a reliable nondestructive methodology able to determine thermal stress or the rail neutral temperature (RNT), defined as the temperature at which the net longitudinal force in the rail is zero, is needed.

Figure 1.2. Thermal buckling in a continuous welded rail (Robertson, 2012).

In the decade 2003-2012, in the United States track buckling was responsible for 297 derailments, which caused $121M in reportable damage, and accounted for 10% of all damage relative to the track bed. In 2012, track buckling caused 27 derailments, $24.2M in reportable damage which represented 25.9% of the all reportable damage for that year (Federal Railroad Administration's website).

In this study, we utilized the propagation of HNSWs to measure axial stress indirectly. HNSWs are compact non-dispersive waves that can form and travel in nonlinear systems such as one-dimensional chains of particles, where they can be generated by the mechanical impact of a striker, by means of a transducer (Li et al., 2013), or by laser pulses (Ni et al., 2011). In chains of particles, the nonlinearity arises from a Hertzian-type contact between two adjacent spheres subjected to compressive force. When the compression is small compared to the dynamic force associated with the propagation of the wave, HNSWs arise (Ni et al., 2011; Nesterenko, 1983; Lazaridi and Nesterenko, 1985; Nesterenko et al., 1995; Coste et al., 1997; Coste and Gilles, 1999; Daraio et al., 2005, 2006; Job et al., 2005, 2007; Nesterenko et al., 2005; Yang et al., 2011, 2014; Carretero-González et al., 2009; Ni et al., 2011). Recent studies about the propagation of

nonlinear solitary waves in one-dimensional chains of spherical elastic beads have demonstrated that these waves can be used as vibration absorbers (Fraternali et al., 2009), impurity detectors (Sen et al., 1998; Hong and Xu, 2002; Li et al., 2013), acoustic diodes (Nesterenko et al., 2005; Boechler et al., 2001), impact locators (Shelke et al., 2014), and can be used for the nondestructive testing of structural and biological materials (Ni et al., 2012a,b; Ni and Rizzo, 2012; Yang et al., 2012a, b). One peculiar feature of the HNSWs is that their amplitude, speed, and number of pulses can be tuned by engineering the granular system, by changing the bead's diameter, or by adding static pre-compression.

We investigated the effect of the axial stress acting in a beam on the propagation of HNSWs along one or two straight and L-shape chains of particles in contact with the beam itself. The objective of the study was to: 1) evaluate the chain configuration, one or two straight or L-shape chains, most sensitive to the variation of stress; 2) determine thermal stress or the beam neutral temperature; 3) determine the optimal combination of particles' diameter and material. The analysis consisted of using a discrete particle model (Nesterenko, 2001) to predict the propagation of the wave along the chain and to derive the shape and amplitude of the solitary pulse at the chain-beam interface. A continuous beam theory was then used to estimate the response of the structure subjected to the forcing function equal to the solitary pulse.

1.2 GUWS FOR NDE AND SHM

GUWs are increasingly used in all those SHM applications that benefit from built-in transduction, moderately large inspection ranges, and high sensitivity to small flaws. Guided waves can travel relatively large distances with little attenuation and offer the advantage of

exploiting one or more of the phenomena associated with transmission, reflection, scattering, and absorption of acoustic energy (Alleyne and Cawley, 1996; Giurgiutiu, 2005; Rizzo and Lanza di Scalea, 2007, Raghavan and Cesnik, 2007; Diamanti, Hodgkinson, and Soutis, 2004; Su et al., 2006; Park et al., 2007; Clarke et al., 2009; Yan, Royer and Rose, 2010; Zhu et al. 2010).

Meantime it is well established that signal processing is essential to enhance any GUW-based SHM. One of the main objectives of any processing is to extract damage-sensitive features that enable to determine the existence, location, and severity of damage. In general, most health monitoring approaches for structural waveguides are based on the comparison of testing data to baseline data. Ideally, the baseline includes scenarios under all possible environmental conditions. This study attempts to develop some baseline-free signal processing methods for NDE and SHM based on the generation of GUWs. The proposed NDE/SHM methods may overcome some of the challenges related to monitoring of plate-like structures. In this study, we present some signal processing approaches for damage identification and localization of pipes and plates that combines the advantages of continues wavelet transform (CWT), empirical mode decomposition (EMD), Hilbert transform (HT), imperialistic competitive algorithm (ICA), and probabilistic methods with the need to deploy baseline-free systems. The approach processes guided waves generated and detected by all possible transducers' pairs of an array to extract damage-sensitive features from the CWT and the EMD. Then, a probabilistic method uses these features to map the structure contained within the array under monitoring and localize the damage. In pipes, the ICA was used to estimate features for healthy status. The methods are numerically validated using commercial finite element software to model an aluminum plate and pipe. Moreover, the method is experimentally validated using an immersed plate when the

propagation of ultrasonic waves induced by means of laser pulses and focused transducer and detected with an array of immersion transducers.

The need of this research is driven by the fact that the rupture of water mains for example, although might be spectacular, is too often accompanied by distress in local communities and avoidable costs for municipalities. Water mains breaks are also the subject of local news primetime as their impact to residential areas and businesses can be very significant. The economic and social costs associated with pipeline breaks in modern water supply systems are rapidly rising to unacceptably high levels. The Environmental Protection Agency reported that there are 240,000 water main breaks per year in the U.S. water distribution systems causing, according to the U.S. Geological Survey, water losses in the amount of 1.7 trillion gallons at a cost of $2.6 billion per year (Environmental Protection Agency's website, 2010).

1.3 OUTLINE

The outline of this dissertation is the following.

For the sake of completeness, Chapter 2 presents a background on the general concepts of HNSWs and the governing equations that describe their propagation along one-dimensional chains of spherical particles. Moreover this chapter summarizes the continuous beam theory utilized to predict the vibration of a slender beam subjected to a forcing function equal to the dynamic force associated with the solitary wave.

Chapter 3 describes the numerical models formulated to simulate the interaction between single or double straight and L-shaped chains in contact with a slender beam at the mid-span.

Chapter 4 presents the numerical results associated with the numerical simulations where the effect on the sensitivity of the proposed technique of certain parameters is evaluated. We discuss the effect of the beam temperature which is known to affect slightly the beam's modulus. Also, we utilize artificial neural networks to map knowledge between some of the selected HNSW-based features and the beam's neutral temperature. Finally, a beam-like rail is simulated and the effects of the rail's axial stress on the characteristics of the solitary waves are investigated.

Chapter 5 reports the experimental results and these results are compared to the numerical prediction. We examined straight and L-shaped chains of particles in the single and in the two-chain configuration. As mentioned in acknowledgments section, this experimental work of this chapter and the next chapter conducted by Miss Emma La Malfa Ribolla, a visiting student, at the University of Pittsburgh's Laboratory for Nondestructive Evaluation and Structural Health Monitoring studies.

Chapter 6 presents a monitoring system for plates based on the generation and detection of GUWs from an array of sparse transducers. In a round-robin manner, ultrasonic waves are generated and measured from all possible different pairs of excitation and sensing transducers. The ultrasonic signals are then processed using continuous wavelet transform and empirical mode decomposition to extract few damage-sensitive features that enable the detection and localization of damage. With respect to most of the existing GUW-based methods, the proposed approach does not require to record data from a pristine structure, and damage is inferred by examining the selected features obtained from all the possible combinations of actuator-sensor pairs of the array. The method is numerically validated by using a finite element model of a square aluminum plate.

Chapter 7 proposes a nondestructive evaluation method for immersed structures based on the propagation of ultrasonic waves induced by means of laser pulses and detected with an array of immersion transducers. The detected signals are processed with an imaging algorithm based on continuous wavelet transform and probabilistic analysis to localize the presence of artificial defects machined in the plate. As mentioned before, the experimental part of this chapter and the next chapter was conducted by Dr. Elisabetta Pistone, a former graduate student, at the University of Pittsburgh's Laboratory for Nondestructive Evaluation and Structural Health Monitoring studies.

Chapter 8 presents an experimental study where guided ultrasonic waves were used for the non-contact non-destructive evaluation of an aluminum plate immersed in water. Broadband leaky Lamb waves were generated using a pulsed laser and detected with an array of immersion transducers arranged in a semi-circle. The signals were processed to extract some features from the time, frequency, and joint time-frequency domains. These features were then fed to a supervised learning algorithm based on artificial neural networks to classify the types of defect. We found that the hybrid laser-immersion transducers system and the learning algorithm enable the detection of the defects and their classification with good success rate.

Chapter 9 presents the results of an experimental study in which guided ultrasonic waves are used for the contactless nondestructive testing of a plate immersed in water. Narrowband leaky Lamb waves are generated using a focused transducer, and are detected with an array of five immersion sensors arranged in a semi-circle. The ultrasonic signals are processed to extract a few damage sensitive features from the time and the frequency domains. These features are then fed to an artificial neural network to identify the presence of hidden defects, i.e. defects devised on the face of the plate not exposed to the probing system.

In Chapter 10, a baseline-free method is proposed for the detection and localization of damages in pipes. The method consists of three main steps: feature extraction, baseline computation, and mapping. The proof-of-concept is proven simulating the propagation of guided waves with a commercial finite element code.

Finally, Chapter 11 presents the main conclusions of this study and some recommendations for future work.

2.0 BACKGROUND

2.1 HIGHLY NONLINEAR SOLITARY WAVES

HNSWs are compact non-dispersive waves that can form and travel in nonlinear systems such as one-dimensional chains of particles, where they are conventionally generated by the mechanical impact of a striker. In chains of particles, the nonlinearity arises from a Hertzian-type contact between two adjacent spheres subjected to compressive force. When the compression is small compared to the dynamic force associated with the propagation of the wave, HNSWs arise (Nesterenko, 1983, 2001; Lazaridi and Nesterenko, 1985, Coste et al. 1997, Daraio et al. 2005, 2006a,b, Job et al. 2005, 2007, Yang et al. 2011, Carretero-González et al. 2009). Recent studies on the propagation of nonlinear solitary waves in one-dimensional chains of spherical elastic beads have demonstrated that these waves can be also used for the nondestructive testing (Ni 2012b; Yang et al. 2011, 2012a,b,c) of structural and biological materials. HNSWs offer a natural versatility (tunability) in terms of choice of wavelength, speed, amplitude, pulse shape, and repetition rate. The choice can be achieved by a simple and reproducible experimental setup adaptable to specific application. The tunability of the solitary waves' properties can be exploited to develop an innovative NDE/SHM paradigm in which the HNSWs are used as the input waveforms. In addition, by relaxing the need for the power requirements (function generators)

for ultrasonic actuation, the approach may facilitate the transition from tethered to wireless ultrasonic technology (Khatri et al., 2008).

For the sake of completeness a brief overview of the general principles of HNSWs and of the discrete particle model used to predict the propagation of the waves is given here. This section is excerpted from Cai et al. (2013a). When two spheres are in contact and compressed by a static force *F*, their interaction is governed by the Hertz law (Landau and Lifshitz 1986):

$$F = A\,\delta^{3/2} \tag{2.1}$$

where

$$A = \begin{cases} A_c = \dfrac{E\sqrt{2R}}{3(1-\nu^2)} \\ A_w = \dfrac{4\sqrt{R}}{3}\left(\dfrac{1-\nu^2}{E} + \dfrac{1-\nu_w^2}{E_w}\right)^{-1} \end{cases} \tag{2.2}.$$

In Eq. (2.2), the stiffness constant A_c refers to the contact between two identical spheres, whereas A_w refers to the contact between a sphere and a semi-infinite wall. In this case, E and ν represent the Young's modulus and the Poisson's ratio of the particles, whereas the index w refers to the properties associated with the wall.

When a solitary pulse propagates along a chain of N identical beads having radius R, mass m, and subjected to a static pre-compression force F_0 and initial approach δ_0, the second Newton's law relative to the i-th particle can be written as:

$$\ddot{u}_i = \eta_c\left[(\delta_0 - u_i + u_{i-1})\right]_+^{3/2} - \eta_c\left[(\delta_0 - u_{i+1} + u_i)\right]_+^{3/2} \quad , \quad 2 \le i \le N-1 \tag{2.3}$$

where u_i denotes the displacement of the i-th particle from its equilibrium position, and η_c is one of the stiffness constants defined in Eq. (2.2) normalized with respect to the mass m, namely $\eta_c = A_c/m$. The bracket $[s]_+$ denotes $max(s,0)$ which identifies a system unable to support a tensile force between particles.

A chain of N beads subjected to the action of a striker in contact with a linear medium is shown in Fig. 2.1. For the particles located at the two ends of the chain, i.e. when $i=1$ and $i=N$, Eq. (2.3) becomes:

$$\ddot{u}_1 = \eta_c \delta_0^{3/2} - \eta_c \left[(\delta_0 - u_2 + u_1) \right]_+^{3/2} \tag{2.4a}$$

$$\ddot{u}_N = \eta_c \left[(\delta_0 - u_N + u_{N-1}) \right]_+^{3/2} - \eta_w \left[\left(\delta_{w0} - u_w + u_N \right) \right]_+^{3/2} \tag{2.4b}$$

where δ_{w0} represents the initial approach between the last bead and the wall, u_w is the displacement of the contact point on the wall, and η_w is the normalized stiffness constant $\eta_w = A_w/m$.

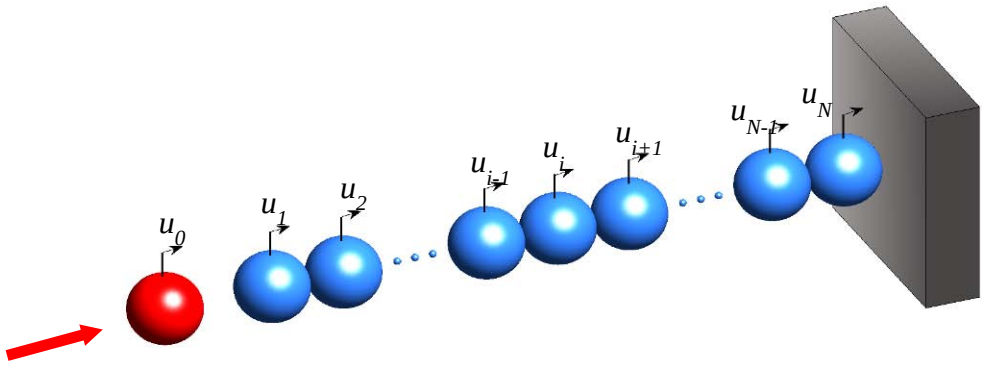

Figure 2.1. Schematics of a 1-D granular system in contact with a linear medium. u_i represents the axial displacement of the i-th particle from its equilibrium position (Figure adapted from Cai et al. (2013a)).

When the static pre-compression or its corresponding strain is small with respect to the dynamic force, the speed V_s of the solitary wave is:

$$V_s = \frac{2}{\sqrt{5}} c \xi_m^{1/4} = 0.6802 \left[\frac{2E}{D\rho^{3/2}(1-\nu^2)} \right]^{1/3} F_m^{1/6} \tag{2.5}$$

and its shape can be closely approximated by:

$$\xi = \left(\frac{5V_s^2}{4c^2}\right)\cos^4\left(\frac{\sqrt{10}}{5D}y\right) \tag{2.6}$$

In Eqs. (2.5) and (2.6) ξ_m and F_m are the maximum strain and the maximum force, respectively. The maximum strain includes the dynamically induced strain. Similarly, the maximum force includes the time-variance force associated with the propagation of solitary waves. D is the particles' diameter and c is a constant which depends on the material's properties. Equation (2.5) demonstrates that the speed has a nonlinear dependence on the strain or on the force.

We used a discrete particle model to simulate the propagation of HNSWs in a straight and in an L-shaped chain of particles. These models will be described in details in the next chapter.

2.2 CONTINUOUS BEAM THEORY

In our simulations, the beam in contact with the granular medium was subjected to an impulse force equal to the solitary wave arriving at the chain/beam interface. To predict the response of the linear medium, we used the continuous beam theory. In the general formulation of this theory, the equation of motion of a beam subjected to a concentrated force *F(t)* and an axial force per unit length *T*, which is considered positive when in tension is (Tedesco et al. 1999):

$$\left[E_b I y''(x,t)\right]'' + m_b \ddot{y}(x,t) - T y''(x,t) = F(t) \tag{2.7}$$

where $y(x,t)$ is the transverse displacement, m_b is the mass per unit length, and E_bI is the flexural stiffness of the beam. By using the method of separation of variables as outlined in Tedesco et al. (1999), the time-independent solution is given by:

$$y(x) = C_1 \sinh \lambda x + C_2 \cosh \lambda x + C_3 \sin \beta x + C_4 \cos \beta x \tag{2.8}$$

In Eq. (2.8), $\lambda^2 = s_1^2$ *and* $\beta^2 = -s_2^2$, where:

$$s_{1,2}^2 = \frac{T}{2E_bI}\left[1 \pm \left(1 + 4m_b \frac{\omega_n^2 E_b I}{T^2}\right)^{1/2}\right] \tag{2.9}$$

and the constants C_1, C_2, C_3 and C_4 are evaluated by satisfying the specific boundary conditions, ω_n is the n-th angular natural frequency. In the study presented in this dissertation, fixed-fixed boundaries were considered.

To simulate the interaction between the chain and the beam, the beam was virtually located at the $(N+1)^{th}$ position of the chain albeit it was not treated as a particle. The beam acceleration $\ddot{u}_b$ can be written:

$$\ddot{u}_b(t) = \sum_{r=1}^{\infty} \phi_r(x)\ddot{q}_r(t) = \sum_{r=1}^{\infty} \phi_r(x)\left[\frac{1}{M_r}\int_0^L F(t)\phi_r(x)dx - \omega_r^2 q_r\right] \tag{2.10}$$

where $\phi_r(x)$, $q_r(t)$, and M_r are the r-th normal mode, normalized coordinate, and generalized (modal) mass, respectively; $F(t)$ is the force applied to the beam by the solitary pulse. For more details the reader is referred to Cai et al. (2013a).

3.0 NUMERICAL STUDIES

In this chapter, we describe the numerical models formulated to simulate the interaction between single or double straight and L-shaped chains in contact with a slender beam at the mid-span. The analysis consisted of using a discrete particle model to predict the propagation of the wave along the chain and to derive the shape and amplitude of the solitary pulse at the chain-beam interface. A continuous beam theory was then used to estimate the response of the structure subjected to the forcing function equal to the solitary pulse.

This chapter was extracted from our published paper entitled “On the use of L-shaped granular chains for the assessment of thermal stress in slender structures”.

3.1 ONE STRAIGHT CHAIN

In this section, we describe the case of a beam in contact with one single chain of particles.

A 914 mm long stainless beam, clamped at both ends, was considered. The beam was 9.525 mm wide and 19.05 mm deep. For the steel we assumed ρ = 7800 kg/m^3, E = 200 GPa, ν = 0.28, and yielding stress σ_Y = 206.8 MPa. The geometric and mechanical properties of the beam were such that its Euler buckling load F_{cr} and the corresponding buckling stress σ_{cr} were equal to -12.95 kN and -71.395 MPa, respectively.

The single chain consisted of fourteen 19.05 mm in diameter particles. Each particle weighed 29 g. and was made of stainless steel for which the Young's modulus and the Poisson's ratio were considered equal to 200 GPa and 0.28, respectively. Figure 3.1 shows the top view of the numerical setup. The force profile associated with the propagation of the solitary pulses was measured at the center of the 5^{th} and 10^{th} particles away from the interface. These particles are hereafter indicated as sensor bead 2 (S2) and sensor bead 1 (S1), respectively, and the location of the measurement is indicated as sensing site. The pre-compression force was set to zero and the effect of a striker was simulated by setting the initial velocity $\dot{u}_0$ of the first particle at 0.3018 m/s. This value was chosen in agreement with some experimental studies conducted in our laboratory.

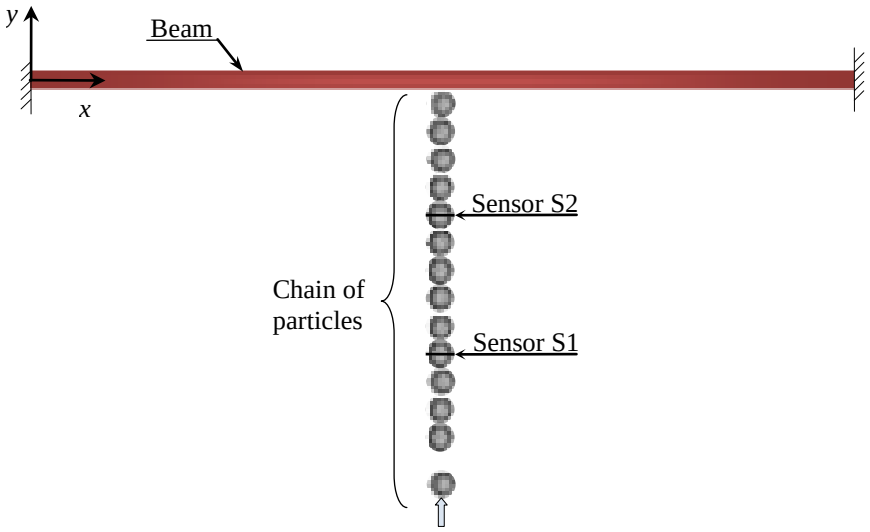

Figure 3.1. Top view of the numerical simulation setup. The beam is fixed-fixed and in contact with the granular medium at the midspan. The chain contains N = 14 particles. (Drawing not to scale)

Figure 3.2 shows the dynamic force measured at the two sensing site when the axial stress in the beam is zero. Few pulses are visible. The first pulse is the incident solitary wave (ISW) traveling from the first particle of the chain towards the beam. The next pulse is the

reflected solitary wave (RSW) which is generated by the reflection of the ISW at the beam-chain interface. Some pulses are induced by the vibration of the beam: as the incident pulse reaches the interface part of its energy is reflected to become the RSW and part triggers the motion of the beam. When the beam bounces back toward the chain a train of pulses, named vibration-based solitary wave (VSW), is generated.

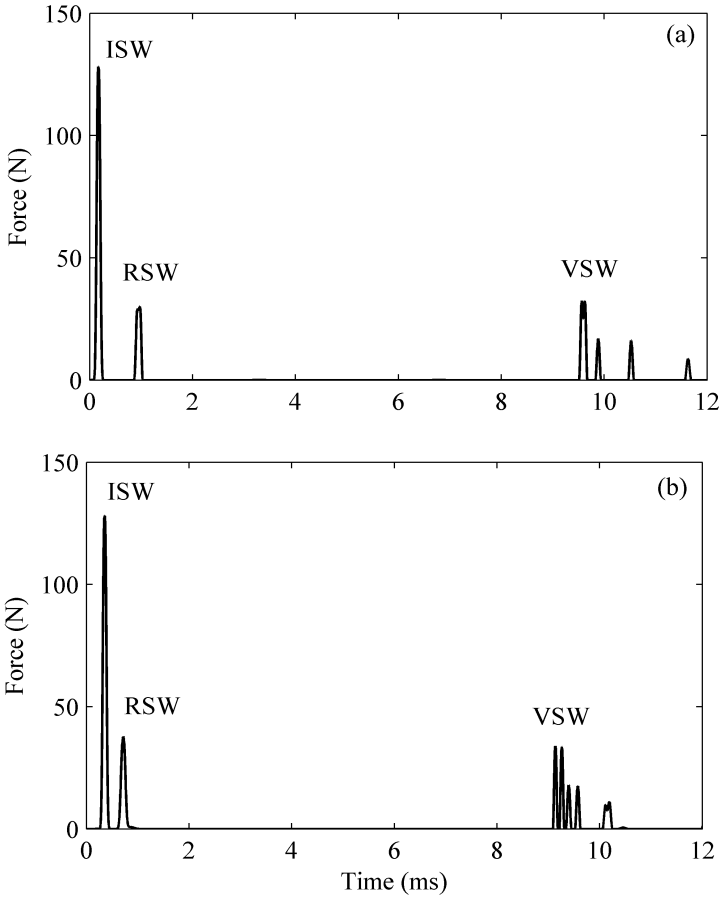

Figure 3.2. One chain configuration. Force profile measured at: (a) sensor S1, and (b) sensor S2, when the axial stress in the beam is zero.

The speed of the ISW was calculated by detecting the arrival time of the pulse's peak at the sensors' site and knowing their relative distance in the chain. We found a numerical value of 516.26 m/s which is 7.1% higher than the analytical value of 481.90 m/s computed by means of

Eq. (2.5). This difference is likely related to the method utilized to solve the equations analytically. Since the static pre-compression is assumed null, we used F_m=128.2 N, i.e. the dynamic force associated with the force propagation of the solitary wave. The speed of the reflected wave is 400.42 m/s which is only 1.6% higher than the analytical prediction of 394.10 m/s computed by considering F_m=38.35 N.

To describe the effect of the axial force *T* on the characteristics of the solitary waves, Fig. 3.3 is presented. It shows the force profile of the solitary wave measured at S2 when the beam is close to buckling (Fig. 3.3a) and close to yielding (Fig. 3.3b). By comparing the time scale of the two graphs, we observe that the arrival time of the VSW is delayed due to the longer period of vibration of the compressed beam. When the axial stress increases the beam's natural frequency increases and its period of vibration decreases. As the ISW is not affected by the force *T*, we evaluated again the difference between the analytical and the numerical speed of the incident wave, and it is still in the order of 5%, suggesting that the discrete particle model is able to predict the propagation of the solitary waves irrespective of the axial stress applied to the beam.

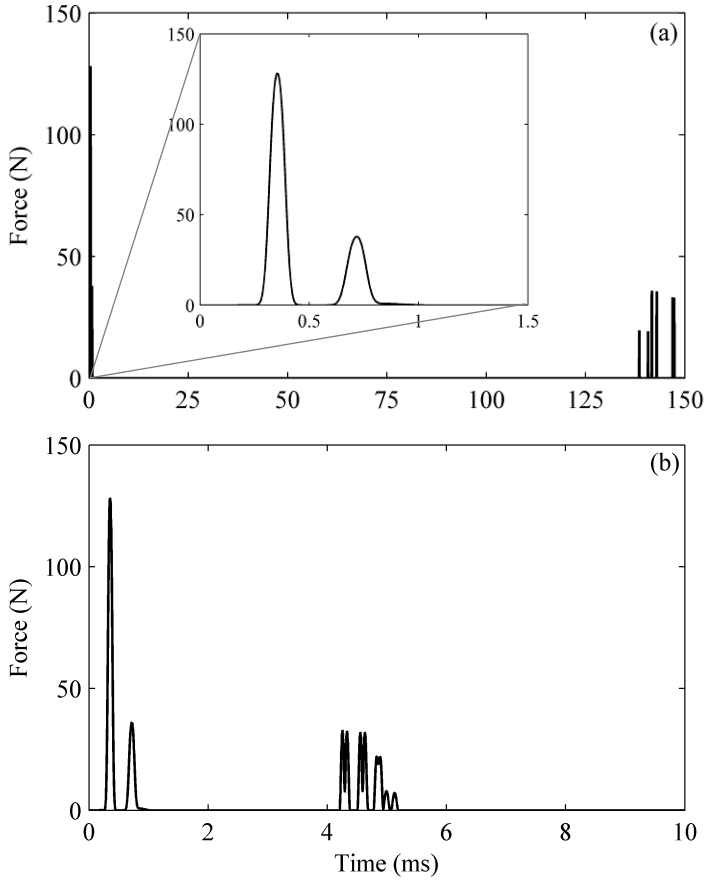

Figure 3.3. One chain configuration. Force profile measured at sensor S2 when the axial stress in the beam is: (a) -66.13 MPa (93% buckling stress), and (b) 192.82 MPa (93% yielding stress).

To quantify the effect of the temperature on the propagation of the HNSWs, the four features summarized in Table 3.1 were extracted from the dynamic force measured at the sensing sites S1 and S2. The first two features are related to the amplitudes of the pulses, whereas the remaining features are related to the time-of-flight (TOF) which is the difference of the time of arrival at the same sensor site.

Table 3.1. One chain configuration. Features extracted from the force profiles.

Feature	Description
RSW/ISW	Ratio of the RSW amplitude divided by the ISW amplitude.
VSW/ISW	Ratio of the VSW amplitude divided by the ISW amplitude
TOF RSW	Transit time between the incident and the reflected wave
TOF VSW	Transit time between the incident and the vibration-induced wave

Figure 3.4 displays the wave features measured at sensor S1 as a function of the beam's stress. The features relative to the reflected wave denote a monotonous trend above -40 MPa. Below that mark, a change in the gradient's sign is visible; this variation is associated with the change of the value of the coefficient ϕ_r^2/M_r, associated with the r-th normal mode and the corresponding generalized mass. This coefficient is the multiple of the force applied to the beam by the solitary pulse (see Eq. (2.10)), it is used to compute the beam acceleration, and it has a trend like the TOF RSW. The value of this coefficient is minimum at -40 MPa. When the value of ϕ_r^2/M_r decreases, the beam's acceleration decreases, and the beam acts as a particle with higher stiffness. Owing to this higher stiffness, the amplitude of the reflected wave increases and its traveling time decreases. The ambiguous response of the VSW/ISW feature is likely due to the combination of the vibrational modes that change with the variation of the axial stress. Nonetheless, the time of flight of the VSW which is computed by finding the arrival of the front wave sharply increases as the stress approaches buckling. By comparing the time of flight associated with both the RSW and the VSW, it can be seen that the latter is more sensitive to the axial stress. This is related with the period of vibration of the beam, which can be expressed in terms of the angular natural frequency ω_n (Tedesco et al. 1999):

$$\omega_n = \frac{\beta_n}{\sqrt{m_b}}\sqrt{T + \beta_n^2 E_b I} \tag{3.1}$$

where T is the axial load, and β_n is the n-th root of the characteristic equation.

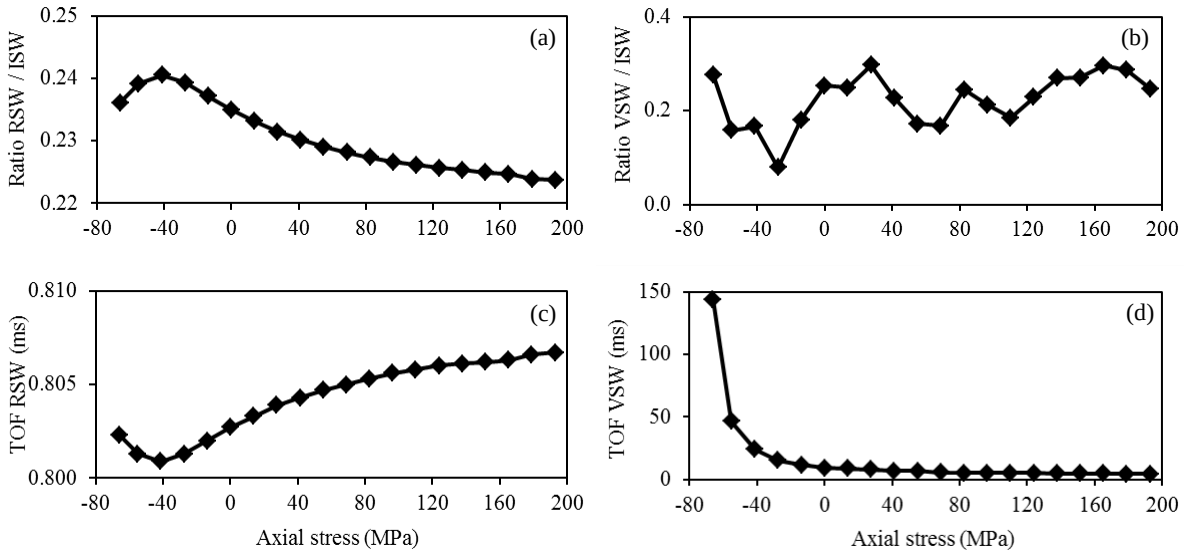

Figure 3.4. One chain configuration. Solitary wave features extracted from the force profiles measured at sensor S1 as a function of the axial stress. (a) Ratio associated with the amplitude of the reflected and incident waves. (b) Ratio associated with the amplitude of the vibration-induced and incident waves. (c) Time of flight of the reflected wave. (d) Time of flight of the vibration-induced wave.

To compare directly the sensitivity of the four features to stress, we normalized the values plotted in Fig. 3.4 with respect to their corresponding maximum value. The results are presented in Fig. 3.5. The feature associated with the amplitude of the reflected wave decreases by 6% when T spans from buckling to yielding. Across the same range, the time of flight relative to the vibration-induced wave decreases by 95%.

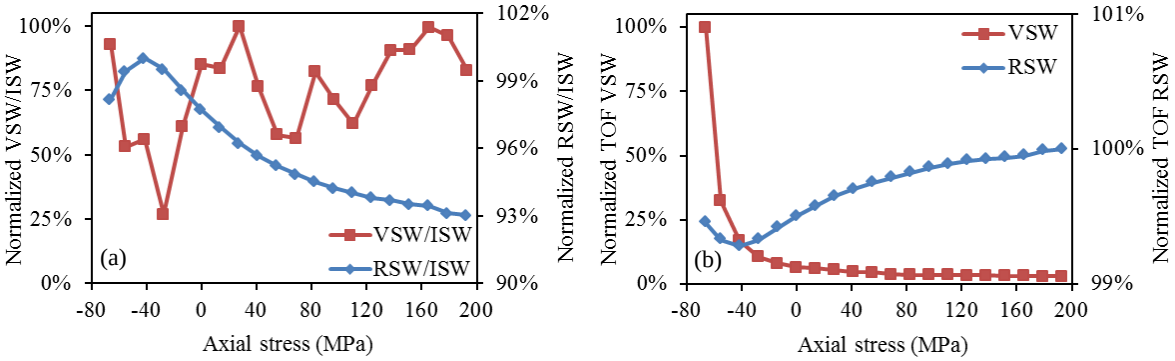

Figure 3.5. One chain configuration. Normalized features extracted from the force profiles measured at sensor S1 as a function of the axial stress. (a) Ratio associated with the amplitude of the reflected and incident waves, and ratio relative to the amplitude of the vibration-induced and incident waves. (b) Time of flight of the reflected wave and the vibration-induced wave.

Finally, Figure 3.6 shows the absolute and the normalized speed of the reflected solitary pulse as a function of the axial stress. The variation is below 2% because the stress T does not alter the beam's stiffness which affects the characteristics of the RSW. Nonetheless, it is interesting to compare these results to the acoustoelastic phenomenon in which the speed of linear waves in a bulk medium or a waveguide depends upon the applied stress. For example, Rizzo and co-authors (Lanza di Scalea et al. 2003, Rizzo and Lanza di Scalea 2003, 2004) found that the velocity of the longitudinal ultrasonic wave propagating in solid circular waveguides made of high-strength steel is in the order of 1% per GPa of stress. This implies that some of the features selected in this study and relative to the propagation of the solitary waves in a granular medium are more effective than the acoustoelastic method at determining applied stress.

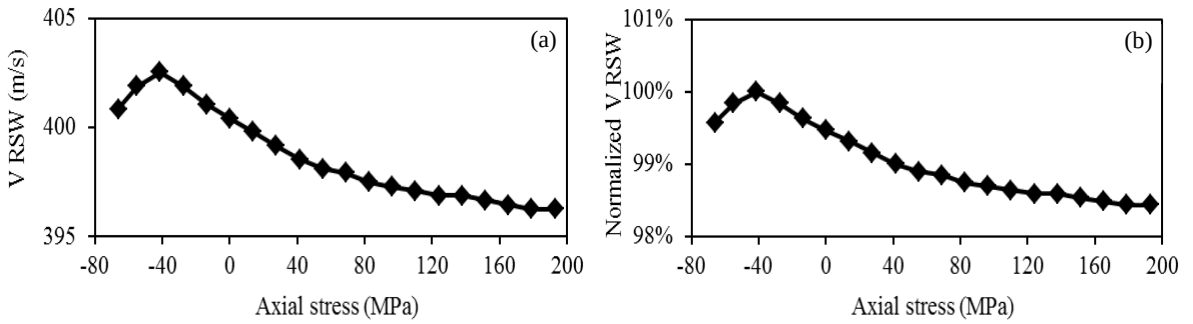

Figure 3.6. One chain configuration. (a) Velocity and (b) normalized velocity of the reflected solitary wave as a function of the axial stress.

3.2 TWO STRAIGHT CHAINS

The use of a single granular medium, although effective, may result unpractical as the contact between the chain and the structure being inspected must be guaranteed. Thus, we also modeled the presence of a second chain of particles located at the opposite face of the beam's mid-span according to the scheme shown in Fig. 3.7. In the second chain the last particle was considered either free to move or fixed. The objective of the study was to determine whether this second configuration offer the same sensitivity to the presence of axial stress when compared to the single-chain configuration.

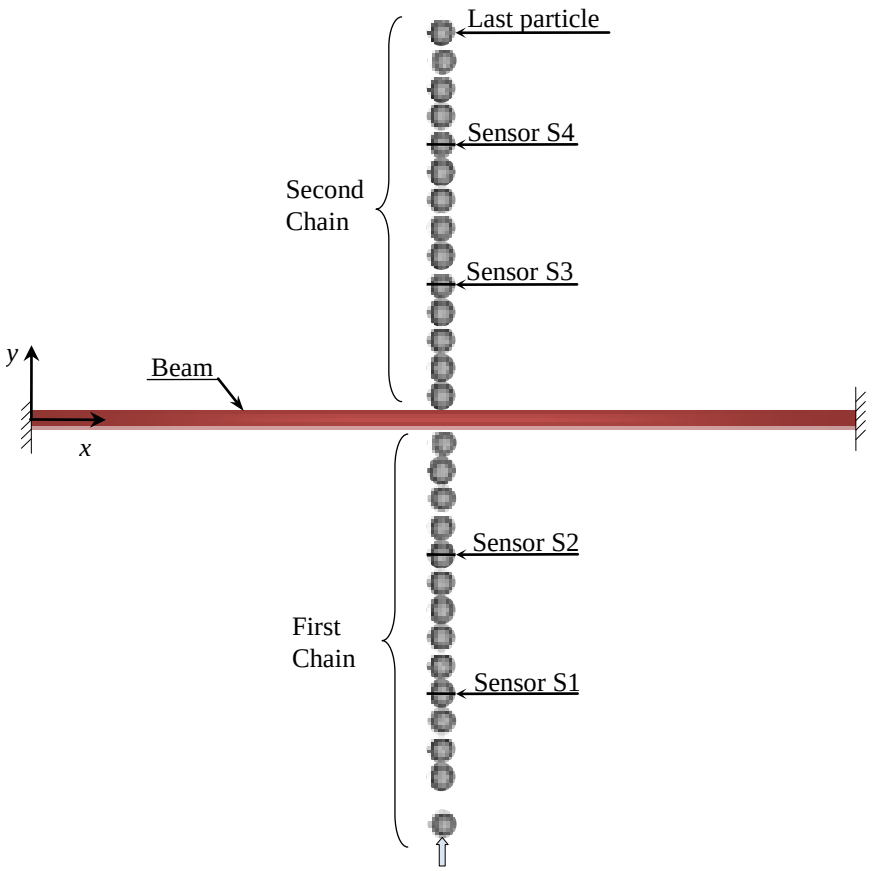

Figure 3.7. Top view of the numerical simulation setup. The beam is clamped at two ends. One or two chains of particles are in contact with the beam at its mid-span. Each chain consists of N=14 particles. (Drawing not to scale)

3.2.1 Numerical formulation

For the sake of clarity we define as chain 1, the granules subjected to the action of the striker, i.e. the granules where the solitary wave pulse is induced. Therefore, chain 2 indicates the chain where the solitary wave is transmitted after traveling through the cross-section of the beam.

The discrete particle model associated with chain 1 is formulated in terms of Eqs. (2.3) and (2.4). For the particles located at the two ends of the first chain, i.e. when $i=1$ and $i=N$, Eq. (2.4) becomes:

$$\ddot{u}_1 = \eta_c \delta_0^{3/2} - \eta_b \left[\left(\delta_0 - u_2 + u_1 \right) \right]_+^{3/2} \tag{3.2a}$$

$$\ddot{u}_N = \eta_c \left[(\delta_0 - u_N + u_{N-1}) \right]_+^{3/2} - \eta_b \left[\left(\delta_{b0} - u_b + u_N \right) \right]_+^{3/2} \tag{3.2b}$$

where δ_{b0} represents the initial approach between the last bead and the beam, u_b is the displacement of the contact point on the beam, and η_b is the normalized stiffness constant $\eta_b = A_b / m_b$. For the particles located at the two ends of the second chain, i.e. when $i=N+1$ and $i=2N$, the equation of motion becomes:

$$\ddot{u}_{N+1} = \eta_b \left[\left(\delta_{b0} - u_b + u_{N+1} \right) \right]_+^{3/2} - \eta_c \left[(\delta_0 - u_{N+2} + u_{N+1}) \right]_+^{3/2} \tag{3.3a}$$

$$\ddot{u}_{2N} = \eta_c \left[(\delta_0 - u_{2N} + u_{2N-1}) \right]_+^{3/2} - \eta_c \left[(\delta_0 + u_{2N}) \right]_+^{3/2} \tag{3.3b}$$

This formulation assumes that the last particle of chain 2 is free. However, if this particle is restrained, then the associated equations of motion are modified as:

$$\ddot{u}_{2N-1} = \eta_c \left[(\delta_0 - u_{2N-1} + u_{2N-2}) \right]_+^{3/2} - \eta_c \left[(\delta_0 + u_{2N-1}) \right]_+^{3/2} \tag{3.4a}$$

$$\ddot{u}_{2N} = \eta_c \left[(\delta_0 + u_{2N-1}) \right]_+^{3/2} - \eta_c (\delta_0)^{3/2} \tag{3.4b}$$

The differential equation of motion for other particles is same as Eq. (2.3). The discrete particle model relative to both equations is then coupled the continuous beam theory as described in the previous sections. In the simulation, the effect of the last particle in the first chain was simulated by applying a force to the beam and vice versa, and the influence of the beam on the first particle in the second chain was simulated by applying a force on the first particle in the second chain and vice versa. The force applied to the beam by the solitary pulse is:

$$F(t) = A_b \left[\left[\left(\delta_{b0} + u_N - u_b \right) \right]_+^{3/2} - \left[\left(\delta_{b0} + u_b - u_{N+1} \right) \right]_+^{3/2} \right] \tag{3.5}$$

By using this force, the beam acceleration $\ddot{u}_b$ can be computed by Eq. (2.10).

From the equations above, it can be found that all particles and the beam are coupled together by differential equations. By inspecting Eqs. (3.2b) and (3.3a), it can be seen that the last particle of the first chain and the first particle of the second chain are coupled to the beam, and they affect together. Moreover, from Eqs. (3.3b) and (3.4b) which are the differential equations of the last particle of the second chain for the free and fixed boundary conditions, respectively, we can find that boundary conditions influence on all other particles, because there are *2N+1* coupled differential equations. The second order differential equations can be solved using the 4^{th} order Runge-Kutta method using MATLAB.

The beam and the granules were the same as in Section 3.1. The dynamic force associated with the propagation of the solitary pulses was measured at the four sensor sites, indicated as S1, …, S4, shown in Fig. 3.7. Sensor S1 was the 5^{th} particle in the first chain, nine beads away from the beam. Site S2 was the 10^{th} particle in chain 1. Sensors S3 and S4 were located at the 5^{th} and 10^{th} particle location, respectively, in chain 2. For generation of the HNSW the same an initial velocity of 0.3018 m/s was applied to the first particle. In order to investigate the effect of boundary condition in the second chain, we used two conditions for the last particle in the chain 2, namely free and fixed condition.

3.2.2 Numerical results: last particle is free

Figure 3.8 shows the force profile measured at the sensing sites S2 and S3 when the axial stress is null. Three main pulses are visible in the first chain (Fig. 3.8(a)). They are the ISW, the RSW, and the vibration-based solitary wave which we indicate here as (FVSW), where the first letter in the acronym identifies the fact that this pulse is measured in the first chain. Figure 3.8(b) shows

the force profile measured in the second chain. To ease the readability of the transmitted wave, the vertical scale was reduced. Many fragmented pulses are visible. The first one is generated by the transmission of the ISW through the beam's thickness and we named it the transmitted solitary wave (TSW). The next few pulses are generated by the vibration of the beam and they are indicated as SVSW, where the first letter of the acronym denotes the second chain. The generation of the reflected wave induces negative acceleration in the particles of the first chain; this acceleration move the particles to the negative *y* direction and this causes a gap between the last particle of chain 1 and the beam. The portion of the acoustic energy carried by the ISW and transmitted through the thickness of the beam induces positive acceleration in the particles of the second chain. These particles move along the positive *y* direction faster than the beam, because they are free and their mass is smaller than the mass of the beam. Thus, a gap is generated between the structure and the first particle of chain 2. The presence of the two gaps allows the vibration of the beam.

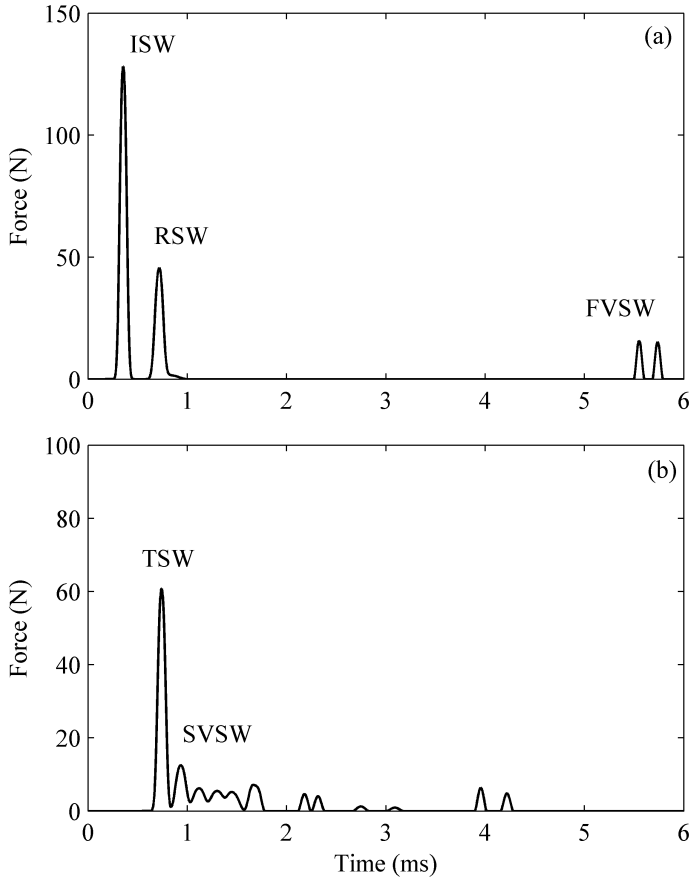

Figure 3.8. Two chains configuration. Force profile measured at: (a) sensor S2, and (b) sensor S3, when the axial stress in the beam is zero and the last particle of the second chain is free to move.

A direct comparison between the use of one and two granular systems is carried out by means of Fig. 3.9, which shows the force profiles measured at S2 for both cases. Note the different time scales. While the incident pulse is identical, differences are visible for both the reflected and the vibration-induced solitary pulses; the presence of a single chain allows for the beam to complete a half cycle vibration.

The waves measured at the sensing sites S2 and S3, i.e. before and after the beam, at axial stress equal to -66.13 and 192.82 MPa are shown in Figure 3.10. There are some differences in the RSWs and TSWs which are related to the beam's stiffness. There are evident

changes in the FVSWs and SVSWs, because they are related to the natural frequencies of the beam.

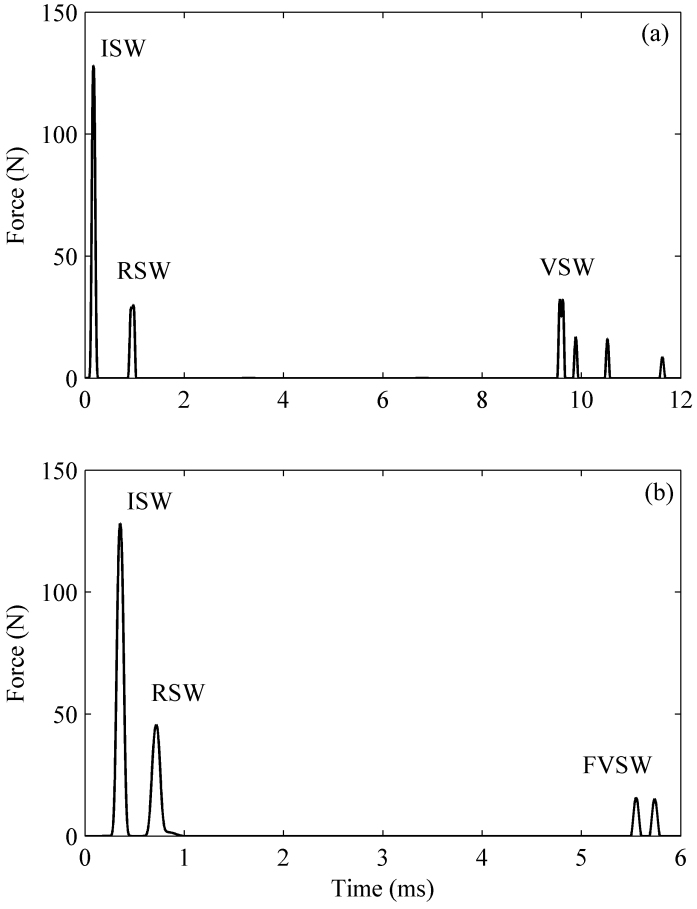

Figure 3.9. Force profile measured at sensor S2 when (a) there is only one chain of particles, and (b) there are two chains of particles. The value of the axial stress in the beam is zero.

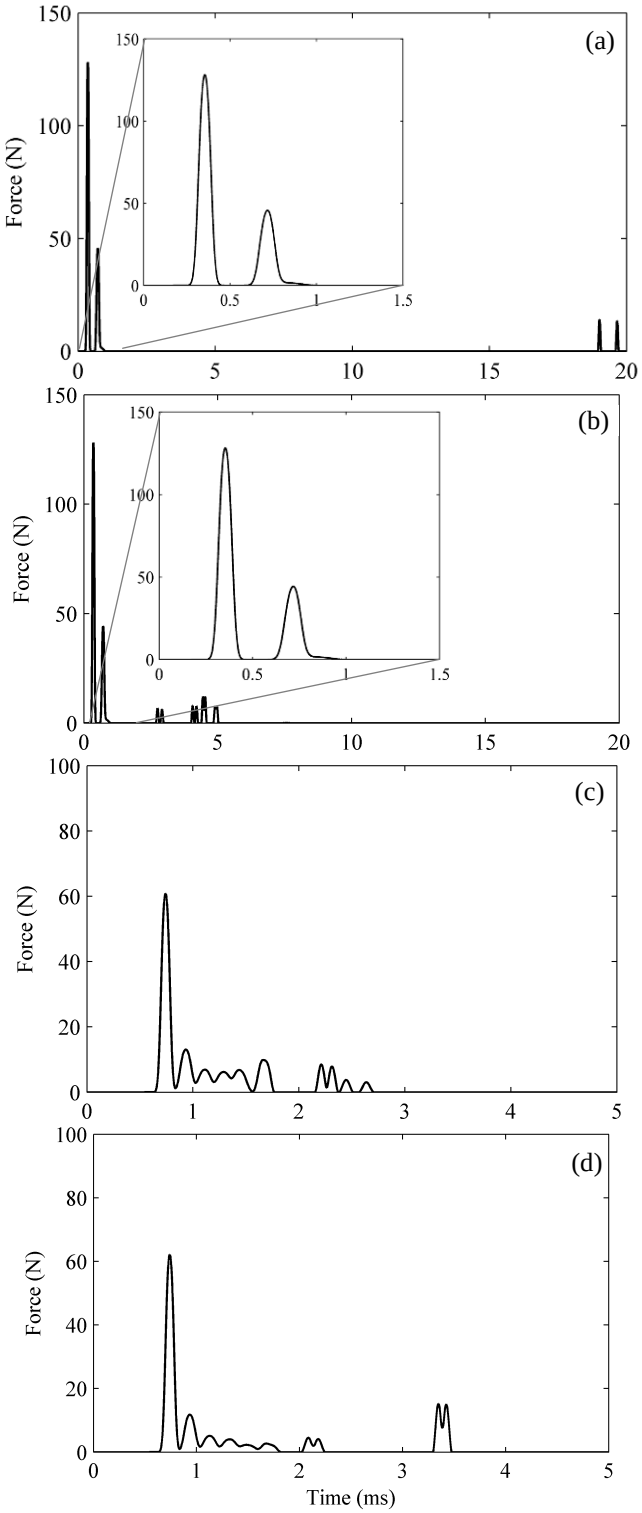

Figure 3.10. Two chains configuration. (a-b) Force profile measured at sensor S2 when the axial stress in the beam is -66.13 MPa (93% buckling stress) and 192.82 MPa (93% yielding stress), respectively. (c-d) Force profile measured at sensor S3 when the axial stress in the beam is -66.13 MPa (93% buckling stress) and 192.82 MPa (93% yielding stress), respectively.

It must be noted that the configuration with a beam in contact with two chains is similar to the case of a single long chain with an impurity at the center. This system was studied by some researchers (Tichler et al., 2013; Li et al., 2013). We will discuss in a later section the analogy between the two systems. Similar to what described in Section 3.1, we extracted the few features listed in Table 3.2.

Table 3.2. Two chains configuration. Features extracted from the force profiles.

Feature	Description
TSW/ISW	Ratio of the TSW amplitude divided by the ISW amplitude.
TSW/RSW	Ratio of the TSW amplitude divided by the RSW amplitude
FVSW/ISW	Ratio of the FVSW amplitude divided by the ISW amplitude
SVSW/TSW	Ratio of the SVSW amplitude divided by the TSW amplitude
TOF RSW	Transit time between the incident and the reflected wave
TOF TSW	Transit time between the reflected wave and the transmitted wave
TOF FVSW	Transit time between the incident and the FVSW
TOF SVSW	Transit time between the transmitted wave and the SVSW

Figure 3.11 presents the normalized features associated with the pulse amplitude (Fig. 3.11(a)) and the pulse TOF (Fig. 3.11(b)) as a function of the axial stress. The features refer to the solitary pulses measured at the sites S2 and S3. The ratios TSW/ISW and TSW/RSW show a few percent variation across the whole range of linear stress and the reason is that the reflected and transmitted pulse are minimally affected by the beam's stiffness and axial load. Similar conclusion can be drawn for the time of flight associated with these two pulses. Random changes are visible for the ratio FVSW/ISW and this is likely due to the contribution of the modes of vibration at any given axial stress. This modes' contribution affects the amplitude but not the time of arrival of the pulses generated in the first chain by the vibration of the beam. For this feature, the TOF of the FVSW sharply decreases with the increase of the axial stress, and it

reduces by 75% within the compression range. Finally, Fig. 3.11 shows the absence of significant changes associated with the ratio SVSW/TSW and TOF SVSW. We believe that this is related to the presence of the vibration higher modes.

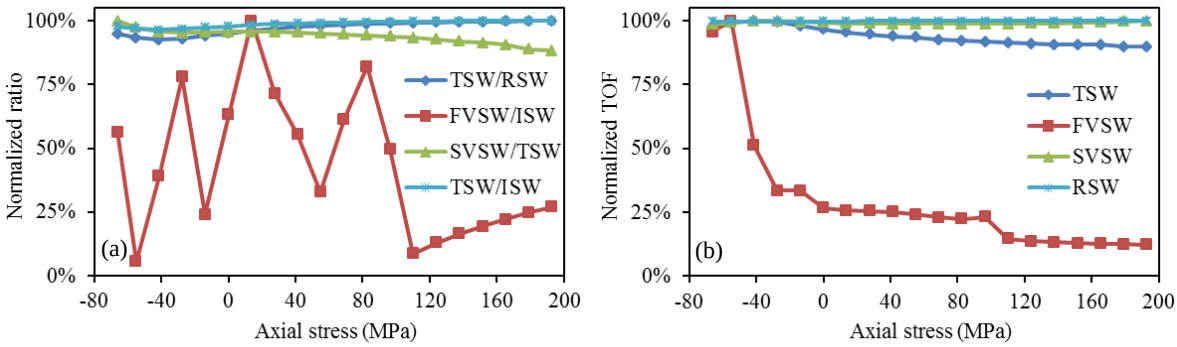

Figure 3.11. Two chains configuration. Normalized features extracted from the force profiles measured at sensors S2 and S3 as a function of the axial stress. The last particle of the second chain is free to move.

The comparison between Fig. 3.5 and Fig. 3.11 suggests that the TOF relative to the beam's vibration measured by the single chain provides the largest sensitivity to the presence of axial stress. This is somehow expected as the presence of the second chain restraints the motion of the linear system.

3.2.3 Numerical results: last particle is fixed

Finally, we assumed that the last particle of the second chain is fixed. The force profile at zero stress of the solitary wave measured at sensor S2 and S3 is shown in Fig. 3.12. Only the pulse induced by the beam vibration shows some differences with respect to Fig. 3.12(a). Figure 3.12(b) reveals the presence of a pulse trailing the SVSW. This pulse is generated by the reflection of the transmitted pulse from the last particle of chain 2 which is fixed; we named this

pulse as the boundary reflected solitary wave (BRSW). The figure shows that the BRSW is higher than the transmitted wave; we hypothesize that this is due to constructive interference of the SVSW and TSW at the end of the second chain; in fact, it can be seen from Fig. 3.12(b) that the amplitude of the BRSW is about the sum of the amplitudes of the TSW and SVSW.

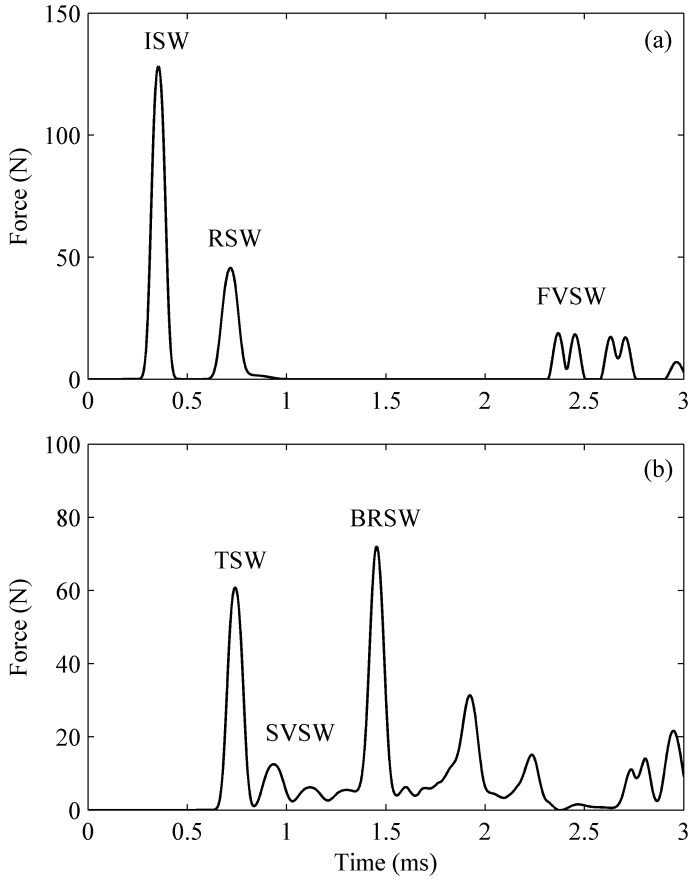

Figure 3.12. Two chains configuration. Force profile measured at: (a) sensor S2, and (b) sensor S3, when the axial stress in the beam is zero and the last particle of the second chain is fixed.

Figure 3.13 shows the results of solitary wave features extracted from the solitary force profiles measured at sensors S1 and S4 as a function of the axial stress of the beam. The normalized values of solitary wave features shown in Figure 3.13 are shown in Figure 3.14. It can be seen that there is high variation with respect to the axial stress for the feature TOF TSW,

but it may not helpful for buckling prediction, because its value is very small, around 10 μs. By comparing these results with those results shown in Figure 2.11, it can be found that there is no significant difference in the trend of results for all features except for feature FVSIW/ISW that is related to have different contribution mode.

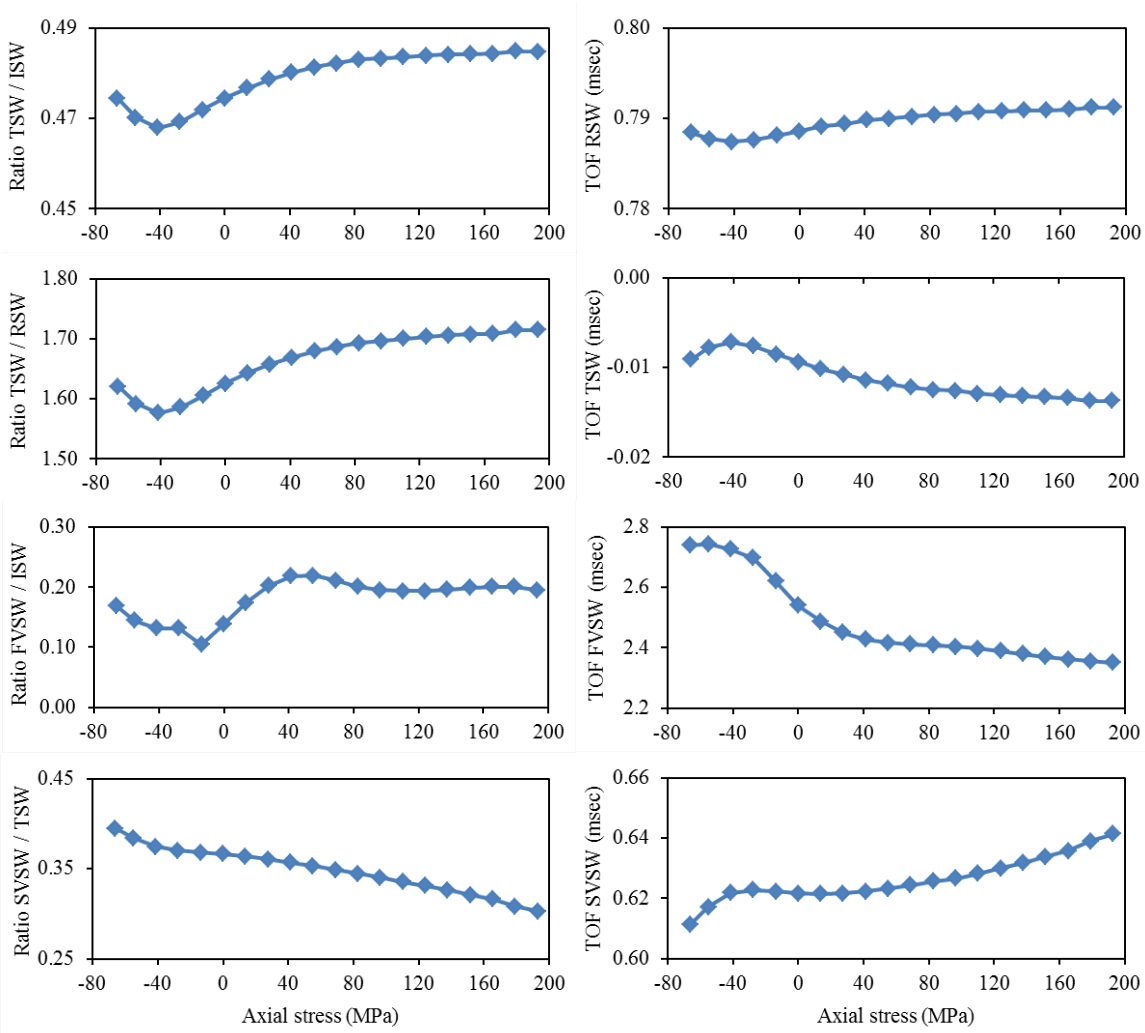

Figure 3.13. Solitary wave features extracted from the solitary force profiles measured at sensors S1 and S4 as a function of the axial stress of the beam. The last particle is fixed.

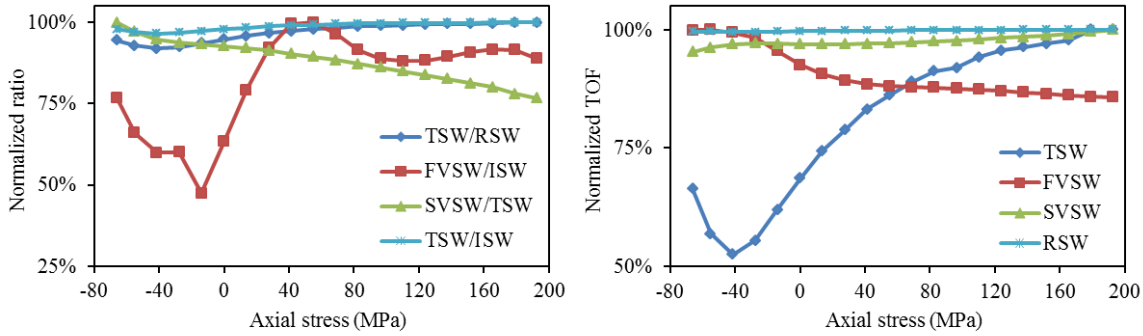

Figure 3.14. Normalized results of solitary wave features extracted from the solitary force profiles measured at sensors S1 and S4 as a function of the axial stress of the beam. The last particle is fixed.

Similar to Fig. 3.14, Fig. 3.15 shows the normalized values at sensing sites S2 and S3. We notice that the variation associated with the time of flight of the vibration-induced wave in the first chain (TOF FSVW) is lower. This is related to the generation of the FSVW by the BRSW not by the vibration of the beam. The largest variation with respect to the axial stress is visible at the feature associated with the amplitude of the vibration-induced solitary wave propagating in the first chain (feature FVSW/ISW). However, this feature is not helpful at predicting buckling as there is no change before buckling.

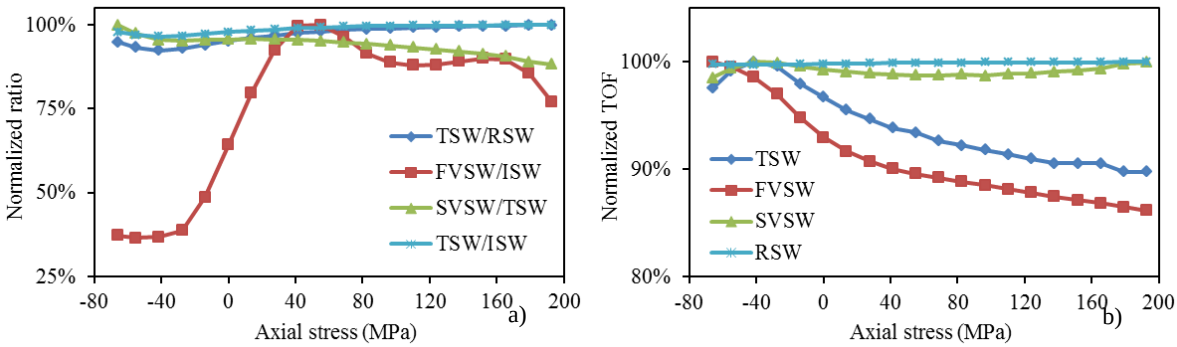

Figure 3.15. Two chains configuration. Normalized features extracted from the force profiles measured at sensors S2 and S3 as a function of the axial stress. The last particle of the second chain is fixed.

3.2.4 Comparative analysis

In order to compare the three probing configurations and their ability to predict incipient buckling, we selected some features from those considered in the previous sections and they are presented in Fig. 3.16. Figure 3.16(a) shows the normalized amplitude ratio relative to the reflected wave single chain and the normalized ratios relative to the vibration-induced waves when two chains are used. All three features vary more than 5% across the entire spectrum of stress considered in this study. Notice that the boundary condition associated with the last particle of the second chain does not have any influence on the feature and the two graphs overlap perfectly. Figure 3.16(b) shows instead the time of flight associated with the vibration-induced solitary waves for the three scenarios. Overall the single chain provides the largest variation with respect to stress; in fact, when the beam is confined by the two chains of particles its vibration is partially restrained by the second chain.

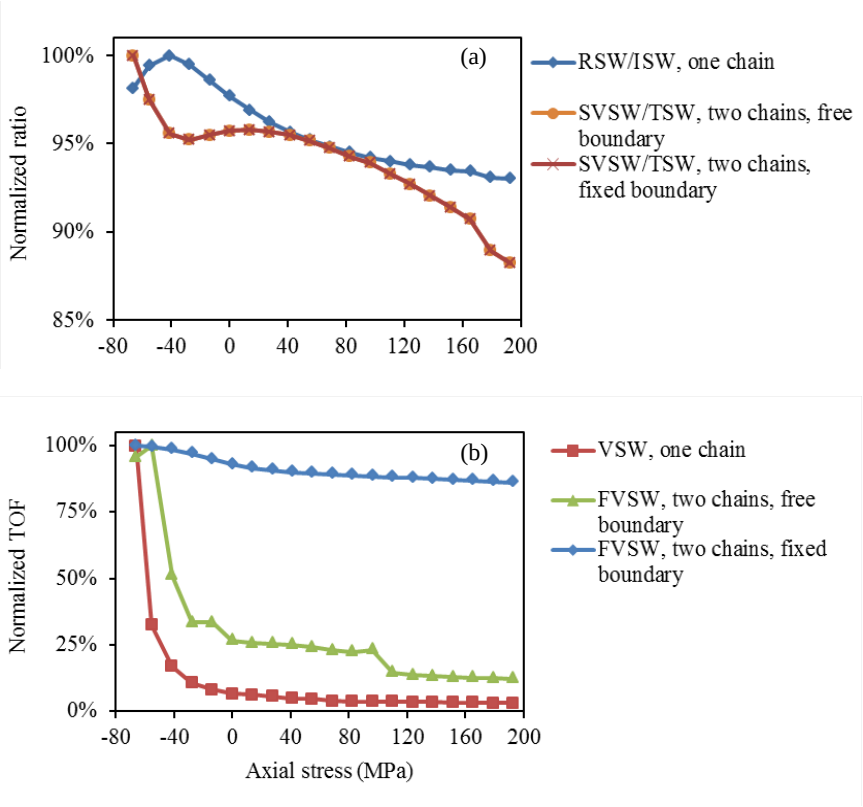

Figure 3.16. Comparison among different normalized features relative to (a) the amplitude and (b) the time of flight of the solitary waves.

3.3 L-SHAPED SINGLE CHAIN

Guaranteeing the contact of the straight chain to the beam might be difficult. Therefore, we studied also L-shaped chains. First, the numerical simulation method by combining the discrete particle model and the continuum beam theory is described. Then, the effect of the beam's axil load is presented.

3.3.1 Implementation

The interaction between two adjacent particles was confined to normal displacement between them whereas the transverse displacement was neglected. Also, normal displacement between a given particle and the guide was considered. Figure 3.17 schematizes the granular system made of identical N beads having radius R, and mass m. When this system is subjected to the dynamic force generated by the propagation of a solitary pulse, the normal approach between two neighboring particles can be written as:

$$u_{n,(i-1,i)} = \left[2R - \left| \mathbf{v}_i - \mathbf{v}_{i-1} \right| \right]_+ \quad , \quad 2 \le i \le N \tag{3.6}$$

where u_n represents the normal approach between two particles due to the dynamic force, and $\mathbf{v}_i$ is the location vector of the i-th particle's center with respect to its origin. Eq. (3.6) does not contain any initial static deformation of the particles due to their weight, which means that precompression was neglected. The bracket $[s]_+$ denotes $max(s,0)$, i.e. the system is unable to support tensile force between particles. Based on the computed normal approach, the normal contact force $\boldsymbol{f}_n$ between two neighboring particles and shown in Fig. 3.17 can be represented as:

$$\boldsymbol{f}_{n,(i-1,i)} = \left[A_n u_{n,(i-1,i)}^{3/2} \right] \hat{\boldsymbol{n}}_{i-1,i} \quad , \quad 2 \le i \le N \tag{3.7}$$

where A_n is the contact coefficient between two spherical particles that can be expressed as $E\sqrt{2R}/[3(1-\nu^2)]$ where E and ν are the Young's modulus and the Poisson's ratio of the grain, respectively; and $\hat{\boldsymbol{n}}_{i-1,i}$ represents the unit normal vector from the center of the $(i+1)$-th particle to the center of the i-th particle, and it can be described as:

$$\hat{\boldsymbol{n}}_{i-1,i} = \frac{\mathbf{v}_i - \mathbf{v}_{i-1}}{\left| \mathbf{v}_i - \mathbf{v}_{i-1} \right|} \tag{3.8}.$$

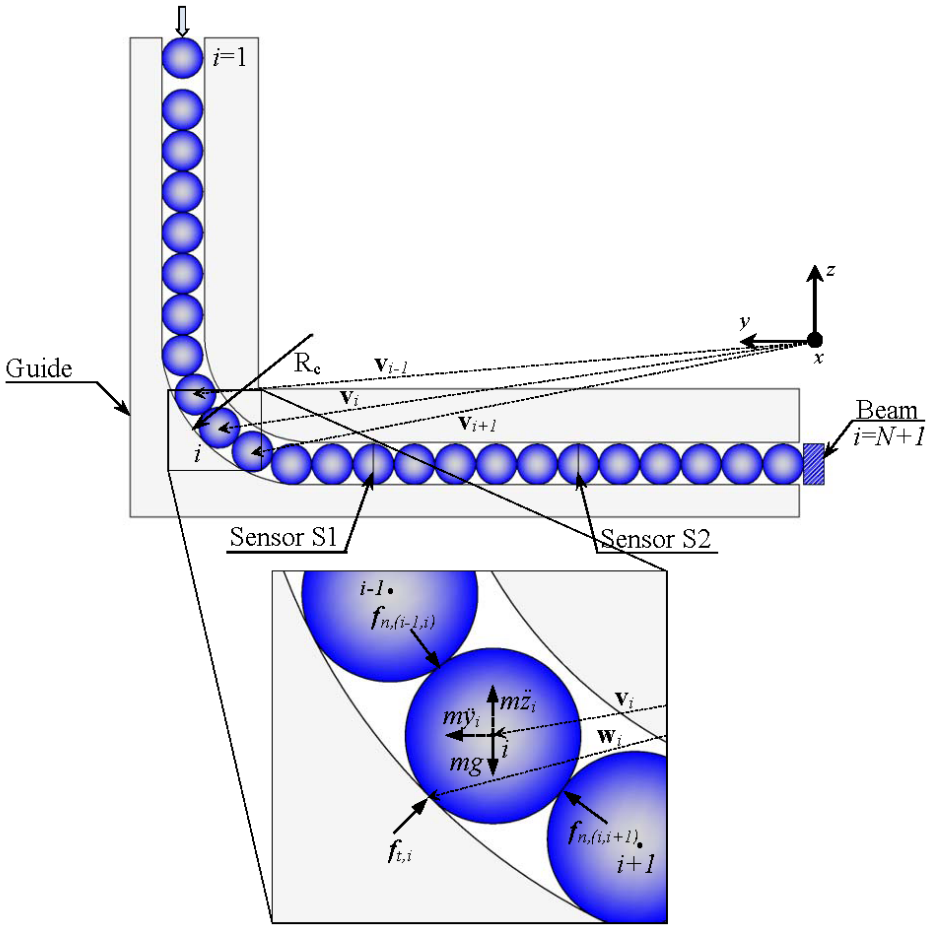

Figure 3.17. Setup for the numerical simulation. The beam is clamped at two ends, and there is one L-shape chain of particles at the mid-span of the beam. The drawing is in scale.

The normal contact force between the *N*-th particle and the beam, which can be considered as the *(N+1)*-th particle, can be written as:

$$\boldsymbol{f}_{n,(N,N+1)} = \left[A_{n,b} \left[R + \frac{w_b}{2} - \left| \mathbf{v}_{N+1} - \mathbf{v}_N \right| \right]_+^{3/2} \right] \hat{\boldsymbol{n}}_{N,N+1} \tag{3.9}$$

where w_b is the width of the beam's cross-section, and $A_{n,b}$ is the contact coefficient between the grain and the adjacent beam given by:

$$A_{n,b} = \frac{4\sqrt{R}}{3} \left(\frac{1-\nu^2}{E} + \frac{1-\nu_b^2}{E_b} \right)^{-1} \tag{3.10}$$

where E_b and ν_b are the Young's modulus and the Poisson's ratio of the beam's material.

For all grains of the chain, the normal approach takes into account the interaction between the *i*-th particle and the guide, and it is expressed as:

$$u_{t,i} = \left[R - \left| \mathbf{v}_i - \mathbf{w}_i \right| \right]_+ \quad , \quad 1 \le i \le N \tag{3.11}$$

where $u_{t,i}$ represents the approach between the *i*-th particle and the guide which is perpendicular to the direction of the wave propagation, and $\mathbf{w}_i$ is the location vector of the *i*-th particle's contact point with the guide (see Fig. 3.17). Based on the computed normal approach, the contact force $\boldsymbol{f}_{t,i}$ between the *i*-th particle and the guide can be expressed as (Yang et al., 2012):

$$\boldsymbol{f}_{t,i} = \left[A_t u_{t,i}^{3/2} \right] \hat{\boldsymbol{t}}_i \quad , \quad 1 \le i \le N \tag{3.12}$$

where A_t is the contact coefficient between a spherical particle and a semi-infinite wall expressed as:

$$A_t = \frac{4\sqrt{R}}{3} \left(\frac{1-\nu^2}{E} + \frac{1-\nu_g^2}{E_g} \right)^{-1} \tag{3.13}$$

where E_g and ν_g represent the Young's modulus and the Poisson's ratio of the guide's material. In Eq. (3.12), $\hat{\boldsymbol{t}}_i$ is the unit vector from the *i*-th particle's contact point with the guide to the center of the *i*-th particle, and it is given by:

$$\hat{\boldsymbol{t}}_i = \frac{\mathbf{v}_i - \mathbf{w}_i}{\left| \mathbf{v}_i - \mathbf{w}_i \right|} \tag{3.14}$$

Once the forces are computed, the equation of motion of the *i*-th particle can be expressed as:

$$\begin{Bmatrix} \ddot{y}_i \\ \ddot{z}_i \end{Bmatrix} = \frac{\boldsymbol{f}_{n,(i,i+1)} + \boldsymbol{f}_{t,i}}{m} + \begin{Bmatrix} 0 \\ g \end{Bmatrix} \quad , \quad i = 1 \tag{3.15a}$$

$$\begin{Bmatrix} \ddot{y}_i \\ \ddot{z}_i \end{Bmatrix} = \frac{\boldsymbol{f}_{n,(i,i+1)} + \boldsymbol{f}_{n,(i-1,i)} + \boldsymbol{f}_{t,i}}{m} + \begin{Bmatrix} 0 \\ g \end{Bmatrix} \quad , \quad 2 \le i \le N \tag{3.15b}$$

where $\ddot{y}$ and z□ represent the particle's accelerations. In the dynamic analysis, the gravity g is included.

We then used the continuous beam theory and the discrete particle model to determine the equation of motion of the beam subjected to a force function represented by the dynamic force of the solitary wave pulse arriving at the interface between the beam and the last particle, $\boldsymbol{f}_{n,(N,N+1)}$. The equation of motion of the beam can be written as:

$$\begin{Bmatrix} \ddot{y}_{N+1} \\ \ddot{z}_{N+1} \end{Bmatrix} = \begin{Bmatrix} \sum_{r=1}^{\infty} \phi_r(x) \left[\frac{\boldsymbol{f}_{n,(N,N+1)}(1)\phi_r(x)}{M_r} - \omega_r^{\,2} q_r \right] \\ 0 \end{Bmatrix} \tag{3.16}$$

where $\varphi_r(x)$, q_r, ω_r, and M_r are the r-th normal mode, normalized coordinate, natural frequency, and generalized (modal) mass, respectively, and $\boldsymbol{f}(1)$ represents the first element of the vector $\boldsymbol{f}$. For more details on the continuous beam theory, the interested reader is referred to Tedesco et al. (1999).

The second order differential equations (3.15) and (3.16) were solved using the 4th order Runge-Kutta method in MATLAB.

3.3.2 Single L-shaped chain: numerical results

We simulated a 914 mm long beam, clamped at both ends, and placed in contact with the granular matter consisting of 24 beads. Each particle was 19.05 mm in diameter, weighing 29 g,

and its material had Young's modulus and Poisson's ratio equal to 200 GPa and 0.28, respectively.

The Young's modulus and Poisson's ratio of the acrylic guide were 3.1 GPa and 0.375, respectively. The effect of axial load on a rectangular beam with 9.525 mm wide, 19.05 mm deep, density = 7800 kg/m^3, Young's Modulus=200 GPa, yielding stress=206.8 MPa, and Poisson's ratio = 0.28 was evaluated. As can be seen from Figure 3.18, two particles S1 and S2 measured the solitary waves. Sensor S2 was four beads away from the beam whereas sensor S1 was nine beads away from the beam. We did not consider any precompression in the granules and the initial velocity applied to the first particle was equal to 0.2881 m/s. The beam's buckling load and the stress are -12.95 kN and -71.395 MPa, respectively.

Figure 3.18 shows the force profile results of the solitary wave at two sensors when the axial stress in the beam is zero. The first pulse is the ISW which is generated in the chain by applying the initial velocity of 0.2881 m/s. In Figure 3.18(a), the second pulse is generated in the elbow whereas the subsequent pulse, the RSW, is the wave reflected from the beam-chain interface and propagating back through the granules and arriving at the sensor site. In Figure 3.18(b), the second pulse is the combination of the RSW and the wave generated by gravity; however, we still name this wave as RSW. The presence of the other waves will be detailed in a later section where we will compare the numerical results with some experimental results.

The solitary waves measured at S1 when the beam's axial loads was -12 kN (stress is -66.13 MPa) and 35 kN (stress is 192.82 MPa) are shown in Figure 3.19a and 3.19b, respectively. The main visible difference is related with the amplitude and the number of pulses beyond 2 ms. When the beam is under compression, its stiffness decreases and thus the amplitude of VSWs decreases.

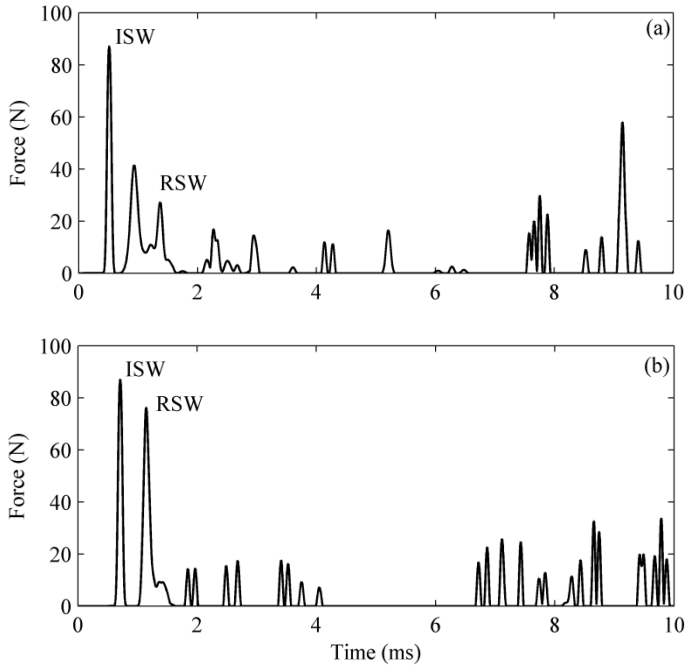

Figure 3.18. Single L-shaped chain. Beam's stress equal to zero. Solitary waves at: (a) sensor S1, and (b) sensor S2.

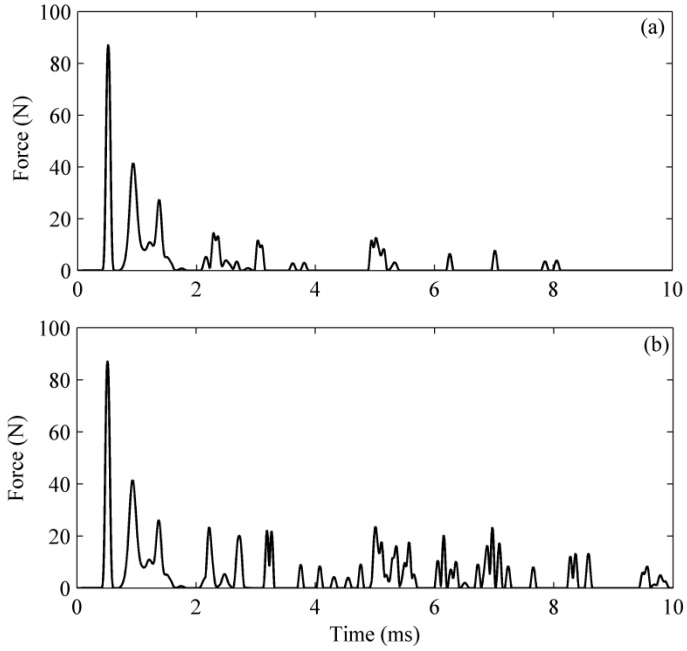

Figure 3.19. Force profile results of solitary waves at sensor S1 for axial load: (a) -12 kN (stress is -66.13 MPa) and (b) 35 kN (stress is 192.82 MPa). The yielding stress of the beam's material is 206.8 MPa, and the buckling stress is -71.395 MPa.

In order to quantify the effect of axial stress on the characteristics of the propagating waves we extracted the features listed in Table 3.3. The first feature is the ratio of the maximum force at two selected pulses, namely RSW and ISW. The RMS and the energy refers to solitary waves after the arrival of the reflected wave.

Table 3.3. L-shaped single chain configuration. Features extracted from the force profiles.

Feature	Description
RSW/ISW	The ratio of amplitude of the RSW to the ISW
TOF RSW	Time between the ISW and the RSW
RMS	The root mean square of waves after the RSW
En	The energy of waves after the RSW

Figure 3.20 shows these features extracted from the solitary force profiles measured at S1 as a function of the beam's axial stress. It can be seen that there is no more changes for features RSW/ISW and TOF RSW which is due to have same beam's stiffness for different axial loads. It is visible that the obtained feature results for the RMS and En increase with increasing the beam's axial stress, and the physical reason is due to increasing the amplitude of VSWs because of increasing the beam's flexural stiffness under tensile load. A stiff beam can generate the VSWs with higher amplitude, and it causes to have more energy for those waves. Figure 3.21 shows the same features computed at S2. Overall, we observe the same trends with the exception of the TOF RSW. This is may due to the constructive interference of the incoming wave from the elbow with the reflected wave from the beam-chain interface.

To better quantify the influence of the axial stress, the results presented in Figs. 3.21 and 3.22 were normalized with respect to the maximum value for each feature and are shown in Figs. 3.22 and 3.23, respectively. From this figures, it can be concluded that feature En has large

variation with respect to the axial stress, it has a given trend, and it decreases before the beam's buckling. Thus, it can be summarized that this feature is the best when a L-shaped chain of particles is adopted.

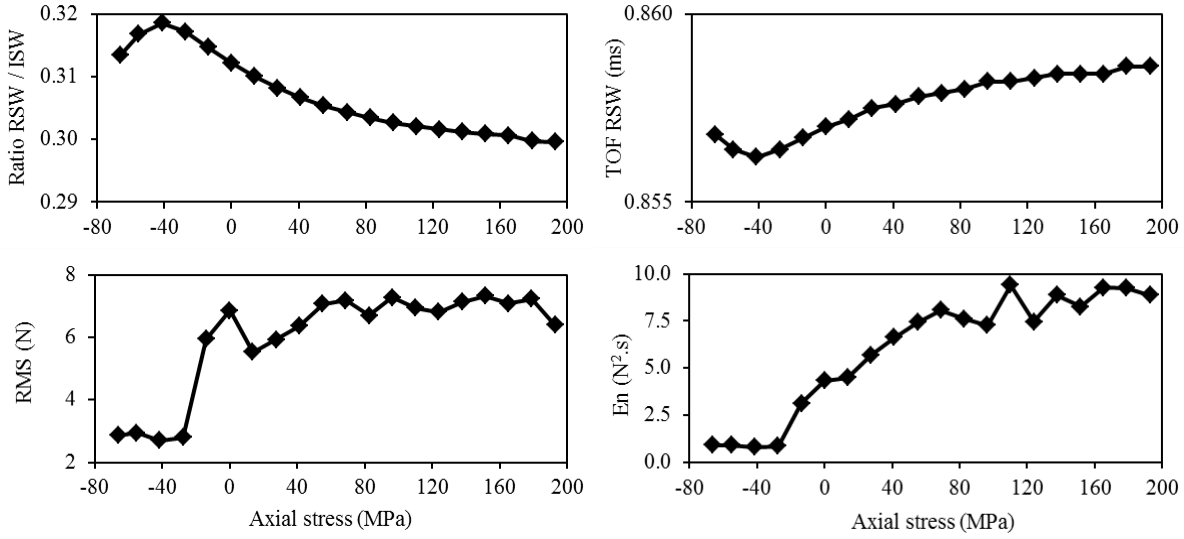

Figure 3.20. Solitary wave features extracted from the solitary force profiles measured at sensor S1 as a function of the axial stress of the beam.

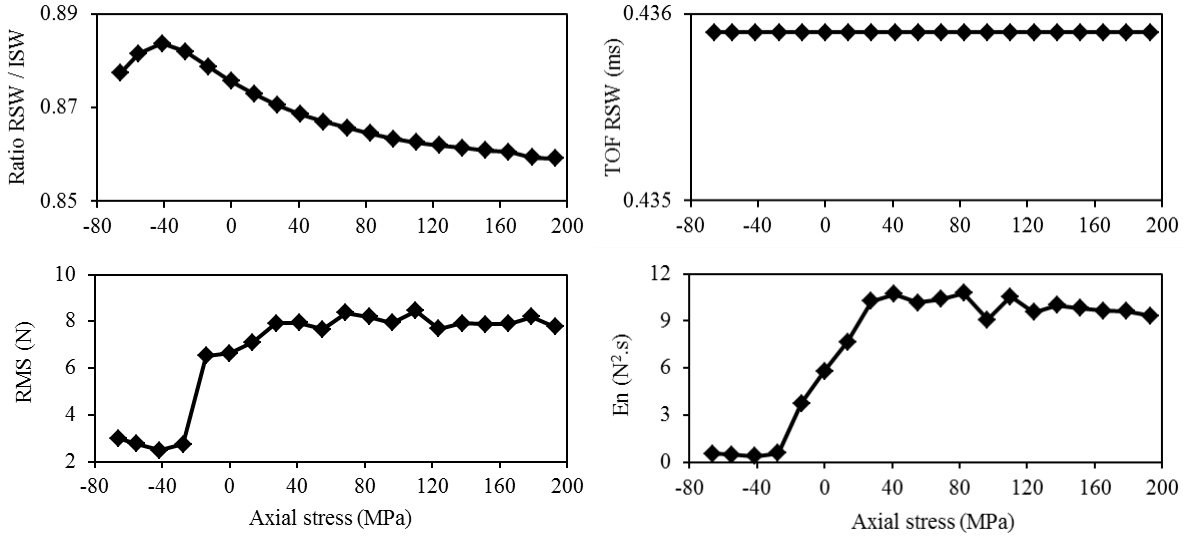

Figure 3.21. Solitary wave features extracted from the solitary force profiles measured at sensor S2 as a function of the axial stress of the beam.

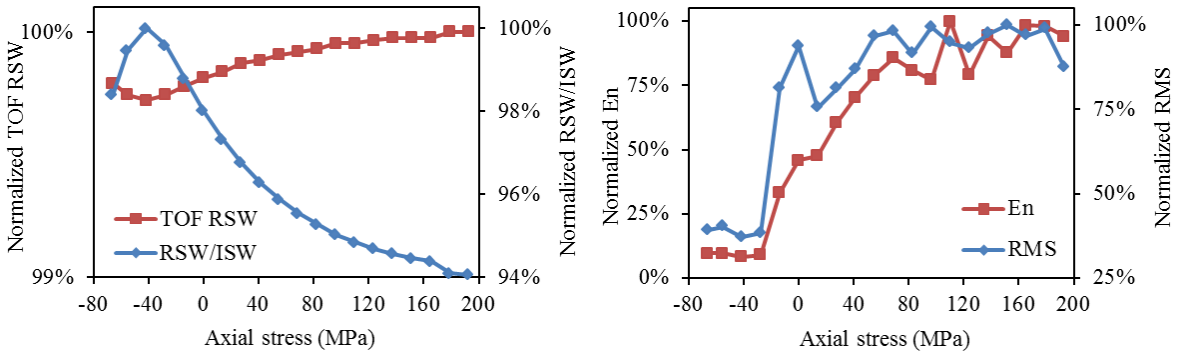

Figure 3.22. Normalized results of solitary wave features extracted from the solitary force profiles measured at sensor S1 as a function of the axial stress of the beam.

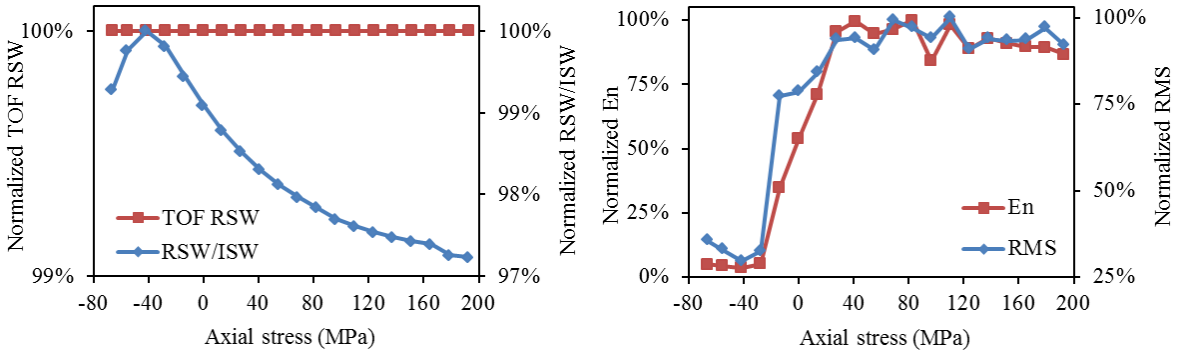

Figure 3.23. Normalized results of solitary wave features extracted from the solitary force profiles measured at sensor S2 as a function of the axial stress of the beam.

3.4 TWO L-SHAPED CHAINS

We also considered the presence of an additional L-shaped granular system according to the scheme presented in Fig. 3.24.

3.4.1 Implementation

Like in the previous section, we used a discrete particle model to study the propagation of the solitary waves along two L-shaped chains in contact with a beam according to the scheme presented in Fig. 3.24. To compute the normal approach and the normal contact force between two neighboring particles, we used Eqs. (3.6) and (3.7), respectively. Similar to Eq. (3.9) the normal contact force between the beam and the (*N+2*)-th particle was calculated as:

$$\boldsymbol{f}_{n,(N+1,N+2)} = \left[A_{n,b} \left[R + \frac{w_b}{2} - \left| \mathbf{v}_{N+2} - \mathbf{v}_{N+1} \right| \right]_+^{3/2} \right] \hat{\boldsymbol{n}}_{N+1,N+2} \tag{3.17}.$$

To find the approach between the *i*-th particle and the guide for $1 \le i \le N$ and $N+2 \le i \le 2N+1$, we used Eq. (3.11). Then, the contact force $\boldsymbol{f}_{t,i}$ between the *i*-th particle and the guide was calculated by means of Eq. (3.12).

The equation of motion of the *i*-th particle can be expressed as:

$$\begin{Bmatrix} \ddot{y}_i \\ \ddot{z}_i \end{Bmatrix} = \frac{\boldsymbol{f}_{n,(i,i+1)} + \boldsymbol{f}_{t,i}}{m} + \begin{Bmatrix} 0 \\ g \end{Bmatrix} \quad , \quad i = 1 \tag{3.18a}$$

$$\begin{Bmatrix} \ddot{y}_i \\ \ddot{z}_i \end{Bmatrix} = \frac{\boldsymbol{f}_{n,(i,i+1)} + \boldsymbol{f}_{n,(i-1,i)} + \boldsymbol{f}_{t,i}}{m} + \begin{Bmatrix} 0 \\ g \end{Bmatrix} \quad , \quad 2 \le i \le N,\ N+2 \le i \le 2N \tag{3.18b}$$

$$\begin{Bmatrix} \ddot{y}_i \\ \ddot{z}_i \end{Bmatrix} = \frac{\boldsymbol{f}_{n,(i-1,i)} + \boldsymbol{f}_{t,i}}{m} + \begin{Bmatrix} 0 \\ g \end{Bmatrix} \quad , \quad i = 2N+1 \tag{3.18c}.$$

The continuous beam theory and the discrete particle model were used to determine the equation of motion of the beam subjected to a force function represented by the dynamic force of the solitary wave pulse arriving at the two interfaces between the beam and particles. In this case, the equation of motion of the beam can be written:

$$\begin{Bmatrix} \ddot{y}_{N+1} \\ \ddot{z}_{N+1} \end{Bmatrix} = \begin{Bmatrix} \sum_{r=1}^{\infty} \phi_r(x) \left[\dfrac{\left(f_{n,(N,N+1)}(1) + f_{n,(N+1,N+2)}(1) \right) \phi_r(x)}{M_r} - \omega_r{}^2 q_r \right] \\ 0 \end{Bmatrix} \quad (3.19).$$

As for Eqs. (3.15) and (3.16), the second order differential equations (3.18) and (3.19) were solved by means of the 4th order Runge-Kutta method.

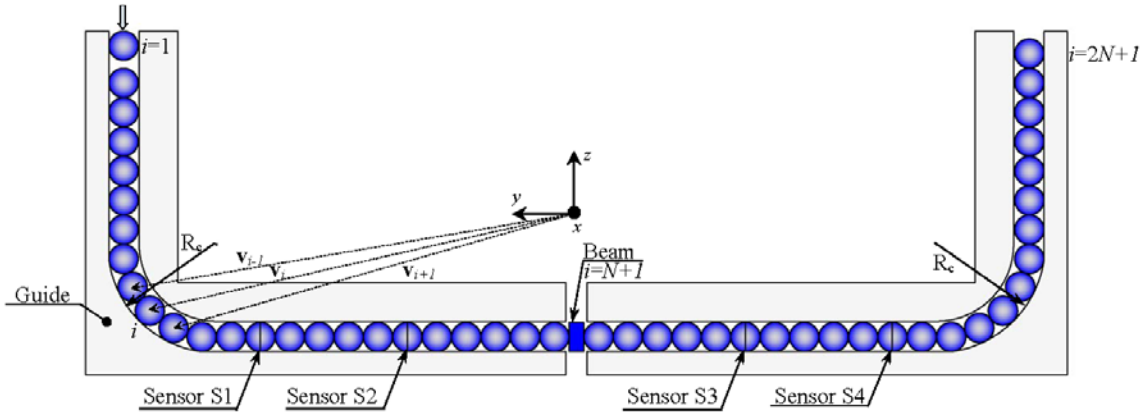

Figure 3.24. Setup for the numerical simulation. The beam is clamped at two ends, and there is two L-shape chains of particles at the mid-span of the beam. The drawing is in scale.

3.4.2 Two L-shaped chains: numerical results

The same beam and particles described in the first paragraph of section 3.3.2 were used here. Figure 3.24 shows the cross section view of the setup. The solitary waves were measured at four sensing sites. S1 is the 14th particle in the first chain of particles whereas sensing site S2 is the 19th particle in the first chain of particles, S3 is the 5th particle in the second chain whereas S4 is the 10th position in the second chain. We assumed an initial velocity was applied to the first particle which was equal to 0.2881 m/s which was computed from the experimental setup.

Figure 3.25 shows the solitary wave at S2 and S3 when the axial stress is zero. As can be seen, there are two main pulses in Figure 3.25a. The first two waves have the same meaning discussed in the previous section. The presence of other waves after the RSW is due to particles and beam's vibration. In Figure 3.25b, the first wave is generated by the transmission of the ISW through the thickness. We name this wave the transmitted solitary wave (TSW). The waves following the TSW are generated by the vibration of the beam. More details will be provided in section relative to the experimental results.

The solitary waves measured at S2 when the beam was subjected to -66.13 MPA and 192.82 MPa are presented in Fig. 3.26a and Fig. 3.26b, respectively.

Similarly, in Fig. 3.27 we present the results associated with the measurement at the sensor site S3. As expected the ISW does not change. There are small differences in the results of the RSWs and TSWs which are related to the beam's flexural stiffness. The VSWs shows instead the largest sensitivity, and this is due to the change of the beam's natural frequencies.

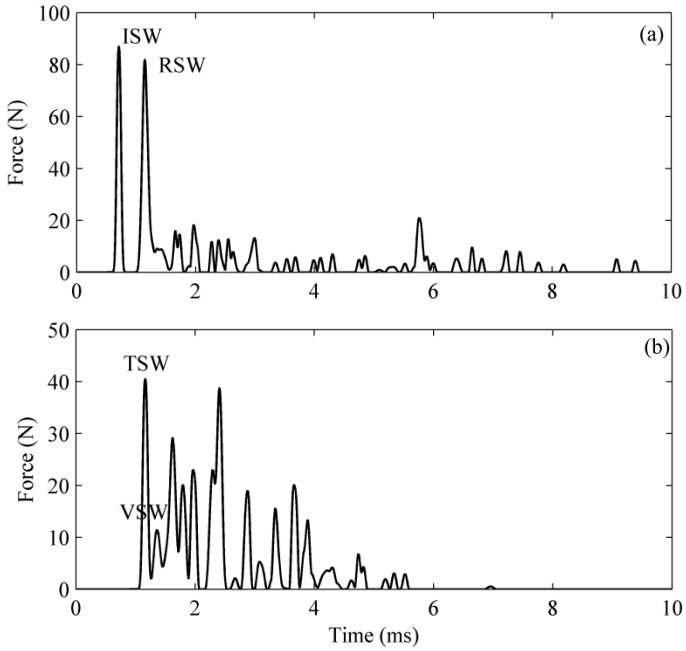

Figure 3.25. Force profile results of solitary waves at: (a) sensor S2, and (b) sensor S3. The value of the axial stress in the beam is zero.

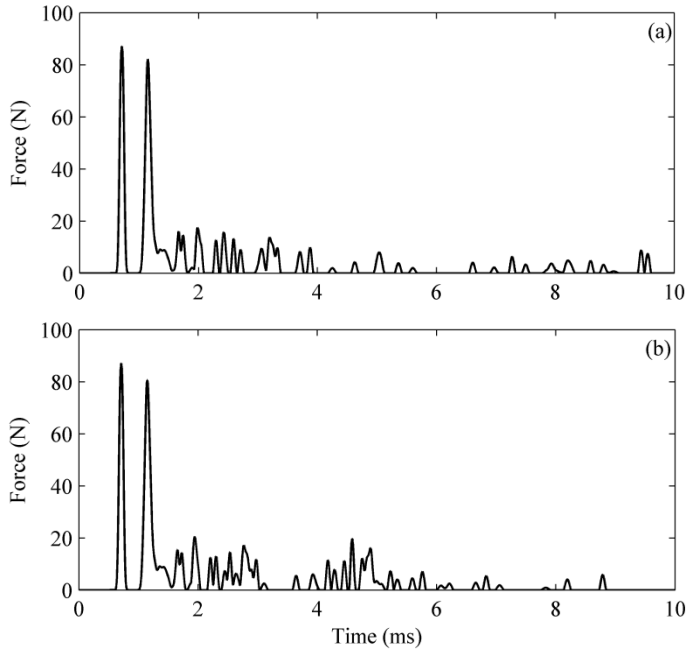

Figure 3.26. Force profile results of solitary waves at sensor S2 for axial stress: (a) -66.13 MPa and, (b) 192.82 MPa. The buckling stress is -71.395 MPa, and the yielding stress of the beam's material is 206.8 MPa.

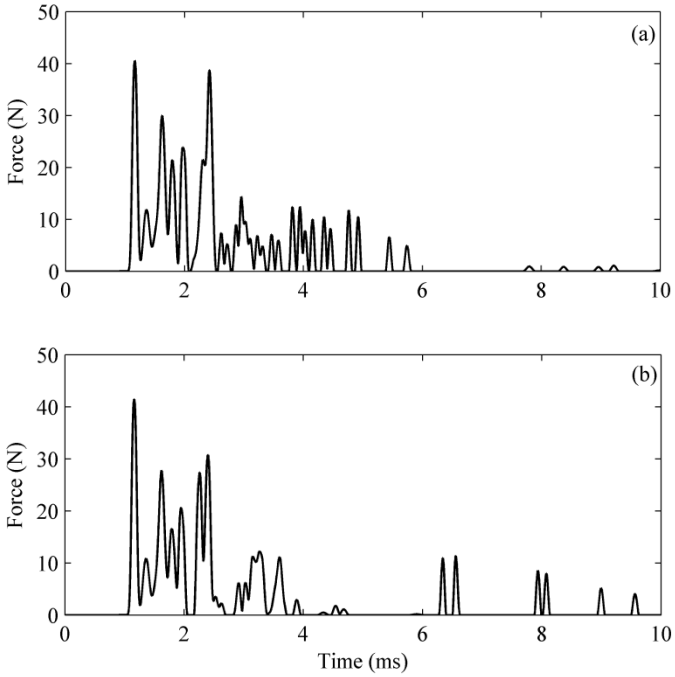

Figure 3.27. Force profile results of solitary waves at sensor S3 for axial stress: (a) -66.13 MPa and, (b) 192.82 MPa. The buckling stress is -71.395 MPa, and the yielding stress of the beam's material is 206.8 MPa.

The features listed in Table 3.4 were used to quantify the effect of the temperature. The last two features are the RMS and energy of waves after the RSW, i.e. solitary waves after 1.5 ms, or the VSW, i.e. solitary waves after the arrival of the reflected wave.

Table 3.4. L-shaped two-chain configuration. Features extracted from the force profiles.

Feature	Description
RSW/ISW	The ratio of amplitude of the RSW to the ISW
TSW/ISW	The ratio of amplitude of the TSW to the ISW
VSW/ISW	The ratio of amplitude of the VSW to the TSW
TOF RSW	Time between the ISW and the RSW
TOF TSW	Time between the ISW and the TSW
TOF VSW	Time between the TSW and the VSW
RMS	The root mean square of waves after the RSW or the VSW
En	The energy of waves after the RSW or the VSW

Figures 3.28 and 3.29 show the solitary wave features extracted from the solitary force profiles measured at S1 and S2 as a function of the axial stress of the beam. It can be seen that there is no significant variation with respect to the axial stress for the ratio of RSW/ISW and TOF RSW, and the reason is that the generated wave by reflecting does not contain more information from the beam's stiffness and axial load. It can be seen that there is a given trend for the results of the RMS and En, and their values decrease with decreasing the axial stress, because of decreasing the beam's stiffness.

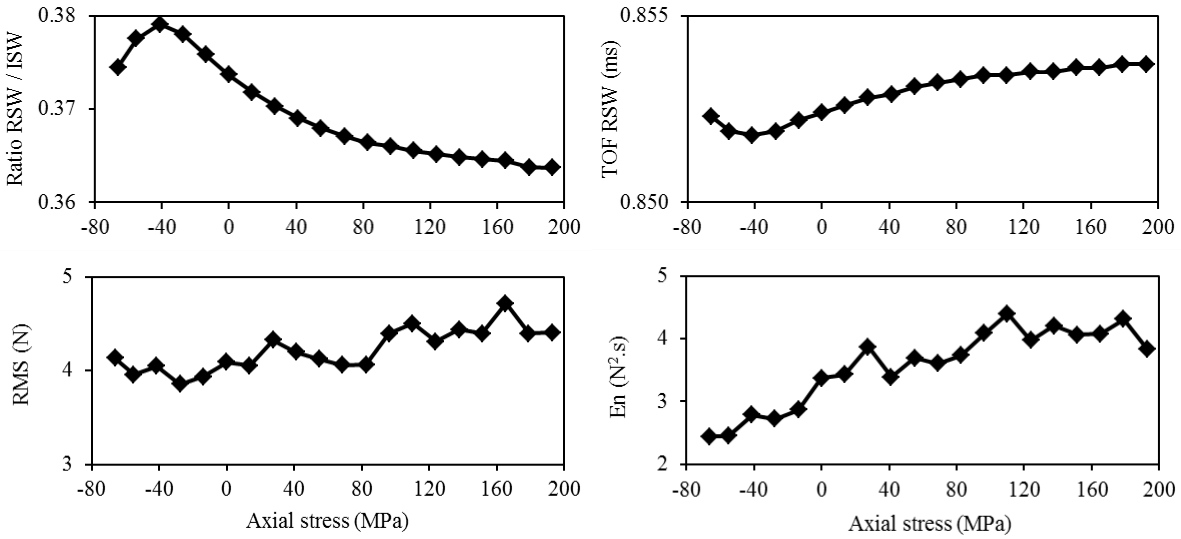

Figure 3.28. Solitary wave features extracted from the solitary force profiles measured at sensor S1 as a function of the axial stress of the beam.

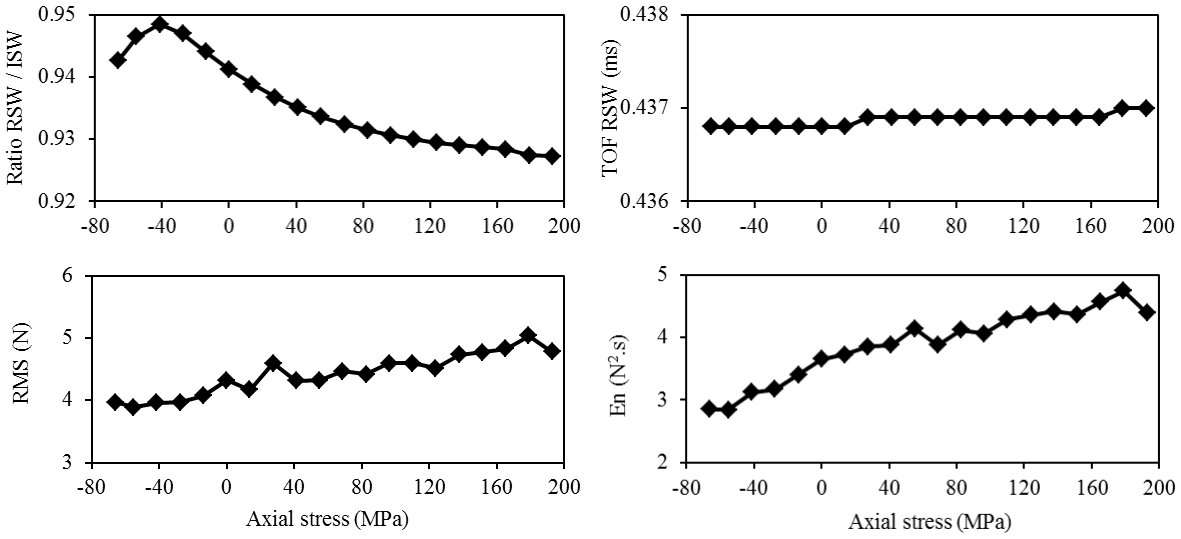

Figure 3.29. Solitary wave features extracted from the solitary force profiles measured at sensor S2 as a function of the axial stress of the beam.

The results shown in Figures 3.29 and 3.30 were normalized and are presented in Figures 3.31 and 3.32. From this figure, it can be concluded that the energy of solitary waves has large variation with respect to the axial stress; also, it has a given relationship with the axial stress.

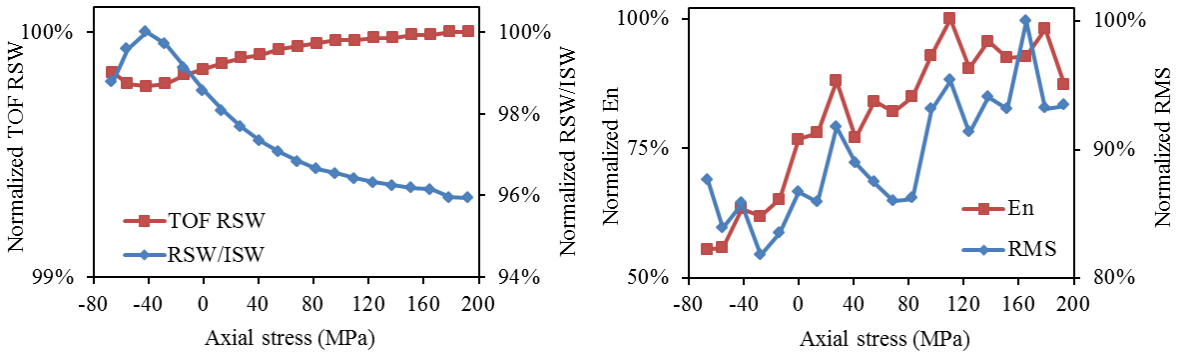

Figure 3.30. Normalized results of solitary wave features extracted from the solitary force profiles measured at sensor S1 as a function of the axial stress of the beam.

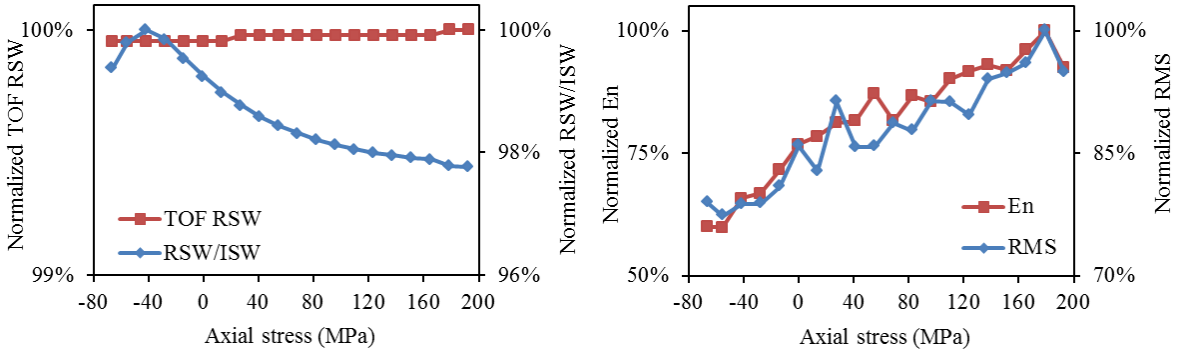

Figure 3.31. Normalized results of solitary wave features extracted from the solitary force profiles measured at sensor S2 as a function of the axial stress of the beam.

Figures 3.32 and 3.33 present features extracted from the measurements at the sensor sites S3 and S4 as a function of the beam's axial stress. The most visible variation is associated with the RMS and energy, and this is due to reasons described earlier.

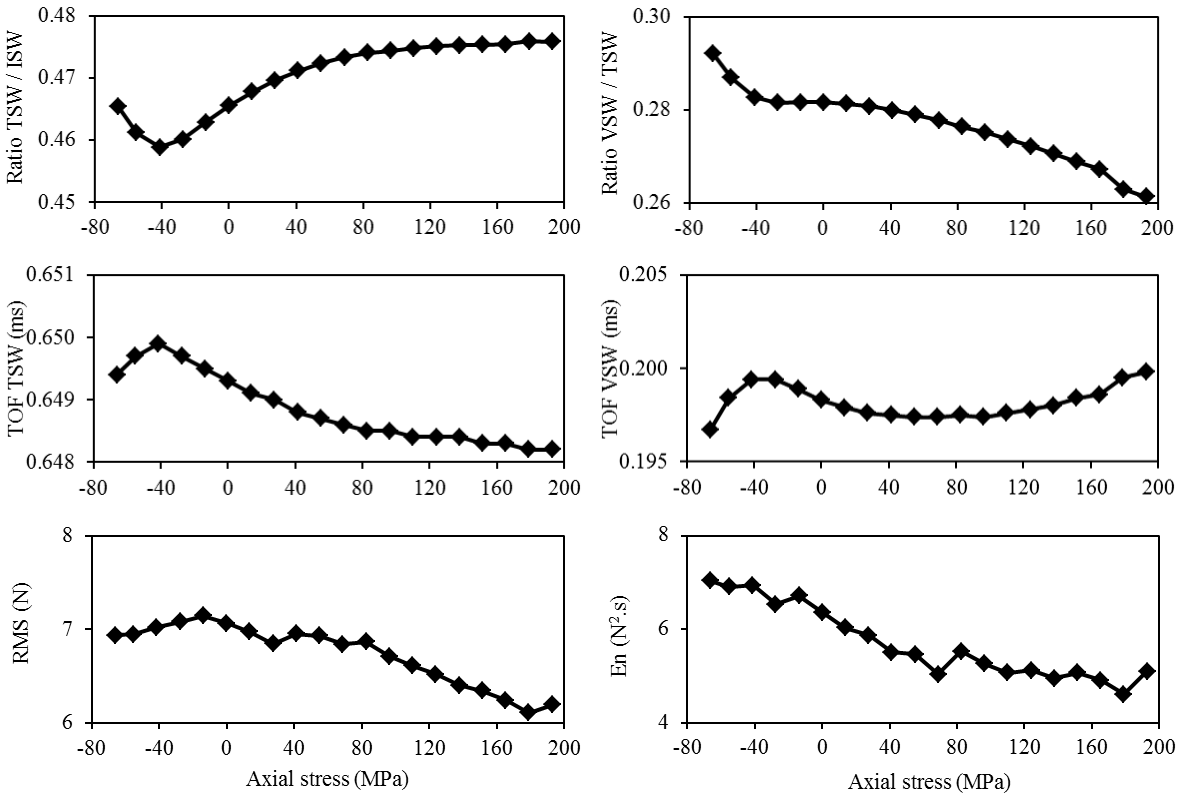

Figure 3.32. Solitary wave features extracted from the solitary force profiles measured at sensor S3 as a function of the axial stress of the beam. The properties of the ISW were extracted from sensor S1.

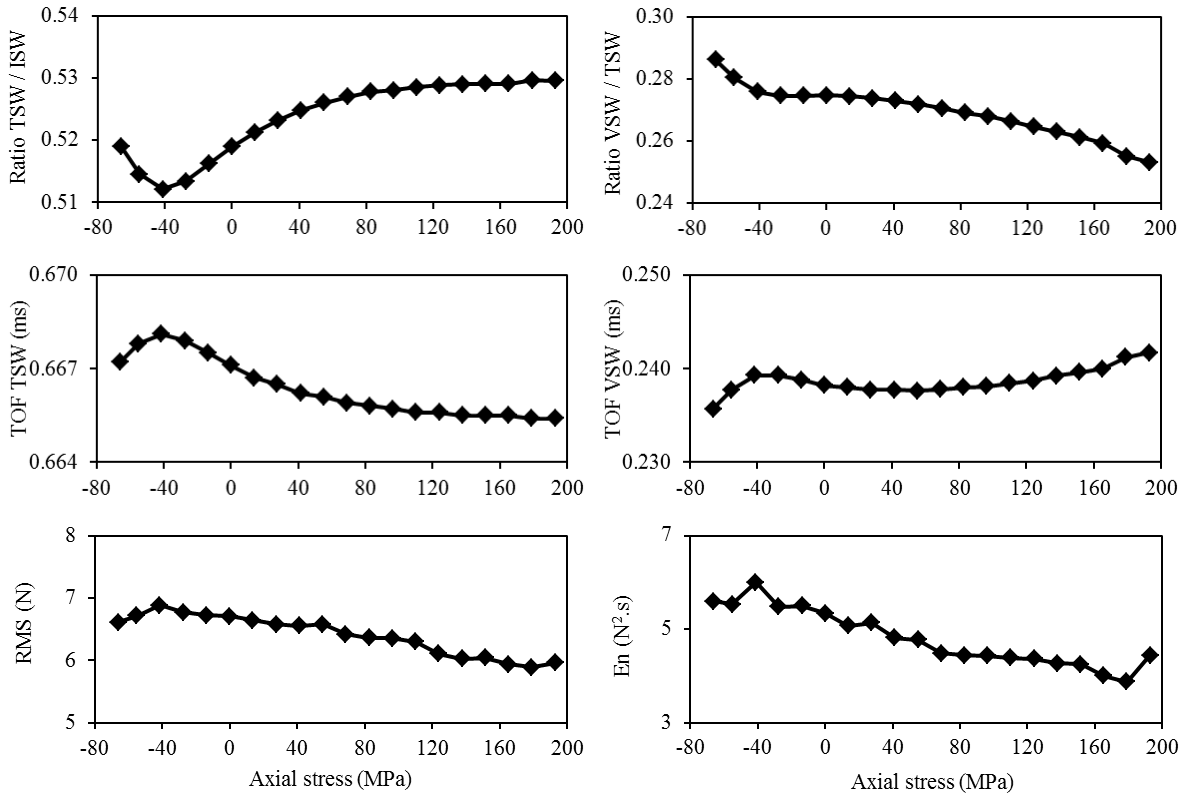

Figure 3.33. Solitary wave features extracted from the solitary force profiles measured at sensor S4 as a function of the axial stress of the beam. The properties of the ISW were extracted from sensor S2.

The normalized values of solitary wave features are shown in Figures 3.34 and 3.35. It can be seen that the En has large variation with respect to the axial stress.

By investigating features' results for one and two curved chains, it can be found that the En in one curved chain configuration has a largest variation with respect to the axial stress. The reason is related to the half vibration cycle allowed when only one chain is present.

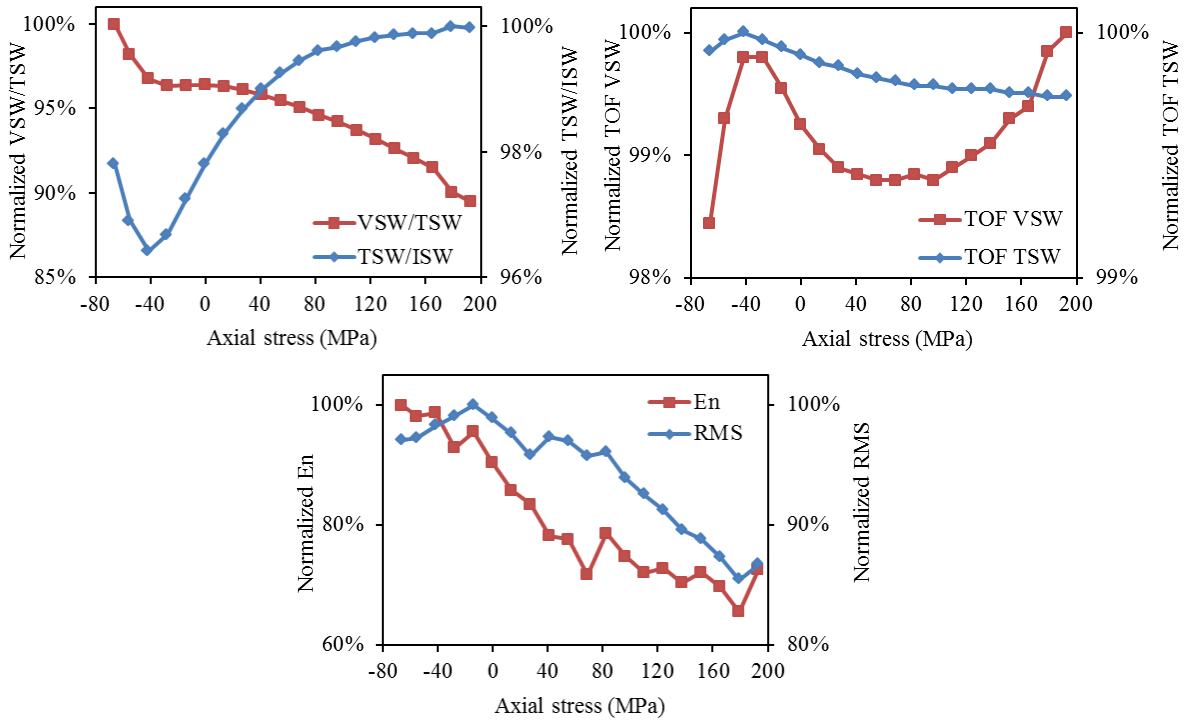

Figure 3.34. Normalized results of solitary wave features extracted from the solitary force profiles measured at sensor S3 as a function of the axial stress of the beam.

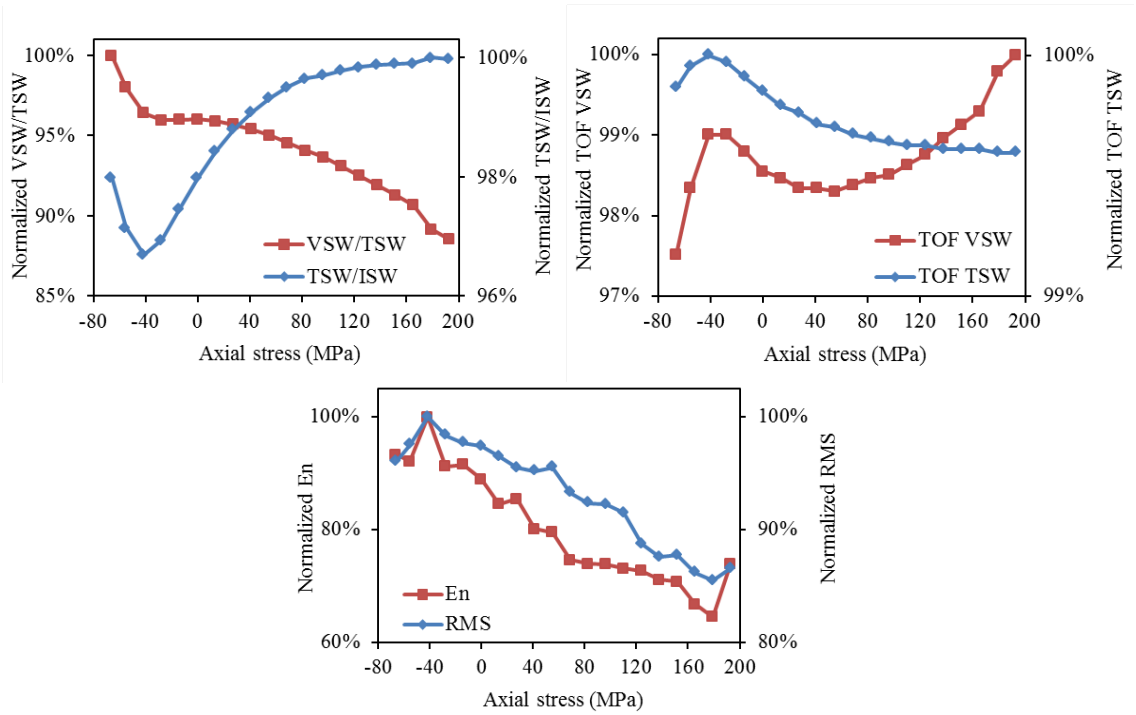

Figure 3.35. Normalized results of solitary wave features extracted from the solitary force profiles measured at sensor S4 as a function of the axial stress of the beam.

4.0 PARAMETRIC STUDIES

In this chapter, we present the results relative to four numerical studies. In Section 4.1, we evaluated the effect of the particles diameter and modulus on the sensitivity of the proposed technology. In Section 4.2, we discuss the effect of the beam temperature which is known to affect slightly the beam's modulus. In Section 4.3, we utilized artificial neural networks to map knowledge between some of the selected HNSW-based features and the beam's neutral temperature. Finally, Section 4.4 describes the buckling prediction of a rail-like beam having the cross-section of a typical AREMA section. First, we present the results of a numerical study relative to one chain of particles. Then, we consider two chains of particles. The simulations were considered using the discrete particle model and the continuous beam theory described in Chapters 1 and 2.

This chapter was extracted from our published papers entitled "On the optimization of granular medium to infer the axial stress in slender structures" and "Determination of the neutral temperature of slender beams by means of nonlinear solitary waves".

4.1 EFFECT OF THE GRAINS' PROPERTIES

We considered the case of a single straight chain. Seven particles' diameters namely 5, 10, 15, 20, 25, 30, and 35 mm, and the eleven materials listed in Table 4.1 were considered. Thus, a total of seventy-seven different chains were examined. The materials were selected based upon commercial availability aimed at future experimental validations.

A 914 mm long stainless beam, clamped at both ends, was considered. The beam was 9.525 mm wide and 19.05 mm deep. For the beam we assumed ρ = 7800 kg/m^3, E = 200 GPa, ν = 0.28, and yielding stress σ_Y = 206.8 MPa. Based upon these properties were such that the beam's Euler buckling load F_{cr} and the corresponding buckling stress σ_{cr} were equal to -12.95 kN and -71.395 MPa, respectively.

For the analysis we simulated the same beam and we extracted the same features considered in Section 3. We applied an initial velocity of 0.2566 m/s to the first particle of the chain and the results presented in this section refers to the solitary pulse measured at the sensing site S2.

Table 4.1. Mechanical properties of grains' material.

Material	**Density (kg/m^3)**	**Young's Modulus (GPa)**	**Poisson's ratio**
Tungsten	19250	411	0.28
Copper	8960	120	0.34
Nickel	8908	200	0.31
Stainless steel 302	8100	196	0.33
Stainless steel 316	8000	193	0.3
Iron	7874	211	0.29
Stainless steel 440C	7800	200	0.28
Zinc	7140	108	0.25
Titanium	4506	116	0.32
Aluminum	2700	70	0.35
Magnesium	1738	45	0.29

A set of features such as those presented in the previous chapter were extracted from the force profile in the time domain. Figure 4.1 shows a 3-D diagram where the ratio RSW/ISW is presented as a function of the axial stress and particles' diameter. The cases of the heaviest (Tungsten), lightest (Magnesium), and intermediate (Iron) density are presented. Overall, we observe that at a given stress the amplitude of the reflected wave decays as the diameter of the granules increases. This trend is more evident for the heaviest particles. When the particles are smaller and lighter the acoustic energy carried by the granular system is not sufficient to trigger the beam's vibration, the energy bounces back to the chain, and the ratio RSW/ISW is close to 1. As the particles become bulkier, the amount of energy carried by the reflected pulse decreases at advantage of the beam's vibration.

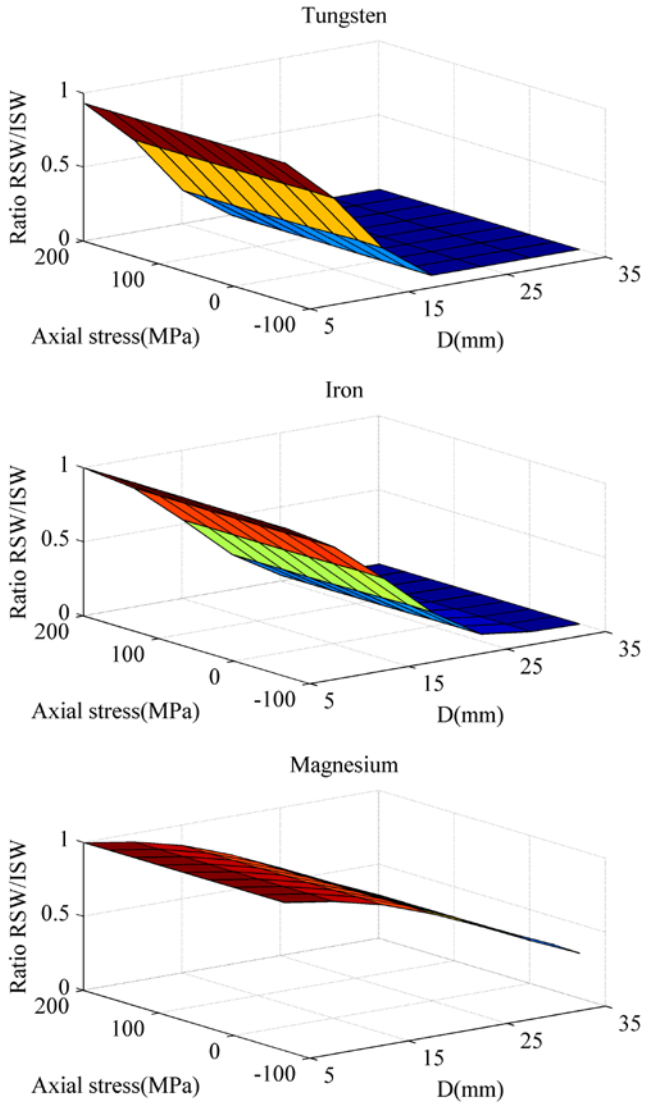

Figure 4.1. One chain configuration. Ratio associated with the amplitude of the reflected and incident waves as a function of the axial stress and the particles' diameter. The case of three particles materials is presented.

This is visible in Fig. 4.2 which displays the results associated with the ratio VSW/ISW. Here the amount of energy carried by the pulse generated by the beam's vibration increases with the bulkiness of the particles. Moreover, the plot surface is not regular any particle diameter or at any material. The force applied to the beam by the solitary pulse depends on the physical and mechanical properties of the particles; in addition, the beam's motion is the combination of many

modes of vibration. We conclude that for this complex dynamical system, the feature associated with the amplitude of the vibration-induced solitary is strongly dependent on the geometry and the modulus of the nonlinear system. At a given diameter the variation of the ratio is similar to what found and discussed in Section 3.1. Not shown here, the same trend was seen for the remaining eight materials.

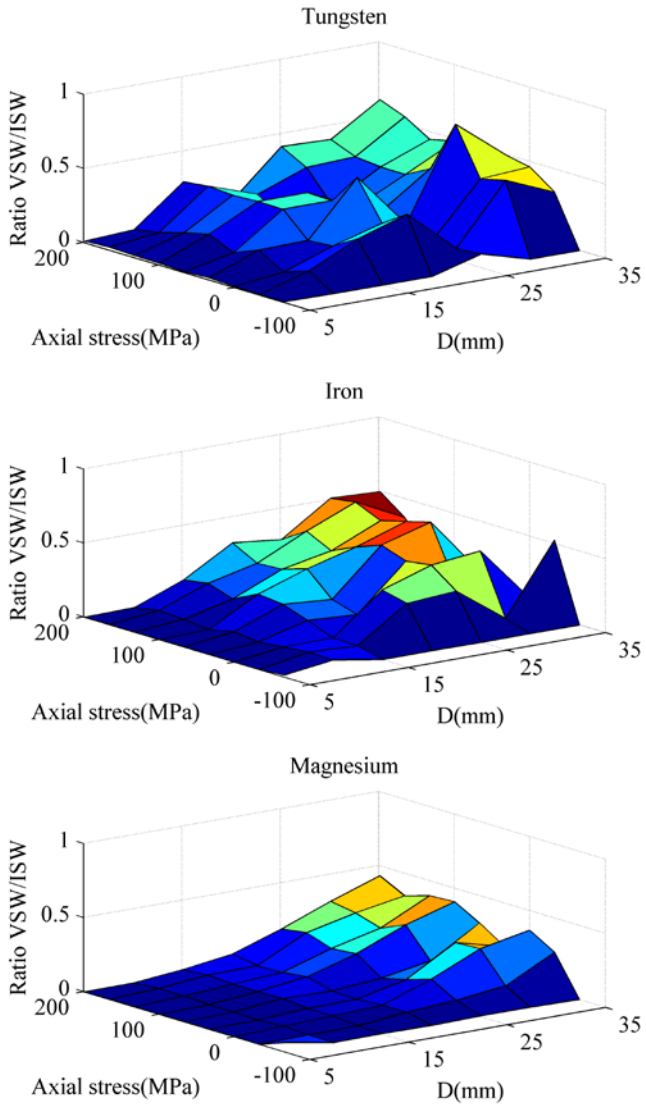

Figure 4.2. One chain configuration. Ratio associated with the amplitude of the vibration-induced and incident waves as a function of the axial stress and the particles' diameter. The case of three particles materials is presented.

Similar to Figs. 4.1 and 4.2, Fig. 4.3 and Fig. 4.4 shows the feature associated with the time of flight of the reflected and the vibration-induced solitary wave, respectively. The travel time of the reflected wave (Fig. 4.3) does not change significantly with stress irrespective of the particles diameter or the particles materials. Thus, the same conclusion drawn in Fig. 3.4 can be applied here. The result is consistent with the findings in section 3.1, i.e. as the axial stress does not affect the beam's stiffness, there is little influence on the generated RSW. At a given stress, the feature's value increases proportionally to the increase of the particle diameter, i.e. proportionally to the relative distance between the sensing sites. In fact, the variation of the travel time due to the change of speed is lower than the variation associated to the increased distance between the sensors. Overall, this trend is identical for all the different materials considered in this study.

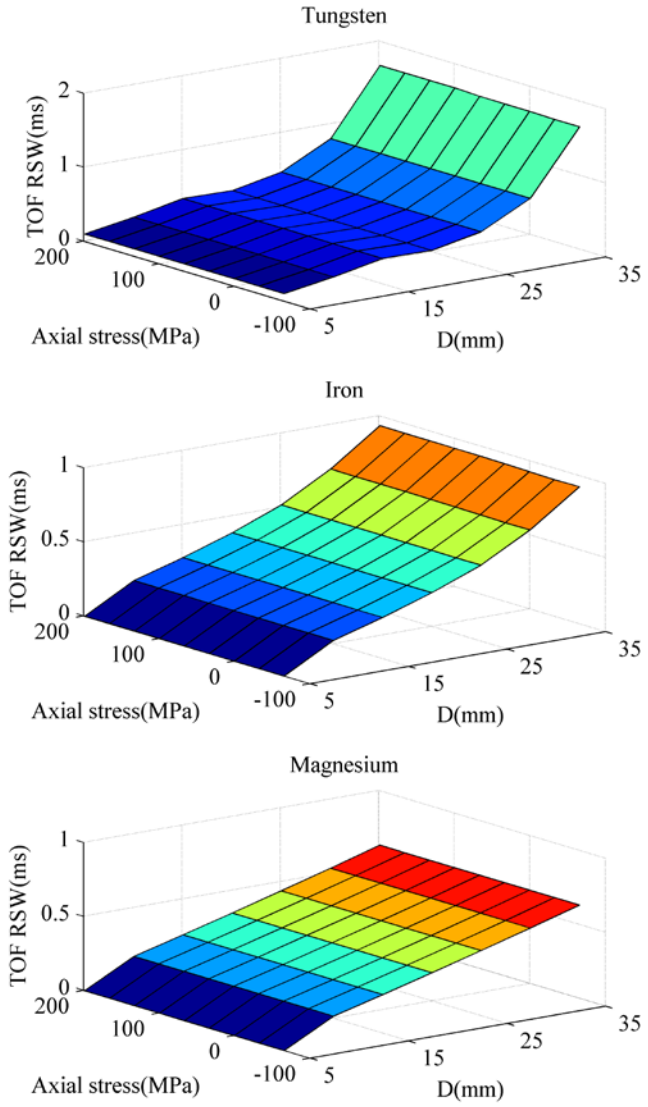

Figure 4.3. One chain configuration. Time of flight of the reflected wave as a function of the axial stress and the particles' diameter. The case of three particles materials is presented.

Figure 4.4 shows the time of flight relative to the vibration-induced solitary wave as a function of the axial stress and the particle diameters. The value of this feature rapidly increases as the stress approaches buckling, due to the sharp decrease of the beam's natural frequency of vibration. The TOF of the wave propagating along the heaviest particles, made of Tungsten, presents the largest gradient with respect to the axial stress. This is likely related to the particles

Young's modulus, which contributes to the stiffness constant A_c (see Eq. 2.2) and to the differential equations of particles (Eqs. 2.33 and 2.4). The value of this constant for different diameters and materials is listed in Table 4.4. It can be seen that the particles made of Tungsten has the highest A_c. Moreover, the A_c varies by 41.9% when the diameter doubles from 5 to 10 mm. Conversely, the same coefficient varies by 8.2% when the diameter increases by 17% spanning from 30 to 35 mm. Particles with small stiffness constant generate an amount of dynamic force lower than same diameter particles with larger stiffness, and therefore lower beam's vibration, which results into shorted period of vibration. This trend is observed in Fig. 18.

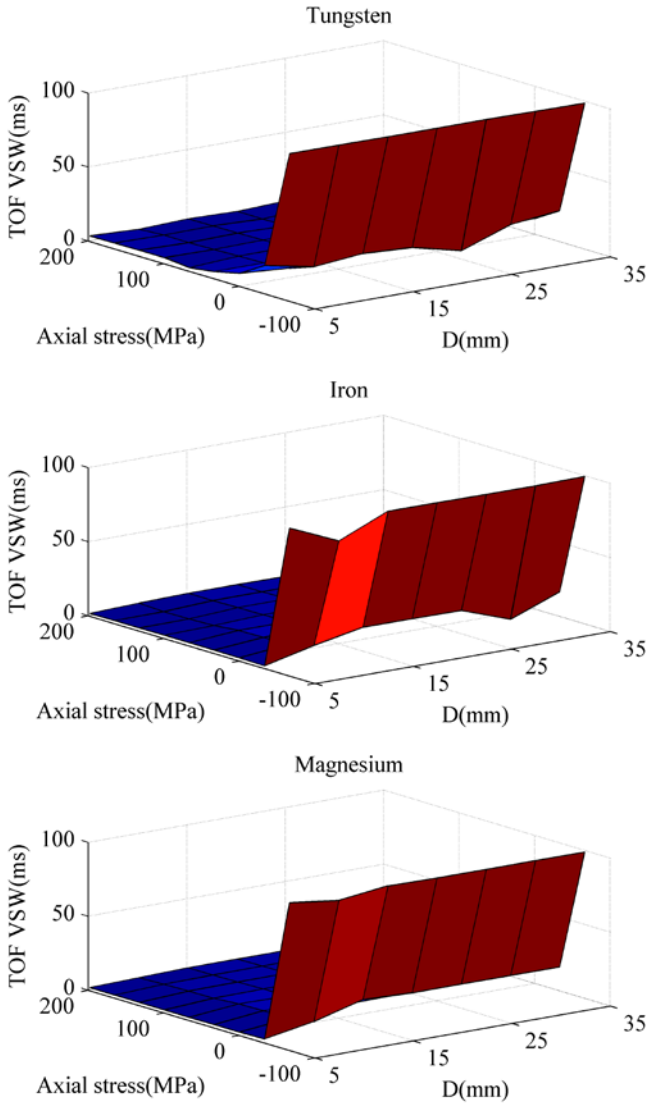

Figure 4.4. One chain configuration. Time of flight of the vibration-induced solitary wave as a function of the axial stress and the particles' diameter. The case of three particles materials is presented.

From the examination of Figs. 4.1-4.4, it is difficult to ascertain which combination of particles' diameter and material provides the largest gradient with respect to the axial stress. To quantify this sensitivity, we fit the numerical data according to a linear and a polynomial (2^{nd} degree) interpolation. We therefore assumed that at a given particle diameter a certain feature

varies linearly (or parabolically) with respect to the axial stress σ, and the coefficients associated with the variable σ and σ^2 were extracted.

Figure 4.5 displays the results relative to the linear interpolation whereas Fig. 4.6 refers to the second order polynomial. The coefficients associated with the first three features, namely the amplitude of the reflected and vibration-induced solitary wave, and the time of flight of the reflected solitary wave are three orders of magnitude smaller than the fourth feature. Overall, we can conclude that the coefficients are dependent on both the particles' diameter and the material type. However, with the exception of a few materials and features, we cannot conclude that the largest diameter or the heaviest particle or both provide the highest sensitivity.

Table 4.2. The value of the stiffness constant A_c for different diameters and materials. The unit of results is GN/m$^{3/2}$.

Material	D (mm)						
	5	10	15	20	25	30	35
Tungsten	10.5	14.9	18.2	21.0	23.5	25.7	27.8
Copper	3.2	4.5	5.5	6.4	7.2	7.8	8.5
Nickel	5.2	7.4	9.0	10.4	11.7	12.8	13.8
Stainless steel 302	5.2	7.3	9.0	10.4	11.6	12.7	13.7
Stainless steel 316	5.0	7.1	8.7	10.0	11.2	12.2	13.2
Iron	5.4	7.7	9.4	10.9	12.1	13.3	14.4
Stainless steel 440C	5.1	7.2	8.9	10.2	11.4	12.5	13.5
Zinc	2.7	3.8	4.7	5.4	6.1	6.7	7.2
Titanium	3.0	4.3	5.3	6.1	6.8	7.5	8.1
Aluminum	1.9	2.7	3.3	3.8	4.2	4.6	5.0
Magnesium	1.2	1.6	2.0	2.3	2.6	2.8	3.1

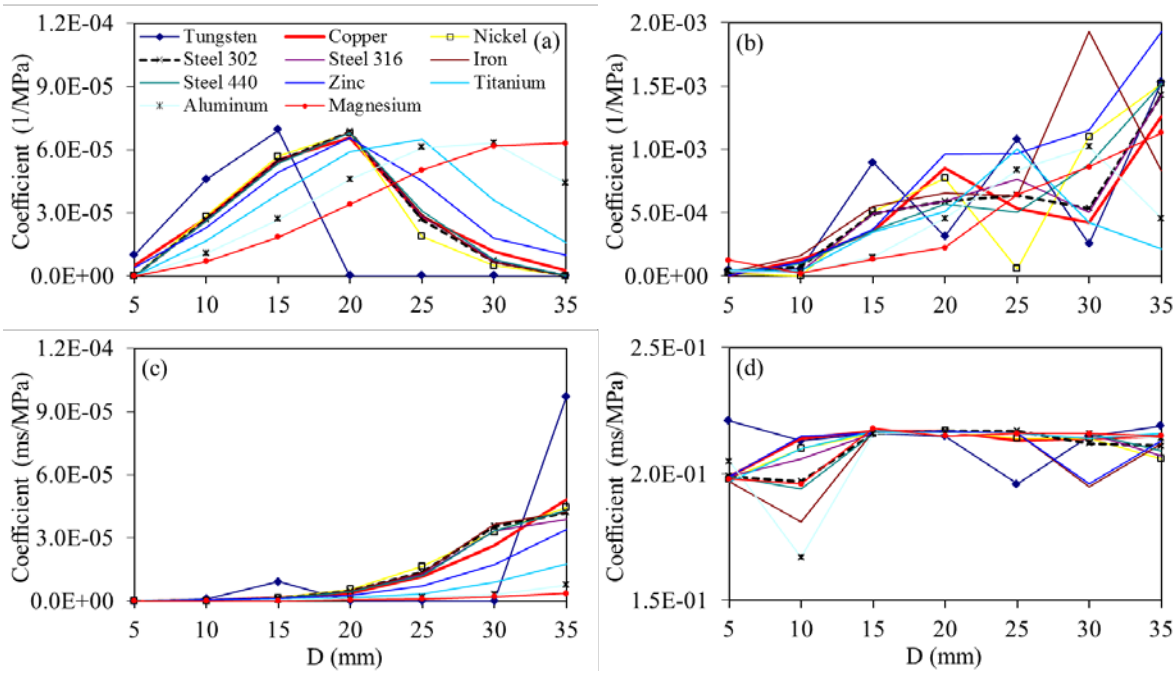

Figure 4.5. Coefficient of the linear interpolation as a function of the particles' diameter for the 11 materials considered in this study. (a) Ratio associated with the amplitude of the reflected and incident waves. (b) Ratio associated with the amplitude of the vibration-induced and incident waves. (c) Time of flight of the reflected wave. (d) Time of flight of the vibration-induced wave.

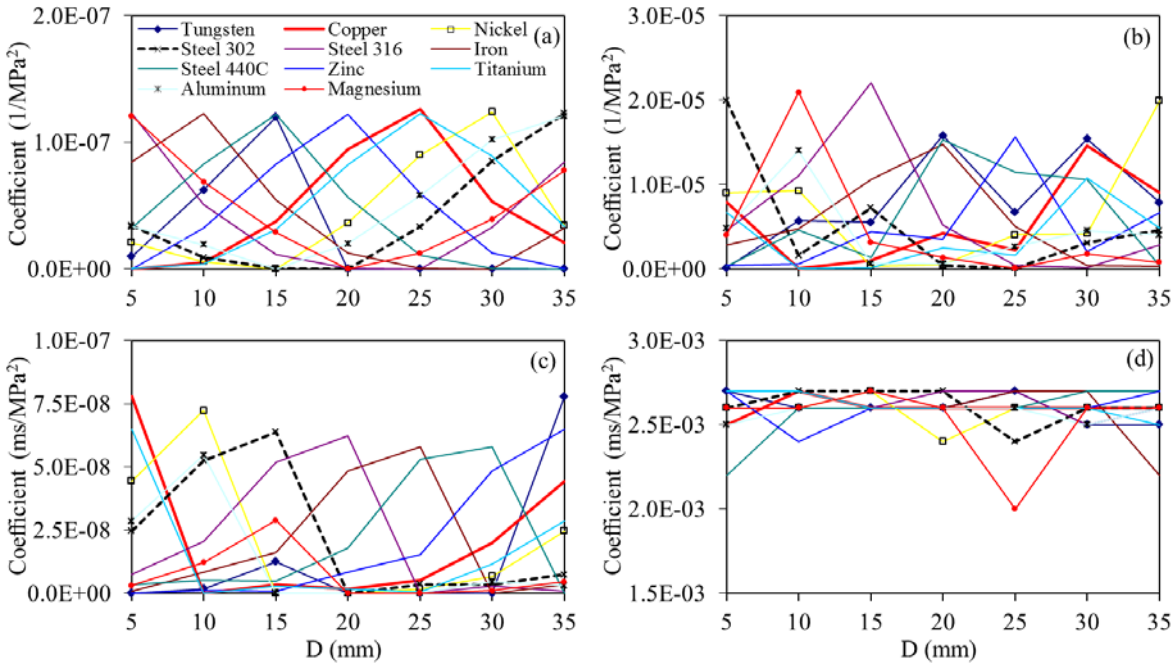

Figure 4.6. Coefficient of the parabolic interpolation as a function of the particles' diameter for the 11 materials considered in this study. (a) Ratio associated with the amplitude of the reflected and incident waves. (b) Ratio associated with the amplitude of the vibration-induced and incident waves. (c) Time of flight of the reflected wave. (d) Time of flight of the vibration-induced wave.

4.2 EFFECT OF THE BEAM'S TEMPERATURE ON THE YOUNG'S MODULUS

Sakumoto et al. (1996) and Chen and Young (2006) studied experimentally the effect of the temperature on the Young's modulus of some steels. Figures 4.7(a) and 4.7 (b) show some of the results from Sakumoto (Fig. 4.4(a)) and Chen and Young (Fig. 4.7 (b)), respectively. Overall, the Young's modulus decreases with increasing temperature. Moreover, Fig. 4.7 (b) compares the experimental values with the elastic modulus predicted by some standards.

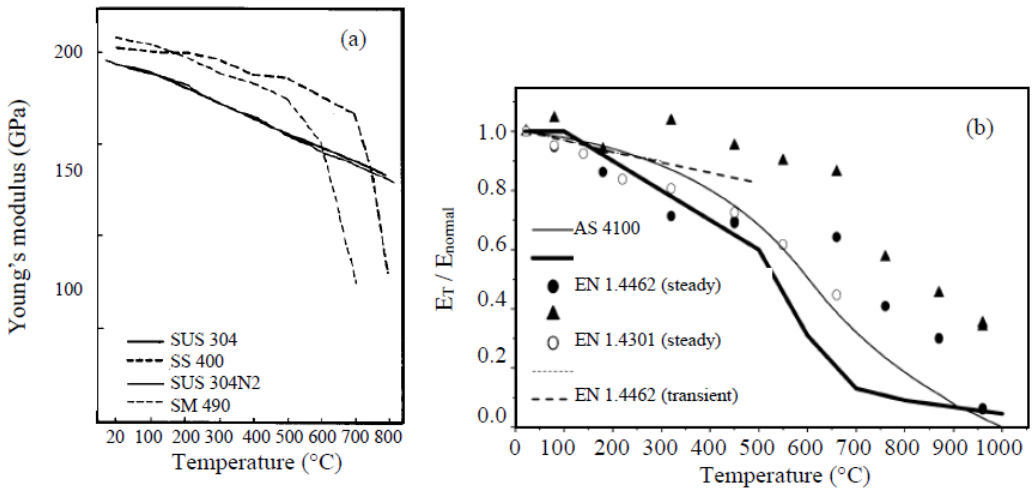

Figure 4.7. Effect of the temperature on the Young's modulus of different steels. Figures adapted from: (a) Sakumoto et al. (1996); (b) Chen and Young (2006).

The standard EC3-1.2 establishes that the elastic modulus of steel at temperatures 20-100 ˚C is constant, and it decreases above 100˚C, whereas the standards EN 10088-1 and AS 4100 determine that the modulus increases above 20˚C. In EC3 -1.2 (2005) the elastic modulus also decreases after temperature 20˚C. Based on this standa rd, the reduction factor of the Young's modulus at different temperatures is listed in Table 4.3. The values of the Young modulus at given temperatures are listed in Tables 4.4 and 4.5 according to Sakumoto et al. (1996) and the standard EN 10088-1. By interpolating the data listed in Table 1c, we derived an empirical relationship between the Young's modulus E and the temperature T:

$$E(GPa) = 201.5 - 0.075T, \quad 20 \le T \le 100 \qquad (4.1),$$

where the temperature is expressed in degree Celsius. We used this relation in the numerical studies presented hereafter.

Table 4.3. Reduction factor in the Young's modulus at different temperatures (EC3-1.2).

Temperature (°C)	Reduction factor
20	1.00
100	0.96
200	0.92
300	0.88

Table 4.4. The value of Young's modulus at different temperatures (Sakumoto et al., 1996).

Temperature (°C)	Stainless steel 304	Stainless steel 316	Stainless steel 304N2
	E(GPa)	*E(GPa)*	*E(GPa)*
Room temperature	191.1	191.1	197.3
100	186.6	186.6	191.7
200	178.4	178.4	183.6
300	170.1	170.1	170.1

Table 4.5. Young's modulus of stainless steel at different temperatures (EN 10088-1).

Temperature (°C)	*E(GPa)*
20	200
100	194
200	186
300	180

4.2.1 Numerical Setup

A 9.525 mm × 19.05 mm × 914 mm stainless steel beam, clamped at both ends, was considered. For the beam, we assumed ρ = 7800 kg/m^3, E = 200 GPa, ν = 0.28, and yielding stress σ_Y = 206.8 MPa. The geometric and mechanical properties of the beam were such that its Euler load P_{cr} was equal to -12.95 kN and corresponding Euler stress σ_{cr} was -71.40 MPa.

The chain consisted of fourteen 19.05 mm in diameter particles. Each particle weighed 29 gr. and was made of stainless steel for which the Young's modulus and the Poisson's ratio were

considered equal to 200 GPa and 0.28, respectively. Figure 4.8 shows the top view of the numerical setup; the chain touches the beam at the midspan. The force profile associated with the propagation of the solitary pulse was measured at the center of the 5^{th} and 10^{th} particles away from the interface. As done before, these particles are indicated as sensing sites 2 (S2) and 1 (S1), respectively. The pre-compression force was set to zero and the effect of a striker was simulated by setting an initial velocity 0.3018 m/s. This value was chosen in agreement with some experiments recently conducted in our laboratory.

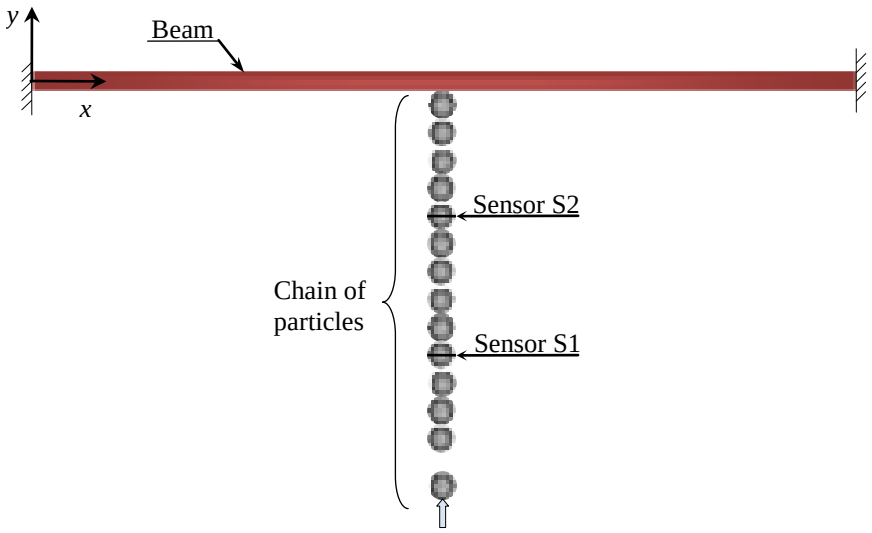

Figure 4.8. Top view of the numerical simulation setup. The beam is fixed-fixed and in contact with the granular medium at the mid-span.

4.2.2 Numerical results

First, we considered a room temperature of 20 °C and increased the beam's temperature at discrete steps until the beam was subjected to a thermal stress near to σ_{cr}. At each step, the Young's modulus of the beam was updated according to Eq. (4.1). Based upon the geometric

and mechanical properties of the beam, as well as its boundary conditions, the critical temperature T_{cr} resulted 40.63 °C. This value can be computed as:

$$T_{cr} = T_n + \frac{\left(\pi r_{\min}\right)^2}{L_e{}^2 \alpha} \tag{4.2}$$

where r_{min} is the least radius of gyration of the beam's cross section, L_e is the effective length of the beam, and T_n represents the beam's neutral temperature.

In order to study the effect of the thermal stress on the propagation of the HNSWs, the same features listed in Table 3.1 were extracted from the dynamic force measured at S1 and S2.

Figure 4.9 displays these features measured at S1 as a function of the temperature raise ΔT. The values associated with the reflected pulse show a polynomial trend. For the amplitudes, the largest variation is small and in the order of 2% due to the fact that only the stiffness of the beam affects the generation of the reflected pulse. While the amplitude of the vibration-induce mode do not show any clear trend, its time of flight (Fig. 4.9(d)) changes significantly especially when the thermal load approaches the critical buckling load. This is related with the period of vibration of the beam. In fact the relationship between the angular natural frequency ω_n and the axial load P is given by (Tedesco et al. 1999):

$$\omega_n = \frac{\beta_n}{\sqrt{m}} \sqrt{P + \beta_n^2 EI} \tag{4.3}$$

where m is the mass per unit length, β_n is the n-th root of the characteristic equation, and EI is the flexural rigidity. Note that when ΔT is equal to 19 °C, for example, the Young's modulus of the beam's material decreases 0.71% in comparison without considering the effect of temperature. The effect of this change of the Young' modulus is such that the value of RSW/ISW, TOF RSW, and TOF VSW increases by 0.21%, 0.05%, and 0.18%, respectively, whereas the value of feature VSW/ISW decreases by 5.14%.

To quantify and compare the selected features, we normalized them with respect to the corresponding maximum value. The results are presented in Fig. 4.10 and they show clearly that the time of flight of the vibration-induced pulse provide the largest sensitivity with respect to the temperature increase.

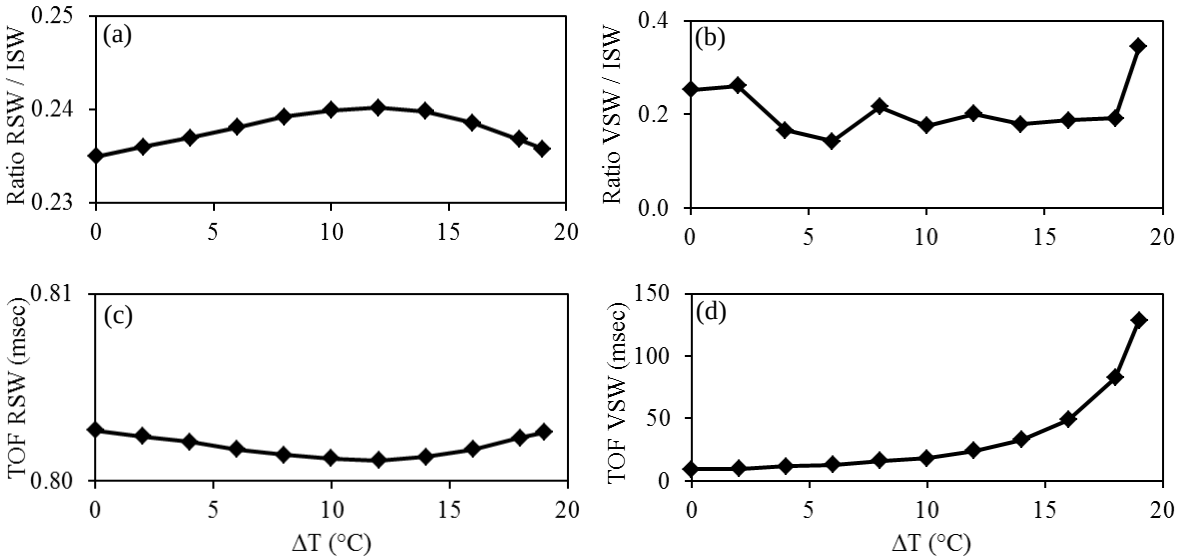

Figure 4.9. Numerical results showing time of flight and amplitude ratio of HNSWs as a function of the temperature rise. Amplitude ratio associated with the (a) reflected solitary wave and (b) vibration-based solitary waves. Time of flight of the (c) reflected solitary wave and (d) vibration-based solitary waves.

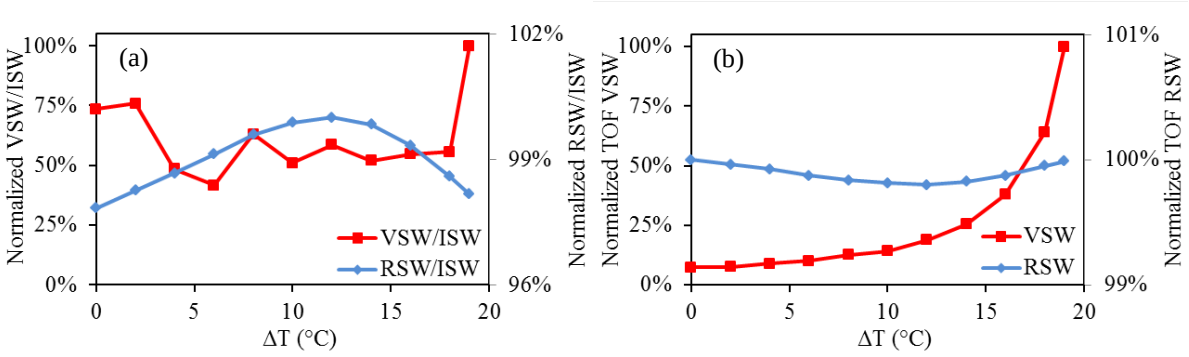

Figure 4.10. Numerical results showing the normalized features selected in this study and presented in Figure 5. (a) amplitude-based features; (b) TOF-based features. The values of the reflected wave are reported on the ordinate axis at the right side of the figure plot area.

To investigate the ability of the proposed method at capturing the neutral temperature of the beam, i.e. the temperature at which the stress is null, we evaluated the effect of the neutral temperature on the selected features. We calculated the stress σ at a certain temperature T_c as:

$$\sigma = E\alpha\left(T_c - T_n\right) \tag{4.4}$$

In the analysis, the Young's modulus of the beam at each current temperature was updated like the previous study. Figure 4.11 shows the solitary wave features extracted from the time waveforms measured at S1 as a function of the beam's temperature for seven different T_n. For each curve the data are ended at the corresponding critical temperature. The results associated with $T_n=0$ are very similar to those presented in Fig. 4.9, because we get same results for ΔT in the beam using both analyses. Overall, we observe similar curves for all the neutral temperatures. These curves are shifted by T_n except for the feature VSW/ISW that does not show any specific trend. The similarity among the curves is related to the correspondence between temperature and thermal stress.

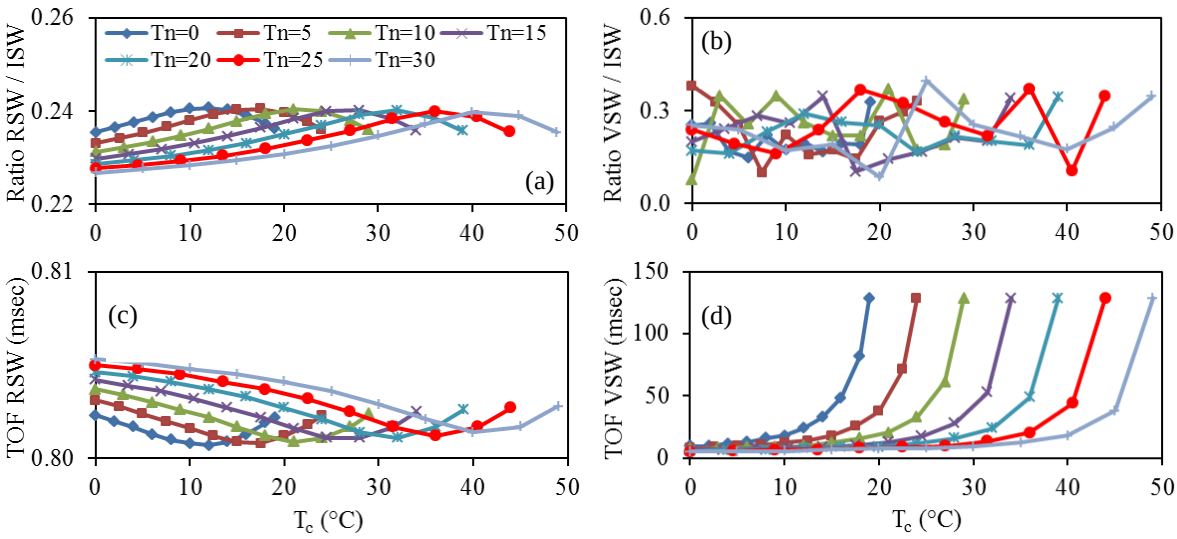

Figure 4.11. Numerical results showing time of flight and amplitude ratio of HNSWs as a function of the temperature rise and relative to different neutral temperature T_n. Amplitude ratio associated with the (a) reflected solitary wave and (b) vibration-based solitary waves. Time of flight of the (c) reflected solitary wave and (d) vibration-based solitary waves.

4.3 USE OF THE ARTIFICIAL NEURAL NETWORK

It is known that ANNs are one of the most effective soft computing algorithms for data processing. They mimic the human brain by implementing the interconnection of artificial neurons. In this study we utilized the ANN to map knowledge between some of the selected HNSW-based features and the beam's neutral temperature T_n. We considered the current temperature T_c and the features of RSW/ISW, TOF RSW, and TOF VSW measured at S1 as the input of the network. Feature VSW/ISW was not considered in the analysis, because this feature did not show a clear trend with respect to the temperature. The neutral temperature represented the output of the neural network.

A feed-forward back propagation ANN with three layers was used. The input layer received the data vector containing the four parameters. The hidden layer processed the data by multiplying the input vectors by weights and adding biases. The results constituted the argument of a transfer function that squashed the output values into a certain range. For the hidden layer, eight neurons were used, and the hyperbolic tangent sigmoid transfer function:

$$f(x) = \frac{2}{1+e^{-2x}} - 1 \tag{4.5}$$

was employed using the *tansig* function in *MATLAB*® software. This function squashed the output values between –1 and +1. For the input and output layers we used the *purelin* transfer function which is $f(x)=x$. The output layer had one node which provided the network's output, and it compared the output with the targets by calculating the mean square error (MSE) as:

$$MSE = \frac{1}{n}\sum_{i=1}^{n}\left[\left(T_n\right)_i - \left(\hat{T}_n\right)_i\right]^2 \tag{4.6}$$

where n is the number of training samples, and $\hat{T}_n$ is the network output for the neutral temperature. If the error was above a certain value, the training process was continued by transmitting the errors backwards from the output layers, and adjusting the weight and biases. If the error was below an established value, the learning process stopped. The training process also stopped when a minimum on the error gradient was reached. To train the network, we used the Levenberg-Marquardt algorithm because of its best performance and speed (Hagan and Menhaj, 1994).

In order to study the capability of ANNs for estimating the neutral temperature, first, we used all the 77 data (see caption of Fig. 4.11) for training the neural network. Figure 4.12a compares the estimated results for the neutral temperature with the actual neutral temperatures. It can be seen that there is no difference between predicted and actual neutral temperature. Then,

we considered a subsample composed by 44 data to train the network. The data belonged to the neutral temperatures set at 0, 10, 20 and 30 °C. The remaining 33 data, associated with T_n = 5, 15, and 25 °C, were used for testing. A comparison between the estimated results for the neutral temperature using ANNs and the actual neutral temperatures is shown in Fig. 4.11b. It is visible that the differences between the estimated results for test data and actual results are negligible for most of data. This second approach simulates a scenario where solitary wave features are measured in-situ by means of HNSW-based transducers and the current temperature is measured by means of a thermocouple.

Finally, we evaluated the effect of the selected features on the accuracy of the estimation of the neutral temperature. We considered all the possible combination of features as the input of an ANN; at each given combination, we used all data except the *i*-th for training and then we used the *i*-th datum for testing. This protocol was iterated 77 times. The measure of success was determined by computing the difference between the estimated and the true neutral temperature. If this difference fell below a set threshold, than testing was considered successful. Finally, the success ratio was computed by the summation of all success iterations divided by the number of the data, i.e. 77. Table 4.6 summarizes the results. The second column shows the features' combination; the third column reports the success rate when the discrepancy between the estimated and the true neutral temperature was lower than 0.5 degrees Celsius. Finally, the last column refers to the results associated with a threshold set at 1 °C. It can be seen that the feature selection is pivotal at determining the proper neutral temperature. By using the current temperature and the three wave-based features, more than 97% of the numerical data were determined within a 1 °C accuracy.

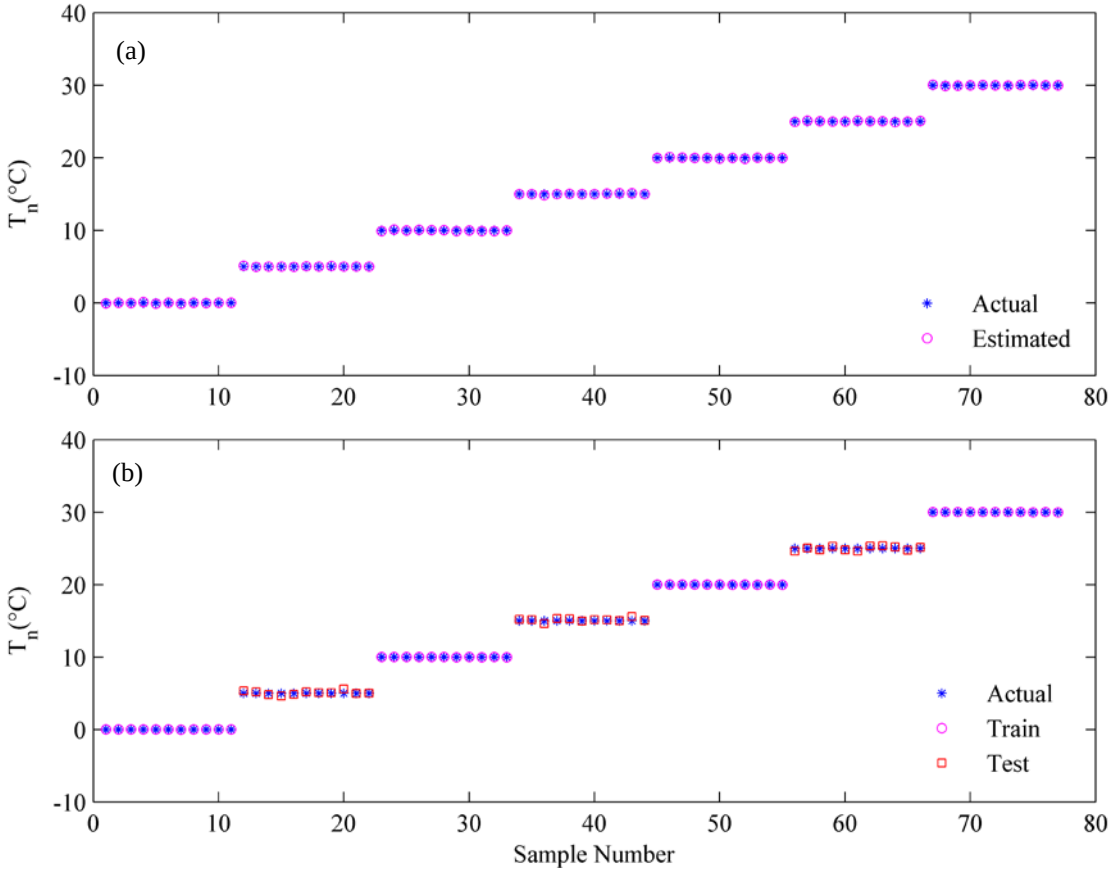

Figure 4.12. Results of the artificial neural network. (a) Estimated and actual neutral temperature for the 77 data samples, when all the data were used for training. (b) Estimated and actual neutral temperature for the 77 data samples, when only 44 data were used for training.

Table 4.6. Artificial neural network results. Values of success ratio (%) for all possible combination of features.

No	Features' combination	Value of threshold	
		0.5 °C	1.0 °C
1	T_c	1.30	2.60
2	RSW/ISW	1.30	5.19
3	TOF RSW	7.79	9.09
4	TOF VSW	6.49	9.09
5	T_c, RSW/ISW	18.2	33.8
6	T_c, TOF RSW	14.3	29.9
7	T_c, TOF VSW	45.5	67.5
8	RSW/ISW, TOF RSW	5.19	15.6
9	RSW/ISW, TOF VSW	2.60	7.79
10	TOF RSW, TOF VSW	5.19	13.0
11	T_c, RSW/ISW, TOF RSW	20.8	33.8
12	T_c, RSW/ISW, TOF VSW	90.9	97.4
13	T_c, TOF RSW, TOF VSW	85.7	93.5
14	RSW/ISW , TOF RSW, TOF VSW	14.3	22.1
15	T_c, RSW/ISW , TOF RSW, TOF VSW	88.3	97.4

4.4 STUDY OF A RAIL-LIKE BEAM

4.4.1 Single chain of particles

A 20 m long beam was considered. This could be a good tradeoff between the analysis of fixed-fixed boundary condition and the fact that CWR can be up to 400 m long but restrained by the ties. The granular matter consisted of fourteen stainless steel 19.05 mm in diameter granules, weighing 29 gr. The effect of axial load on an AREMA 141 rail section with cross-section area 8.9×10^{-3} m^2 and smallest moment of inertia 6.21×10^{-6} m^4 was evaluated. The properties of the beam's material were considered as: density=7863 kg/m^3, Young's Modulus=210 GPa, yielding stress=510.2 MPa, and Poisson's ratio = 0.296 (Lim et al. 2003). Figure 4.13(a) shows the cross

section of the numerical setup. It should be noted that the 1-chain configuration does not need the knowledge of the beam thickness.

Two sensor sites, S1 and S2, located at the center of two grains were considered to measure the dynamic contact force. Their location is shown in Fig. 4.13(a). The pre-compression force in numerical studies was considered zero, and for generation HNSW in the system, an initial velocity was applied to the first particle which was equal to 0.3018 m/s. For this beam, the buckling load and the corresponding buckling stress are -128.67 kN and -14.45 MPa, respectively. The Euler stress is based on the assumptions associated with ideal homogeneous beam clamped at both ends. However, experiences in the field have shown that real rails sometimes buckles when they experience a temperature raise in the order of 50 F or even 60 F above the neutral temperature which translates into a buckling stress, if computed using Eq. (1.1), close or above 75 MPa, depending upon the coefficient of thermal expansion considered. The ability to withstand higher stress is provided by the presence of the lateral restraints and ties.

Figure 4.14 shows the solitary waves measured at S1 and S2 when the axial stress in the beam is zero. Only two pulses are visible, the incident and the reflected wave which have the same meaning as discussed throughout this document. It is noteworthy that the rail-like beam is too stiff to vibrate and therefore to induce VSW. Moreover, the rail appears to be too stiff to allow for local oscillations of the grains at the beam-chain interface due to gap openings induced by the dynamic force carried by the waves. This findings however needs experimental validations.

In order to study the effect of the axial stress in the beam on the solitary force profile, some features were extracted from the solitary force profiles. Figure 4.15 shows the solitary wave features extracted from the solitary force profiles measured at sensor S1 as a function of

the axial stress of the beam. It can be seen that there is some variation with respect to the axial stress for the results of the ratio RSW/ISW, but there is not any variation for the results of the TOF RSW.

Changing the beam's axial load causes to change somewhat the beam's stiffness which only affects the amplitude of the RSW. The normalized values of solitary wave features extracted from the solitary force profiles measured at sensor S1 as a function of the axial stress of the beam are provided in Fig. 4.16. The normalized values reveal that the variation with respect to stress is almost null. It should be emphasized here that the axial stress consider in this example is much narrower than that considered in Chapter 3. When the reflected pulse propagates in the granular system, it displaces most particles of the chain away from the beam. To prevent this movement, the action of a nonlinear spring was introduced according to the scheme shown in Fig. 4.13(a). This spring works only when the pulses propagate from right to left side. The force profiles are presented in Fig. 4.17. Besides the incident and the reflected pulses, a third and a fourth pulse are visible and they we named them secondary ISW (SISW) and secondary RSW (SRSW), respectively. The SISW is generated by the reflection of the RSW from the second particle, and the SRSW is the SISW reflected from the beam-chain interface and propagating back through the granules and arriving at the sensor site.

Two features of the SRSW were extracted and shown in Figure 4.18. It can be seen that there is not a given trend in the results for both features, and it can be concluded that the SRSW is not sensitive at predicting axial stress or estimating.

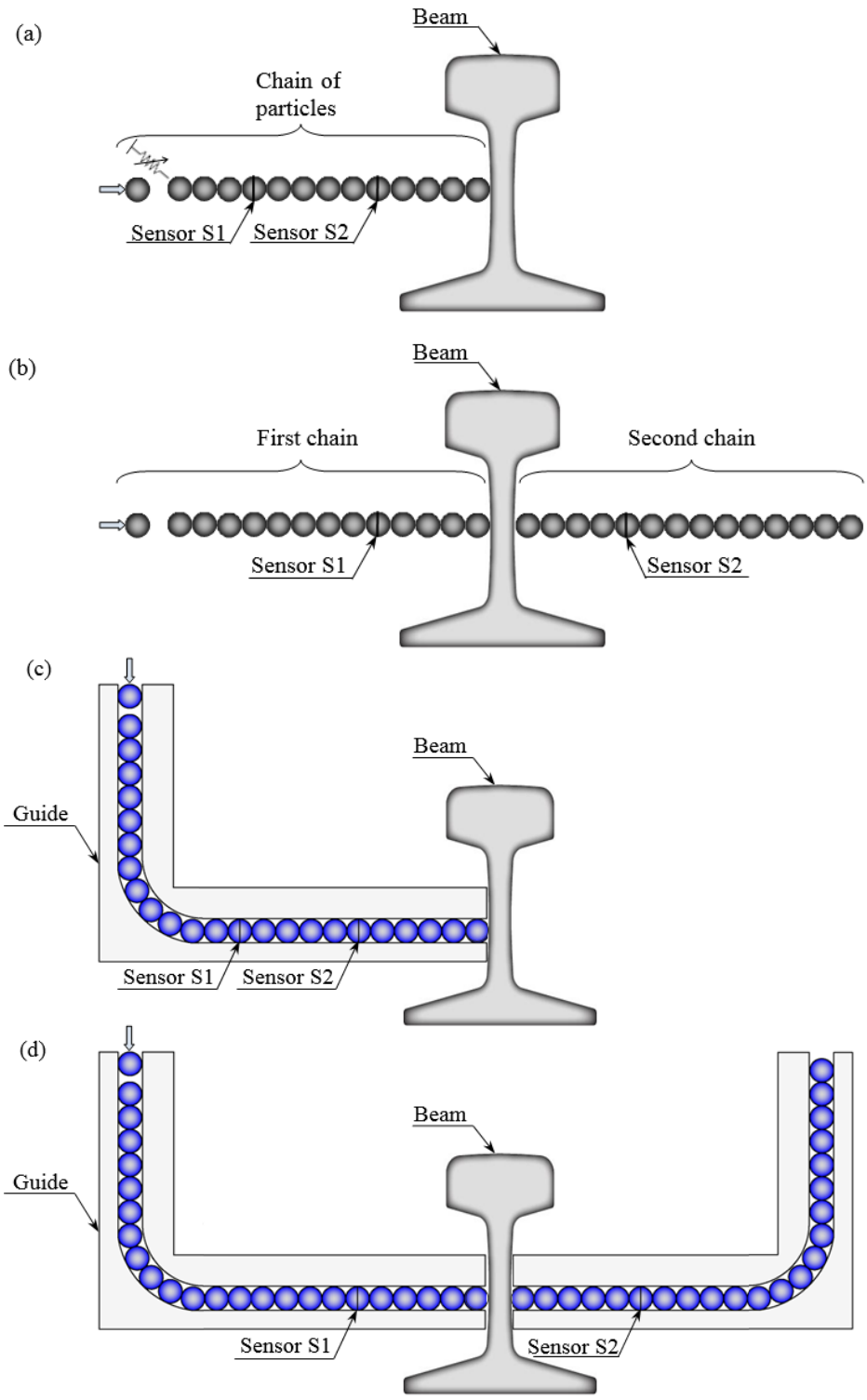

Figure 4.13. Cross section of the numerical simulation setup for: (a) one straight chain, (b) two straight chains, (c) one curved chain, and (d) two curved chains. The beam is fixed-fixed and in contact with the granular medium at the midspan.

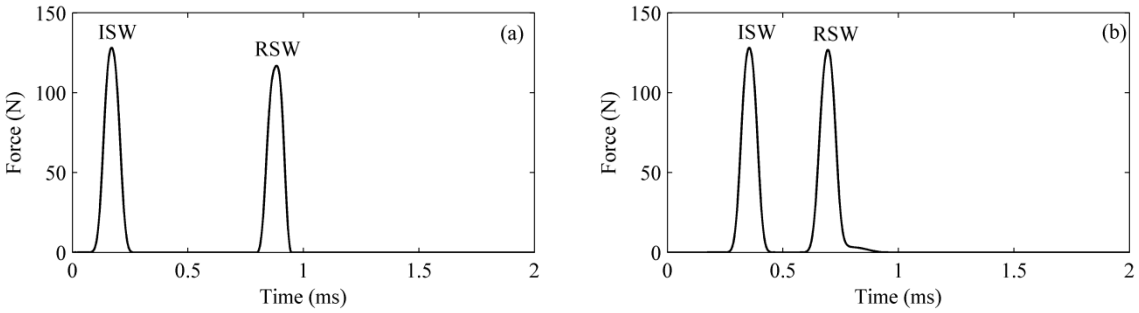

Figure 4.14. Single straight chain configuration. Force profile measured at: (a) S1, and (b) S2 when the axial stress in the rail-like beam is zero.

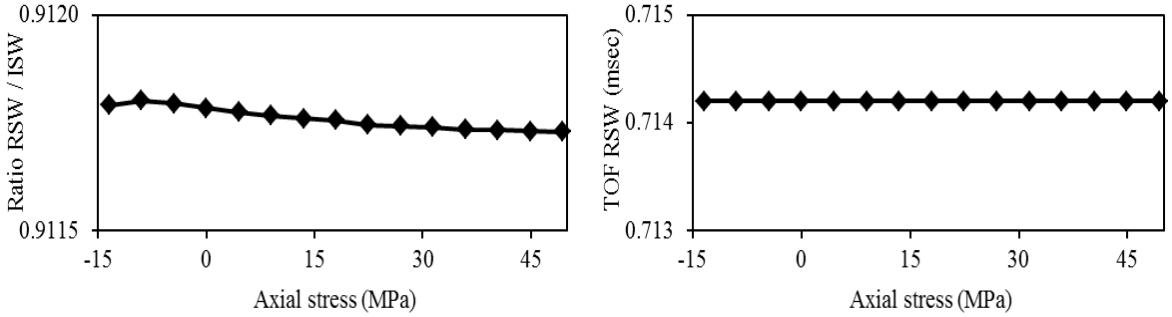

Figure 4.15. Single straight chain configuration. Solitary wave features extracted from the solitary force profiles measured at S1 as a function of the axial stress.

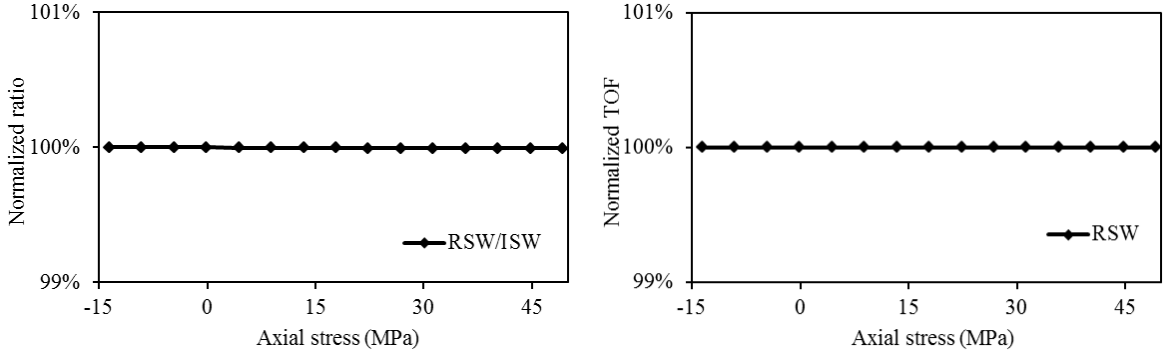

Figure 4.16. Single straight chain configuration. Normalized values of solitary wave features extracted from the solitary force profiles measured at S1 as a function of the axial stress.

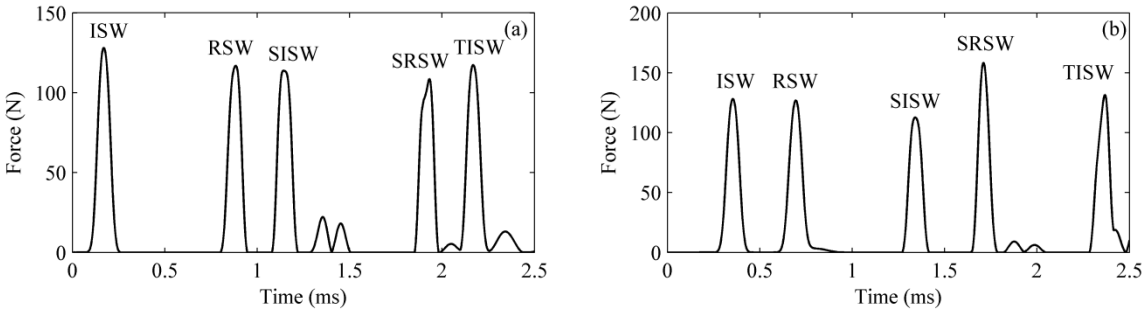

Figure 4.17. Single straight chain configuration in presence of a reactive spring. Force profile measured at: (a) S1, and (b) S2 when the axial stress is zero and a force was applied on the second particle.

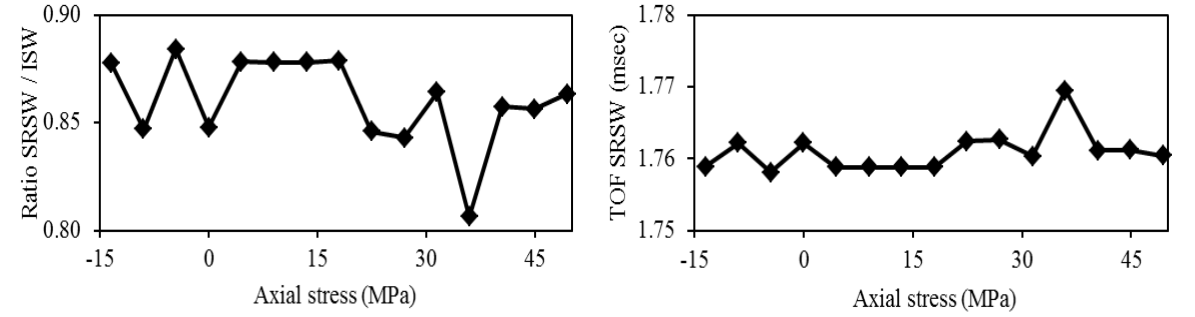

Figure 4.18. Single straight chain configuration in presence of a reactive spring. Solitary wave features extracted from the solitary force profiles measured at S1 as a function of the axial stress when a force was applied on the second particle.

4.4.2 Two chains of particles

A second chain, identical to the first one, was placed in contact with the rail-like beam as shown in Fig. 4.13(b). In this case the thickness of the beam was 11/16 inches which is the nominal thickness of the AREMA 141 web. Two sensor sites were considered at a distance of 4.5 particle diameters from the web surface. Figure 4.19 shows the force profile results of the solitary wave at sensors S1 and S2 when the axial stress in the beam is zero. As can be seen, there are two pulses in Figure 4.19(a) which are like the results shown in Figure 4.14(b). In Figure 4.19(b), the first wave is the TSW which is generated by transmitting the ISW through the beam and

propagating along the chain and arriving at sensor S2. The next remaining wave in the figure is generated by the vibration of the beam. The amplitude of the transmitted waves is three orders of magnitude lower due to the high stiffness of the beam.

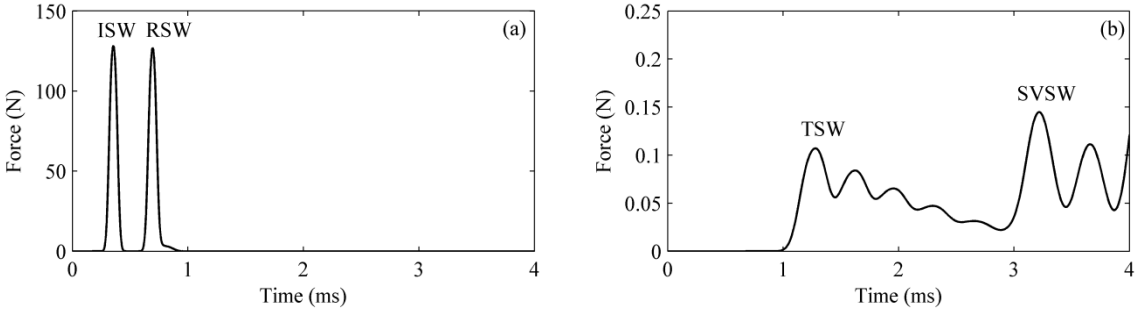

Figure 4.19. Two straight chains configuration. Force profile results of solitary waves at (a) S1, and (b) S2 when the axial stress is zero.

Some selected features were computed and plotted against the axial stress. Figure 4.20 shows the features extracted at sensors S1 and S2 as a function of the beam's axial stress. It can be seen that there is significant variation with respect to the axial stress The features relative to the reflected and transmitted wave denote a monotonous trend in the domain above -10 MPa. Below that mark, there is a change in the gradient; the reason for this change is due to changing the value of the coefficient, ϕ_r^2/M_r, of the force applied to the beam by the solitary pulse with respect to the axial stress (see Eq. (2.10)). This coefficient was used to compute the beam' acceleration, and its value has a trend like the TSW/ISW. When the value of this coefficient decreases, the beam' acceleration decreases and the beam works as a particle with higher stiffness, due to this effect, the amplitude of the RSW increases. From Figure 4.20, it can be seen some changes for the ratio of SVSW/ISW which are related to the combination of many vibrational modes of the beam for generating SVSW, and for a given axial load, there is different modes' contribution that effects on the amplitude of the SVSW not the arriving time. Thus, there

is a given trend for the results of the TOF SVSW, and the value of the feature decreases with increasing the axial stress, because of increasing the beam's stiffness.

The values shown in Figure 4.20 were normalized with respect to the maximum value for each feature and are presented in Figure 4.21. It can be seen that certain features vary by 5% despite the considered stress range is narrow. The findings illustrated in this section suggest that the configuration with two chains of particles is effective at detecting stress variation and it should be preferred to the single-chain configuration.

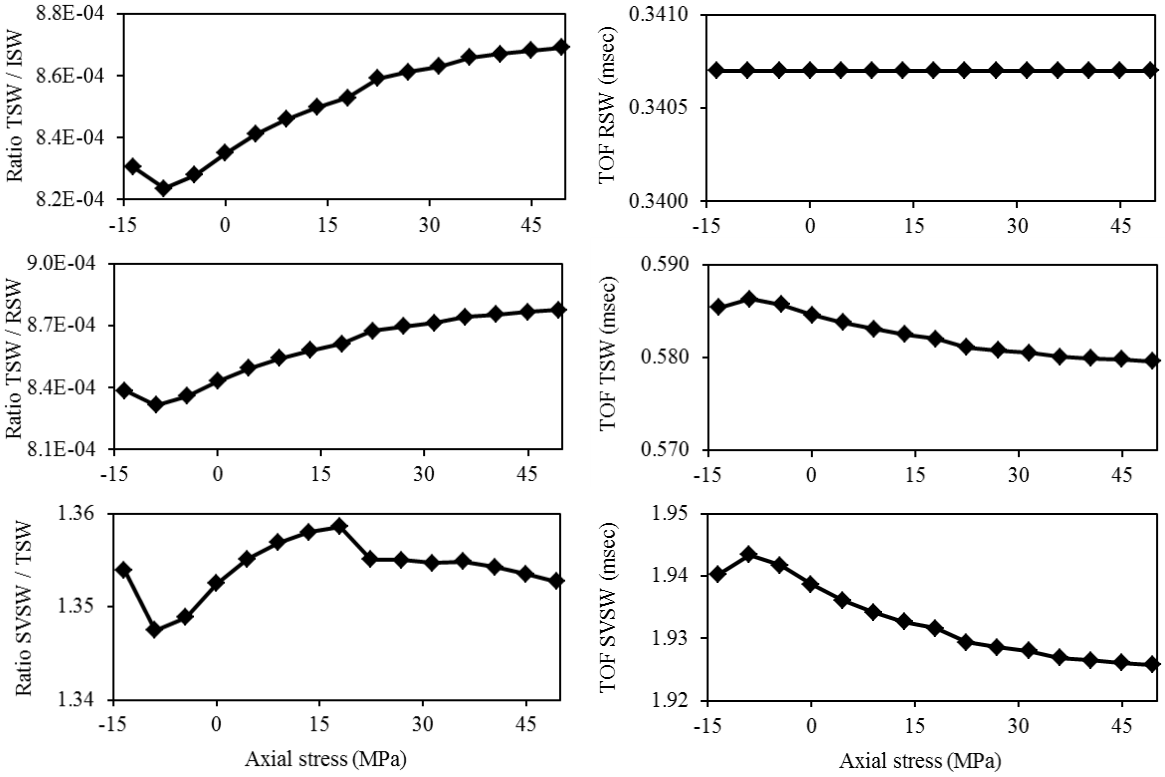

Figure 4.20. Two straight chains configuration. Solitary wave features extracted from the force profiles measured at S1 and S2 as a function of the axial stress.

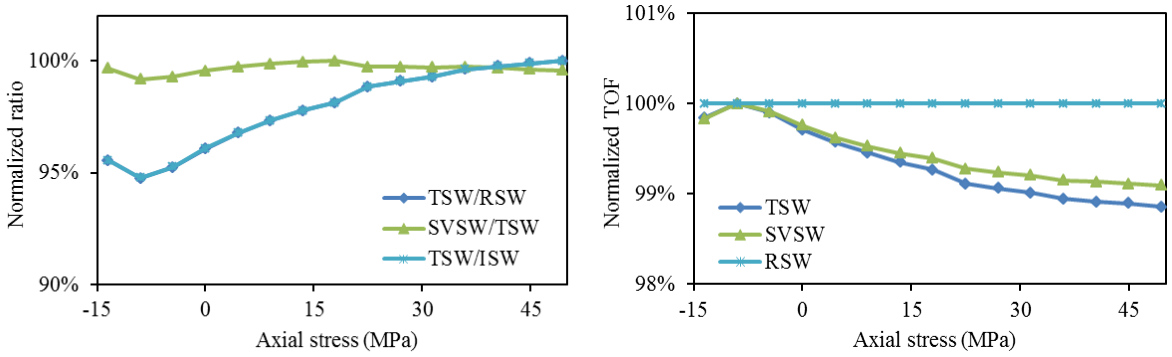

Figure 4.21. Two straight chains configuration. Normalized features extracted from S1 and S2 as a function of the axial stress.

4.4.3 Single L-shaped chain

We used the same numerical approach presented in Chapter 3 for one curved chain to study a beam with AREMA 141 rail section as shown in Fig. 4.13(c). In the numerical simulation, the beam and particles have same properties presented in Section 4.4.1. The granular matter consists of 24 beads at the curved chain. Two sensing sites were considered to measure the dynamic force associated with the waves. Sensing site S1 was at the center of the 11th bead away from the rail whereas the sensing site S2 was at the center of the sixth bead away from the rail.

Figure 4.22 shows the force profile results of the solitary wave at two sensors when the axial stress in the beam is zero. The first pulse is the ISW which is generated in the chain by applying an initial velocity to the first particle. In Figure 4.22(a), the second pulse is generated in the curved section, CISW, whereas the subsequent pulse, the RSW, is the wave reflected from the beam-chain interface and propagating back through the granules and arriving at the sensor site. In Figure 4.22(b), the second pulse is the combination of the RSW and the CISW; however, we name that wave as a RSW in this report.

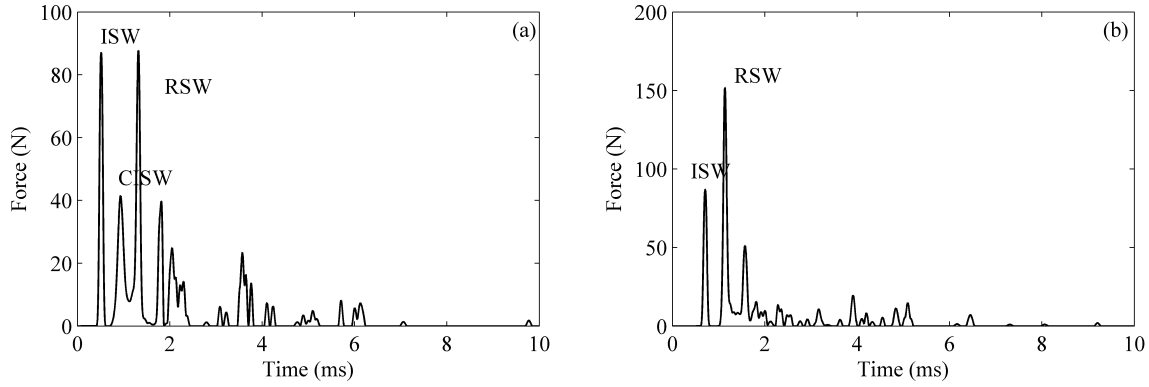

Figure 4.22. Single L-shaped chain configuration. Force profile measured at (a) S1, and (b) S2 when the axial stress is zero.

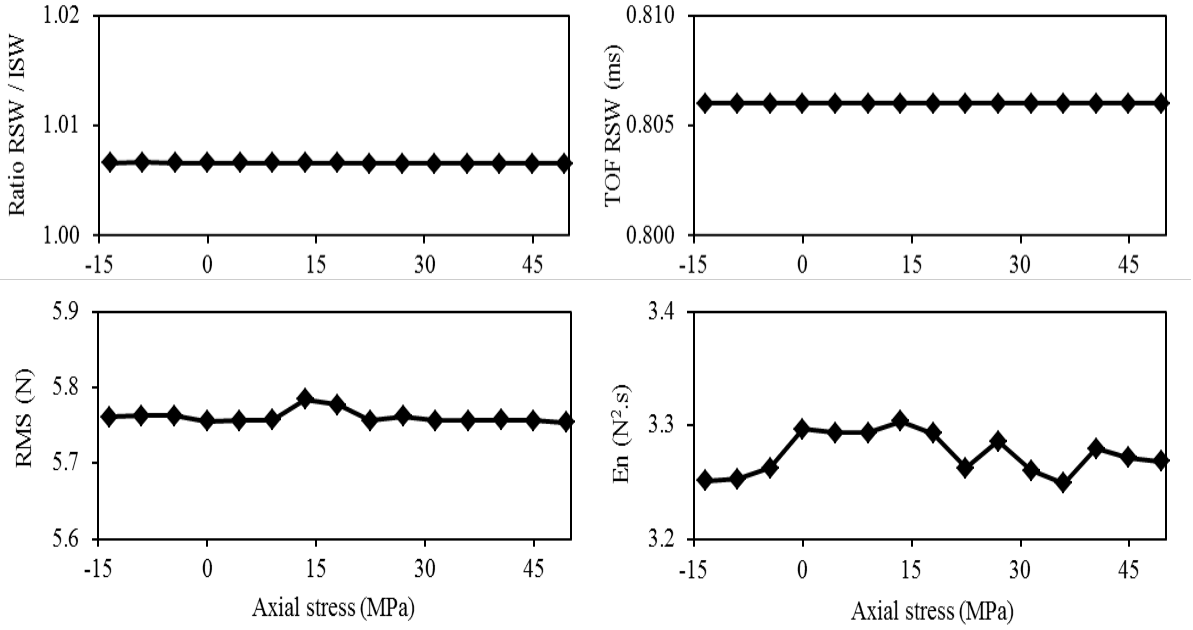

Figure 4.23. Single L-shaped chain configuration. Solitary wave features extracted from the force profiles measured at S1 as a function of the axial stress.

To study the effect of the axial stress in the beam on the solitary force profile, some features were extracted from the solitary force profiles. Figures 4.23 and 4.24 indicate the solitary wave features extracted from the solitary force profiles measured at sensors S1 and S2 as a function of the axial stress of the beam. We can see that there is not variation with respect to

the beam's axial stress for the RSW/ISW and the TOF of the RSW, but there are somewhat variations for the results of the RMS and the En. Changing the beam's axial stress causes to change somewhat the beam's stiffness which affects the amplitude of the vibration-induced waves.

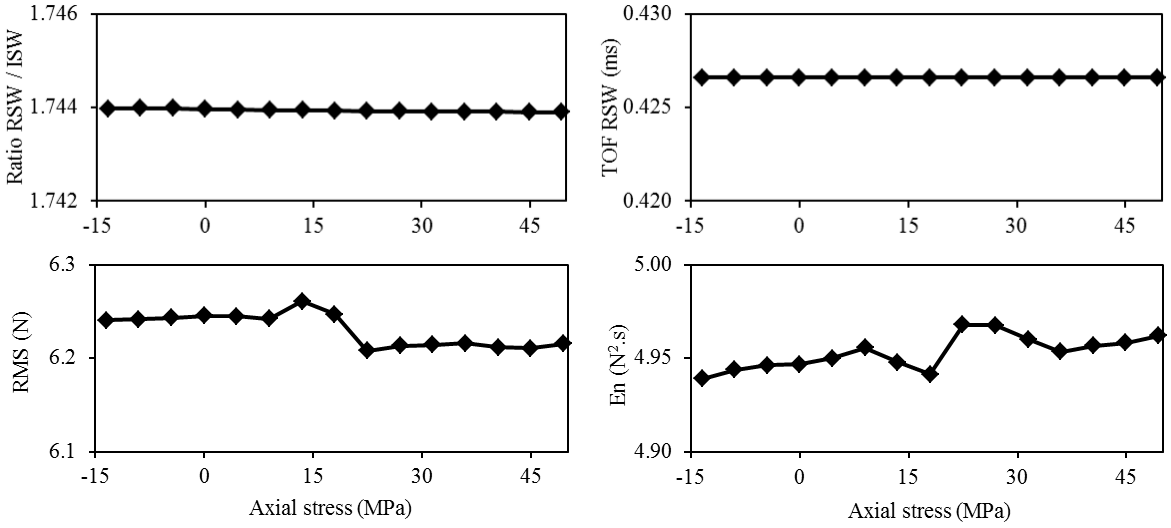

Figure 4.24. Single L-shaped chain configuration. Solitary wave features extracted from the force profiles measured at S2 as a function of the axial stress.

4.4.4 Two L-shaped chains

The numerical simulation method described in Chapter 3 for two curved chains was used here to study a beam with rail cross section as shown in Fig. 4.13(d). In the simulation, each curved chain has 24 beads, and two sensing sites were used at the positions indicated in Fig. 4.13(d).

Figure 4.25 shows the solitary wave at positions S1 and S2 when the axial stress in the beam is zero. As can be seen, there are two main pulses in Figure 4.25(a). The first wave has the same meaning discussed in the previous section, namely the ISW, and the second pulse is the combination of the RSW and the CISW. In Fig. 4.25(b), the first wave is the combination of the

wave generated by the transmission of the ISW through the web and the wave generated by the weight of particles located in the vertical segment of the second chain. However, we still name it transmitted solitary wave (TSW).

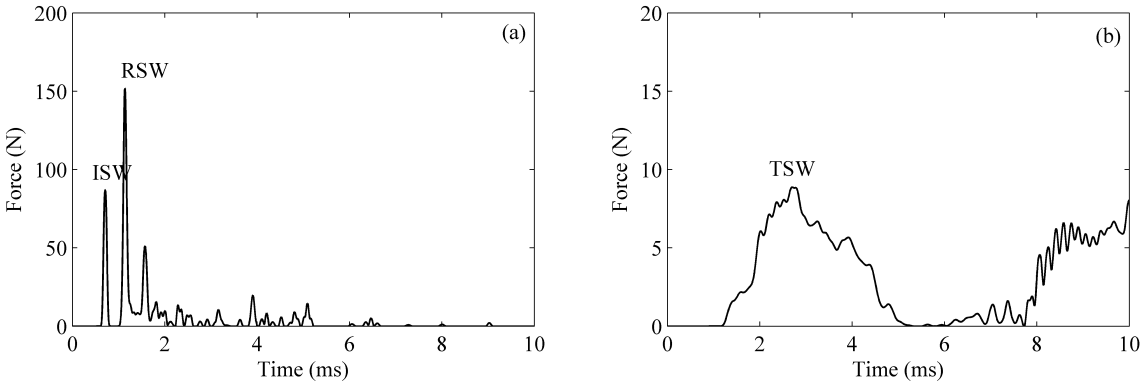

Figure 4.25. Two L-shaped chains configuration. Solitary waves measured at (a) S1 and (b) S2 when the axial stress is zero.

To study the influence of the axial stress in the beam on the solitary force profile, some features were extracted from the solitary force profiles. Figures 4.26 and 4.27 show the solitary wave features extracted from the solitary force profiles measured at sensors S1 and S2 as a function of the axial stress of the beam. It can be seen that there is no significant variation with respect to the axial stress for features extracted from the RSW and the TSW, and the reason is the generated wave by reflecting or transmitting does not change the properties of the waves due to changing the beam's axial load. As a result, there is no more variation with respect to the axial stress From Fig. 4.26, it can be seen some changes for the RMS and En, but they do not have a given trend for the results.

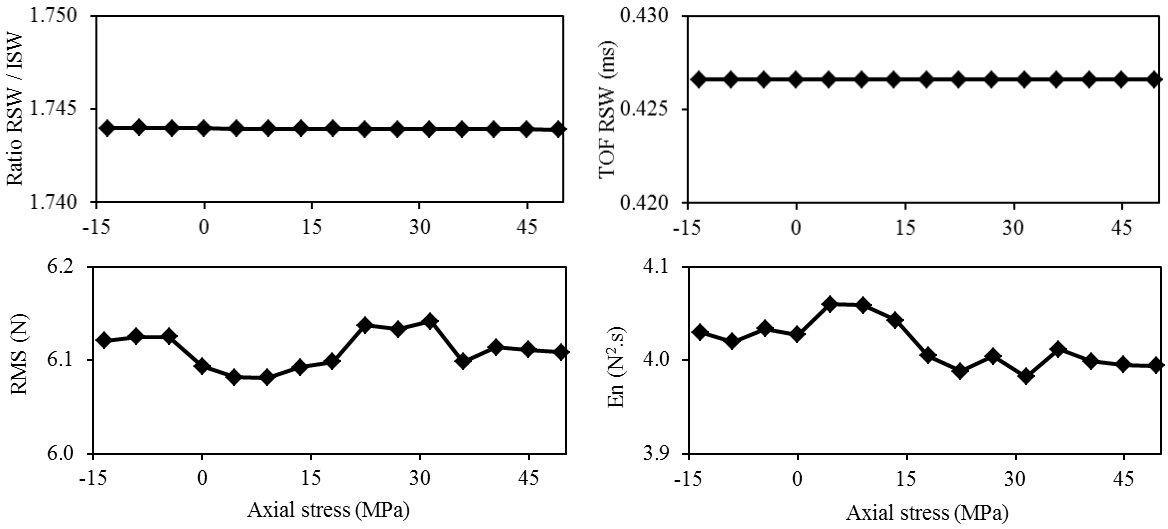

Figure 4.26. Single L-shaped chain configuration. Solitary wave features extracted from the force profiles measured at S1 as a function of the axial stress.

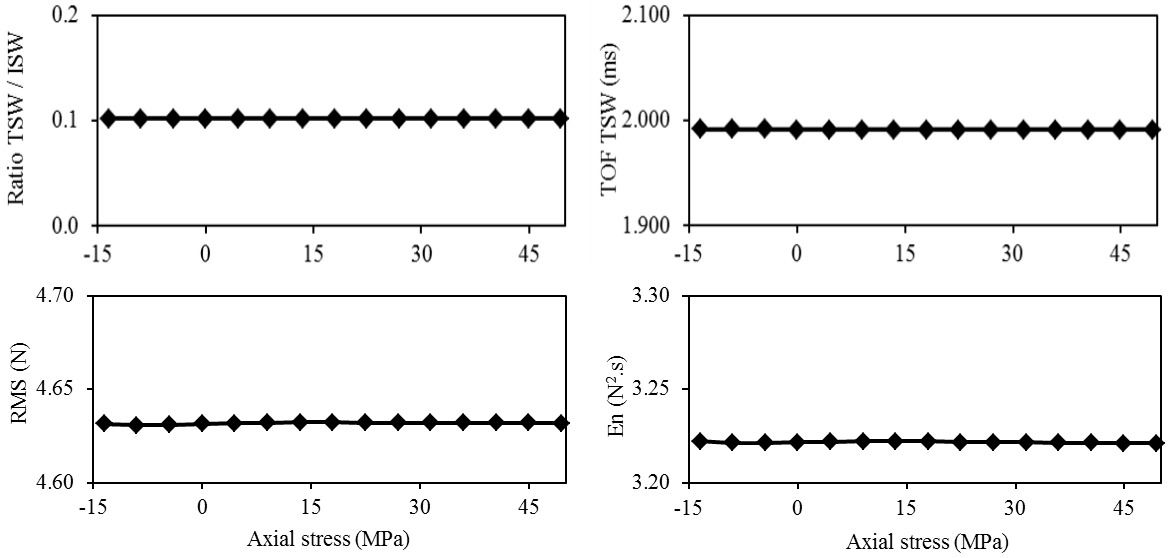

Figure 4.27. Single L-shaped chain configuration. Solitary wave features extracted from the force profiles measured at S2 as a function of the axial stress.

4.4.5 Conclusions

The results presented results in the last four sections demonstrated that some features extracted from the solitary waves vary with respect axial stress. Moreover, it should be emphasized that the compression stress considered in our simulation is much lower than the actual stress experienced by real rail, thus we can argue that in real scenario the variation of the solitary wave-based features is much larger than what seen in the models presented here.

We also found that the chain setup that optimizes the sensitivity of slender beam does not work as well as for the rail section. While in slender beam the most sensitive configuration is the one with a single straight chain, in the analysis of the AREMA 141 we found that two straight chains provide better sensitivity to the variation of stress. Future study may consider performing the same parametric analysis presented in sections 4.1, 4.2, and 4.3 to design the chain of particles that provides the largest sensitivity. Moreover, in order to simulate real railroad tracks in contact with a granular system, we shall consider the effect of sleepers, fastenings, and ballast on the model of the structure. For this purpose, it would be more appropriate model the rail with the finite element method instead of the continuous beam theory.

5.0 EXPERIMENTAL STUDIES

In this chapter, we compare the numerical prediction to some experimental results obtained by one member of our research group. First, we describe the experiments conducted by using the L-shaped transducers. Then, we illustrate the experiments conducted using the straight chains.

Some parts of this chapter were extracted from our published paper entitled “On the use of L-shaped granular chains for the assessment of thermal stress in slender structures”.

5.1 L-SHAPED TRANSDUCERS

We experimentally coupled one L-shaped chain of particles at the mid-span of a prismatic beam held in tension and then heated by means of a thermal tape. A few features were extracted from the time waveforms to quantify the effect of thermal stress on the propagation of the solitary wave induced in the chain. Then, a second L-shaped chain was located on the other side of the beam opposite to the first chain and the same testing protocol was adopted. This latter configuration may resemble the case of a single chain with an impurity at the middle.

5.1.1 Setup

We used the setup presented in Fig. 5.1. A 19.05 mm × 9.525 mm (type 304, McMaster-CARR) steel beam was clamped with a free length of 914 mm to a MTS machine having a capacity of 1179.3 kN and a resolution of 4.45 N. The following mechanical properties were considered: density = 7800 kg/m^3, Young's Modulus=200 GPa, yielding stress=206.8 MPa, and Poisson's ratio = 0.28. These properties were such that the beam's Euler load and the corresponding stress were equal to -12.95 kN and -71.395 MPa, respectively. Heat was applied by means of a thermal tape (McMaster-CARR product number 3631K63) secured to the beam, and a thermocouple was used to measure the temperature.

A chain of 24 beads was assembled inside a cast acrylic L-shaped guide with Young's modulus and Poisson's ratio equal to 3.1 GPa and 0.375, respectively. The elbow contained 5 grains and its radius of curvature R_c was equal to 70.4 mm. The particles were stainless steel bearing-quality balls (type 302, McMaster–Carr) with a diameter D = 19.05 mm, mass m = 29 g, elastic modulus E = 200 GPa, Poisson's ratio v = 0.28, and density ρ= 8000 kg/m^3. 7 beads and 12 beads were located in the vertical and in the horizontal segment, respectively, of the guide which was supported by a house-built steel frame.

An electromagnet located above the vertical segment was used to drive the striker from a falling height of about 4.2 mm, resulting in the striker velocity of 0.288 m/s. The electromagnet was driven by a National Instruments-PXI running in LabVIEW. A LabVIEW front panel was designed to operate the actuator automatically.

Two sensor particles, hereafter indicated as sensor 1 (S1) and sensor 2 (S2) were assembled and used to measure the propagation of the HNSWs generated by the mechanical impact of the striker. Each sensor bead contained a piezoelectric ceramic disc (circular plate with

0.3 mm thickness and 19.05 mm diameter) with silver electrodes and microminiature wiring (see inset in Fig. 5.1). S1 and S2 were positioned at the middle of the 14-th and 19-th particle as shown in Fig. 5.1(a). The details of the sensor assembly can be found in previous works where similar sensors were used (Daraio et al., 2005; Yang et al., 2011). The sensors were connected to the same NI-PXI and the signals were digitized at 2 MHz sampling rate.

The testing protocol was as follow. The beam was initially loaded in tension up to 20% of its yield load. Then the MTS machine, operated in displacement control, held the beam and heat was applied. We measured the HNSWs during the heating phase at step of 5°C until the beam reached the 60% of its Euler load. In order to assess the repeatability of the setup, we took 15 measurements at each step. The test was repeated, i.e. two heating processes, hereafter indicated as Test 1 and Test 2, were completed.

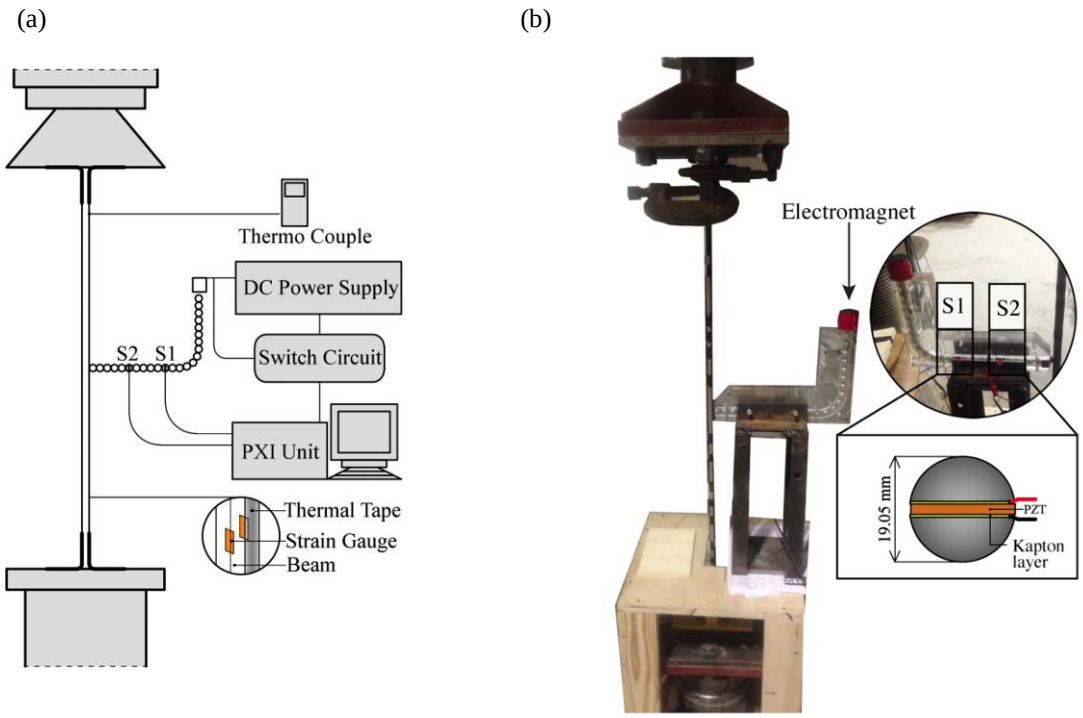

Figure 5.1. Single-chain configuration. (a) Scheme and (b) photo of the experimental setup. The beam is clamped at its ends and an L-shaped chain made of 24 particles is in contact with the beam at the beam's mid-span. Two sensor particles S1 and S2 were assembled and used to measure the propagation of the waves. Each sensor bead contained a piezoelectric ceramic disc with silver electrodes and microminiature wiring.

The same setup and test protocol were adopted when a second identical chain was added according to the scheme presented in Fig. 5.2. The sensors in this second chain, namely S3 and S4 recorded the solitary waves transmitted through the beam's thickness. The objective of this portion of the study was to determine whether this configuration enhances the sensitivity of the noninvasive methodology proposed here.

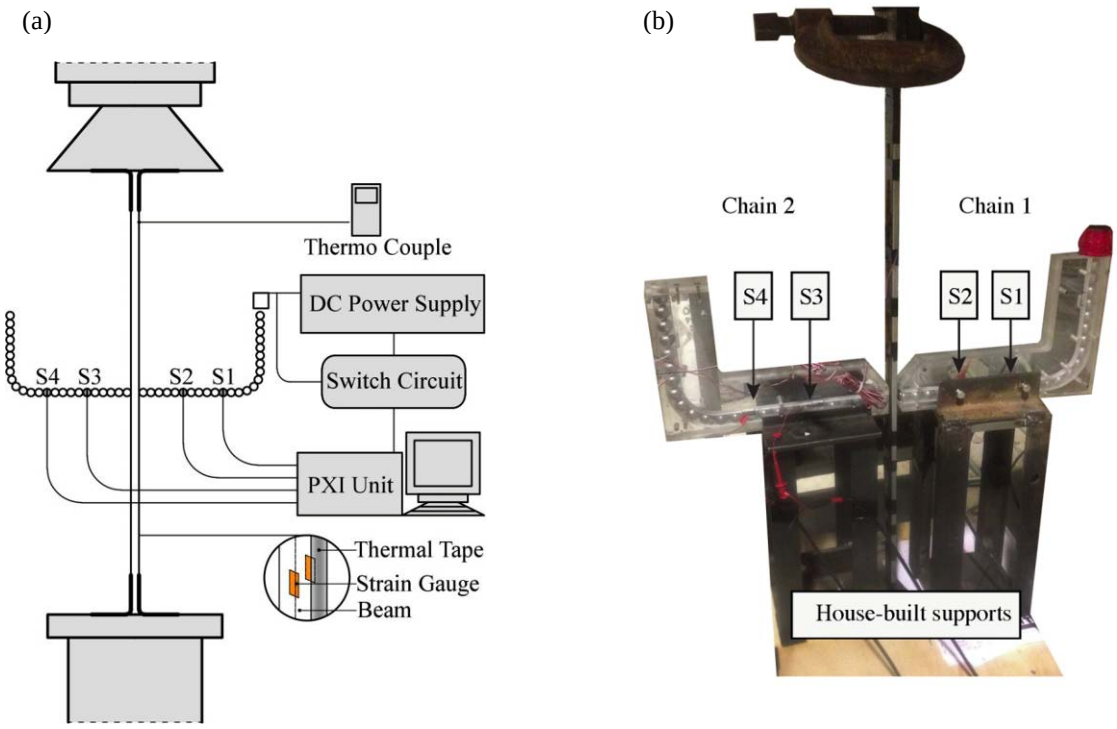

Figure 5.2. Two-chain configuration. (a) Scheme and (b) photo of the experimental setup. The beam is clamped at its ends and two L-shaped chains made of 24 particles each are in contact with the beam at the beam's mid-span. Four sensor particles were assembled to measure the propagation of the waves. Sensors S1 and S2 are embedded in the first chain where the solitary waves are generated. Sensors S3 and S4 are embedded in the second chain.

5.1.2 Results

In this section, we present both the numerical and the experimental results. Figure 5.3(a) shows the axial stress as a function of the temperature raise ΔT for both heating ramps when a single chain was used. The data show the very good repeatability of the testing protocol. We observe that at zero stress there is a slight change of the slopes of the experimental data. This may be attributed to some settling of the machine's grips. By interpolating the experimental data, a linear relationship between the stress and the temperature is found, in agreement with Eq. (4.4). By

solving the linear fit for the zero stress we find that the neutral temperature occurred at ΔT=23.01 °C, and by using room temperature 21 °C which was used during the experiment we can find that the neutral temperature is equal to 44.01 °C

Similarly, the stress as a function of the beam's temperature when two chains were used is presented in Fig. 5.3(b). The graph is similar to Fig. 5.3(a) and it confirms the repeatability of the setup. For this second round of experiments the neutral temperature occurred at ΔT=24.75 °C.

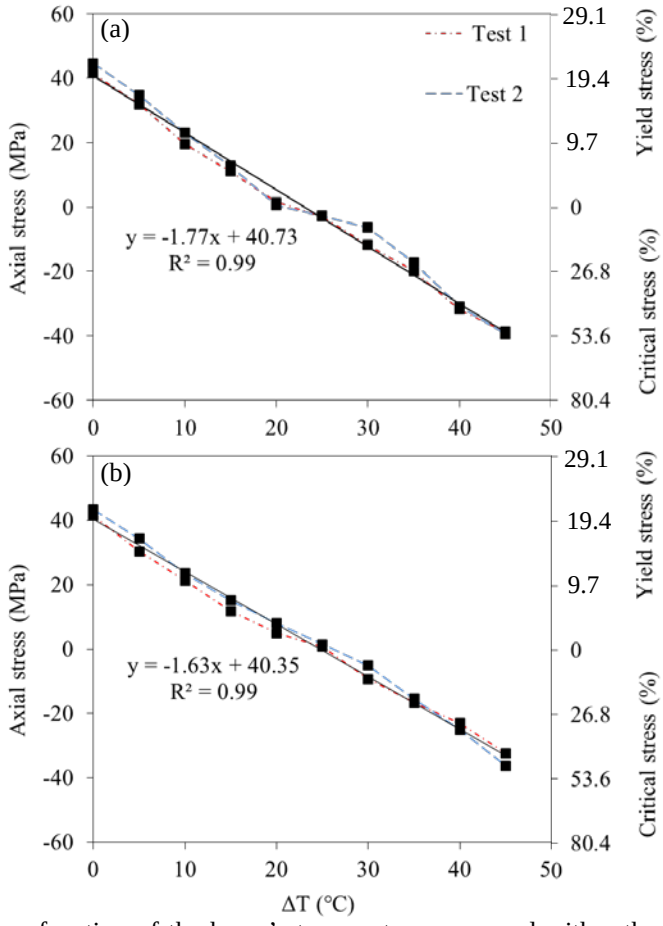

Figure 5.3. Axial stress as a function of the beam's temperature measured with a thermocouple. (a) Single-chain configuration, and (b) two-chains configuration. The continuous line is the linear interpolation of both heating loads.

Figures 5.4(a) and (b) show the experimental and the numerical solitary waves measured during test 1 under the largest tension at 41.4 MPa by sensors S1 and S2, respectively. Similarly, Figs. 5.4(c) and (d) show the results relative to the largest compression at -38.7 MPa. The numerical results are overlapped to the first of the corresponding 15 measurements. To ease the comparison between numerical and experimental data, the abscissas were shifted horizontally in order to overlap the arrival of the first pulse. This was necessary since the numerical t=0 corresponded to the motion onset of the first particle, whereas the experimental trigger was set to the arrival of the first pulse at the sensor bead S1. Moreover, the amplitudes were normalized with respect to the amplitude of the corresponding first peak. This was necessary as the numerical pulse refers to force whereas the experimental values refer to voltage.

In Fig. 5.4(a), the first pulse is the incident solitary wave (ISW) generated by the striker. This pulse is tailed by another pulse that is generated at the elbow. We will detail about this second pulse later. The wave visible at about 1.5 ms is the reflected solitary wave (RSW) which is the wave backscattered from the beam-chain interface. These three waves occur also under large compression as shown in Fig. 5.4(c). In Fig. 5.4(b) we notice that the second pulse and the RSW coalesce into a single pulse which, for the sake of simplicity, we still name RSW. When the incident pulse reaches the interface part of the chain with the beam, its energy is reflected into the RSW and part triggers the motion of the beam. Between 2 ms and 6 ms a series of small pulses is visible. They are created by the local oscillations of the last few particles adjacent to the beam. Another cluster of waves is visible beyond 6 ms. We indicate it as vibration-based solitary waves (VSWs) since they are generated by the vibration of the beam. Overall, the numerical and the experimental waveforms agree fairly well. The possible main sources of error are the absence of pre-compression and dissipation in the numerical model. Nonetheless, since the scope of the

study is to evaluate the effect of the thermal stress, we believe that these simplifications have minimal effects on the objective of the study. The qualitative comparison between the largest tension and largest compression shows less and smaller pulses in the 2 – 6 ms range and a delay of the arrival of the VSWs. The latter occurs because the beam's natural frequency decreases significantly.

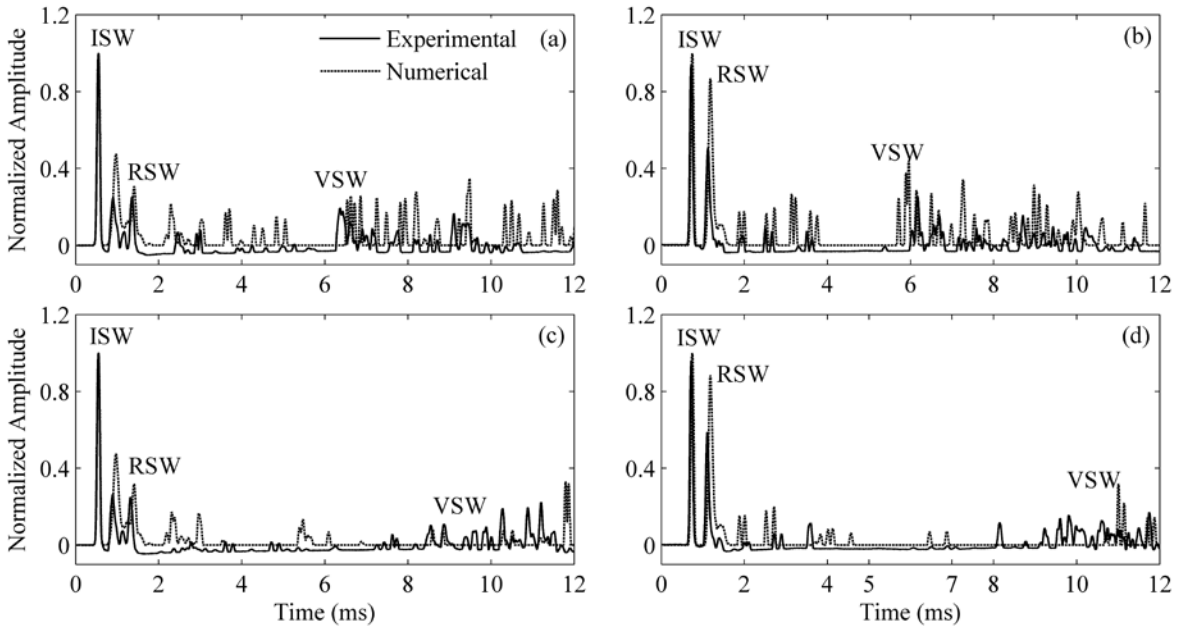

Figure 5.4. Single-chain configuration. Experimental and numerical normalized amplitudes. (a) Time waveform measured by S1 at the largest tensile stress equal to 41.39 MPa. (b) Time waveform measured by S2 at the largest tensile stress equal to 41.39 MPa. (c) Time waveform measured by S1 at the largest compressive stress equal to -38.7 MPa. (d) Time waveform measured by S2 at the largest compressive stress equal to -38.7 MPa.

In order to find the origin of the pulse tailing the incident wave, Fig. 5.5 displays a waterfall plot of the force profiles measured at the 19 particles' center after the striker. By observing the dashed line overlapped to the front edge of this pulse we determine that it is generated at the ninth grain, i.e. at the beginning of the elbow. As described in previous studies (Job et al. 2005; Yang et al. 2011) and summarized in Cai et al. (2013a), the formation of this

pulse is similar to the mechanism that allows the formation of secondary solitary waves. When a granule collides against a "soft" wall, its contact time tends to be longer, due to the low contact stiffness at the wall interface. This causes the separation of the particle from the rest of the chain. Eventually, the rebounding particle against the wall collides with the chain, causing the partial reflection of an incoming solitary wave. At the same time, the transmitted solitary wave experience the disintegration into a group of primary and secondary solitary waves due to the multiple collisions among the granules. A similar interaction between the particles and the elbow occurs here. The absolute values of the dashed lines have different slope suggesting that the forward pulse, named here curve-induced solitary wave (CISW1), is faster than the backward wave called CISW2.

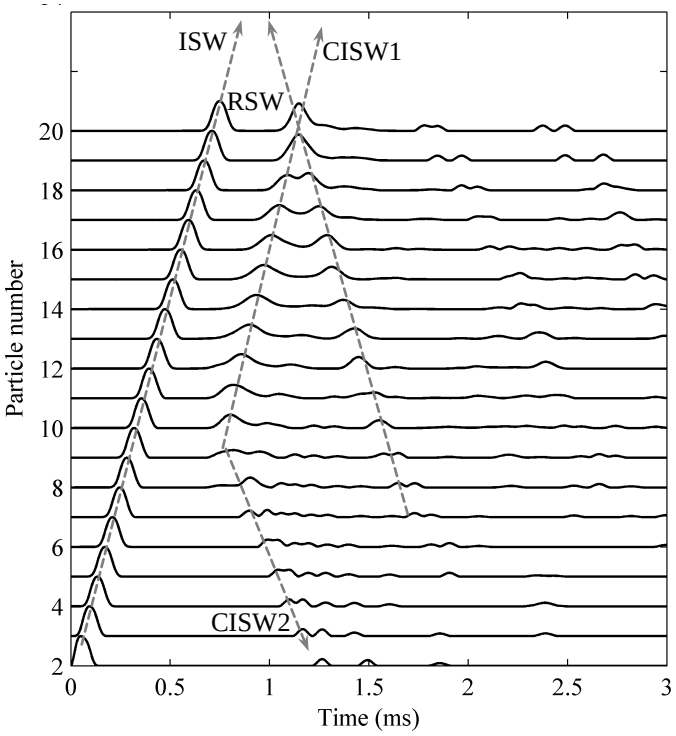

Figure 5.5. Waterfall chart of the numerical force profiles measured at the center of the first 20 particles of the single chain. The beam's axial stress is zero.

To assess the effect of the temperature on the solitary wave propagation, Fig. 5.6 displays a waterfall chart containing the average of the 15 signals taken at each temperature step and relative to two time intervals. The amplitude of the ISW should not be affected by the beam, however the chart exhibits some variability, which is likely associated with the velocity of the striker and the dissipation along the chain. This variability also affects the absolute value of the RSW's amplitude. Interestingly, the time of arrival of the RSW seems to decrease with the increase of the temperature. By observing Fig. 5.6(b) we clearly notice that the VSW is delayed by the increase of the compressive load.

The variations observed in Figs. 5.4 and 5.6 may not be perceived even by an experienced operator. Thus, in order to quantify the effect of the thermal stress on the propagation of the HNSWs, four features were extracted from the time series measured at S1 and S2. The features are summarized in Table 1. The first two are related to the amplitude of the pulses normalized with respect to the amplitude of the incident pulse. The normalization was chosen in order to minimize any error relative to the variability mentioned earlier. The remaining features are the time-of-flight (TOF) which is the transit time at a given sensor bead between the incident and the reflected or vibration-induced waves. The features associated with the VSW were computed by picking the maximum amplitude of the cluster and the cluster's front edge.

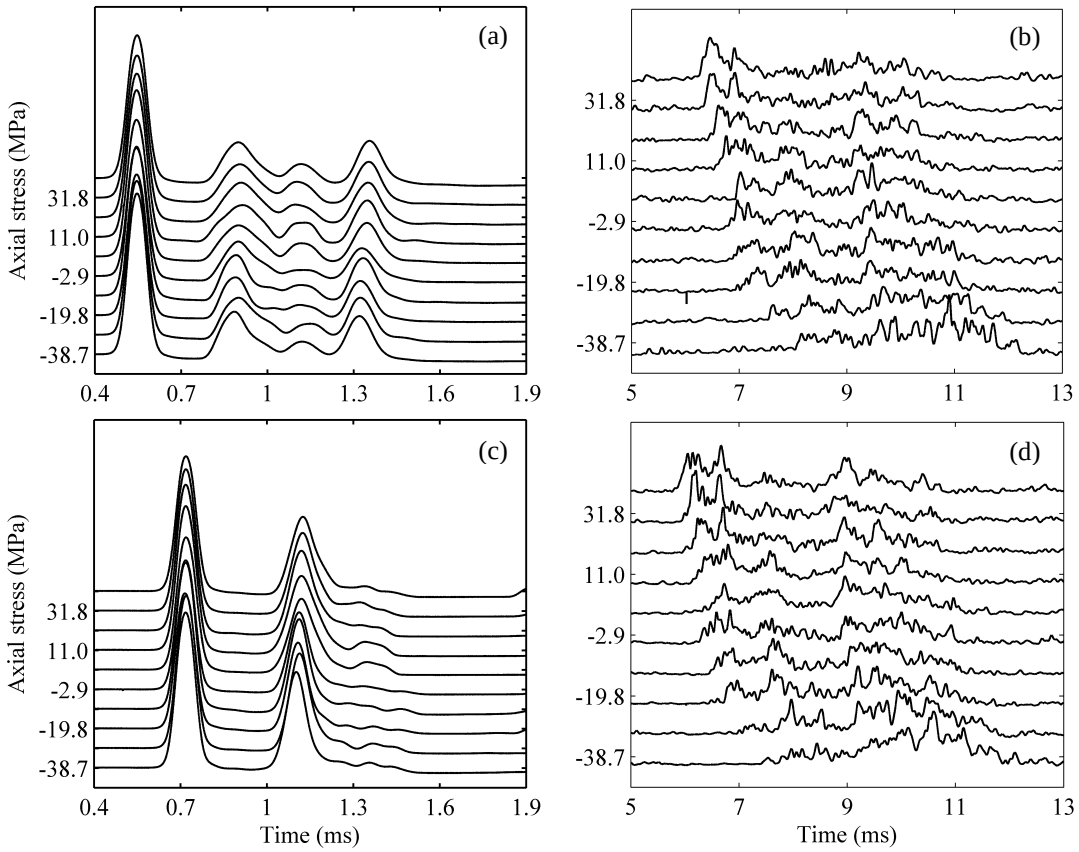

Figure 5.6. Single-chain configuration. Waterfall chart of the experimental solitary waves measured at (a, b) S1 and (c, d) S2 for the ten levels of stress considered in this study. The results refer to the first heating ramp and they are the average of the 15 measurements taken at each temperature. Panels (a) and (c) emphasize the arrival of the incident, elbow-generated, and reflected waves. Panels (b) and (d) emphasize the arrival of the vibration-induced waves.

Table 5.1. One chain configuration. Features extracted from the force profiles.

Feature	Description
RSW/ISW	The ratio of amplitude of the RSW to the ISW
VSW/ISW	The ratio of amplitude of the VSW to the ISW
TOF RSW	Time between the ISW and the RSW
TOF VSW	Time between the ISW and the VSW

Figure 5.7 shows the features measured at S1 as a function of stress. The experimental data are the average value of the 15 measurements and the corresponding 2σ confidence interval. The amplitude of the reflected wave does not present a monotonic trend and the variations are within the standard deviations. Similar conclusions can be drawn for the amplitude of the vibration-induced wave. Overall, the numerical and experimental results show the same trend but different quantitative results. The mismatch is likely due to the negative offset caused by PZT compression and to the effect of the dissipative phenomena already discussed. Also, it is known that the pre-compression in the granules affects the speed of the waves, resulting in a sooner arrival of the experimental reflections. The arrival of the train of waves associated with the vibration of the beam increases with the temperature in agreement with the fact that the period of vibration is directly proportional to the compression.

Similar to Fig. 5.7, Fig. 5.8 shows the selected features associated to the wave measured at S2. Here the ratio RSW/ISW presented in Fig. 5.8a is biased by the constructive interference of two pulses traveling along opposite directions. Overall, the features have the same trends shown in Fig. 5.7 except for the ratio VSW/ISW displayed in Fig. 5.8b. The reason is still under investigation; we believe that it may be related to the combination of many beam's vibrational modes, and/or the complexity of the oscillations of the particles adjacent to the beam. Figures 5.7 and 5.8 suggest that the time of arrival of the VSW is the most sensitive parameter to the beam's axial stress.

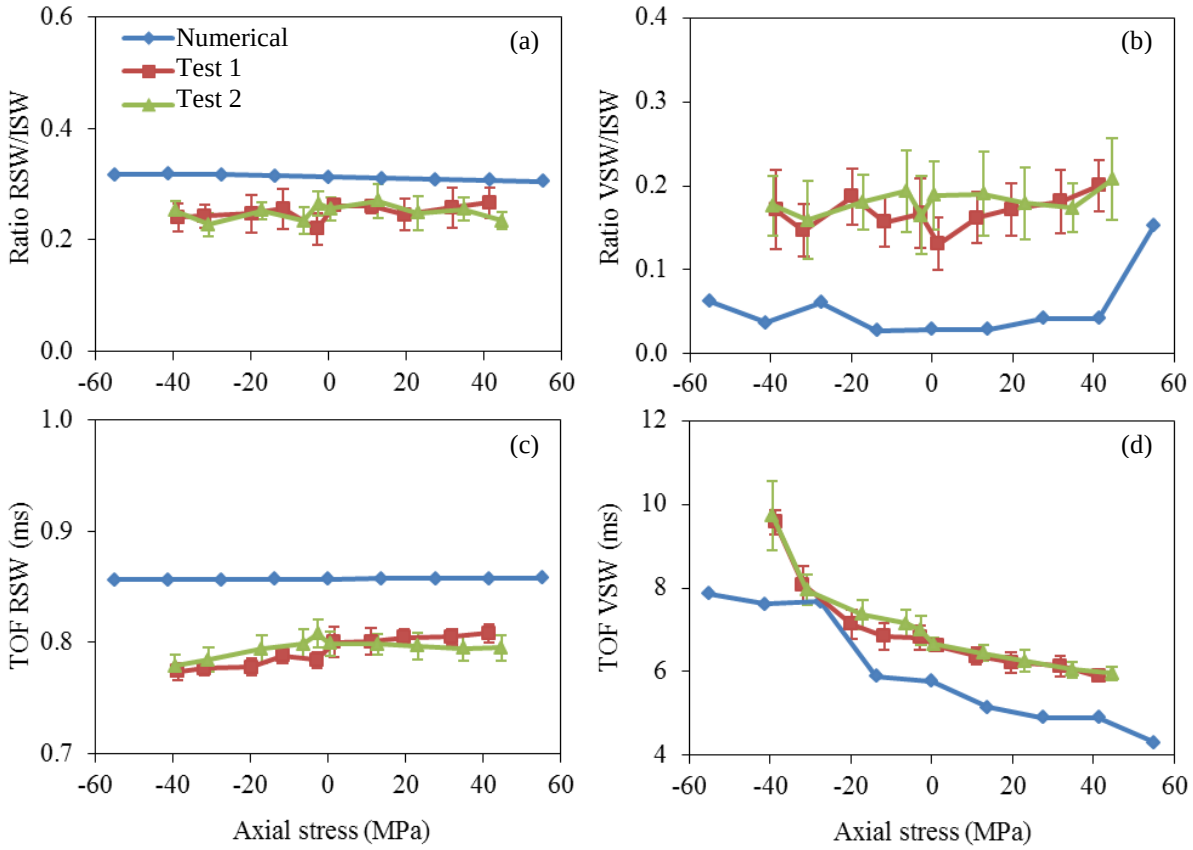

Figure 5.7. Single-chain configuration. Extraction of some selected features from the time waveforms measured at S1 as a function of the axial stress. (a) Ratio associated with the amplitude of the reflected and incident waves. (b) Ratio associated with the amplitude of the vibration-induced and incident waves. (c) Time of flight of the reflected wave. (d) Time of flight of the vibration-induced wave.

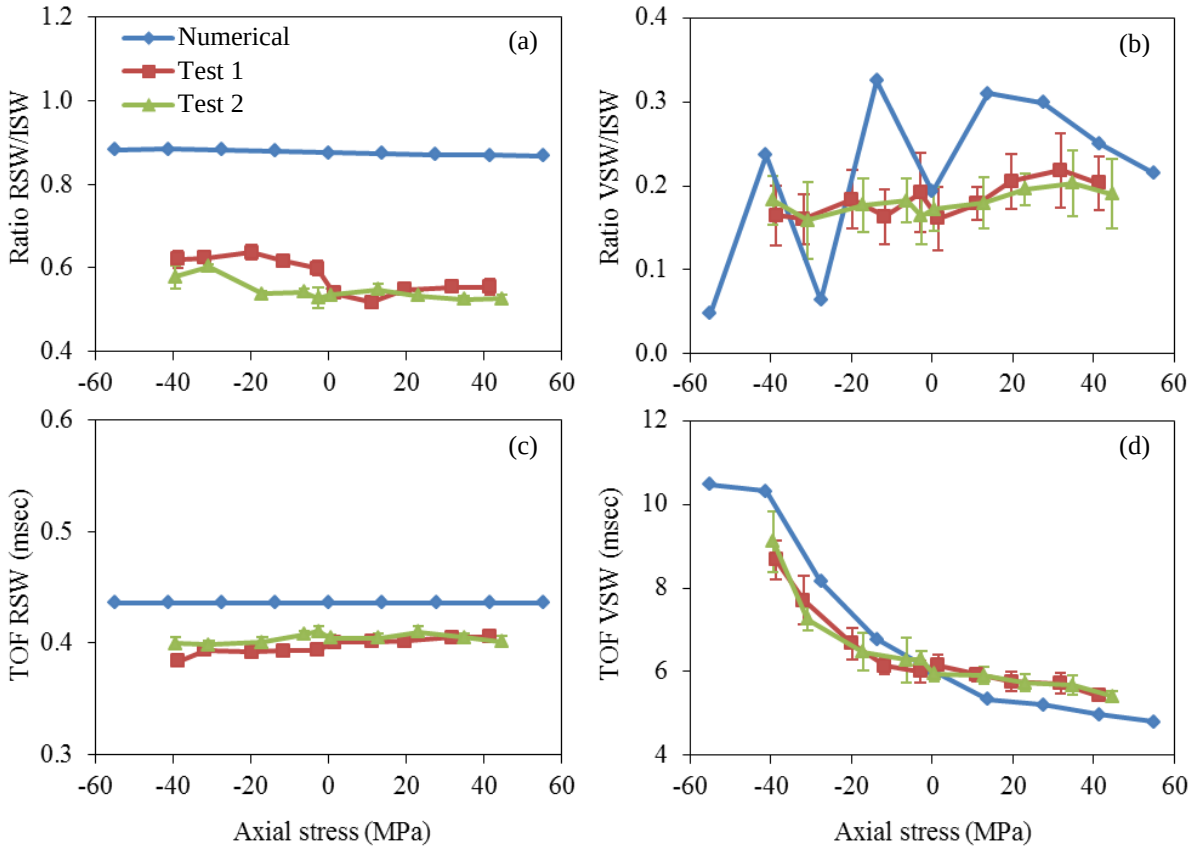

Figure 5.8. Single-chain configuration. Extraction of some selected features from the time waveforms measured at S2 as a function of the axial stress. (a) Ratio associated with the amplitude of the reflected and incident waves. (b) Ratio associated with the amplitude of the vibration-induced and incident waves. (c) Time of flight of the reflected wave. (d) Time of flight of the vibration-induced wave.

From the experimental and the numerical times of flight, we extrapolated the curve fit presented in Fig. 5.9. Ideally, the equations displayed in the figure can be used to determine the neutral temperature T_N of any beam having the same geometric and mechanical properties and probed with a single chain made of the same particles. In fact, in a blind test the temperature T_c can be measured with a thermocouple and the solitary wave parameters are measured. From the polynomials in Fig. 5.9, the actual stress σ_c acting on the beam can be retrieved and then Eq. 1.1 can be applied to estimate the unknown T_N.

For illustrative purpose, let use the polynomial displayed in Fig. 5.9(a). The fifteen measurements obtained at temperature 56 °C during the same test (Test 2) are considered and the arrival time of the vibration-induced wave cluster from sensor S1 is computed. The average value of this feature is computed and replaced in the polynomial which determines that the actual stress is equal to -15.05MPa. Using this value in Eq. 1.1, we determine that the beam's neutral temperature is T_N=47.64°C, which agrees well with the computed value of T_N=44.01 °C found in Fig. 5(a). If we apply the data of sensor S2 from the same test to the polynomial shown in Fig. 5.9(b), we find that the neutral temperature is T_N=50.11°C. By inspecting Figs. 5.9(a) and (b), we fund that when an experimental data as a point is close to the polynomial curve we can get a suitable value for the neutral temperature.

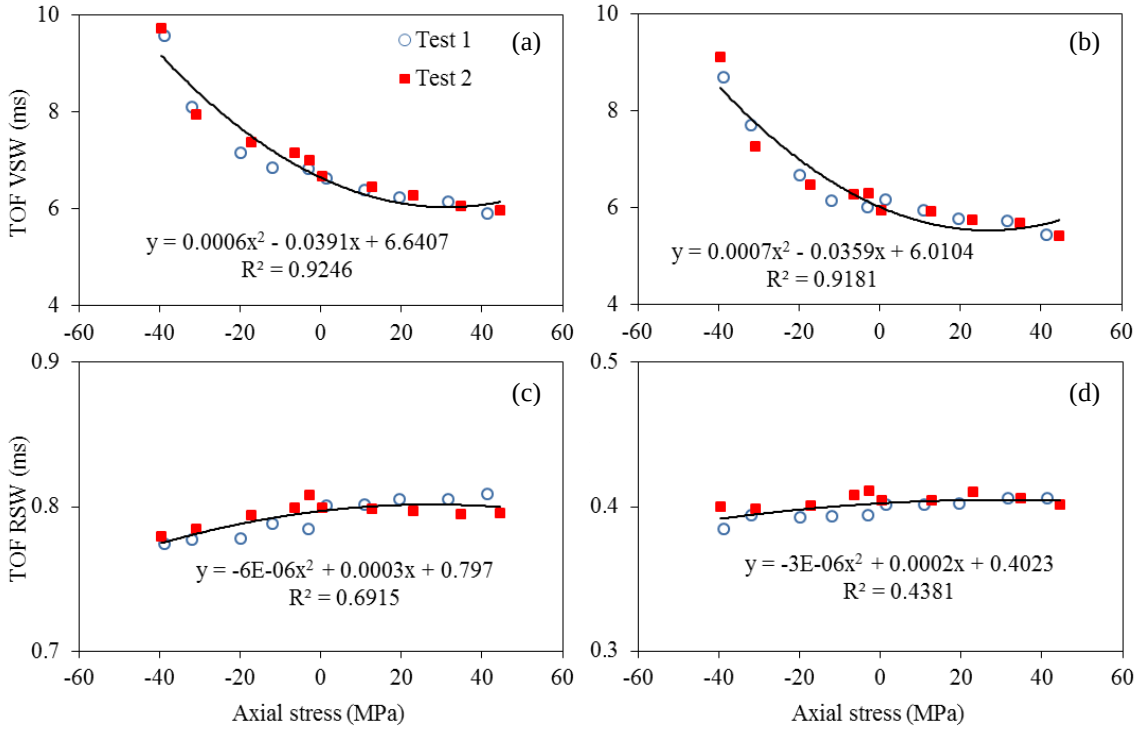

Figure 5.9. Single-chain configuration. Polynomial interpolation of the experimental data from both Test 1 and test 2. (a) Time of flight of the vibration-induced wave measured at sensor S1; (b) Time of flight of the vibration-induced wave measured at sensor S2; (c) Time of flight of the reflected wave measured at sensor S1; (d) time of flight of the reflected wave measured at sensor S2. Each equation refers to both tests.

We compare in Fig. 5.10 the numerical waveforms recorded at the sensor site S1 for one- and two-chains configurations. The solitary waves relative to the zero axial load are presented. The amplitude of the incident wave and its tail generated at the curved segment is identical, whereas there is a small difference in the amplitude of the RSW. The number of peaks and their arrival once the beam starts vibrating is significant. The amplitude of these pulses is larger in the single chain case as the beam is free to vibrate and the energy is not dissipated into the waves propagating in the second chain.

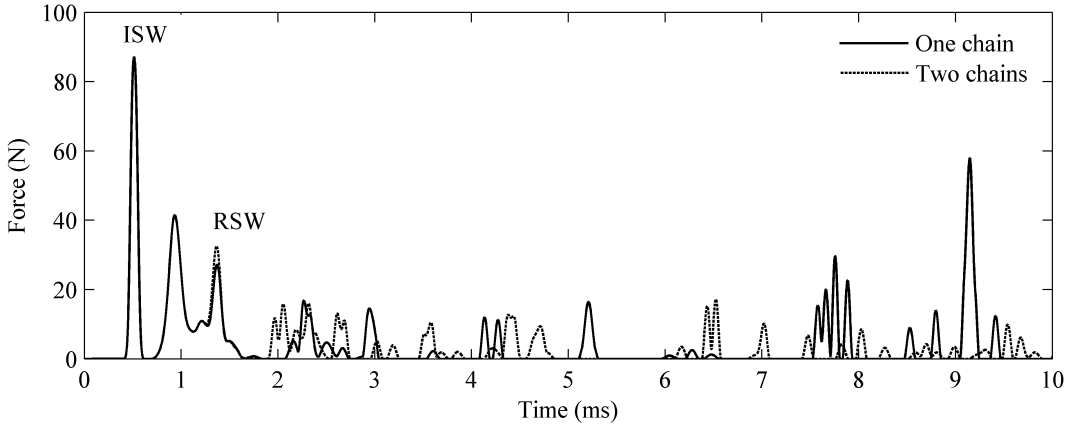

Figure 5.10. Numerical profiles measured at sensing site S1 when one and two chains were used. The beam is at zero axial stress.

The panels on the left of Fig. 5.11 show the experimental and the numerical time waveforms measured by the four sensor beads when the beam was subjected to the largest tension. Similarly, the panels on the right present the results relative to the largest compression. The bottom half panels show that a train of pulses is transmitted through the thickness. The first pulse in this train is the TSW. Overall we observe a fair agreement between the numerical and the experimental time series. The experimental normalized amplitudes are smaller due to the absence of dissipation in the numerical model. In this configuration we do not observe a

significant delay in the arrival of the reflected pulses since the vibration of the beam is restrained by the presence of the second chain.

The features listed in Table 2 were extracted from the time domain. Here we considered also the energy *En* associated with the train of waves observed in the first and in the second chain. It was computed as:

$$En = \sum_{t} S(t)^2 \Delta t \tag{5.1}$$

where *S(t)* represents the time series, and Δt is the sampling period.

Table 5.2. Two chains configuration. Features extracted from the force profiles.

Feature	Description
RSW/ISW	The ratio of amplitude of the RSW to the ISW
TSW/ISW	The ratio of amplitude of the TSW to the ISW
TOF RSW	Time between the ISW and the RSW
TOF TSW	Time between the ISW and the TSW
En	The energy of waves after the RSW or the TSW

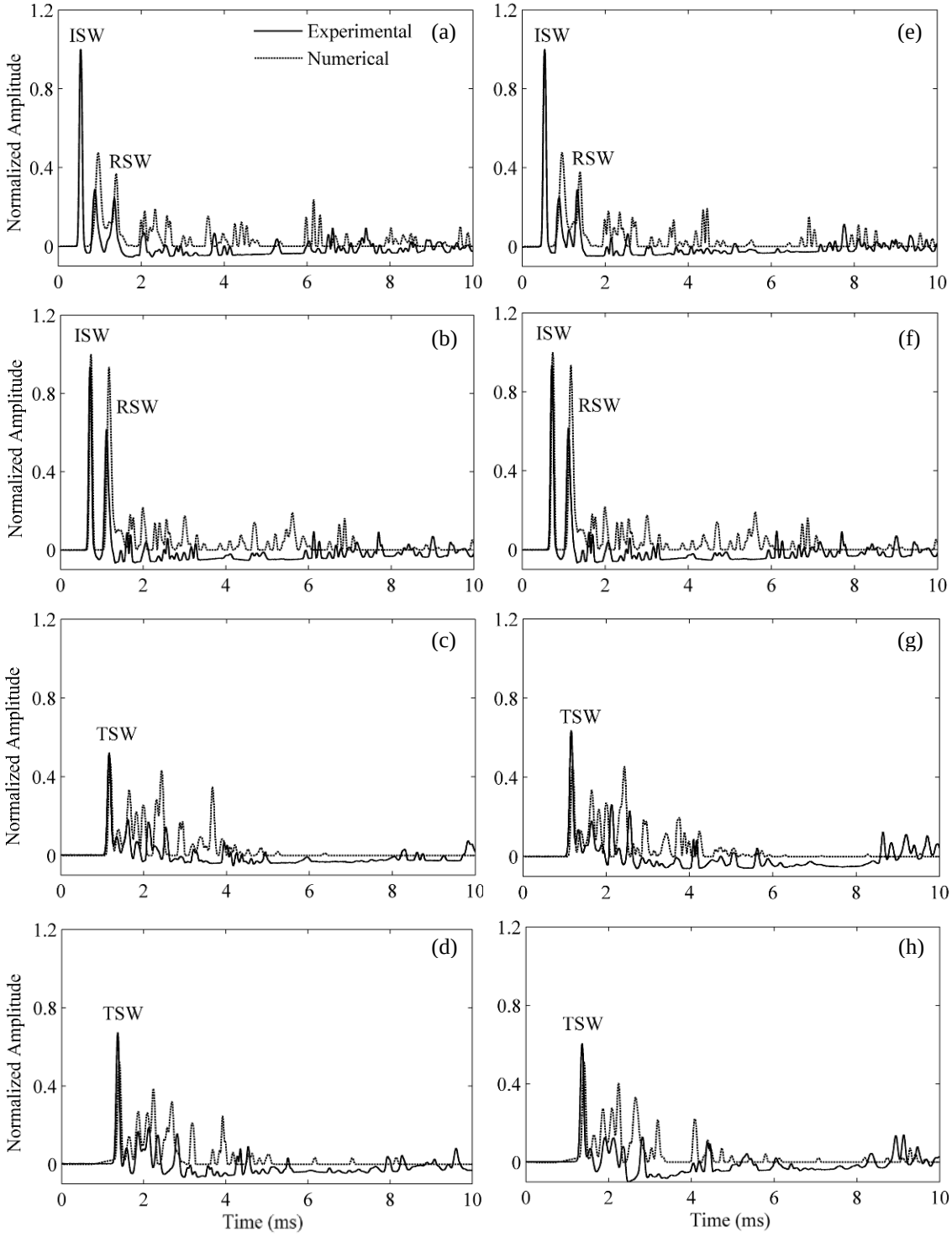

Figure 5.11. Two chains configuration. Experimental and numerical normalized amplitudes. Left panels: beam under largest tension at 43.4 MPa, (a) sensor S1, (b) sensor S2, (c) sensor S3, and (d) sensor S4. Right panels: beam under largest compression at -36.3 MPa, (e) sensor S1, (f) sensor S2, (g) sensor S3, and (h) sensor S4.

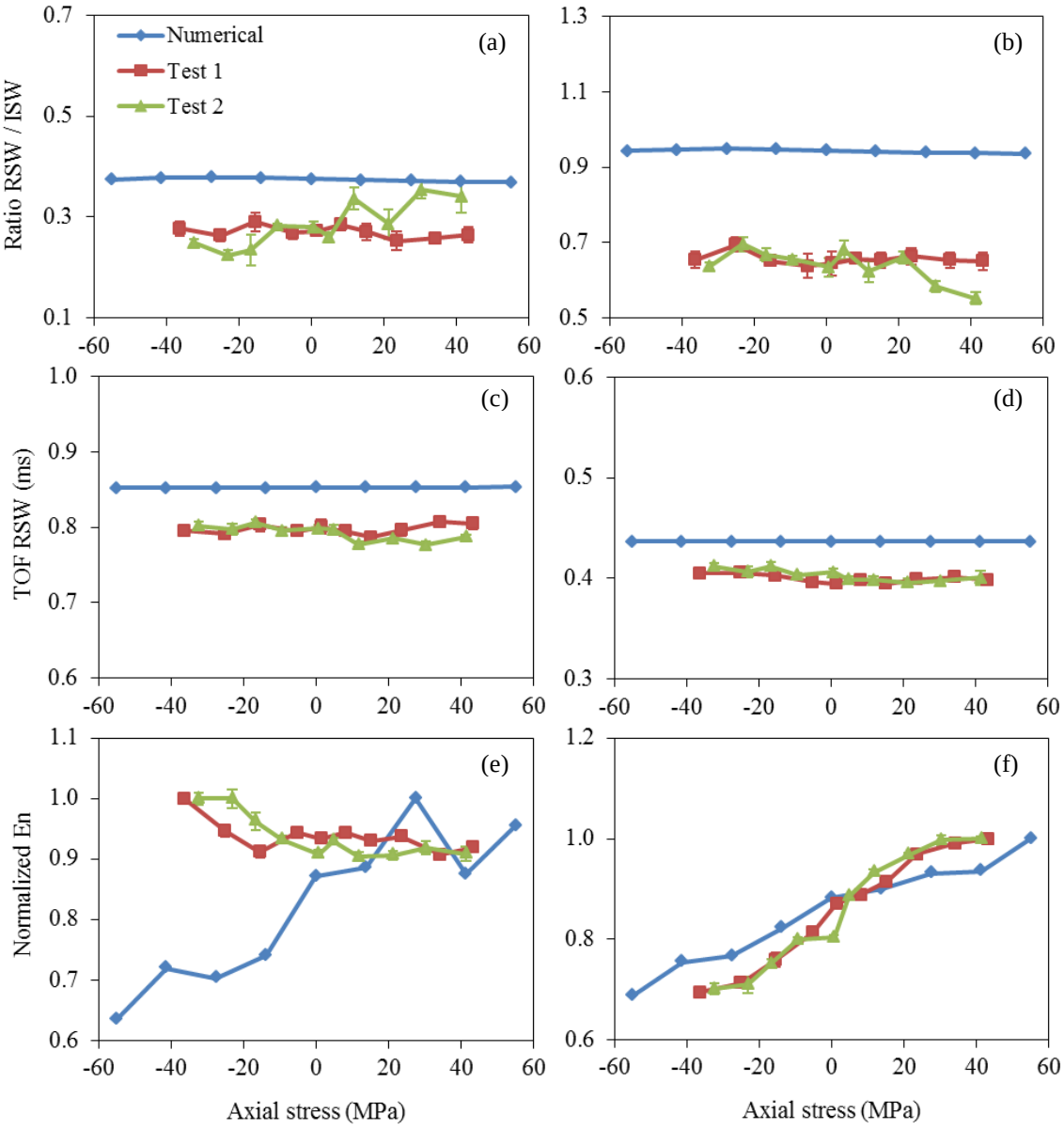

Figure 5.12. Two chains configuration. Extraction of some selected features from the time waveforms measured at S1 (left panels) and at S2 (right panels) as a function of the axial stress. (a, b) Ratio associated with the amplitude of the reflected and incident waves. (c, d) Time of flight of the reflected wave. (e, f) Energy of the solitary waves arriving after the reflected wave.

Figure 5.12 shows the features associated with the reflected wave as a function of the axial stress as measured by S1 and S2. The trends relative to the amplitudes are similar to those discussed in Fig. 5.8. As said earlier the ratio measured at S2 is biased by the superposition of

the CISW1 and the backscattered pulse. The overestimation of the numerical RSW/ISW at both sensors is caused by the absence of dissipation in the numerical model and by the vertical shift of the experimental values due to the static compression on the PZT caused by the weight of the vertical segment.

The time of arrival of the reflected wave is almost constant and little information can be retrieved in terms of stress sensitivity. Finally, the numerical trends of the En show a significant change with respect to stress. This trend is matched by the experimental data in S2 (Fig. 5.12(f)) but it is not confirmed in S1 (Fig. 5.12(e)). We think that the proximity with the elbow may affect the readings from S1. Overall, the energy is inversely proportional to the temperature raise. As the frequency of vibration of the beam increases, the speed at which it bounces back to the granules increases, determining higher pulses in the first chain. Because the current position of the sensor S2 is influenced by the arrival of the CISW1 but it favors the measurement of the energy of the cluster beyond 1.5 ms, future development should consider L-shaped chains with a longer horizontal segment.

Similar to Fig. 5.12, Fig. 5.13 shows the selected features computed from the time waveforms measured at S3 and S4. Overall there is a good agreement between numerical and experimental data in terms of the energy and the time of flight. However, we also notice the low repeatability of the signal amplitude. We believe that an accidental misalignment of the sensor particles altered the sensitivity of the particles to the propagation of the wave.

The speed V of the solitary waves was also considered as:

$$V = \frac{D_{S2-S1}}{t_{S2} - t_{S1}} \tag{5.2}$$

where $D_{S2\text{-}S1}$ is the distance between sensors S1 and S2 equal to five particle diameters, and t_{S1} and t_{S2} are the arrival time of the amplitude peaks.

Figure 5.14(a) shows the velocity of the incident and the reflected waves as a function of the axial stress relative to single chain configuration. The experimental results which represent the average of the 15 measurements demonstrate once more the repeatability of the test as the results from Test 1 and Test 2 overlap. The numerical value of the ISW velocity is lower than the experimental speed. This is because the model did not include pre-compression, which affects the speed of the HNSWs. For the experimental results, we considered the average velocity of the solitary waves from the 15 measurements. As expected, the speed of the incident wave does not change with stress. The speed of the reflected wave is slower since it is proportional to its amplitude. Moreover, the speed slightly changes with respect to the axial stress.

Similarly, Fig. 5.14(b) shows the speed relative to the incident, reflected, and transmitted waves for the two-chain configurations. There is a very good agreement between the experimental and the numerical results. The speed of the transmitted wave is slightly higher than the RSW, consistent with the corresponding amplitudes.

Finally, Figure 5.15 shows the relative speed variation with respect to the maximum tensile stress considered at the beginning of the loading ramp. The response is not the same for both Tests 1 and 2, however the variation of the speed is remarkably much higher than any relative speed variation visible in acoustoelastic-based method.

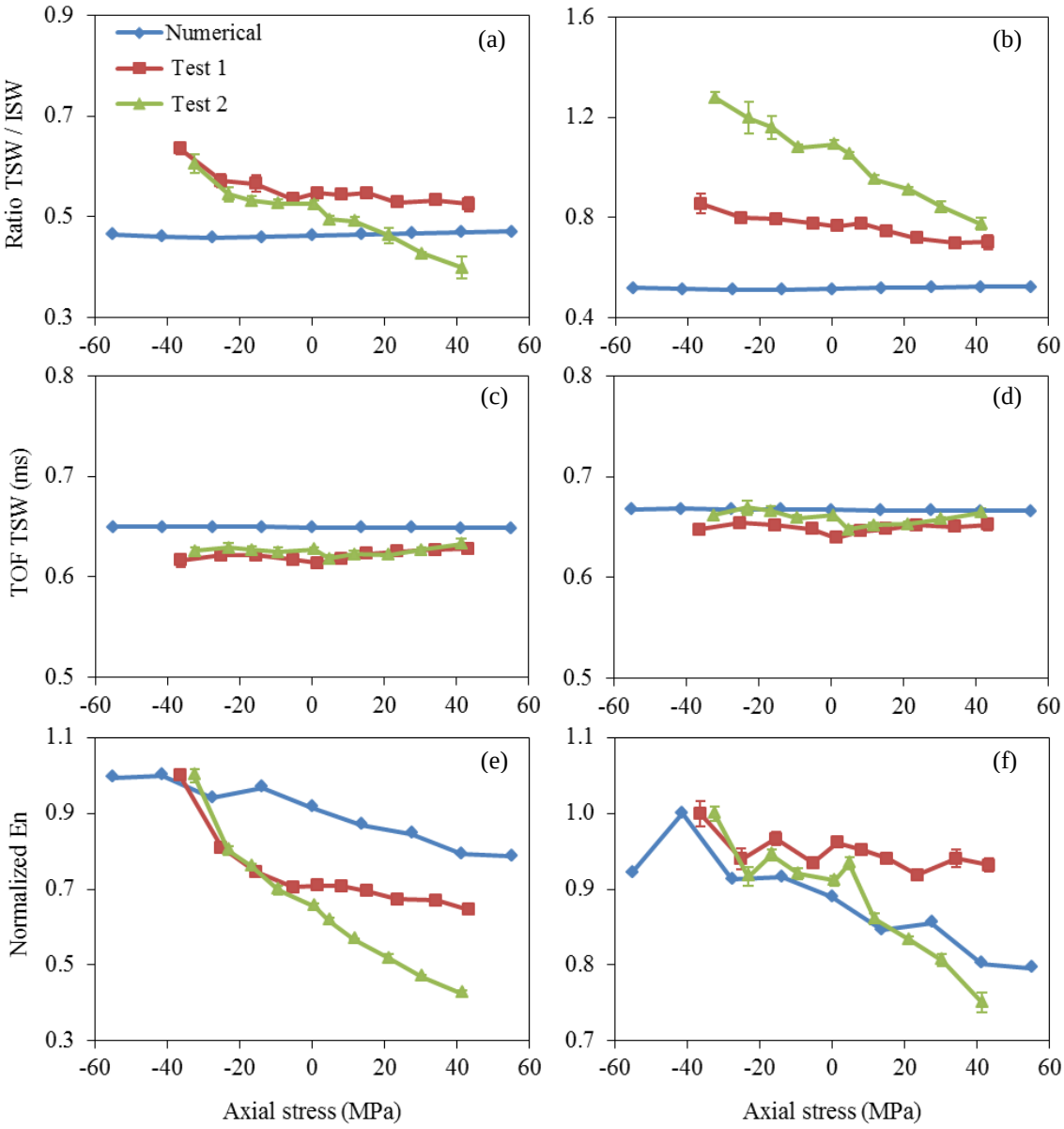

Figure 5.13. Two chains configuration. Extraction of some selected features from the time waveforms measured at S3 (left panels) and at S4 (right panels) as a function of the axial stress. (a, b) Ratio associated with the amplitude of the transmitted and incident waves. (c, d) Time of flight of the transmitted wave. (e, f) Energy of the solitary waves tailing the transmitted wave.

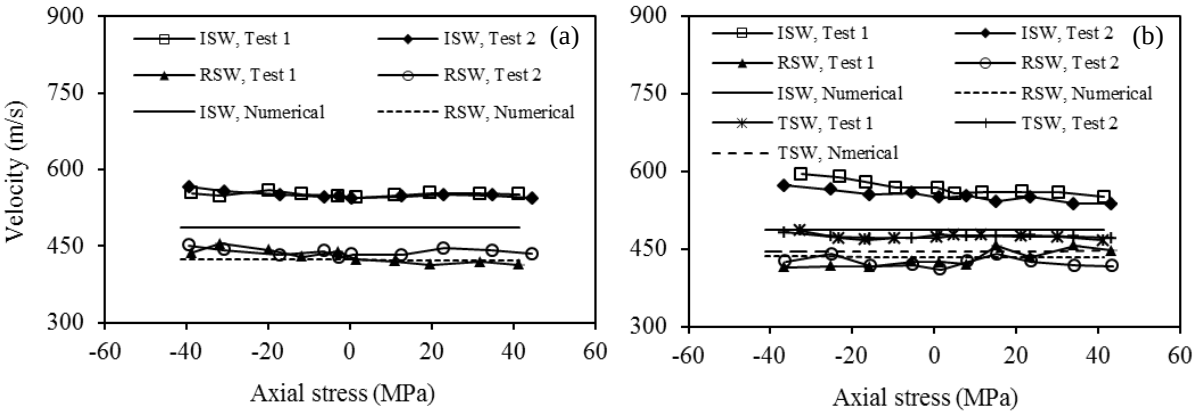

Figure 5.14. Experimental and numerical velocity of the solitary waves as a function of the beam's axial stress. (a) single-chain configuration, and (b) two-chains configuration.

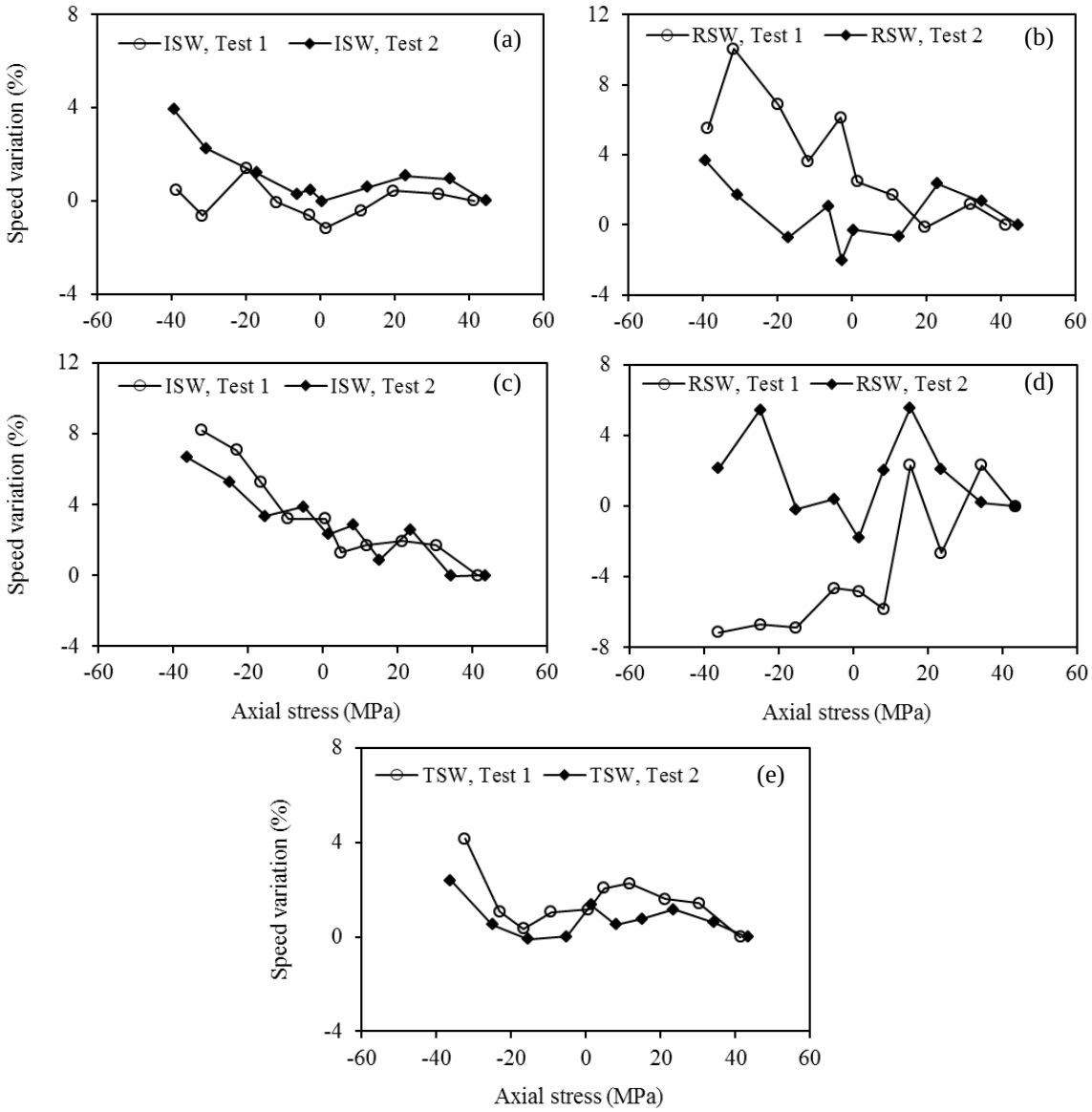

Figure 5.15. Speed variation of the experimental solitary waves as a function of the beam's axial stress. (a, b) single-chain configuration; and (c, d, e) two-chains configuration.

5.1.3 Discussion

The two chains arrangement may resemble a single chain that contains a single impurity. As summarized by Szelengowicz et al. (2012) the elementary interaction of light or heavy intruders with shock waves has been investigated numerically by Hascoët and Herrmann (2000) which

showed that a light defect acts as a secondary source of solitary waves, whereas a heavier defect is simply translated, creating a train of solitary waves forward and a stable reflected wave. In our application since the beam's density is similar to the density of the grains but its thickness is half the particles' diameter we may argue that the beam resemble the case of a light impurity. As such we may argue that when reached by the incident wave, the beam starts oscillating between its neighbor beads. Those oscillations are damped as the beam becomes a secondary source of solitary waves, and one can observe trains of solitary waves of decreasing amplitudes in both directions as the beam collides with its nearest neighbors (Szelengowicz et al. 2012; Tichler et al. 2013). However, the beam may instead be considered a heavy impurity as its total weight was 1.3 kg. In this case the incident wave will simply shift it in its moving direction and a stable reflected wave will propagate backward, while the forward propagating solitary wave will be decomposed in a train of pulses (Szelengowicz et al. 2012). Recently, Li et al. (2013) studied the solitary wave interaction with an impurity heavier than the bead composing the chain. They pointed out that during the collision process, the heavy particle gains momentum in the forward direction, which results in the partial transmission of solitary waves. Due to its high inertia, the impurity develops multiple collisions with the next neighboring bead causing the fragmentation of a single solitary wave into a train of solitary waves with an exponentially decaying shape.

In our study, both the numerical and the experimental time waveforms show the presence of train of pulses propagating backward and forward. As such a conclusive remark about the analogy between our system and a single chain with an impurity cannot be made.

5.2 STRAIGHT CHAINS

The results of similar investigation conducted using one and two straight chains are reported in this section.

5.2.1 Setup

We used a setup similar to that shown in Fig. 5.1. The schematics and a photo of the setup is presented in Fig. 5.16. The same 19.05 mm × 9.525 mm (type 304, McMaster-CARR) steel beam was clamped with a free length of 914 mm to the same MTS machine.

A chain of 14 beads was assembled inside a house-made horizontal channel made of structural fiber glass square tube, having size 25.4 mm × 25.4 mm, and thickness 3.175 mm (see Fig. 5.16(c)). The chain of particles contained in the horizontal channel was supported by a house-built steel frame and was placed in contact with the beam in its mid-point. The same stainless steel bearing-quality balls were used.

An electromagnet located above the first grain was used to drive the striker from a falling height of about 6.5 mm, resulting in the striker velocity of 0.3018 m/s. The electromagnet was driven by a National Instruments-PXI running in LabVIEW. A LabVIEW front panel was designed to operate the actuator automatically.

Two sensor particles, S1 and S2 were assembled and used to measure the propagation of the HNSWs generated by the mechanical impact of the striker. The sensor particles were the same used in the experiments illustrated previously. The piezoceramic disks were positioned at

the middle of the 5-th and 10-th particle as shown in Fig. 5.17. The signals were digitized at 2 MHz sampling rate.

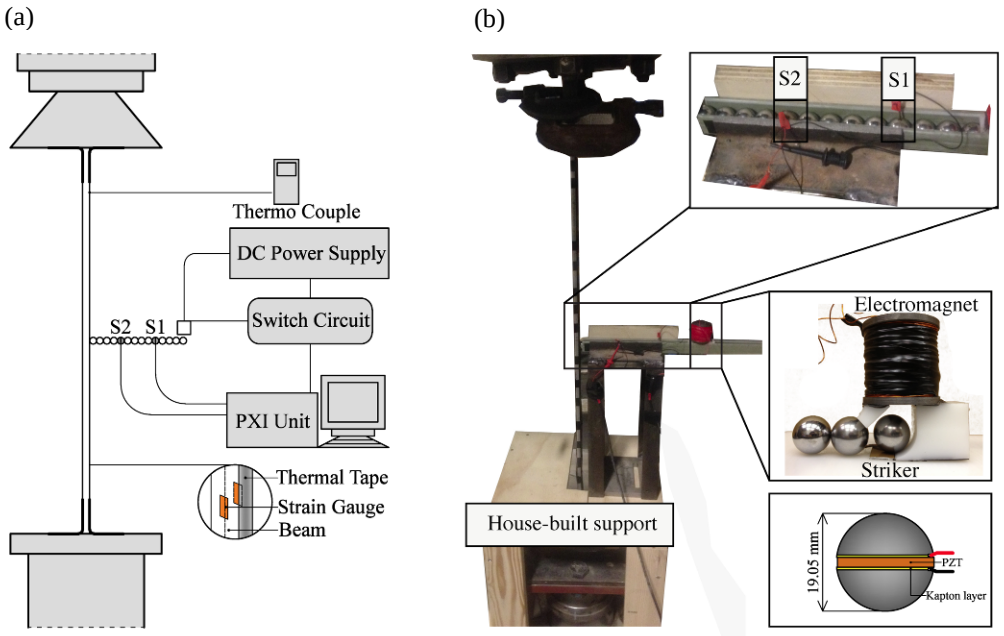

Figure 5.16. Single-chain configuration. (a) Scheme and (b) photo of the experimental setup. The beam is clamped at its ends and a straight chain made of 14 particles is in contact with the beam at the beam's mid-span. Two sensor particles S1 and S2 were assembled and used to measure the propagation of the waves. Each sensor bead contained a piezoelectric ceramic disc with silver electrodes and microminiature wiring (Yang et al. 2011).

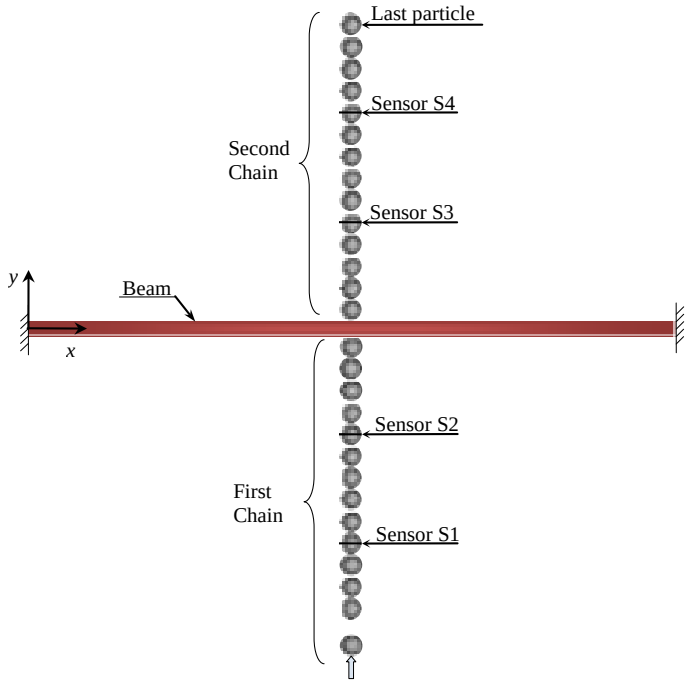

Figure 5.17. Top view of the numerical simulation setup. The beam is clamped at two ends. One or two chains of particles are in contact with the beam at its mid-span. Each chain consists of N=14 particles. (Drawing is not to scale.)

The testing protocol was as follow. The beam was initially loaded in tension up to 20% of its yield load. Then the MTS machine, operated in displacement control, held the beam and heat was applied. We measured the HNSWs during the heating phase at step of 5 °C until the beam reached the 60% of its Euler load. In order to assess the repeatability of the setup, we took 15 measurements at each step. The test was repeated, i.e. two heating processes, hereafter indicated as Test 1 and Test 2, were completed.

The same setup and test protocol were adopted when a second identical chain was added according to the scheme presented in Fig. 5.18. The sensors in this second chain, namely S3 and S4 recorded the solitary waves transmitted through the beam's thickness. The objective of this

portion of the study was to determine whether this configuration enhances the sensitivity of the noninvasive methodology proposed here.

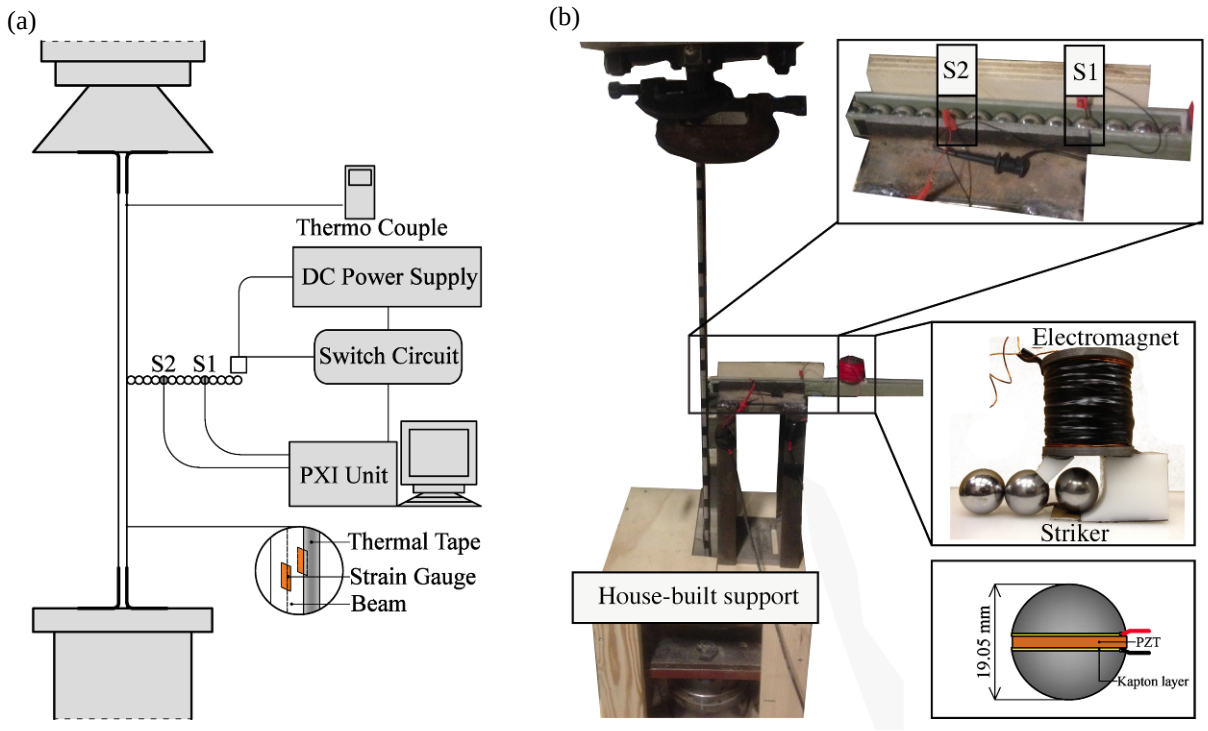

Figure 5.18. Two-chain configuration. (a) Scheme and (b) photo of the experimental setup. The beam is clamped at its ends and two straight chains made of 14 particles each are in contact with the beam at the beam's mid-span. Four sensor particles were assembled to measure the propagation of the waves. Sensors S1 and S2 are embedded in the first chain where the solitary waves are generated. Sensors S3 and S4 are embedded in the second chain.

5.2.2 Results

Figure 5.19(a) shows the axial stress as a function of the temperature raise ΔT for both heating ramps when a single straight chain was used. The data show the very good repeatability of the testing protocol. As noted in the L-shaped experiments, there is a slight change of the slopes of the experimental data. This may be attributed to some settling of the machine's grips. By

interpolating the experimental data, a linear relationship between the stress and the temperature is found. By solving the linear fit for the zero stress we find that the neutral temperature occurred at ΔT=22.61 °C, and by using room temperature 21 °C which was used during the experiment we can find that the neutral temperature is equal to 43.61 °C

Similarly, the stress as a function of the beam's temperature when two chains were used is presented in Fig. 5.19(b). The graph is similar to Fig. 4(a) and it confirms the repeatability of the setup. For this second round of experiments, the neutral temperature occurred at ΔT=21.46 °C.

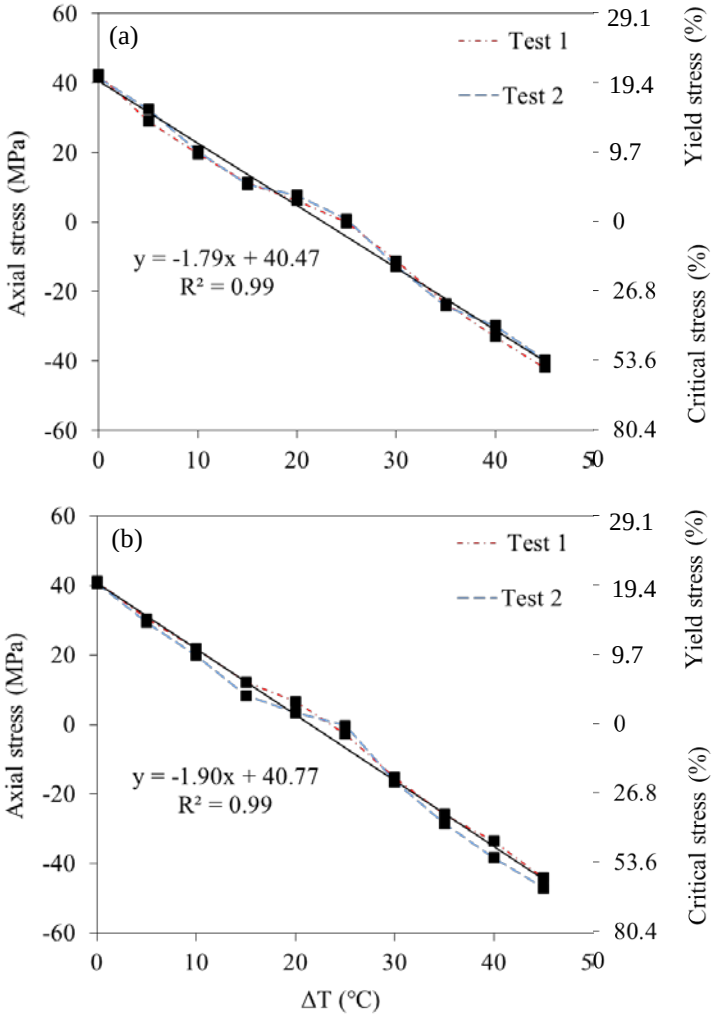

Figure 5.19. Axial stress as a function of the beam's temperature measured with a thermocouple. (a) Single-chain configuration, and (b) two-chains configuration. The continuous line is the linear interpolation of both heating loads.

Figures 5.20(a) and (b) show the experimental and the numerical solitary waves measured during test 1 under the largest tension at 41.4 MPa by sensors S1 and S2, respectively. Similarly, Figs. 5(c) and (d) show the results relative to the largest compression at -39.7 MPa. The numerical results are overlapped to the first of the corresponding 15 measurements. To ease the comparison between numerical and experimental data, the abscissas were shifted horizontally in order to overlap the arrival of the first pulse. This was necessary since the numerical t=0 corresponded to the motion onset of the first particle, whereas the experimental trigger was set to

the arrival of the first pulse at the sensor bead S1. Moreover, the amplitudes were normalized with respect to the amplitude of the corresponding first peak. This was necessary as the numerical pulse refers to force whereas the experimental values refer to voltage.

In Fig. 5.20(a), the first pulse is the incident solitary wave (ISW) generated by the striker. The second pulse is the reflected solitary wave (RSW) which is the wave backscattered from the beam-chain interface. These two waves occur also under large compression as shown in Fig. 5.20(c). In Fig. 5.20(b), the ISW and the RSW are also present. Between 2 ms and 5 ms a series of small pulses is visible, and they are created by the local oscillations of the particles adjacent to the beam and likely by side collisions of the granules with the inner wall of the guide. When the incident pulse reaches the interface, part of its energy is reflected into the RSW and part triggers the motion of the beam. As a result, a cluster of vibration-based solitary waves is visible beyond 6 ms. Overall, the numerical and the experimental waveforms agree fairly well. The possible main sources of error are the absence of dissipation in the numerical model. The qualitative comparison between the largest tension and largest compression shows less and smaller pulses in the 2–5 ms range and a delay of the arrival of the VSWs. The latter occurs because the beam's natural frequency decreases significantly. Numerical profiles show a very good agreement in tension while, when the beam is compressed, the arrival of the VSW at the sensor site occurs later with respect to the experimental profiles.

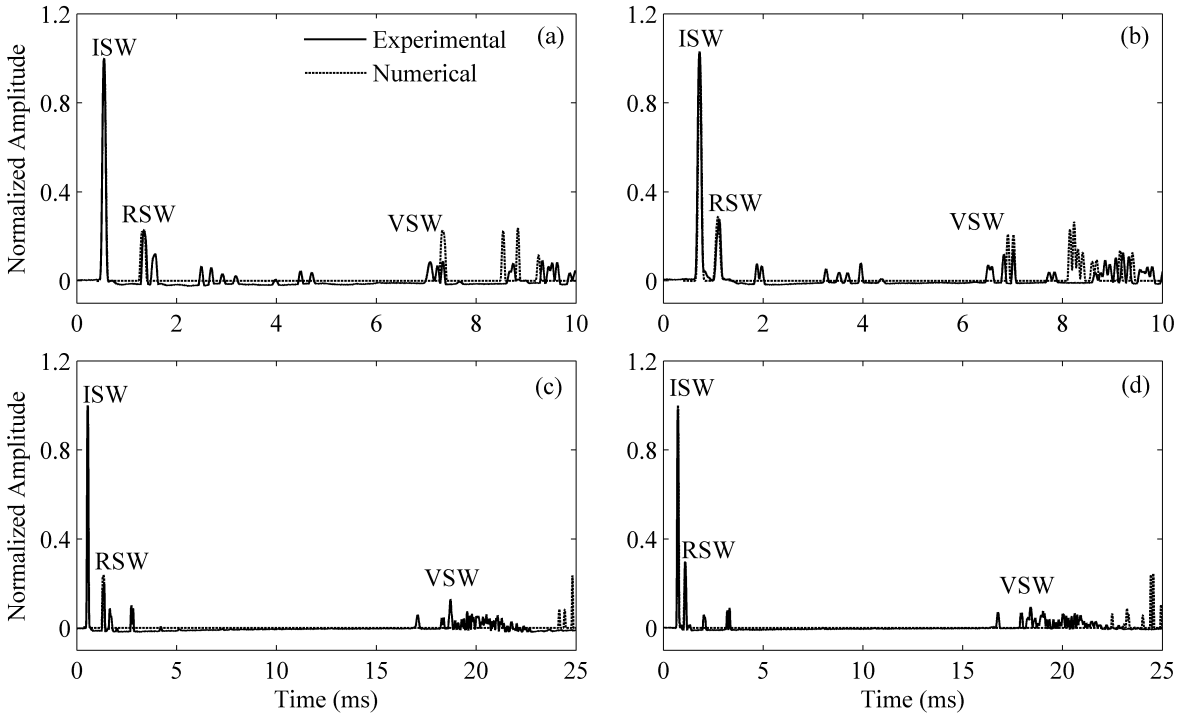

Figure 5.20. Single-chain configuration. Experimental and numerical normalized amplitudes. (a) Time waveform measured by S1 at the largest tensile stress equal to 41.43 MPa. (b) Time waveform measured by S2 at the largest tensile stress equal to 41.43 MPa. (c) Time waveform measured by S1 at the largest compressive stress equal to -39.7 MPa. (d) Time waveform measured by S2 at the largest compressive stress equal to -39.7 MPa.

To assess the effect of the temperature on the solitary wave propagation, Fig. 5.21 displays a waterfall chart containing the average of the 15 signals taken at each temperature step and relative to two time intervals. The amplitude of the ISW should not be affected by the beam, however the chart exhibits some variability, which is likely associated with the velocity of the striker and the dissipation along the chain. This variability also affects the absolute value of the RSW's amplitude. Interestingly, the time of arrival of the RSW seems to decrease with the increase of the temperature. By observing Figs. 5.21(b) and (d), we clearly notice that the VSW is delayed by the increase of the compressive load.

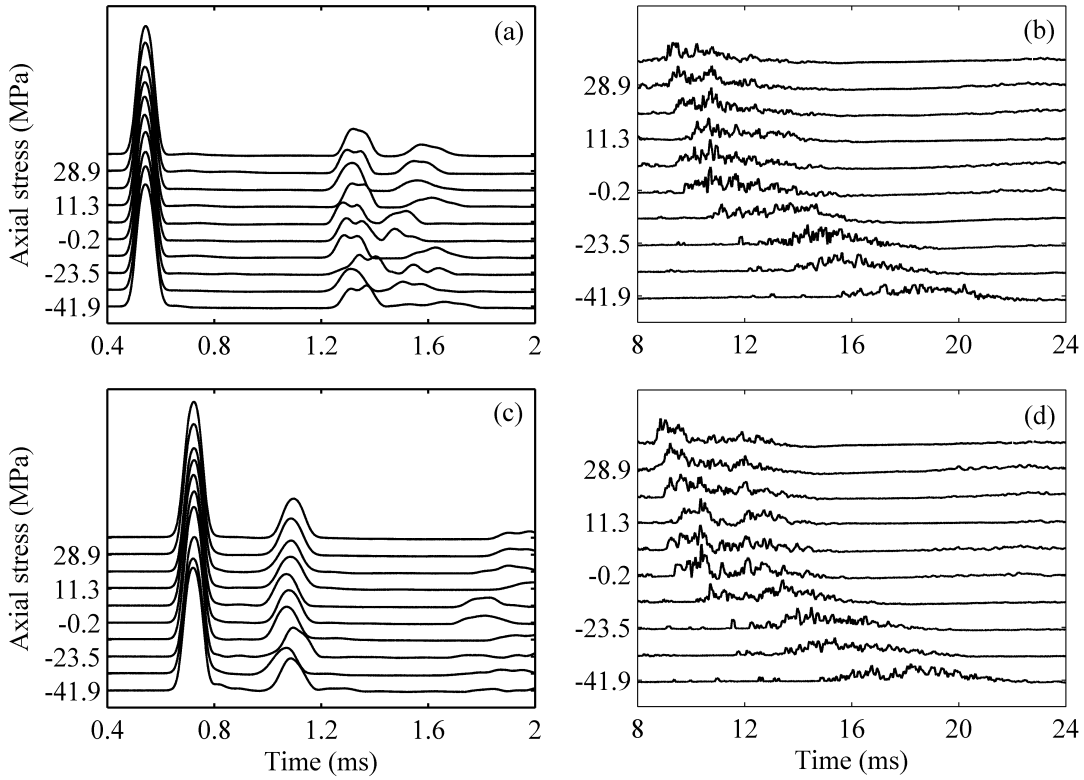

Figure 5.21. Single-chain configuration. Waterfall chart of the experimental solitary waves measured at (a, b) S1 and (c, d) S2 for the ten levels of stress considered in this study. The results refer to the first heating ramp and they are the average of the 15 measurements taken at each temperature. Panels (a) and (c) emphasize the arrival of the incident, and reflected waves. Panels (b) and (d) emphasize the arrival of the vibration-induced waves.

To quantify the effect of the thermal stress on the propagation of the HNSWs, five features were extracted from the time series measured at S1 and S2. The features are summarized in Table 5.3 and their meaning was described in the previous two tables.

Table 5.3. Features selected in this study for one straight chain configuration.

Feature	Description
RSW/ISW	The ratio of amplitude of the RSW to the ISW
VSW/ISW	The ratio of amplitude of the VSW to the ISW
TOF RSW	Time between the ISW and the RSW
TOF VSW	Time between the ISW and the VSW
En	The energy of waves in the time range 1.25-25 ms

Figure 5.22 shows the features measured at S1 as a function of stress. The experimental data are the average value of the 15 measurements and the corresponding 2σ confidence interval. The amplitude of the reflected wave does not present a monotonic trend and the variations are within the standard deviations. Similar conclusions can be drawn for the amplitude of the vibration-induced wave. Overall, the numerical and experimental results show the same trend but different quantitative results. The mismatch is likely due to the negative offset caused by PZT compression and to the effect of the dissipative phenomena already discussed. Also, other discrepancy is visible in the numerical trend VSW/ISW. The reason may be related to the combination of many modes that change with the variation of the axial stress. The arrival of the train of waves associated with the vibration of the beam increases with the temperature in agreement with the fact that the period of vibration is directly proportional to the compression. The feature En increases with increasing the beam's axial stress, and the reason is due to applying a force with high amplitude to the chain by the vibrated beam with a high axial load.

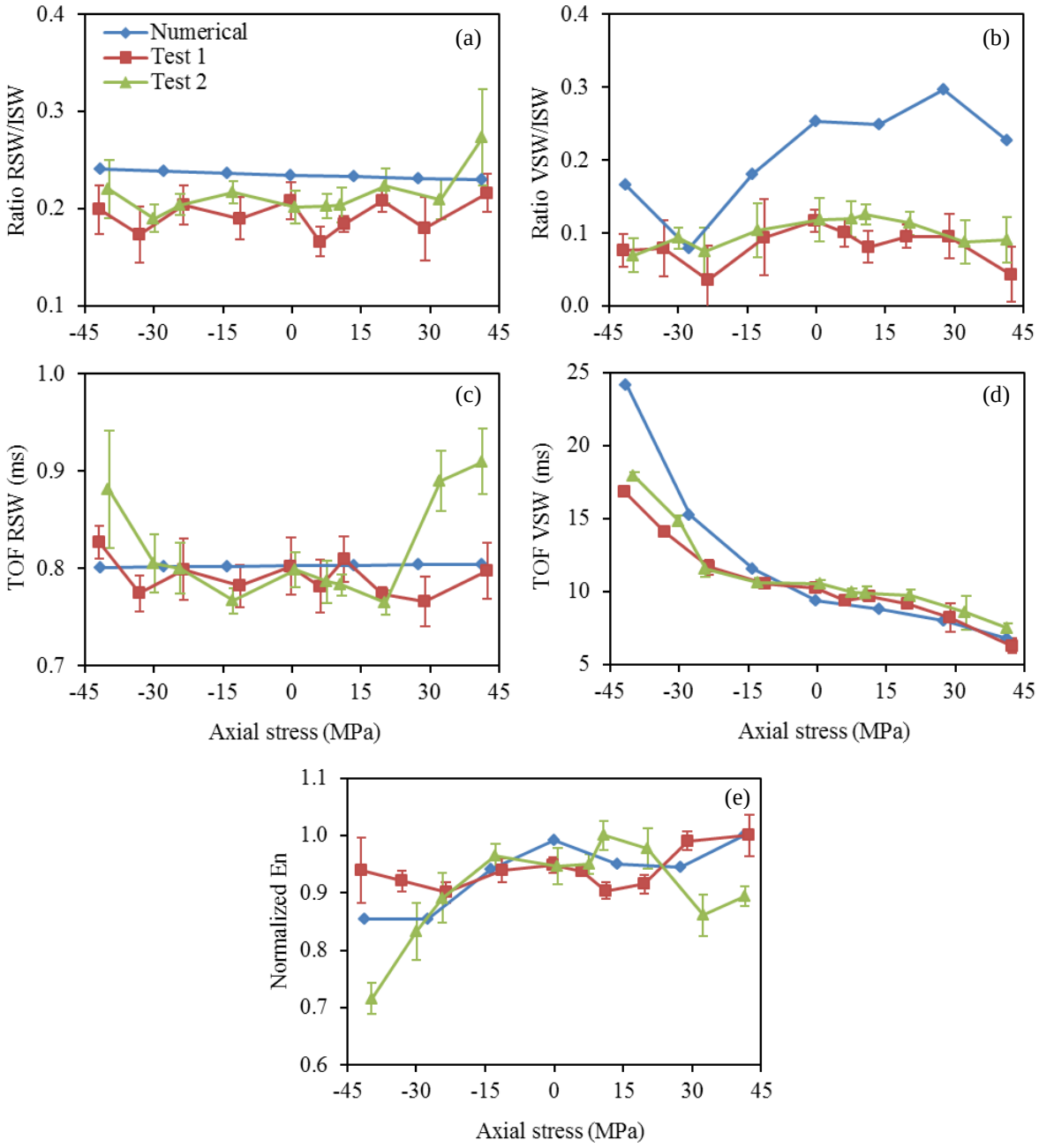

Figure 5.22. Single-chain configuration. Extraction of some selected features from the time waveforms measured at S1 as a function of the axial stress. (a) Ratio associated with the amplitude of the reflected and incident waves. (b) Ratio associated with the amplitude of the vibration-induced and incident waves. (c) Time of flight of the reflected wave. (d) Time of flight of the vibration-induced wave. (e) Normalized energy of solitary waves in the time range 1.25-25 ms.

Similar to Fig. 5.22, Fig. 5.23 shows the features associated to the wave measured at S2. The same trends is visible except for the ratio VSW/ISW displayed in Fig. 5.23b. The reason is still under investigation; we believe that it may be related to the combination of many beam's vibrational modes, and/or the complexity of the oscillations of the particles adjacent to the beam. Figures 5.22 and 5.23 suggest that the time of arrival of the VSW is the most sensitive parameter to the beam's axial stress.

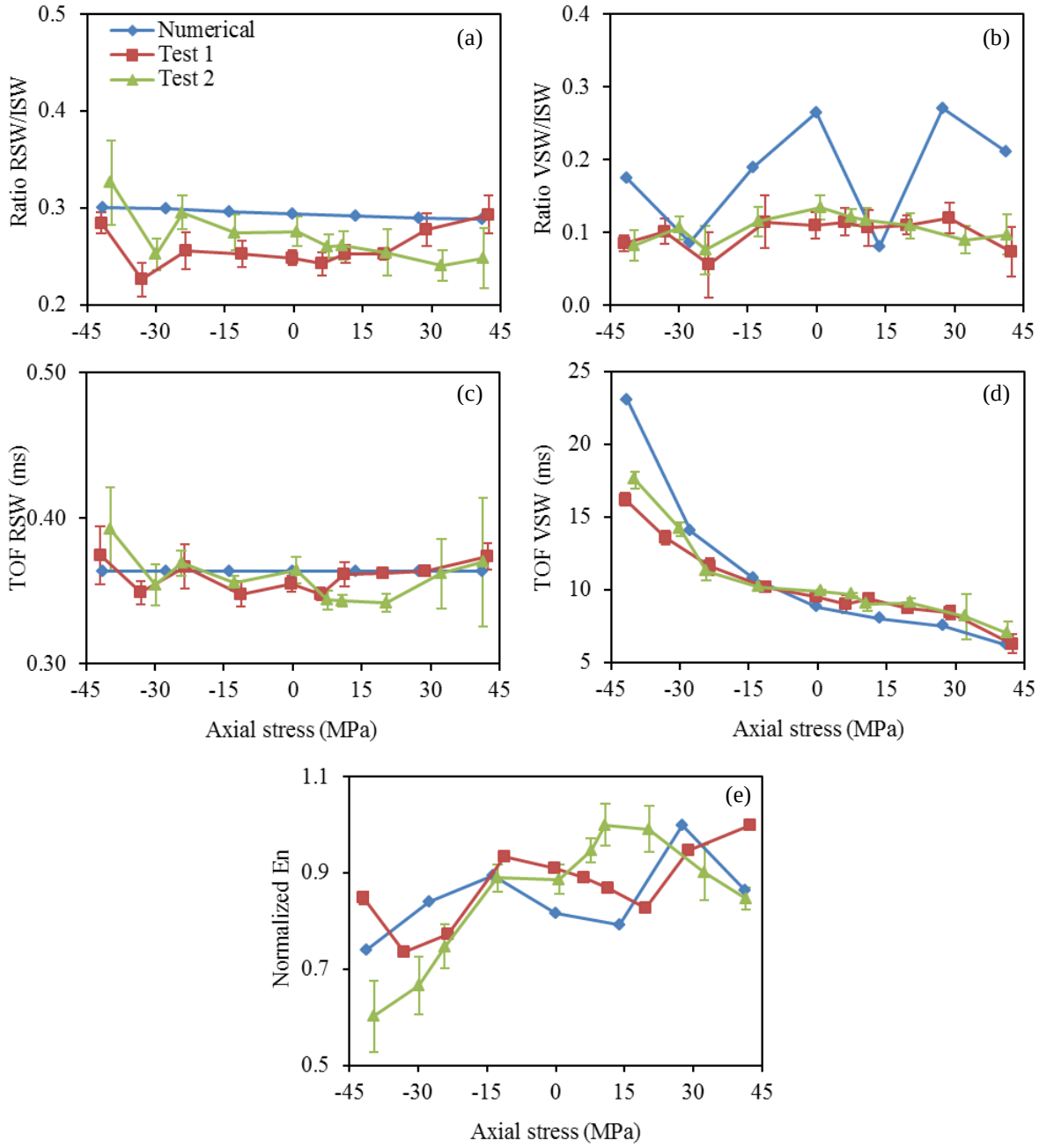

Figure 5.23. Single-chain configuration. Extraction of some selected features from the time waveforms measured at S2 as a function of the axial stress. (a) Ratio associated with the amplitude of the reflected and incident waves. (b) Ratio associated with the amplitude of the vibration-induced and incident waves. (c) Time of flight of the reflected wave. (d) Time of flight of the vibration-induced wave. (e) Normalized energy of solitary waves in the time range 1.25-25 ms.

Since the highest variation with respect to the beam axial stress is associated to the TOF VSW, we extrapolated the curve fit presented in Fig. 5.24. Ideally, the equations displayed in the figure can be used to determine the neutral temperature T_N of any beam having the same geometric and mechanical properties and probed with a single chain made of the same particles. In fact, in a blind test the temperature T_c can be measured with a thermocouple and the solitary wave parameters are measured. From the polynomials in Fig. 5.24, the actual stress σ_c acting on the beam can be retrieved and then Eq. 1.1 can be applied to estimate the unknown T_N.

For illustrative purpose, let use the polynomial displayed in Fig. 5.24 (a). The fifteen measurements obtained at temperature 41 °C during the same test (Test 2) are considered and the arrival time of the vibration-induced wave cluster from sensor S1 is computed. The average value of this feature is computed and replaced in the polynomial which determines that the actual stress is equal to 1.76 MPa. Using this value in Eq. 1.1, we determine that the beam's neutral temperature is T_N=41.98 °C, which agrees well with the computed value of T_N=43.61 °C found in Fig. 5.19(a). If we apply the data of sensor S2 from the same test to the polynomial shown in Fig. 5.24 (b), we find that the neutral temperature is T_N=41°C. By inspecting Figs. 5.24 (a) and (b), we found that when an experimental data as a point is close to the polynomial curve we can get a suitable value for the neutral temperature.

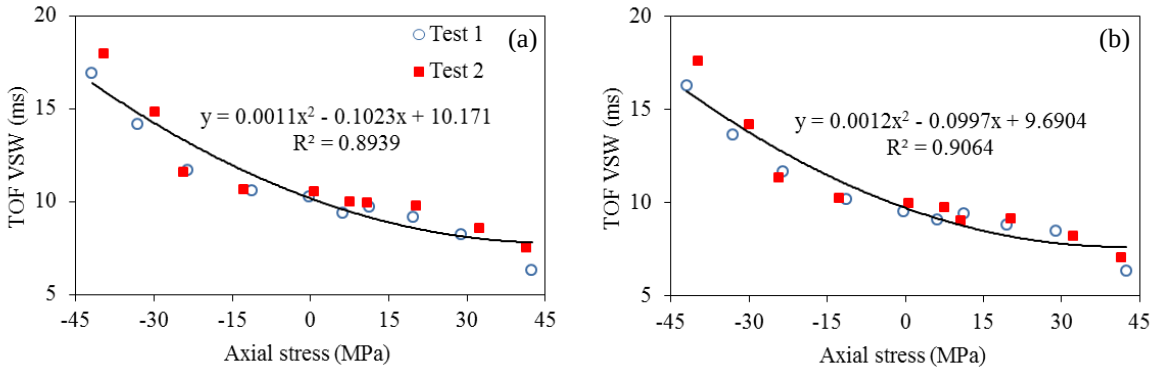

Figure 5.24. Single-chain configuration. Polynomial interpolation of the experimental data from both Test 1 and Test 2. (a) Time of flight of the vibration-induced wave measured at sensor S1; (b) Time of flight of the vibration-induced wave measured at sensor S2.

In what follows we present the results associated with the two chains. We compare in Fig. 5.25 the numerical waveforms recorded at the sensor site S2 for one- and two-chains configurations. The solitary waves relative to the zero axial load are presented. The amplitude of the incident wave and its tail generated at the curved segment is identical, whereas there is a small difference in the amplitude of the RSW. The amplitude of the RSW increased due to the effect of the second chain which causes more energy of the ISW reflects from the beam-chain interface. The arrival time of the VSW is larger in the single chain case as the beam is free to vibrate and the energy is not dissipated into the waves propagating in the second chain.

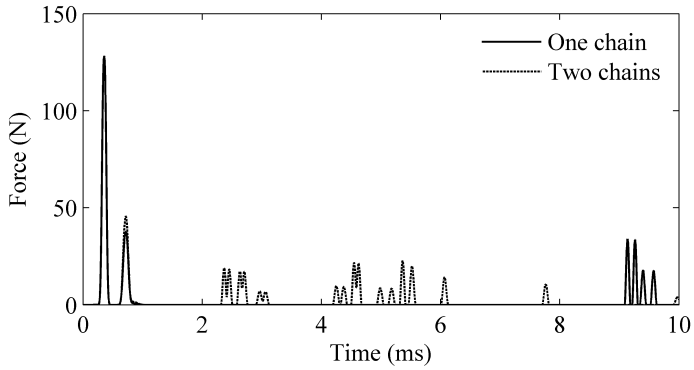

Figure 5.25. Numerical profiles measured at sensing site S2 when one and two chains were used. The beam is at zero axial stress.

The panels on the left of Fig. 5.26 show the experimental and the numerical time waveforms measured by the four sensor beads when the beam was subjected to the largest tension. Similarly, the panels on the right present the results relative to the largest compression. The bottom half panels show that a train of pulses is transmitted through the thickness. The first pulse in this train is herein indicated as transmitted solitary wave (TSW). The second pulse is due to reflecting the TSW from the steel block (see Fig. 5.18(b)) located at the end of the second chain, and this pulse is named as boundary reflected solitary wave (BRSW). Overall, we observe a fair agreement between the numerical and the experimental time series. The experimental normalized amplitudes are smaller due to the absence of dissipation in the numerical model. In this configuration we do not observe a significant delay in the arrival of the reflected pulses since the vibration of the beam is restrained by the presence of the second chain.

The features listed in Table 5.4 were extracted from the time domain.

Table 5.4. Features selected in this study for two straight chains configuration.

Feature	Description
RSW/ISW	The ratio of amplitude of the RSW to the ISW
VSW/ISW	The ratio of amplitude of the VSW to the ISW
TSW/ISW	The ratio of amplitude of the TSW to the ISW
TOF RSW	Time between the ISW and the RSW
TOF VSW	Time between the ISW and the VSW
TOF TSW	Time between the ISW and the TSW
En	The energy of solitary waves in the time range 1.4-4 ms

Figure 5.27 shows the features associated with the reflected wave as a function of the axial stress as measured by S2. The trends relative to the amplitudes are similar to those discussed in Fig. 5.22. The overestimation of the numerical RSW/ISW is caused by the absence of dissipation in the numerical model and by the vertical shift of the experimental values due to

the static compression on the PZT caused by the weight of the vertical segment. The time of arrival of the reflected wave is almost constant and little information can be retrieved in terms of stress sensitivity. Finally, the numerical trends of the En show a significant change with respect to stress. Overall, the energy is inversely proportional to the temperature raise. As the frequency of vibration of the beam increases, the speed at which it bounces back to the granules increases, determining higher pulses in the first chain.

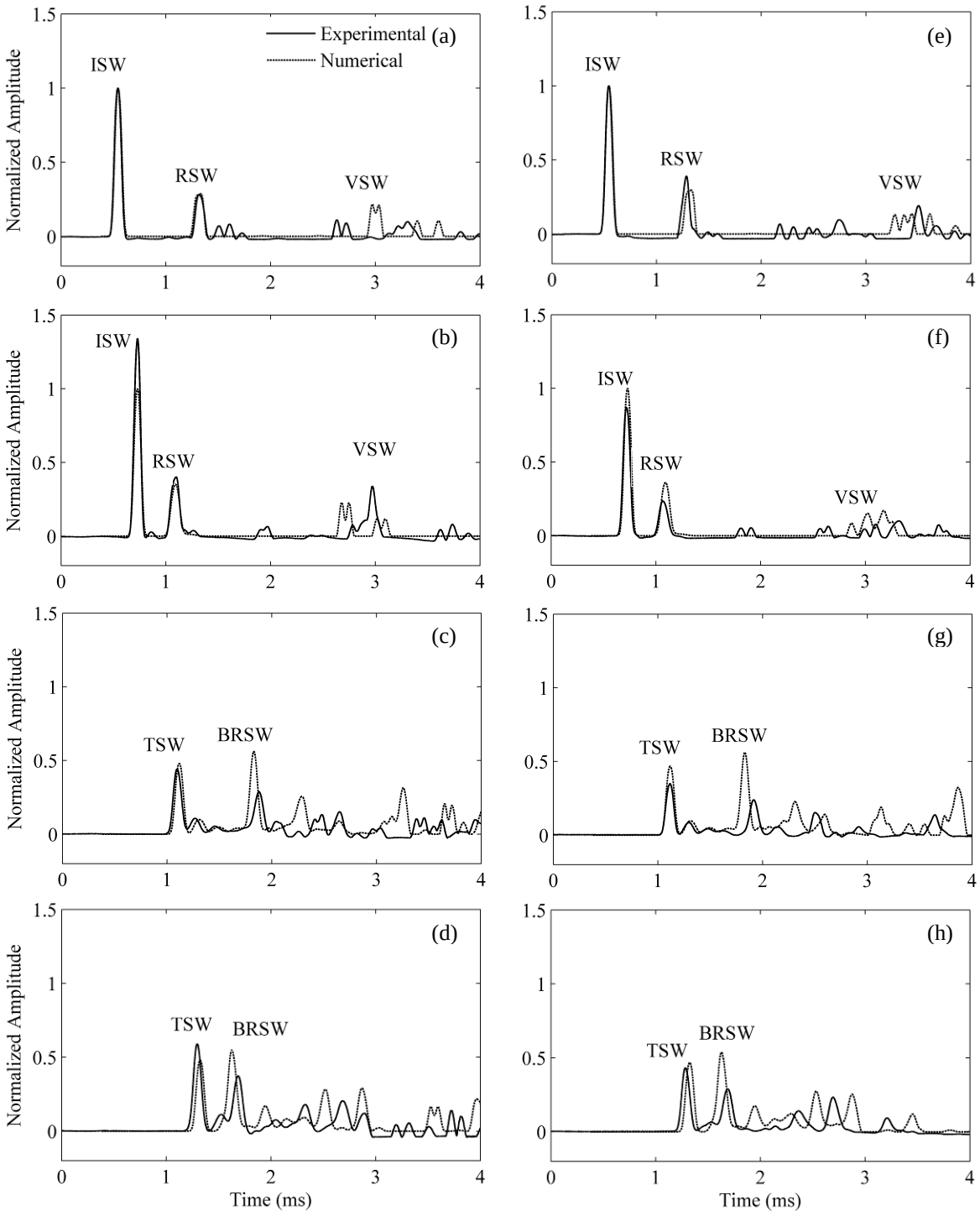

Figure 5.26. Two chains configuration. Experimental and numerical normalized amplitudes. Left panels: beam under largest tension at 41.2 MPa, (a) sensor S1, (b) sensor S2, (c) sensor S3, and (d) sensor S4. Right panels: beam under largest compression at -44.1 MPa, (e) sensor S1, (f) sensor S2, (g) sensor S3, and (h) sensor S4.

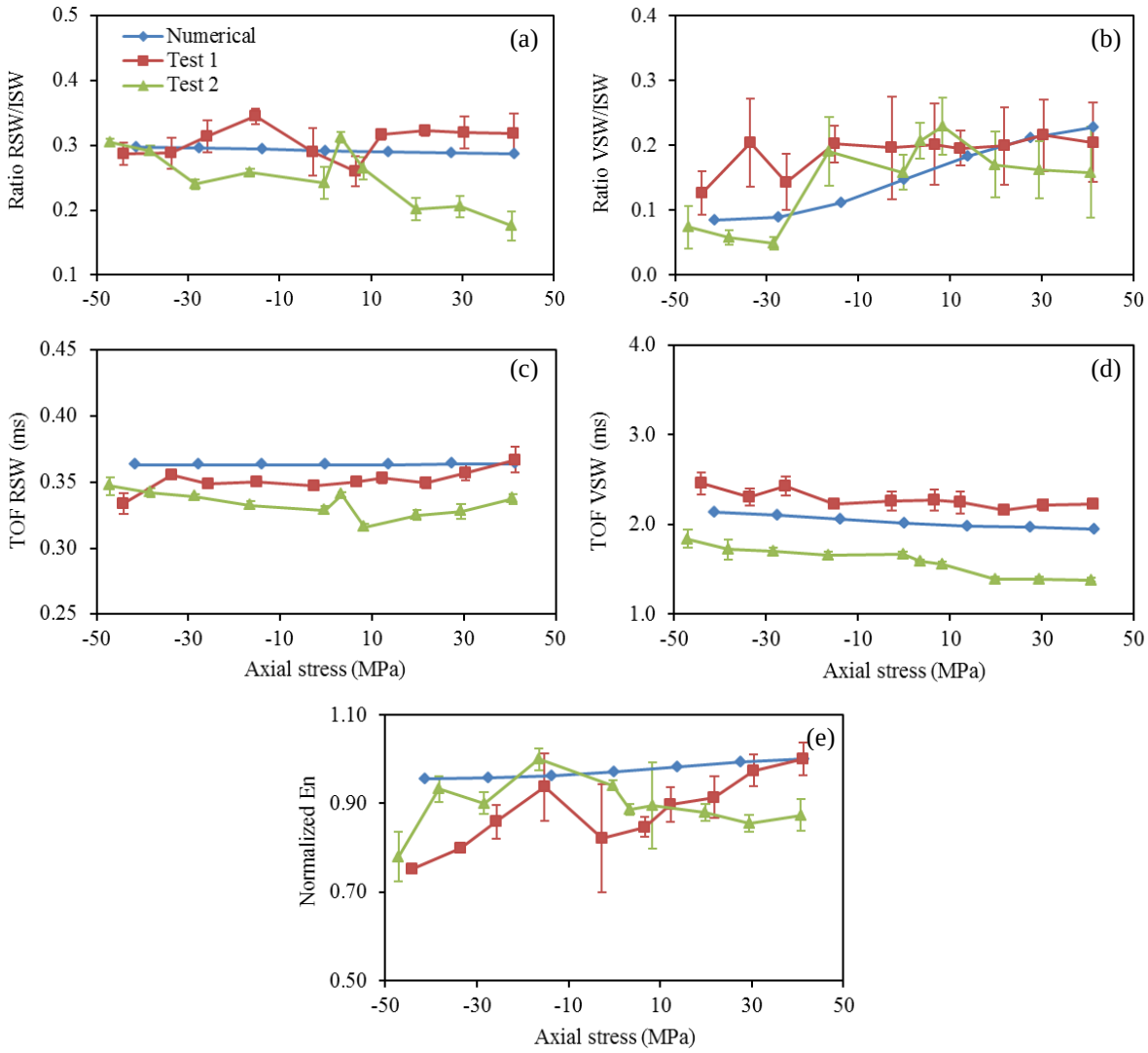

Figure 5.27. Two chains configuration. Extraction of some selected features from the time waveforms measured at S2 as a function of the axial stress. (a) Ratio associated with the amplitude of the reflected and incident waves. (b) Ratio associated with the amplitude of the vibration-induced and incident waves. (c) Time of flight of the reflected wave. (d) Time of flight of the vibration-induced wave. (e) Normalized energy of solitary waves in the time range 1.4-4 ms.

Overall, with respect to the test involving one straight chain, the responses obtained from these two experimental tests present higher variations between each other. It should be noted that the repeatability of the setup could be compromise if many phenomena occurs, the two chains are not perfectly aligned and perpendicular to the beam, the two chains does not touch the beam

with the perfectly same contact. The two chains monitoring in this sense appears more sensitive to the setup.

Similar to Fig. 5.27, Fig. 5.28 shows the selected features computed from the time waveforms measured at S3. Overall, there is a good agreement between numerical and experimental data in terms of the force ratio and the time of flight. It is visible that the En is unstable compared to the same feature shown in Fig. 12(e). The reason could be that chain 1 is only affected by the propagation and backscattering of solitary waves whereas the chain 2 is instead affected by the transmission and fragmentation of solitary waves, which could be a very sensitive and not repeatable phenomenon. The numerical model predicts an overall constant trend for the axial stresses measured during the experiments presented in this study. However, we also notice the low repeatability of the signal amplitude. We believe that an accidental misalignment of the sensor particles altered the sensitivity of the particles to the propagation of the wave.

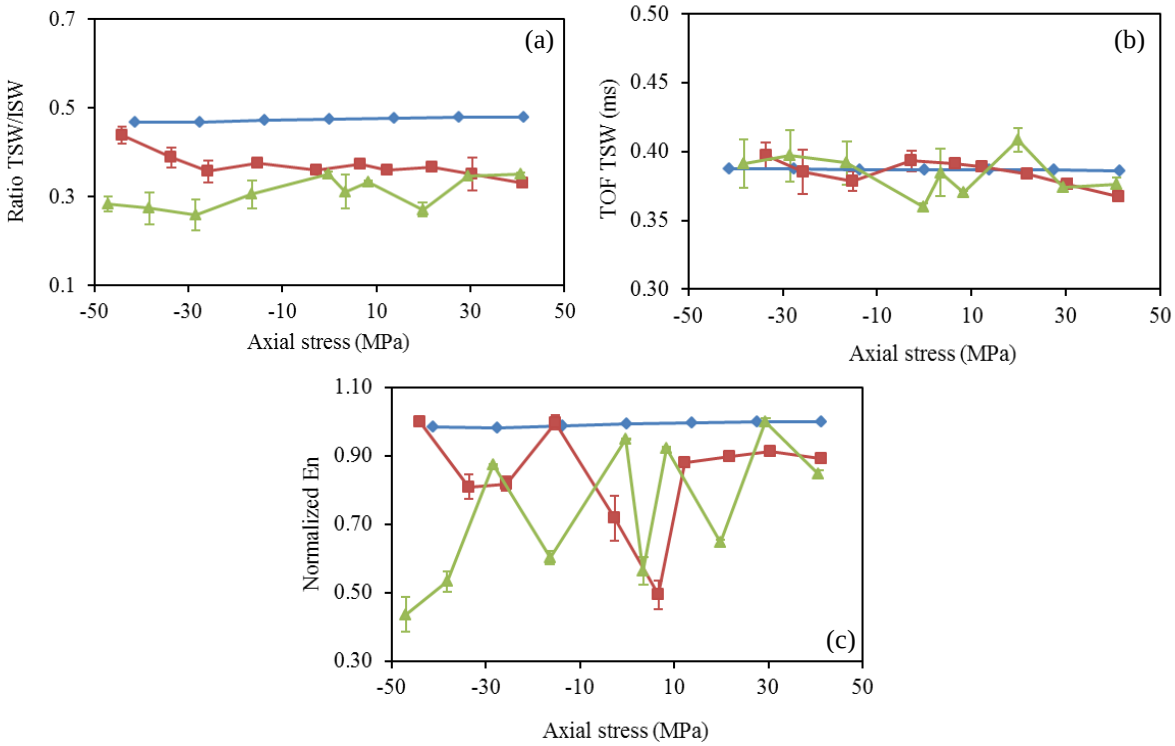

Figure 5.28. Two chains configuration. Extraction of some selected features from the time waveforms measured at S3 as a function of the axial stress. (a) Ratio associated with the amplitude of the transmitted and incident waves. (b) Time of flight of the transmitted wave. (c) Normalized energy of solitary waves in the time range 1.4-4 ms. Incident wave measured at S2 was used in preparing this figure.

Figure 5.29(a) shows the velocity of the incident and the reflected waves as a function of the axial stress relative to single chain configuration. The experimental results which represent the average of the 15 measurements demonstrate once more the repeatability of the test as the results from Test 1 and Test 2 overlap. For the experimental results, we considered the average velocity of the solitary waves from the 15 measurements. As expected, the speed of the incident wave does not change with stress. The speed of the reflected wave is slower since it is proportional to its amplitude. Moreover, the speed slightly changes with respect to the axial stress.

Similarly, Fig. 5.29(b) shows the speed relative to the incident, reflected, and transmitted waves for the two chains configuration. There is a very good agreement between the experimental and the numerical results. The speed of the transmitted wave is slightly higher than the RSW, consistent with the corresponding amplitudes.

Finally, Figure 5.30 shows the relative speed variation with respect to the maximum tensile stress considered at the beginning of the loading ramp. The response is not the same for both Tests 1 and 2, however the variation of the speed is remarkably much higher than any relative speed variation visible in acoustoelastic-based method.

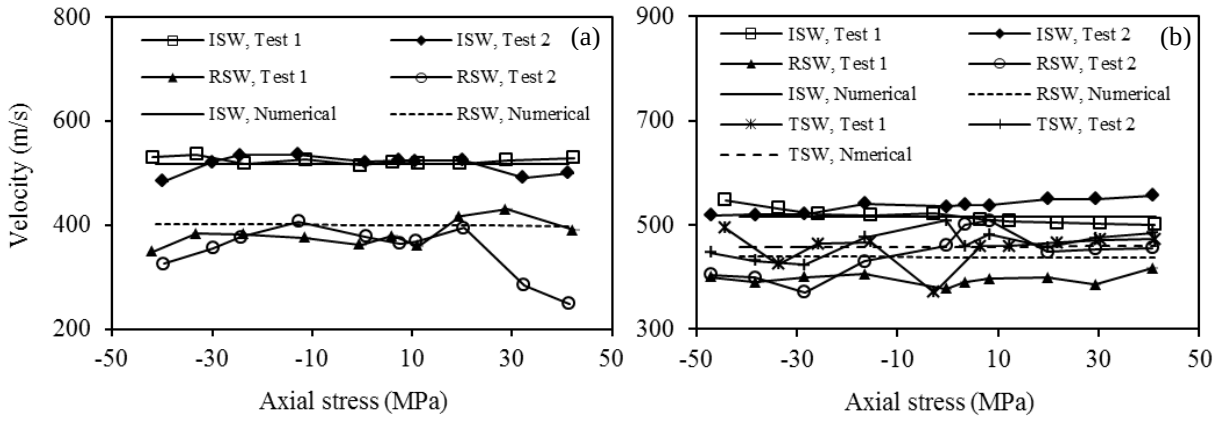

Figure 5.29. Experimental and numerical velocity of the solitary waves as a function of the beam's axial stress. (a) single-chain configuration, and (b) two-chains configuration.

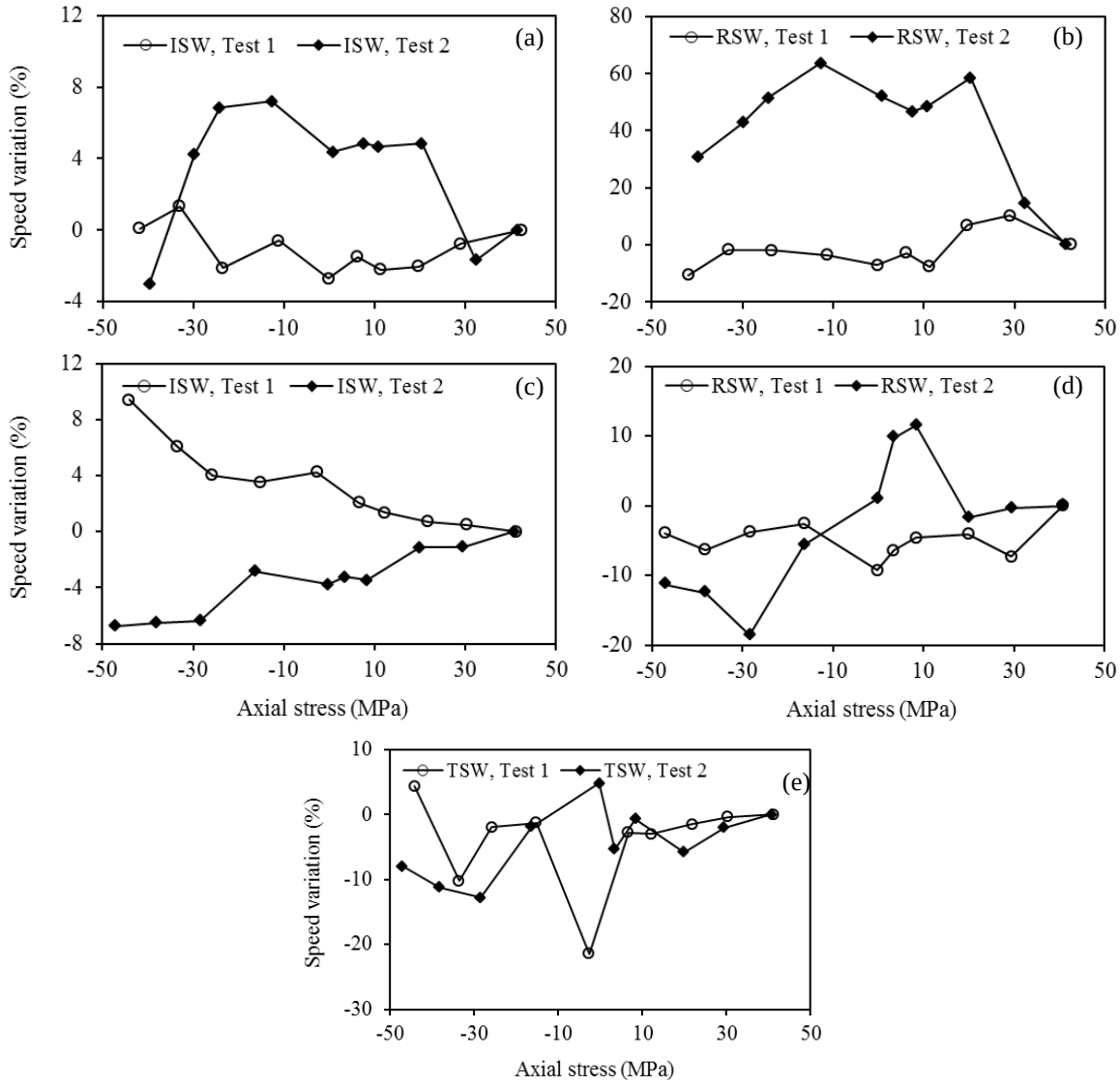

Figure 5.30. Speed variation of the experimental solitary waves as a function of the beam's axial stress. (a, b) single-chain configuration; and (c, d, e) two-chains configuration.

5.2.3 Discussion

The two straight chains arrangement may resemble a single chain that contains a single impurity. The discussion carried in Section 5.1.3 can be carried out here as well. In our study, both the numerical and the experimental time waveforms show the presence of train of pulses propagating

backward and forward. As such a conclusive remark about the analogy between our system and a single chain with an impurity cannot be made.

6.0 REFERENCE-FREE DAMAGE DETECTION USING GUIDED WAVES

In the second half of the present work, some signal processing algorithms for damage identification and localization in pipes and plates based on GUWs are presented.

This chapter describes a monitoring system based on the generation and detection of GUWs from an array of sparse transducers. In a round-robin manner, ultrasonic waves are generated and measured from all possible different pairs of excitation and sensing transducers. The ultrasonic signals are then processed using continuous wavelet transform and empirical mode decomposition to extract few damage-sensitive features that enable the detection and localization of damage. With respect to most of the existing GUW-based methods, the proposed approach does not require to record data from a pristine structure (baseline data), and damage is inferred by examining the selected features obtained from all the possible combinations of actuator-sensor pairs of the array. The method is validated using commercial finite element software to model the presence of ten ultrasonic transducers bonded onto an aluminum plate.

In this chapter, first, a literature review of GUW-based methods for SHM of plate-like structures is presented. Then, in Section 6.2, the general principles of CWT and EMD are described. Then the features extracted from the wave signals to identify and locate the presence of damage are described. Section 6.3 introduces the numerical model whereas Section 6.4 describes the damage indexes and the probabilistic approach used. The results of the numerical

study are then presented in Section 6.5. The chapter ends with some concluding remark and the description of ongoing studies and the path for future studies.

This chapter was extracted from our published paper entitled “Reference-free damage detection by means of wavelet transform and empirical mode decomposition applied to Lamb waves”.

6.1 INTRODUCTION

GUWs are widely acknowledged as an effective tool for the SHM of waveguides that are ubiquitous in civil, mechanical and aerospace structures. Guided waves can travel relatively large distances with little attenuation and offer the advantage of exploiting one or more of the phenomena associated with transmission, reflection, scattering, and absorption of acoustic energy (Alleyne and Cawley, 1996; Giurgiutiu, 2005; Rizzo and Lanza di Scalea, 2007, Raghavan and Cesnik, 2007; Diamanti, Hodgkinson, and Soutis, 2004; Su et al., 2006; Park et al., 2007; Clarke et al., 2009; Yan, Royer and Rose, 2010; Zhu et al. 2010).

Meantime it is well established that signal processing is essential to enhance any GUW-based SHM. One of the main objectives of any processing is to extract damage-sensitive features that enable to determine the existence, location, and severity of damage. Methods based on the discrete wavelet transform (Rizzo and Lanza di Scalea, 2006; Lanza di Scalea et al., 2007) are effective to de-noise and compress signals whereas the continuous wavelet transform (CWT) characterizes the time-frequency content of non-stationary signals. Both transforms can be used for damage identification and sizing as well (Staszewski et al., 1997; Paget et al., 2003; Ip, Tse and Tam, 2004; Reda Taha et al., 2006; Rizzo et al., 2007; Grabowska, Palacz and Krawczuk,

2008; Giridhara et al., 2010; Gu and Wang, 2009). The empirical mode decomposition (EMD) in combination with the Hilbert spectrum analysis (i.e. the Hilbert-Huang transform) or in combination with the short-time Fourier transform is also a proven tool for GUW-based SHM (Wei et al., 2006; Kažys, Tumšyset and Pagodinas, 2008; Lu, Oruklu and Saniie, 2008; Xu, Xu and Zhou, 2010; Xu, Xiong and Wu, 2011; Leo et al., 2012).

Sometimes probabilistic methods are used in SHM. Correlation and probability-based damage identification methods were presented by several researchers (Hay et al., 2006; Zhao et al., 2007a, 2007b; Lu at al., 2009; Wang, Ye and Lu, 2009; Wang et al., 2010a, 2010b, Dehghan Niri and Salamone, 2012). Hay et al. (2006) described an approach for Lamb wave tomography using a circular array of piezoceramic transducers and signal difference coefficients to estimate the probability of defect occurrence at a certain point. Lu at al. (2009) proposed an inverse algorithm based on the correlation of the digital damage fingerprints (DDFs) of wave signals extracted from baseline and damaged composite panels of stiffeners. Wang, Ye and Lu (2009) and Wang et al. (2010a, 2010b) combined probabilistic methods and correlation analysis to detect damage by means of guided wave propagation.

In general, most health monitoring approaches for structural waveguides are based on the comparison of testing data to baseline data. Ideally, the baseline includes scenarios under all possible environmental conditions. To overcome the need for reference data, baseline-free methods were proposed in the past five years (Sohn at al., 2007; Anton, Inman and Park, 2009; Qiang and Shenfang 2009; Park, Lee and Sohn, 2010; Kim et al., 2011; Lee et al., 2012). In this study, we present a reference-free approach for damage identification and localization that combines the advantages of CWT, EMD, and probabilistic methods with the need to deploy baseline-free systems. The approach processes Lamb waves generated and detected by all

possible transducers' pairs of an array to extract damage-sensitive features from the CWT and the EMD. Then, a probabilistic method uses these features to map the structure contained within the array under monitoring and localize the damage. In this study, the method is numerically validated by using a finite element model where ten nodes, which simulate ten transducers bonded to a square aluminum plate, are subjected to a time-dependent force orthogonal to the plate surface. The excitation consists of a narrowband toneburst centered at 100 kHz able to simulate the generation and propagation of the first anti-symmetric (A_0) mode. Then, the wavelet energy spectrum and the energy extracted from the EMD's first intrinsic mode function (IMF) are used to compute two damage-sensitive features that constitute the inputs of a probabilistic method that does not require baseline data. With respect to the probabilistic methods applied to GUWs, that use correlation analysis between baseline and newly generated data, in this study baseline data are not necessary. The term baseline data is here intended as a set of data associated with a pristine structure subjected to all those operational variations, such as temperature, weight, or moisture, that do not constitute damage *per se*. The fact that the proposed method does not require the measurements from at least two structure's scenarios (pristine and damaged) implies that the approach described in this section is reference-free.

6.2 BACKGROUND

6.2.1 Continuous Wavelet Transform

The CWT is a powerful method to assess the time-frequency content of time-series. This transform has a multi-resolution capability deriving from a flexible window that is broader in time for observing low frequencies and shorter in time for observing high frequencies, as required by the Heisenberg uncertainty principle (Sale, Rizzo and Marzani, 2011). This capability is given by the mother wavelet function utilized as the basis of the decomposition. The mother wavelet is defined by two parameters, the scaling parameter *a* and the translation parameter *b* (Daubechies, 1992). Applied to a time transient waveform, the CWT yields a scalogram contour plot that retains the time-frequency information of the propagating wave's energy.

The wavelet transform of a guided wave signal *S(t)* is a transformation that decomposes the signal into a superposition of scaled and translated functions $\psi_{a,b}(t)$ obtained from a mother wavelet $\psi(t)$ given by:

$$\psi_{a,b}(t) = |a|^{-\frac{1}{2}} \psi\left(\frac{t-b}{a}\right) \tag{6.1}$$

where the translation parameter *b* shifts the wavelet in time, and the scaling parameter *a* controls the wavelet frequency bandwidth. The CWT of the guided wave signal *S(t)* is defined as:

$$W_{\psi}(a,b) = \int_{-\infty}^{+\infty} S(t)\psi^{*}\left(\frac{t-b}{a}\right)dt \tag{6.2}$$

where ψ^{*} is the complex conjugate of ψ. $W_{\psi}(a,b)$ is called the wavelet coefficient for the wavelet $\psi_{a,b}(t)$. Equation (6.2) can be also expressed as:

$$W_{\psi}(a,b) = \left\langle S(t).\psi^{*}_{a,b}(t) \right\rangle \tag{6.3}$$

where $\langle . \rangle$ represents the inner product. In this study, the Gaussian mother wavelet of order 8 shown in Fig. 6.1 was used because of its similarity with the shape of the excitation.

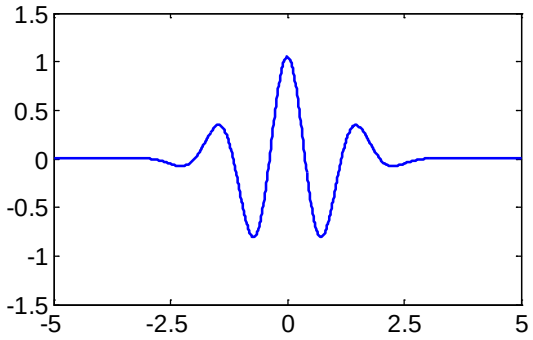

Figure 6.1. The Gaussian mother wavelet of order 8

6.2.2 Empirical Mode Decomposition

Any guided wave signal can be decomposed into different, simple, modes of oscillations represented by IMFs that need not to be sinusoidal (Zhang et al., 2003). Each IMF satisfies two conditions: 1) the number of extreme and zero crossings must be either equal or can be different at most by one in the thorough data set; 2) at any point, the mean value of the envelope defined by the local maxima and the envelope defined by the local minima is zero. The EMD is an iterative procedure to extract IMFs. First, the local maxima and minima are computed and a cubic spline is used to build the upper and lower envelopes which connect all the local maxima and all the local minima, respectively (Huang et al., 1998). It must be mentioned that, in the present study, the local maxima or minima were computed for the time-window that included the

fastest mode only. Then, the mean $m_1(t)$ of these envelopes is computed and subtracted to the original guided wave $S(t)$, i.e.

$$h_1(t) = S(t) - m_1(t) \tag{6.4},$$

to compute the first component $h_1(t)$. If $h_1(t)$ satisfies the two conditions mentioned above then it is an IMF otherwise the previous process, called sifting, is repeated. In general the sifting process associated with the first IMF component can be written as:

$$h_{1,j+1}(t) = h_{1,j}(t) - m_{1,j+1}(t), \quad j = 1, 2, ..., k \tag{6.5}$$

where $m_{1,j+1}(t)$ is the mean of the upper and lower envelopes of $h_{1,j}(t)$. The first IMF component $h_{1,k}(t)$ contain the finest-scale or the shortest-period component of the signal. The first step of the sifting process to extract the next IMF component $h_{2,k}(t)$ is:

$$h_2(t) = r_1(t) - m_2(t) \tag{6.6}$$

where $r_1(t)$ is the residue

$$r_1(t) = S(t) - h_{1,k}(t) \tag{6.7}$$

that constitutes new time series to be subjected to the sifting process. The iteration can be terminated either because the n-th IMF component $h_{n,k}(t)$ or the residue $r_n(t)$ becomes too small or because the $r_n(t)$ is a monotonic function, which implies that no more IMF can be extracted. At the end of the decomposition, the original guided wave $S(t)$ can be denoted in terms of n IMFs:

$$S(t) = \sum_{j=1}^{n} h_j(t) + r_n(t) \tag{6.8}.$$

6.3 NUMERICAL SETUP

The propagation of Lamb waves in a square aluminum plate was numerically simulated by using a time-transient analysis run under ANSYS v.13.0. The effectiveness of conventional finite element models to simulate the propagation of elastic guided waves in structural components was demonstrated by several researchers (Alleyne and Cawley, 1991; Moser, Jacobs and Qu, 1999; Bartoli et al., 2005; De Marchi et al. 2010; Sale, Rizzo and Marzani, 2011). It is known that the accuracy of the procedure is dependent upon the temporal and the spatial resolution of the analysis. To achieve good accuracy, both the integration time step and the finite element size must be in accordance with the maximum frequency of interest (f_{max}) of the dynamic problem. A good rule for time step resolution Δt is to use a minimum of 20 points per cycle at the highest frequency (Bartoli et al., 2005), i.e.:

$$\Delta t \leq \frac{1}{20 f_{max}} \tag{6.9}$$

For a good spatial resolution 10 nodes per wavelength are required even though some researchers (Bartoli et al., 2005, Moser, Jacobs and Qu, 1999) recommend 20 nodes per wavelength. The latter condition yields to the definition of the maximum element length L_e as:

$$L_e = \frac{\lambda_{min}}{20} \tag{6.10}$$

where λ_{min} is the wavelength corresponding to the highest frequency of the wave mode of interest.

In this study a 400×400×5.08 mm aluminum plate was discretized using the 3-D 8-node "SOLID185" element with three degrees of freedom per node. Each element of the mesh was 1.27 mm thick, and 1.52 mm wide and long. The following properties were assumed for the

aluminum: density ρ=2700 kg/m^3, Young's modulus E=69.00 GPa, shear modulus G=25.94 GPa, and Poisson's ratio ν=0.33. Damage was simulated in the form of a notch with dimensions 50×3×5.08 mm. Figures 6.2a and 6.2b show the geometry of the plate and the location of the damage.

Lamb waves were excited by imposing a modulated 3- or 5-cycles toneburst forcing function perpendicular to the plate surface (Fig. 6.2c and 6.2d). The toneburst was centered at 100 kHz. The orientation and the frequency of the forcing function allowed for the excitation of the first A_0 mode. The 3-cycle signal has short duration and lower energy than the 5-cycle toneburst yielding to a better isolation of the signals of interest but with lower signal-to-noise ratio. The frequency bandwidth of the 5-cycle toneburst is narrower with the advantage of being less dispersive.

The force was applied at ten locations, named A to J, of the plate. This simulates the presence of a sparse array formed by ten transducers. An unconditionally stable implicit Newmark procedure with a decay factor of 0.005 and integration parameters α=0.252 and δ=0.505 was used to perform the time integration. The out-of-plane z-displacement occurring at the ten transducer positions (nodes) located at the top surface of the plate were monitored. In order to satisfy Eq. (6.9) the integration time step (sampling period) Δt was set equal to 0.5 μsec. The number and the location of the transducers induced a total of 90 sensing paths resulting in 8 different path lengths. Table 6.1 clusters all the paths according to the actuator-sensor distance.

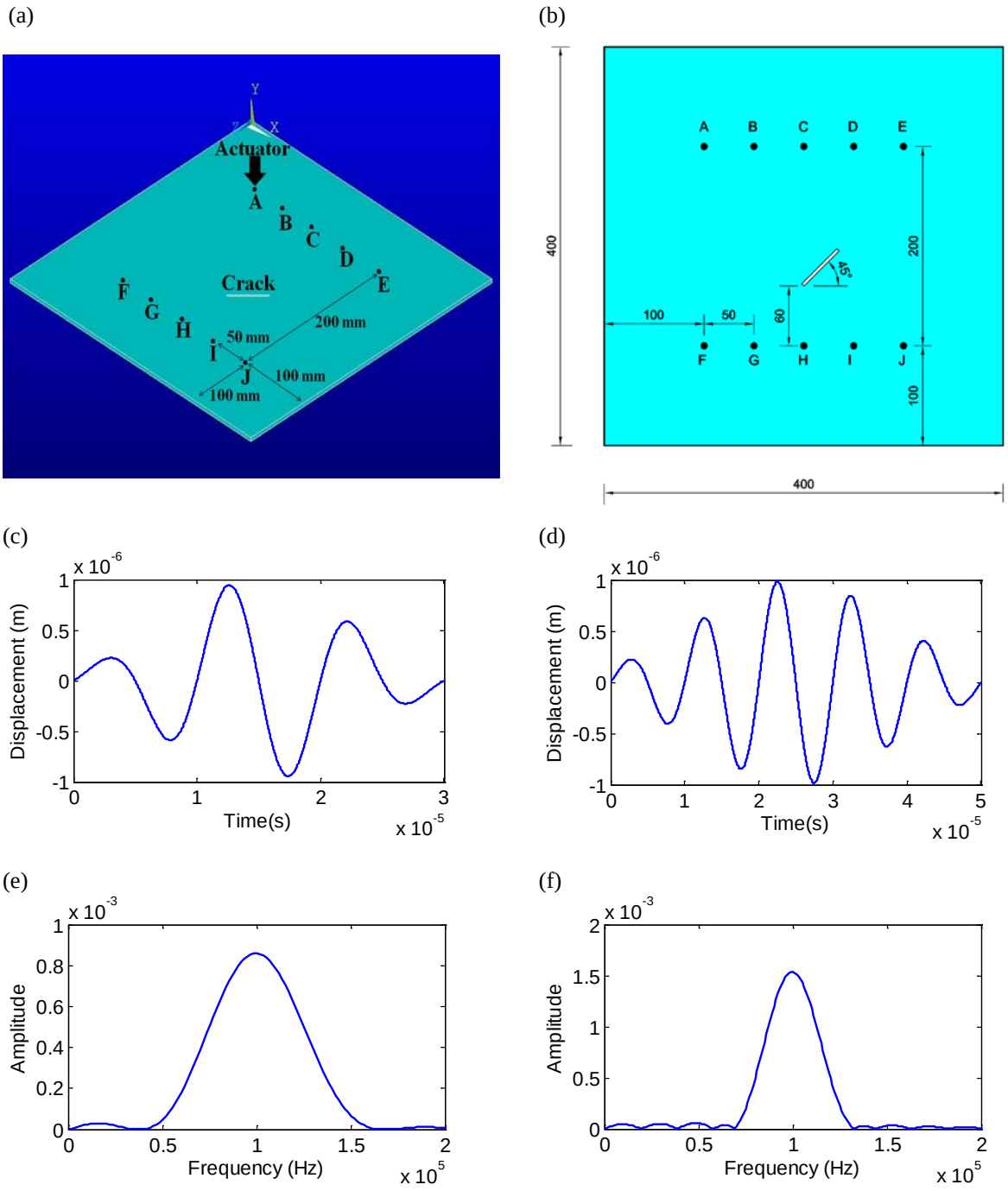

Figure 6.2. (a) Finite element model of the plate. (b) Location of damage and of the sparse array (dimensions in mm). (c) 3-cycle tone burst. (d) 5-cycle tone burst. (e) Fast Fourier transform of the 3-cycle tone burst. (f) Fast Fourier transform of the 5-cycle tone burst.

Table 6.1. The number of total paths and the geometric distances between each path

Actuator – sensor distance (mm)	Sensing path	Total number of paths
50	AB, BC, CD, DE, FG, GH, HI, IJ (and viceversa)	16
100	AC, BD, CE, FH, GI, HJ (and viceversa)	12
150	AD, BE, FI, GJ (and viceversa)	8
200	AE, FG, AF, BG, CH, DI, EJ (and viceversa)	14
206	AG, BF,BH, CG, CI, DH, DJ, EI (and viceversa)	16
224	AH, BI, CF, CJ, DG, EH (and viceversa)	12
250	AI, BJ, DF, EG (and viceversa)	8
283	AJ, EF(and viceversa)	4

6.3.1 Time waveforms and scalograms results

Figures 6.3a and 6.3b show the contour graphs of the Von Mises stress at 75 μsec and 120 μsec, respectively, when the 5-cycle tone burst was applied to node A. The position of some sensor node is overlapped for clarity. At 75 μsec, the wave reached the nodes E and G. The effect of the presence of the notch on the amplitude of the lead wavefront as well as the reflections from the edges is visible in Fig. 6.3b.

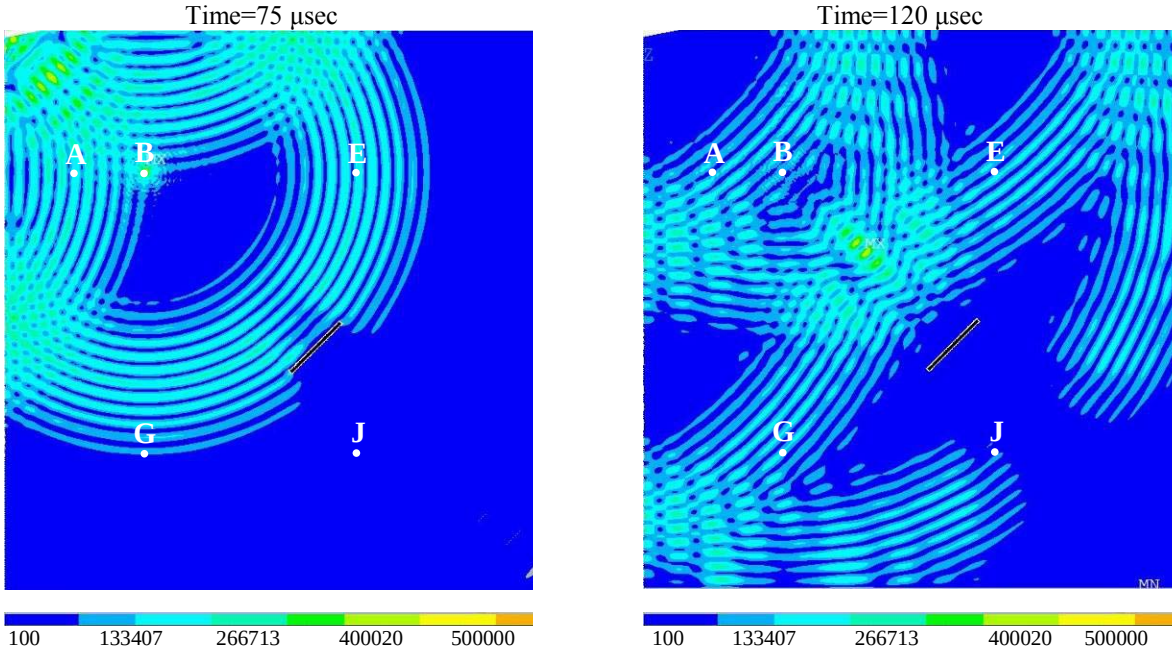

Figure 6.3. Von Mises stress when the 5-cycle tone burst was applied at point A.

The time-history of the out-of-plane displacement *S(t)* at nodes namely B, E, G, and J, when the transducer A generated the 5-cycles signal is shown in Fig. 6.4. The first packet is the A_0 mode traveling along the line of sight between A and the corresponding sensor node. The subsequent packets represent the same mode reflected from the plate edges. As the distances AE and AG are almost identical (200 mm vs. 206 mm), the amplitude and the shape of the direct arrival are identical. The corresponding scalograms are presented in Fig. 6.5. The out-of-plane axis of the scalogram refers to the CWT amplitude of the nodal displacement. In order to provide a direct comparison between the outcomes of the CWT and the frequency content of the signals, the figures are presented in terms of frequency and time rather than scale and time, using the well-known relationship (Rizzo and Lanza di Scalea, 2006):

$$f_i = \frac{F_c \cdot s_f}{a} \tag{6.11}$$

where f_i is the wave frequency, F_c is the center frequency of the Gaussian mother wavelet, a is the scale, and s_f is the sampling frequency. As expected, the main energy is located around 100 kHz.

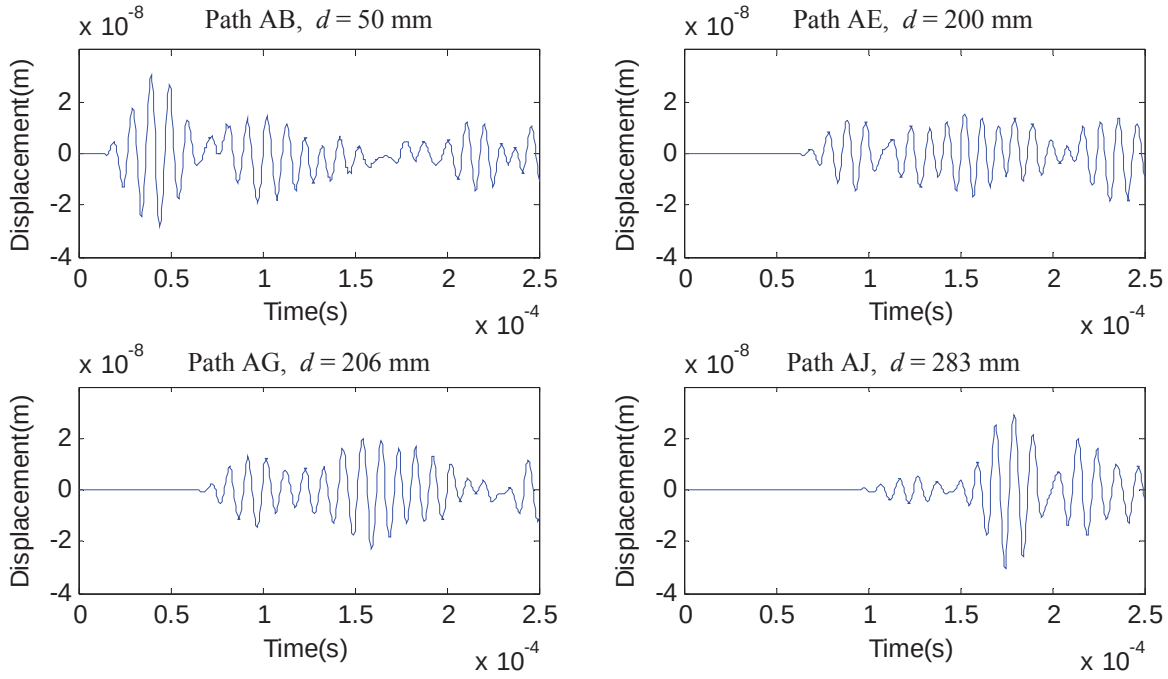

Figure 6.4. Out-of-plane (y) displacements measured at nodes B, E, G, and J, when the 5-cycle tone burst was applied at node A. Only the A0 mode propagating along the line of sight of each transducers' pair combination was considered in the analysis.

6.4 DAMAGE IDENTIFICATION METHOD

6.4.1 Feature extraction

There are many ways to process an ultrasonic signal and there are many features that can be extracted. In this study, the signals were processed with the CWT to extract a features from the joint time-frequency domains. The CWT is particularly attractive because it provides the best balance between time and frequency resolution since it uses the smallest possible Heisenberg uncertainty box (Mallat 1999).

From the waves' scalogram, the wavelet energy spectrum $\mathbf{E}_j^i$ can be calculated as:

$$\mathbf{E}_j^i(t,f) = \left|\mathbf{W}_j^i(t,f)\right|^2, \quad i = 1,2,...,n \quad j = 1,2,...,m(i) \tag{6.12}$$

where $\mathbf{W}_j^i$ is the scalogram associated with the *j*-th guided wave signal associated with the *i*-th sensing path. In the framework of the numerical analysis presented here *n* is equal to 8 and *m* is equal to 16 and 4 when *i=1* and *i=8*, respectively. From the scalogram the following feature is computed:

$$F_j^i = \sum_t \sum_f \mathbf{E}_j^i(t,f), \quad i = 1,2,...,n \quad j = 1,2,...,m(i) \tag{6.13}$$

where *F* is the CWT-based feature. Here, we used symbol Σ, because our signals are discrete.

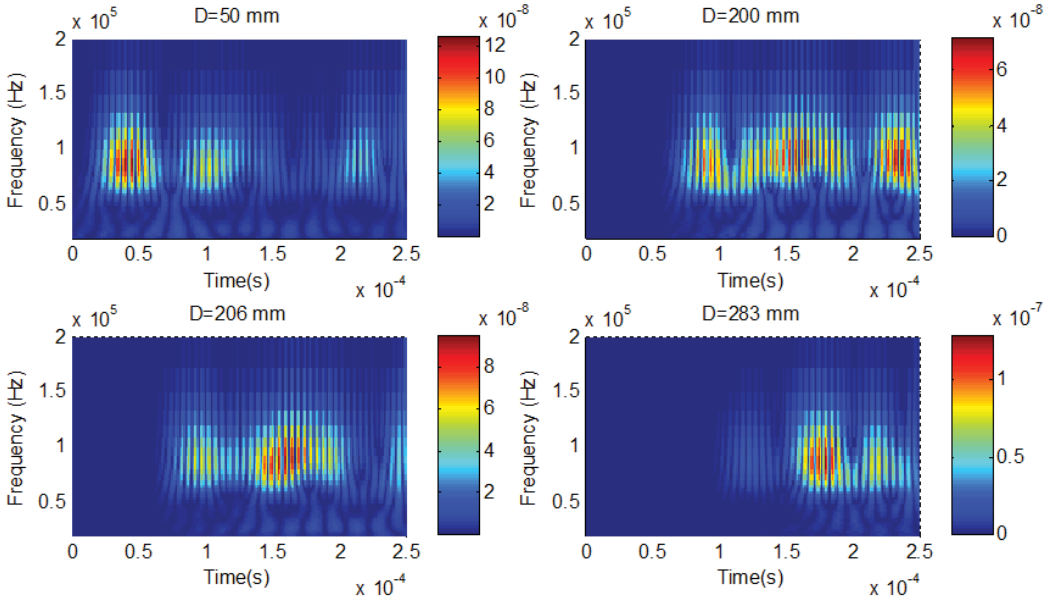

Figure 6.5. Wavelet scalograms associated with the out-of-plane displacements shown in Fig. 6.4.

A second feature was extracted from the first IMF of the ultrasonic signals. This feature can be defined as:

$$H_j^i = \sum_t \left| h_{1,j}^i \right|^2, \quad i = 1,2,...,n \quad j = 1,2,...,m(i) \tag{6.14}$$

where $h_{1,j}^{\ i}(t)$ is the first IMF of the j-th guided wave signal in the i-th sensing path, and m and n have the same meaning as in Eqs. (6.12) and (6.13).

Thus, for each path distance, the maximum values F^i and H^i of the CWT-based and EMD-based features were calculated and they identify the healthy condition of the structure.

6.4.2 Feature ratios and the probabilistic method

For each sensing path i, two feature ratios (FRs) were defined as:

$$FR_{i,j}^F = \left| \frac{F_j^i - F^i}{F^i} \right| \tag{6.15a}$$

$$FR_{i,j}^H = \left| \frac{H_j^i - H^i}{H^i} \right| \tag{6.15b}$$

Then, the plate was meshed into a uniform 1×1 mm grid. The probability $P(x, y)$ that damage occurred at a grid node position (x, y) was defined as:

$$P(x,y) = \sum_{i=1}^{n} \sum_{j=1}^{m} FR_{i,j} W_{i,j} \left[r_{i,j}(x,y) \right] \tag{6.16}$$

where $W_{i,j}(r_{i,j}(x, y))$ is the probabilistic weight for the j-th guided wave signal at the i-th sensing path at (x,y), and $r_{i,j}(x, y)$ is the relative distance of the node (x, y) to the actuator and to the sensor associated with the j-th guided wave signal at the i-th sensing path, i.e.:

$$r_{i,j}(x,y) = \frac{d_{i,j}^s(x,y) + d_{i,j}^a(x,y)}{d_{i,j}} - 1 \tag{6.17}.$$

In Eq. (6.17), $d_{i,j}$ is the length of the actuator-sensor line of sight, $d^a_{i,j}(x, y)$ is the node-actuator, and $d^s_{i,j}(x, y)$ is the node-sensor distance, respectively. The relative distance is zero at

any grid node located along the line of sight of the actuator-sensor pair, and it linearly increases at locations away from that path. For illustrative purposes the relative distance r of the sensing path AH is presented in Fig. 6.6.

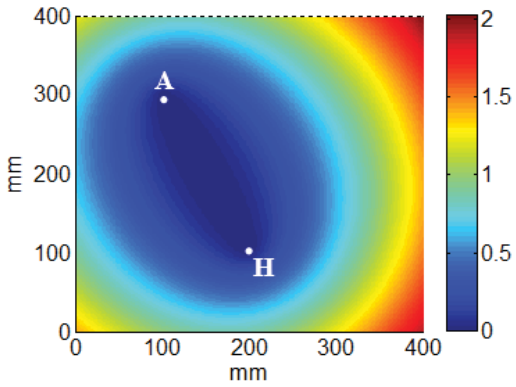

Figure 6.6. Relative distance associated with sensing path AH.

In this study, the probabilistic weight was the Gaussian function:

$$W_{i,j}\left(r_{i,j}(x,y)\right)=\exp\left[-\left(\frac{r_{i,j}(x,y)}{\beta}\right)^2\right] \tag{6.18}$$

where β is a coefficient. The weight is a number comprised between 0 and 1. A weight equal to 1 indicates a point located on the line of sight between an actuator and a sensor, whereas a null weight is assigned to a point far from the sensing path. The constant β was determined by trial and error method and it is dependent on the distance between transducers. A small coefficient reduces the zone of influence of the transducer pair. This means that flaws nearby the travel path across a pair of transducers might go undetected. Conversely, a large β expand the zone of influence of the probabilistic weight. This however, may cause unwanted overlap among different transducers' pairs of the array. Figures 6.7a and 6.7b show the weight relative to path AH for β =0.02 and β =0.04. The difference in the "area of influence" between the two is

evident. In this study, we used β =0.02 as it proved a good trade-off between sensitivity to damage and broad coverage area.

Finally, at each node *(x, y)* of the grid the following discontinuity index *DI* was defined:

$$DI(x,y) = \frac{P(x,y) - \mu_D}{\sigma_D} \tag{6.19}$$

where μ_D and σ_D are the mean and standard deviation value of *P(x,y)*, respectively. The index of Eq. (6.19) is normalized and a threshold is applied such that all the values below the threshold are set to zero. In this study, we arbitrarily set the threshold to 0.7. It must be emphasized that only the A_0 mode propagating along the line of sight of each transducers' pair combination was considered in the analysis and any contribution associated with the scattering, mode conversion, or reflections from the plate edges was ignored. This was done by gating the original window in order to include the first wave packet only in the analysis.

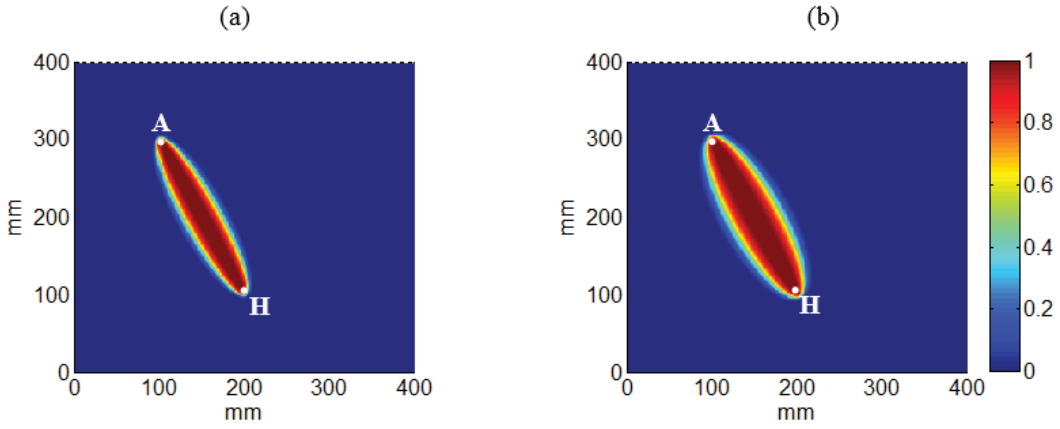

Figure 6.7. Probabilistic weight W for the sensing path AH when (a) β =0.02 and (b) β =0.04.

6.5 RESULTS

Figure 6.8 shows the values of the 90 features F_j^i calculated according to Eq. (6.13). Each inset is relative to a specific actuator-sensor distance and refers to the results associated with the propagation of the 3-cycle tone burst. For each inset, the values of the histograms are constant with the exception of those pairs that are affected by the presence of the notch. By comparing the overall values of the CWT-based features, the histograms demonstrate that damage is located along paths CH and DI (case with distance d = 200 mm), CI (d = 206 mm), BI and EH (d = 224 mm), AI and BJ (d =250 mm), and AJ (d =283 mm). The results demonstrate that the approach is baseline-free provided that part of the array is not affected by damage. In fact, the method does not consider any data taken from a pristine plate. Overall the quantitative values of the feature are higher for the short distance cases. This is expected, as the wave beam attenuates due to geometric expansion and therefore its energy per unit area diminishes.

Similarly to Fig. 6.8, Fig. 6.9 presents the results associated with the propagation of a 5-cycle 100 kHz toneburst. The information provided by this latter simulation is identical to the information provided by Fig. 6.8 and there are no significant differences between Fig. 6.8 and Fig. 6.9. The values of the features are slightly higher, as the ultrasonic energy generated by the 5-cycle toneburst is larger.

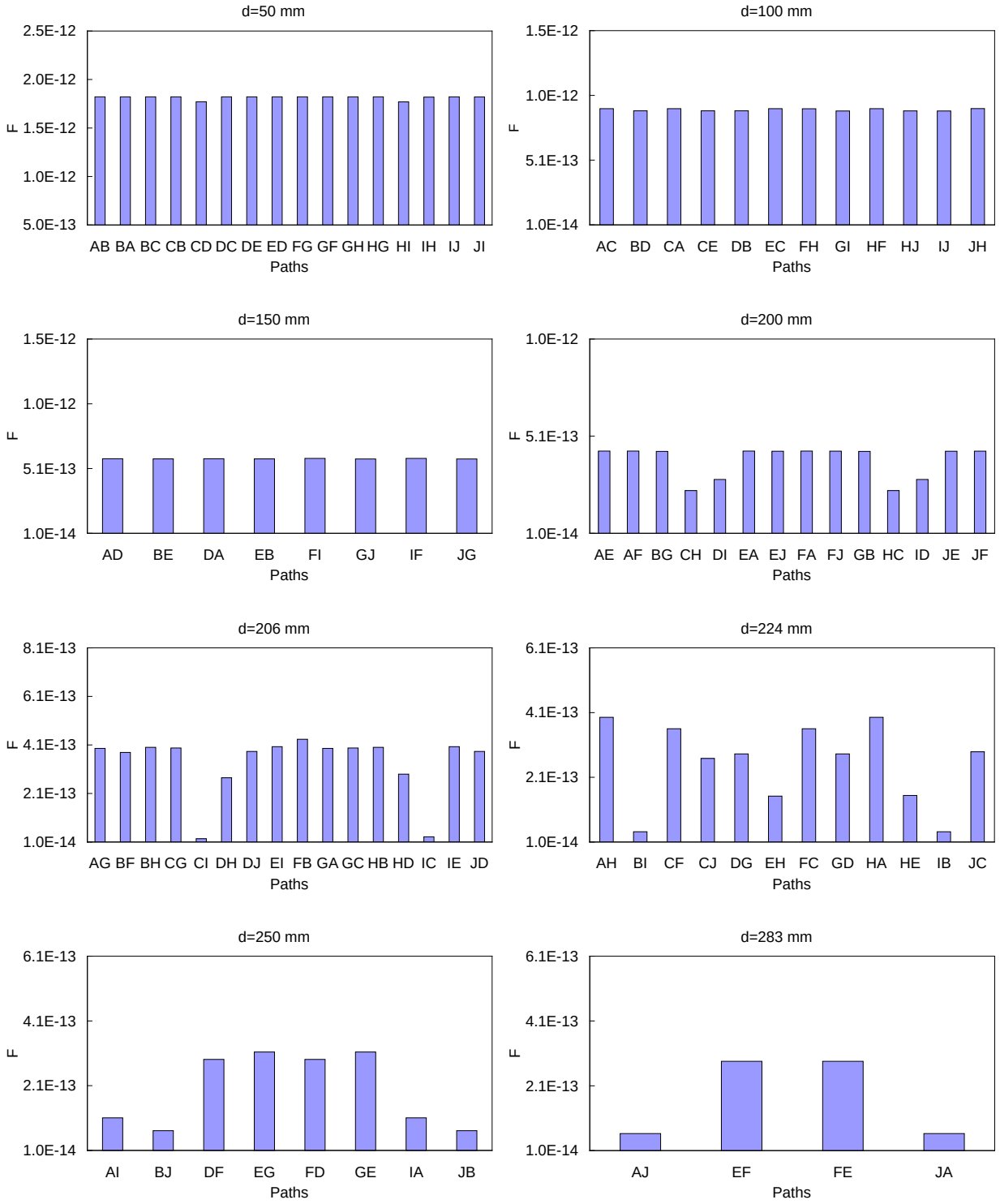

Figure 6.8. Values of the CWT-based feature *F* for each sensing path. The results refer to the 3-cylce excitation source and are grouped according to the actuator-sensing distance *d*.

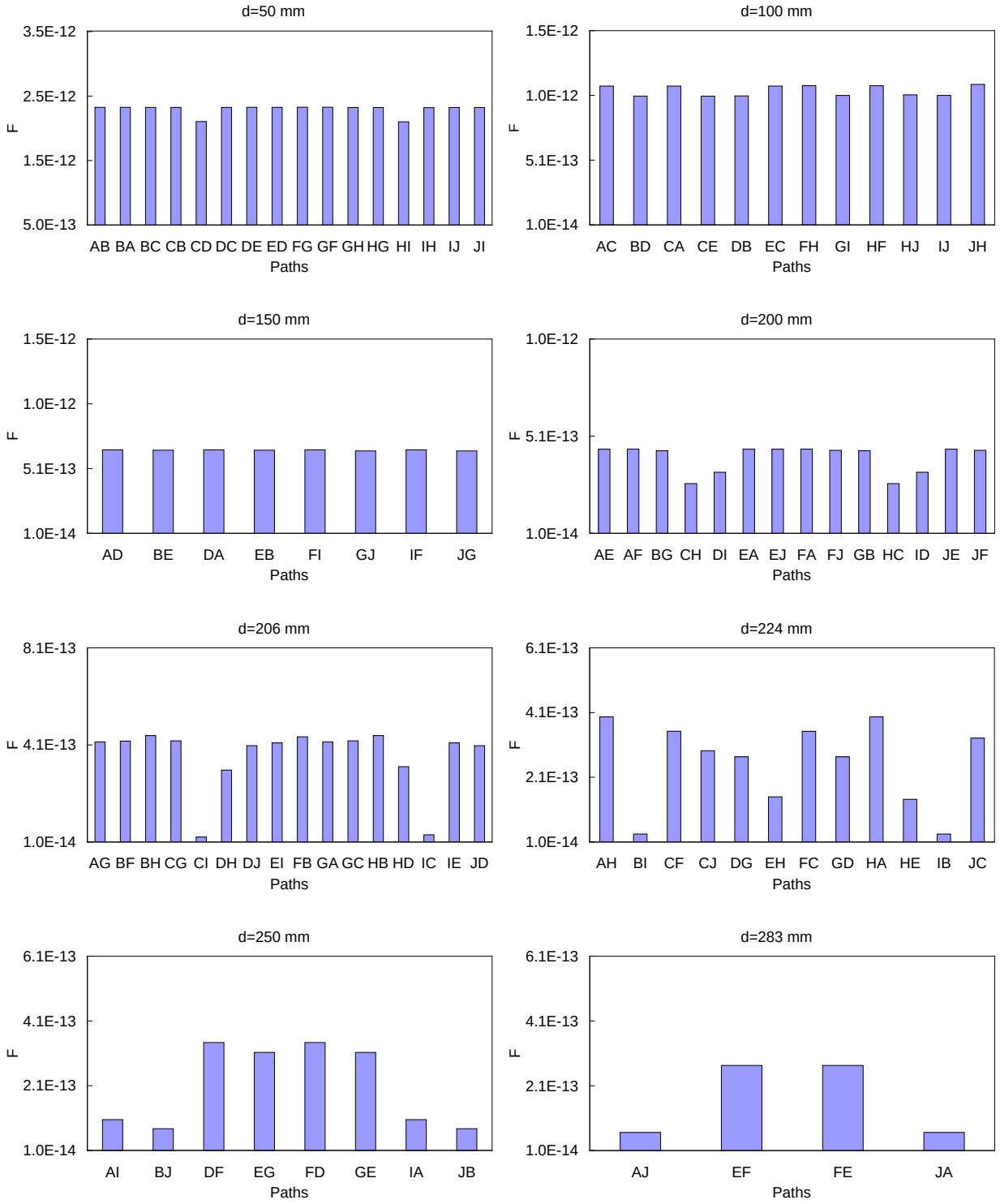

Figure 6.9. Values of the CWT-based feature *F* for each sensing path. The results refer to the 5-cylce excitation source and are grouped according to the actuator-sensing distance *d*.

Figure 6.10 presents the features H_j^i associated with the EMD when the 5-cycle tone burst propagate. The meaning of the 8 insets is identical to those presented in Figs. 6.8 and 6.9. The histograms relative to the three shortest distances are uniform and it can be concluded that there is no defect along those paths. For the remaining cases, certain paths clearly denote the presence of damage. Overall it can be said that the information provided by the EMD-based feature is very similar to that given by the CWT-feature and this adds redundancy to the monitoring algorithm. Not shown here, the data from to the 3-cycle case provide the same information.

The results illustrated above can be synthesized with the plots presented in Fig. 6.11, which displays at each inset the maximum, minimum and average of the 90 features as a function of the distance path. The vertical lines symbolize the difference between the maximum and minimum. The fact that the longest bars are visible at sensing gages 206 and 224 mm implies that some of the paths having those distances were affected the most by the presence of the flaw. This result, however, cannot be generalized but it is the effect of the relative position of the notch with respect to the array. The decay in value is the effect of the signal's geometric attenuation and mode dispersion and it appears to be larger for the CWT-based feature (Figs. 6.11a and 6.11b) over the EMD-based feature. This is because the wavelet-based features included the whole energy of the signal, while the EMD-based feature considered only the first IMF.

The results presented in Fig. 6.8-6.11 indicate the presence of a structural anomaly but they are unable to locate it precisely. The location of damage can be ascertained by applying the probabilistic method described in Section 6.4.2. Figures 6.12a shows the results of the localization algorithm when the CWT-based feature was applied to the 5-cycle excitation case. The contour plot describes the amplitude of the discontinuity index DI as computed by using Eq. (6.19) based on the CWT feature. The black line overlapped to the image represents the position

and the size of the notch. Owing to the threshold set in this study, the contour plot goes from 0.7 to 1 and all the DI below 0.7 were set to zero. The non-zero area is roughly orthogonal to the notch's direction because it is known that the effect of the notch on the wave amplitude is largest when the direction of propagation is perpendicular rather than parallel to the damage. Figure 6.12b shows the value of the discontinuity index as calculated using the EMD-based feature. Overall the image is very similar to Fig. 6.12a.

Real monitoring systems contain always noise which may affect the performance of an algorithm. To test the robustness of the proposed approach against noise, we added random noise to the numerical signals. The noised signal $S^n(t)$ was determined as:

$$S^n(t) = S(t)\left[1 + \eta \times \delta(t)\right] \tag{6.21}$$

where η is the noise level and $\delta(t)$ is white Gaussian noise introduced in Matlab using the know function *awgn*. Figure 6.13 shows the same time waveforms presented in Fig. 6.4 corrupted by noise level equal to 0.2. Similarly to Fig. 6.12, Fig. 6.14 shows the map of the plate in terms of the discontinuity index defined in Eq. (6.20) utilizing the CWT- and EMD-based feature. When compared to Fig. 6.12, Fig. 6.14 does not show any significant difference except for the presence of few sporadic pixels visible for the case of the EMD-based feature (Fig. 6.14b).

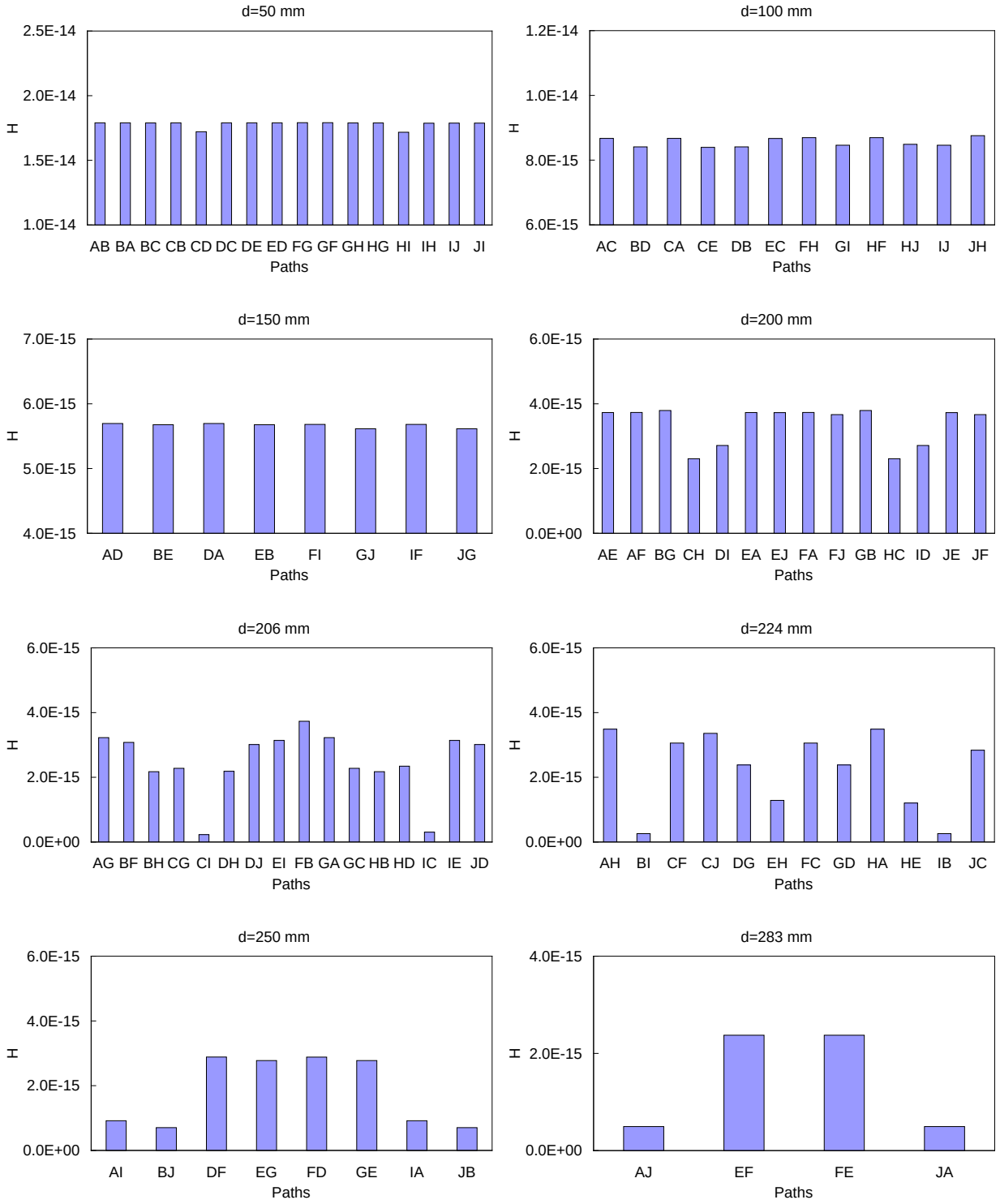

Figure 6.10. Values of the EMD-based feature *H* for each sensing path. The results refer to the 5-cylce excitation source and are grouped according to the actuator-sensing distance *d*.

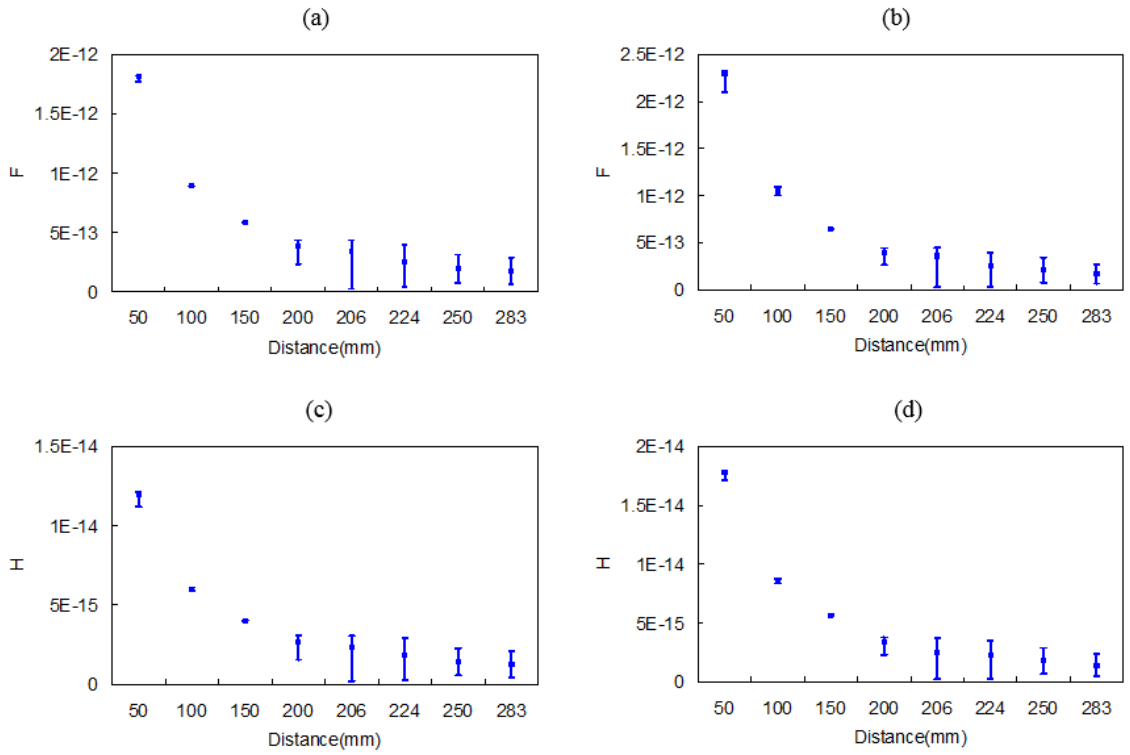

Figure 6.11. The maximum, minimum and average value of features as a function of the sensing path distance. (a) CWT-based feature applied to the 3-cycle excitation. (b) CWT-based feature applied to the 5-cycle excitation. (c) EMD-based feature applied to the 3-cycle excitation. (d) EMD-based feature applied to the 5-cycle excitation.

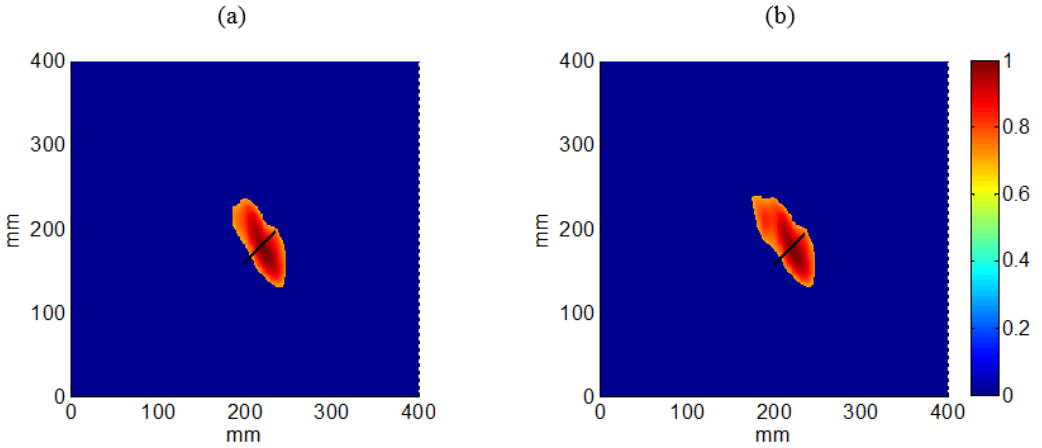

Figure 6.12. Mapping the damage index on the plate using: (a) the CWT-based feature and (b) the EMD-based feature.

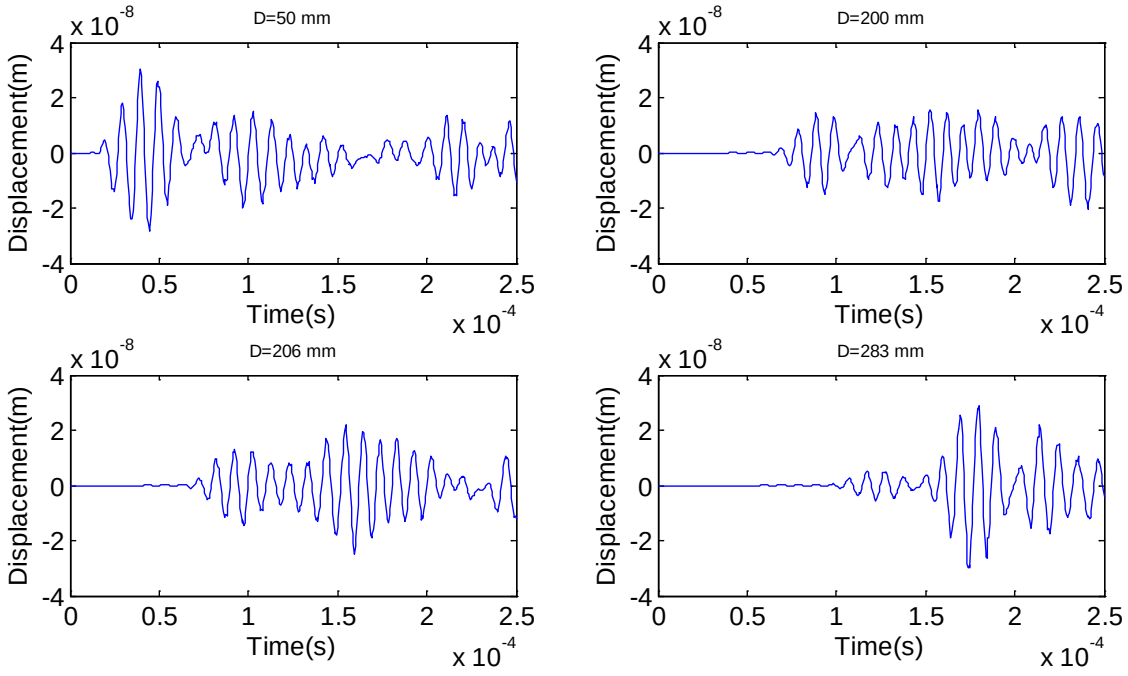

Figure 6.13. Corrupting original data using 20% random noise. Out-of-plane (z) displacements measured at nodes B, E, G, and J, when the 5-cycle tone burst was applied at node A.

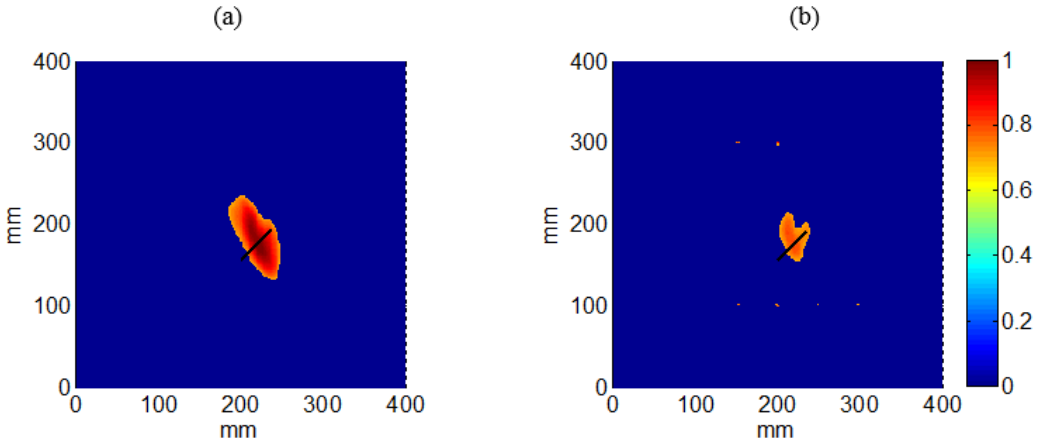

Figure 6.14. Mapping the damage index on the plate when the original data are corrupted with random noise. (a) Results from the CWT-based feature. (b) Results from the EMD-based feature.

7.0 GUIDED ULTRASONIC WAVE IMAGING FOR IMMERSED PLATES

In this chapter, we propose a NDE method for immersed structures based on the propagation of ultrasonic waves induced by means of laser pulses and detected with an array of immersion transducers. In the study, a laser operating at 532 nm is employed to excite leaky guided waves on an aluminum plate immersed in water. An array of immersion transducers is used to record the waves radiating from the laser-illuminated point. The detected signals are processed with an imaging algorithm based on continuous wavelet transform and probabilistic analysis to localize the presence of artificial defects machined in the plate. With respect to the existing imaging methods for plates, the proposed algorithm is pseudo baseline free, because it does not require data recorded from a pristine plate but it requires that only a fraction of the plate is free from defects.

This chapter is organized as follows. Section 7.1 describes a review of the NDE and SHM of plates, and Section 7.2 illustrates the experimental setup. Section 7.3 describes the damage-sensitive feature and the probabilistic method used to map the structure whereas Section 8.4 shows the results. Finally, Section 7.5 includes some concluding remarks.

This chapter was extracted from our published paper entitled “Guided ultrasonic wave imaging for immersed plates based on wavelet transform and probabilistic analysis”.

7.1 INTRODUCTION

One of the recent trends in GUW-based damage detection is the use of an array made of ultrasonic transducers that, operating in actuator-sensor pairs, enable the creation of an image of the structure. There are several imaging algorithms and they can be clustered in three main techniques (Velichko and Wilcox, 2010): the total focusing method, the inverse wave field extrapolation, and the wavenumber algorithms (Yan et al., 2010; Michaels, 2008; Michaels and Michaels, 2007; Clarke and Cawley, 2011; Holmes et al., 2005; Pörtzgen et al., 2007). As stated by Velichko and Wilcox (2010), these methods exhibit similar performance in terms of resolution and, therefore, it is difficult to ascertain which method is better. Some of these algorithms make use of probabilistic analysis, i.e., the image of the structure is reconstructed by estimating the probability that a defect occur at a certain point (Hay et al., 2006; Zhao et al., 2007; Lu et al., 2009; Wang et al., 2009, 2010; Zhou et al., 2011; Moustafa and Salamone, 2012). Some of the proposed imaging algorithms compare signals collected from two structure's conditions: pristine and damaged. This approach may not be feasible in real situations where ultrasonic signals may vary due to environmental and operational variability or in those cases where pristine conditions may not be available. Thus, there is an escalating interest in reference-free imaging methods based on guided waves. Hou et al. (2004) used a set of estimated arrival times as the inputs for tomographic reconstruction. However, the method required numerous transducers. Wang et al. (2004) and Qiang and Shenfang (2009) combined time-reversal theory and a simple imaging method to present a baseline-free method. Miao et al. (2011) tested a time-reversal guided waves method based on probability analysis to identify multiple damages. A baseline free delay-and-sum method was developed by Higuti et al. (2010) and Hall and Michaels (2010) whereas Lee et al. (2012) presented a novel imaging method based on adaptive

source removal. Here, delay-and-sum technique was used to reconstruct the image of a defect by using the waveforms scattered from the damage.

The above studies (Hou et al., 2004; Wang et al., 2004; Qiang and Shenfang, 2009; Miao et al., 2011; Higuti et al., 2010; Hall and Michaels, 2010; Lee et al., 2012) were numerically and/or experimentally validated in dry plates by means of sparse arrays of transducers bonded to the waveguide. In this study, we present instead a pseudo baseline-free imaging approach based on the non-contact generation and detection of GUWs propagating along an immersed plate. We exploit the optical transparency of water to induce broadband stress waves directly onto the plate by means of short duration laser pulses. The waves propagating along the plates leak into the surrounding water and are detected with an array of four ultrasonic immersion transducers. The signals are then processed using a continuous wavelet transform (CWT) and probabilistic analysis to map the plate in search of a few defects artificially machined on the plate. The CWT was considered because it is a well-established method to capture the time-frequency characteristics of dispersive and non-dispersive signals (Kishimoto et al., 1995; Inoue et al., 1996; Gaul et al., 2001) as it was also demonstrated by one of the authors (Rizzo and F. Lanza di Scalea, 2004; Lanza di Scalea et al., 2004; Sale et al., 2011). The novelty of the proposed work is in the combination of the following: 1) use of laser pulses to excite broadband waves in immersed structures; 2) development of a contactless ultrasonic guided waves approach for underwater structures; 3) creation of images using a probabilistic approach. To the authors' best knowledge, the proposed nondestructive approach was never reported before. For example, our work significantly differ from Chen et al. (2010) where a pair of water-proof immersion transducers were attached to a plate surmounted by a 10 mm layer of water and the data were

processed using a probability-based diagnostic imaging method proposed a few years earlier (Su et al., 2009) and based on the waves' time of flight.

7.2 EXPERIMENTAL SETUP

A 8 ns Q-switched Nd:YAG pulsed-laser operating at 532 nm was used to probe an aluminum plate (750 mm × 1605 mm × 2.54 mm) immersed in a tank filled with water. A 1 mm diameter laser beam was delivered to the surface of the plate by means of a mirror and a plano-convex lens with focal length of 100 mm. Four immersion transducers resonant at 1 MHz were used to receive the laser-generated ultrasounds. According to the Snell's law, we inclined them at 15° to maximize the sensitivity to the leaky S_0 mode. Photos of the setup are presented in Figs. 8.1(a)-(c). A foam panel was suspended between the laser and the immersion transducers in order to attenuate the acoustic energy generated by the laser and that travels directly through water. The plate was positioned on four supports and the level of water above the plate was 65 mm. Figure 7.1(d) schematizes the plan view of the setup, showing the position of the supports, and the relative distance of the transducers from the laser-illuminated point. A B-scan system was built *in house* and it consisted of the laser head and the transducers secured to a movable metallic bench plate. The motion of the bench plate was guaranteed by pulleys and belts driven by a National Instrument PXI unit. The bench plate, the laser, and the data storage were controlled by a single LabVIEW program. The ultrasonic signals were sampled at 20 MHz.

Four defects, displayed in Figures 7.2(a)-(d), were machined at the locations schematized in Figure 7.2(e). Defect 1 was a surface notch 1 mm deep, defect 2 and 3 were a through-thickness and a surface hole, respectively, and defect 4 was a surface abrasion that simulated

corrosion. In the study presented in this dissertation, the B-scan was conducted by irradiating 55 points of the plate spaced 20 mm apart and aligned 425 mm from the right edge of the plate. Figure 7.2(e) shows the location of the first and last scanned point. To increase the statistical population of the experimental data, ten laser pulses were generated at each point. The plate was inspected four times to prove the repeatability of the methodology.

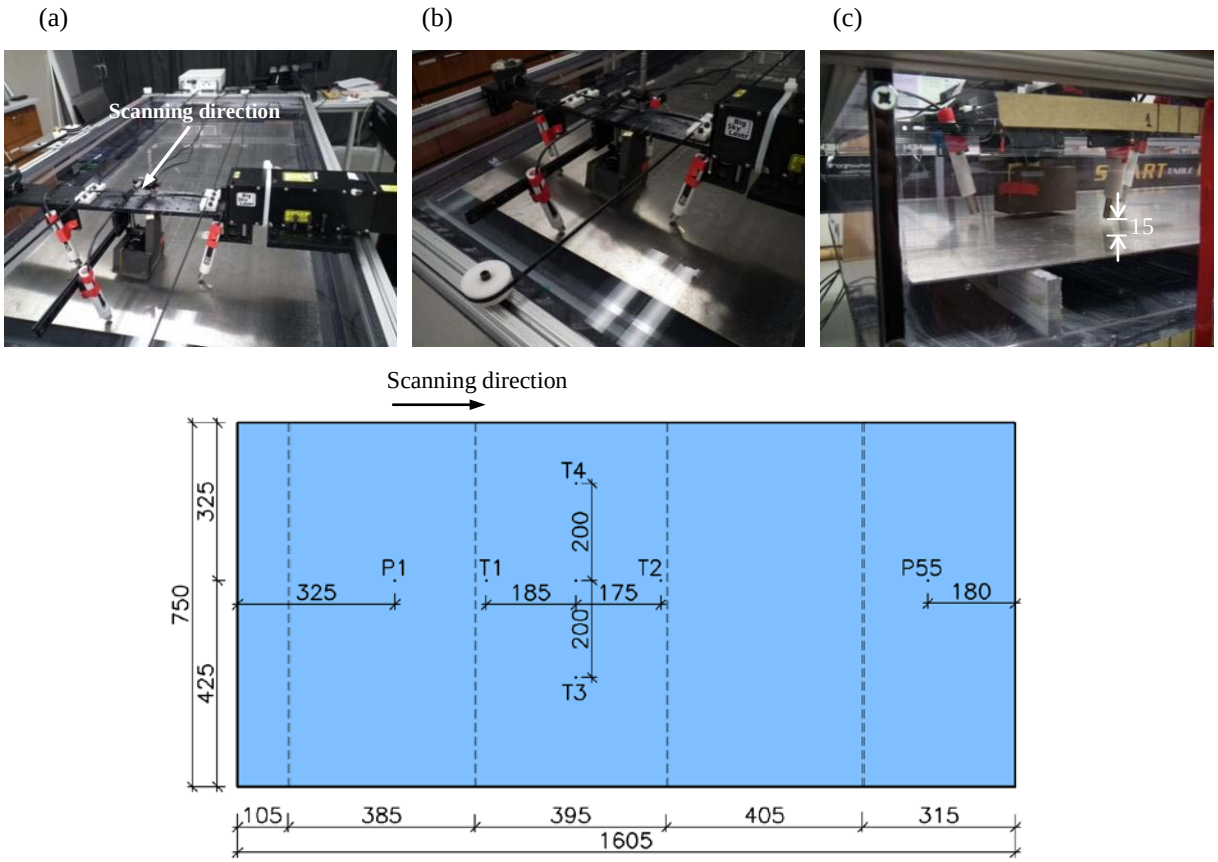

Figure 7.1. Experimental setup. (a) Top view of the scanning system. A steel bench plate supports the laser head and the immersion transducers. (b) Close up-view of the transducers. (c) Elevation view that shows three transducers inclined to maximize the detection of the leaky S_0 mode and the foam suspended from the bench plate. The lift-off distance (15 mm) between the plate and the transducers is indicated. (d) Schematics of the setup. T1, …, T4 denote the transducer. The intersection point of segments T1-T2 and T3-T4 identifies the location of the point on the plate illuminated by the laser pulse. P1 and P55 indicate the first and the last scanning point.

All the quotes and dimensions are in millimeters.

The dispersion curves associated with the propagation of Lamb waves in a dry aluminum plate, i.e. in vacuum, having the same mechanical and geometric properties of the test samples used in this study are presented in Fig. 7.3. When compared to an equivalent dry plate, the speed of the Lamb waves in an immersed plate is similar however, owing to leakage, wave attenuation is larger (Pavlakovic, 1998; Xu et al., 2011). The dispersion equations also predict another wave called quasi-Scholte (q-S) which is a wave propagating along the water-plate interface. The speed of the q-S wave is lower than the A_0 mode, and it is highly dispersive at low frequencies and nondispersive at high-frequency where its speed is very close to the speed of bulk waves in water, i.e., 1.5 km/sec.

Typical time waveforms recorded by the four transducers are shown in Fig. 7.4. As the plate-liquid interface cannot transmit shear stress into water, only the out of plane component of the leaky Lamb waves could be detected. Three wave packets are visible: the first packet at about 40 μsec is the leaky S_0 mode traveling along the line of sight between the scanning point and the corresponding sensor node. The second packet comprised between 50 μsec and 65 μsec is likely generated by the interaction of the leaky S_0 mode with the foam and the subsequent solid-liquid and liquid-air interfaces, whereas the third wave packet beyond 80 μsec is the superposition of the quasi-Scholte mode and the bulk waves propagating from the source through water. The amplitude of the S_0 mode is small due to the predominance of the in-plane motion of the particles associated with its propagation (Chen et al., 2010; Moilanen et al., 2006).

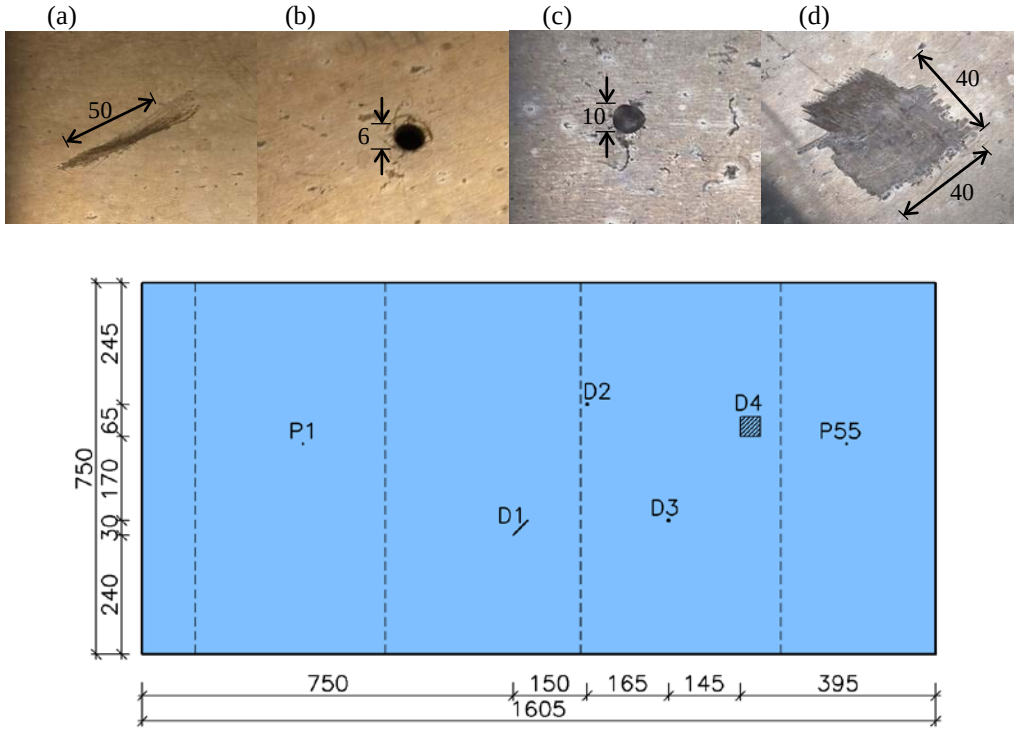

Figure 7.2. Photos of (a) Defect 1, (b) defect 2, (c) defect 3, (d) defect 4. (e) Schematics of the plate, location of the defects, and of the first and last laser-illuminated points. The drawing is in scale and all the quotes are in millimeters.

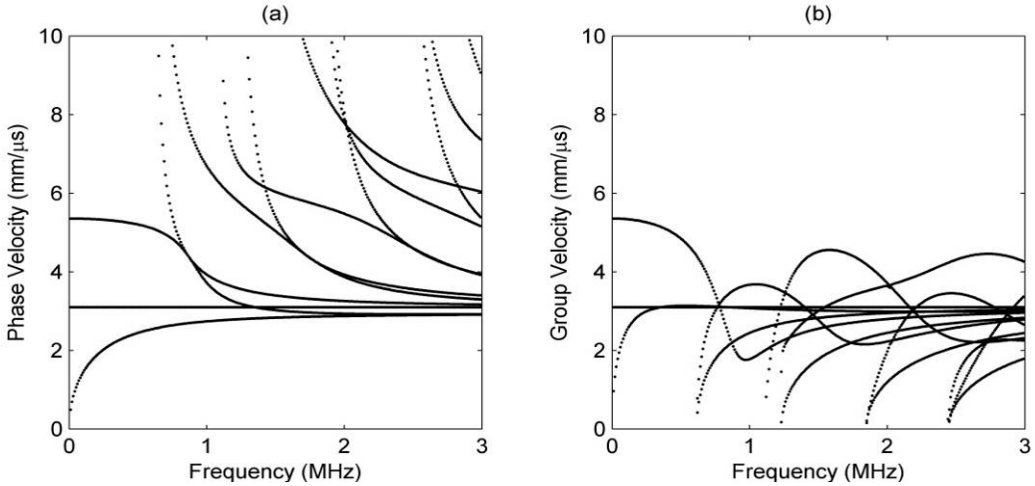

Figure 7.3. Dispersion curves of an aluminum plate 2.54 mm thick in vacuum: (a) phase velocity and (b) group velocity.

The raw signals were then processed using the CWT. We used the Gabor mother wavelet as it provides the best balance between time and frequency resolution, i.e., the smallest Heisenberg uncertainty box (Mallat 1999). The CWT of the waveforms shown in Fig. 7.4 is presented in Fig. 7.5. It should be noted that many signal processing techniques can be used to extract meaningful features from raw signals. For example, an article by Yadav et al. (2012) provides a comprehensive study on the many feature extraction techniques to determine holes in a plate.

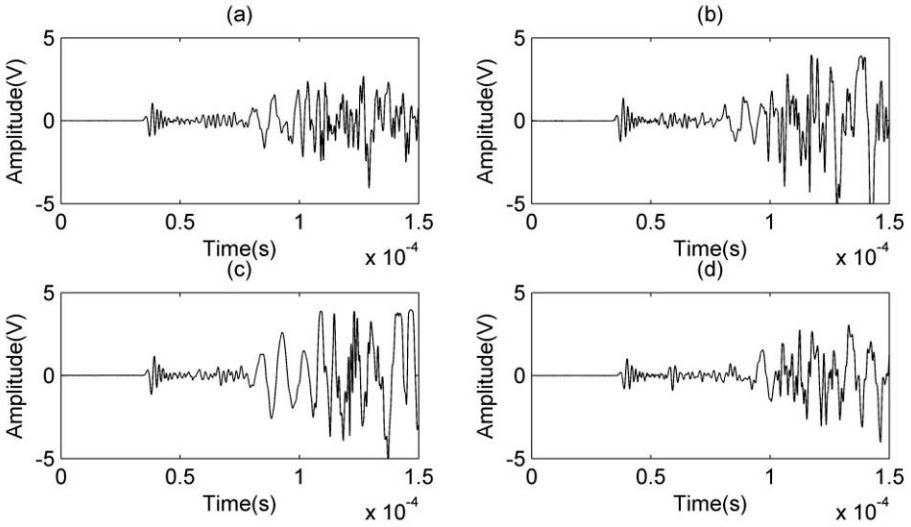

Figure 7.4. Experimental time waveforms at scanning point 16 measured by: (a) transducer 1, (b) transducer 2, (c) transducer 3, and (d) transducer 4.

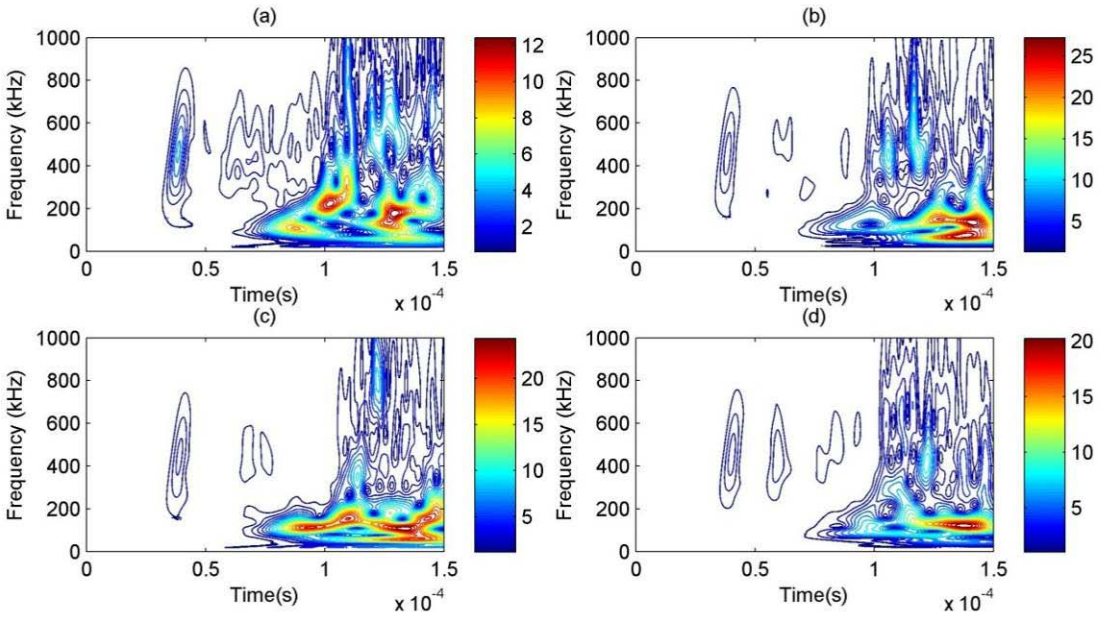

Figure 7.5. Gabor wavelet transform of the experimental signals presented in Fig. 7.4.

7.3 IMAGINING METHOD

In the study presented in this chapter, the leaky S_0 mode only was considered, and any contribution associated with scattering, mode conversion, and reflections from the plate edges or water surface was ignored. As such, any signal processing discussed hereafter was conducted retaining the time window 32-48 μsec of the raw signal.

7.3.1 Sensing paths

Conventionally, imaging methods based on GUWs rely upon the combination of ultrasonic signals transmitted and reflected across many sensing paths. In this study, we defined two kinds of sensing paths: actual and virtual. The actual sensing paths were obtained by considering the four paths that depart from the point on the plate irradiated by the laser, move along the plate,

leak in the surrounding water at an inclination angle of 15°, and reach the transducers. These paths are idealized with solid lines in the schematics of Fig. 8.6. As 55 points of the plate were irradiated, 220 actual sensing paths were available for the analysis. These paths allowed for to monitor a region between the laser irradiated point and a given transducer. To expand the region on interest provided by the inspection system, we defined a *virtual* path as the path that connected two transducers along their line of sight. These virtual paths assumed that one of the transducer acted as a *virtual* actuator. They are idealized as dashed lines in Fig. 7.6. Table 7.1 lists the actual and the virtual sensing paths.

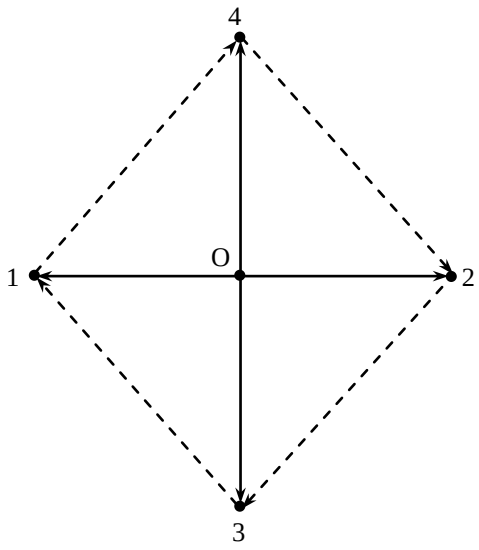

Figure 7.6. Schematics of actual (solid line) and (dashed line) virtual sensing paths at a given scanning point O of the plate illuminated by the laser pulse.

Table 7.1. Actual and virtual paths and corresponding lengths

Sensing path	Actuator–sensor distance (mm)	Label of sensor	Total number of paths
O-1	185.00	1	55
O-2	175.00	2	55
O-3	200.00	3	55
O-4	200.00	4	55
1-4	272.44	4	55
4-2	265.75	2	55
2-3	265.75	3	55
3-1	272.44	1	55

7.3.2 Damage-sensitive feature extraction

As is said earlier, the experimental time waveforms were processed using the CWT. The wavelet energy $\mathbf{E}_{j,k}{}^{i}$ of a transformed signal $\mathbf{W}_{j,k}{}^{i}$ can be written as:

$$\mathbf{E}^{i}_{j,k}(t,\, f) = \left|\mathbf{W}^{i}_{j,k}(t,\, f)\right|^{2}, \quad i = 1,2,3,4 \quad j = 1,2,...,10 \quad k = 1,2,...,55 \tag{7.1}$$

The counter i refers to the actual paths, whereas the indexes j and k refer to the measurements taken at each scanning point and to the location of the scan, respectively. In Eq. (7.1), the variables t and f represent time and frequency, respectively. In the framework of the experimental study presented here, 10 is the number of measurements at each of the 55 scanning points. From the wavelet energy the following scalar:

$$TE^{i}_{j,k} = \sum_{t}\sum_{f}\mathbf{E}^{i}_{j,k}(t,\, f), \quad i = 1,2,3,4 \quad j = 1,2,...,10 \quad k = 1,2,...,55 \tag{7.2}$$

was extracted and it represents the total energy of the wavelet spectrum of the signal.

From the total energy of the recorded signals for each path, we computed the following feature $F_{k}{}^{i}$ for the i-th sensing path associated with the k-th scanning point, which is expressed in terms of the Euclidean length:

$$F_k^i = \left\| TE_{j,k}^i \right\|, \quad i = 1,2,3,4 \quad j = 1,2,...,10 \quad k = 1,2,...,55 \tag{7.3}$$

where $\| \ \|$ represents the Euclidean length.

To predict the CWT-based feature associated with the virtual paths, we used the features defined in Eq. (7.3) to compute the following feature F_k^i:

$$\frac{1}{F_k^i} = \frac{1}{F_k^h} + \frac{1}{F_k^v}, \quad i = 5,6,7,8 \quad k = 1,2,...,55 \quad h,v = 1,2,3,4 \quad h \neq v \tag{7.4}$$

where F_k^h and F_k^v are, respectively, the feature values for the neighboring actual paths in the horizontal and vertical direction.

The features F_k^i defined through Eqs. (7.3) and (7.4) are based on the overall hypothesis that the amplitude of a guided waves decreases due to the existence of a defect between the laser-irradiated point and a transducer; therefore, the value of the feature decreases when it is related to a sensing path with a damage. Based on this hypothesis, we can extract the feature value F_h for a pristine path even when inspecting a damaged structure. In this study, the value F_h was obtained by averaging the values of the CWT-based feature associated with the first ten scanning points. This approach may be considered as pseudo baseline-free since it does not require the inspection of a sound structure but it only requires that a small portion of the whole structure is pristine.

7.3.3 Imaging method

The imaging method is same as the method used in the previous chapter. Only differences are the last number of indexes *i* and *k* which are 8 and 55, respectively.

7.4 RESULTS

Figure 7.7 shows the values of the feature *F* calculated according to Eq. (7.3), relative to the real paths, and computed considering the first out of the ten measurements per scanning point. Each panel is relative to a specific actual path. For each inset, the values of the histograms are expected to be constant with the exception of those paths that are affected by the presence of the defects. Overall, the histograms suggest that damage is located somewhere close to scanning points 23, 24 and transducer 3, and close to points 46-49 and transducer 4. Some elevated values are also visible and they are likely related to the existence of random noise or environmental changes.

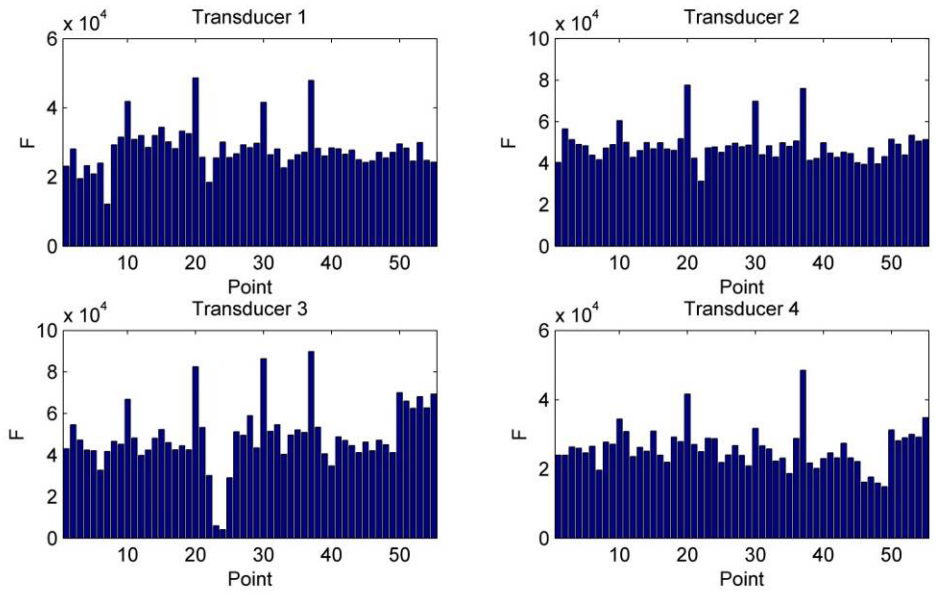

Figure 7.7. Wavelet transform-based feature *F* as defined in Eq. (7.3) as a function of the scanning point. Each panel refers to one actual sensing path. The results refer to the analysis of the first of the ten signals recorded at each scanning point.

To mitigate this problem, we considered the values of the features associated with the ten measurements and we computed their mean at each scanning point. The results are presented in Fig. 7.8; they provide the same information given by Fig. 7.7 in terms of damage location, but no outliers are now visible. Moreover, the presence of some anomalies close to paths O-3 and O-4 is visible. The results presented in Figs. 7.7 and 7.8 demonstrate that the approach is pseudo reference-free, because the method does not consider any data taken from a pristine plate but only from a healthy fraction of it. The results of the imaging method discussed in section 7.4.3 are presented next.

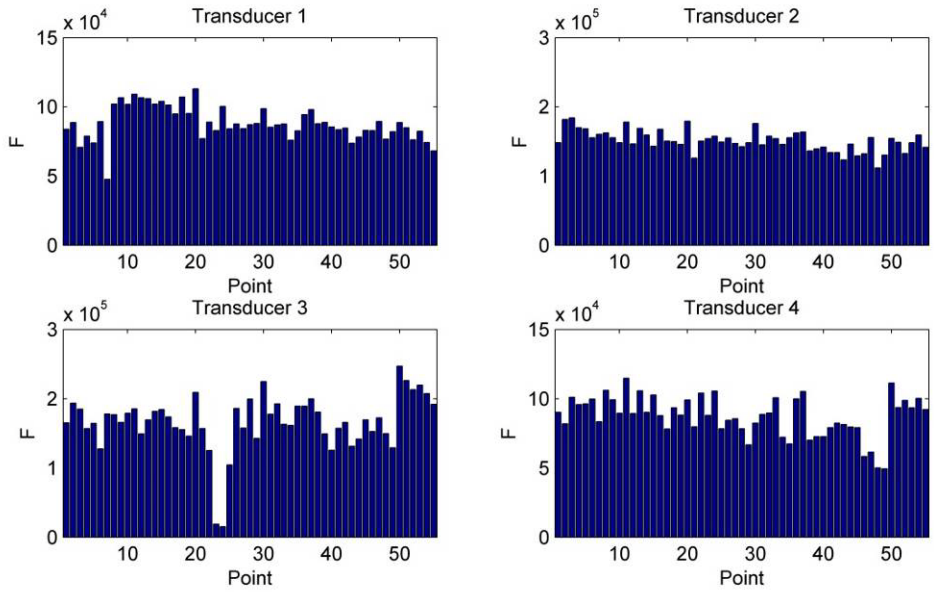

Figure 7.8. Wavelet transform-based feature F as defined in Eq. (7.3) as a function of the scanning point. Each panel refers to one actual sensing path. The results refer to the analysis of the ten signals recorded at each scanning point.

Figure 7.9 presents the image of the plate constructed when a single measurement per scanning point was considered and coefficients β=0.005 and β=0.010 were used. The contour

plot maps the amplitude of the damage index *DI* as defined in Eq. (7.9) when paths O-3 and O-4 are considered. In this and subsequent images, the position of the plate supports is identified by dashed vertical lines, and the position of the defects are denoted by an oblique line, two small dots, and an empty square. The image associated with β=0.010 (Fig. 7.9(b)) is better, because the damage index in the region near to the defects is larger.

The images of the structure constructed using all the actual paths are presented in Fig. 7.10. These images are similar to those in Fig. 7.9. The centerline, which is coincident to the location of the scanning points, is the effect of the superposition of the ellipses associated with the travel paths O-1 and O-2.

Figures 7.11 and 7.12 are equivalent to Fig. 7.9 and 7.10 with the exception that the ten measurements per scanning point were considered in the analysis. The location of defects D1 and D4 can be clearly determined. Interestingly, the presence of the supports does not alter the overall image of the immersed plate. Finally, we achieved better results by considering β=0.010.

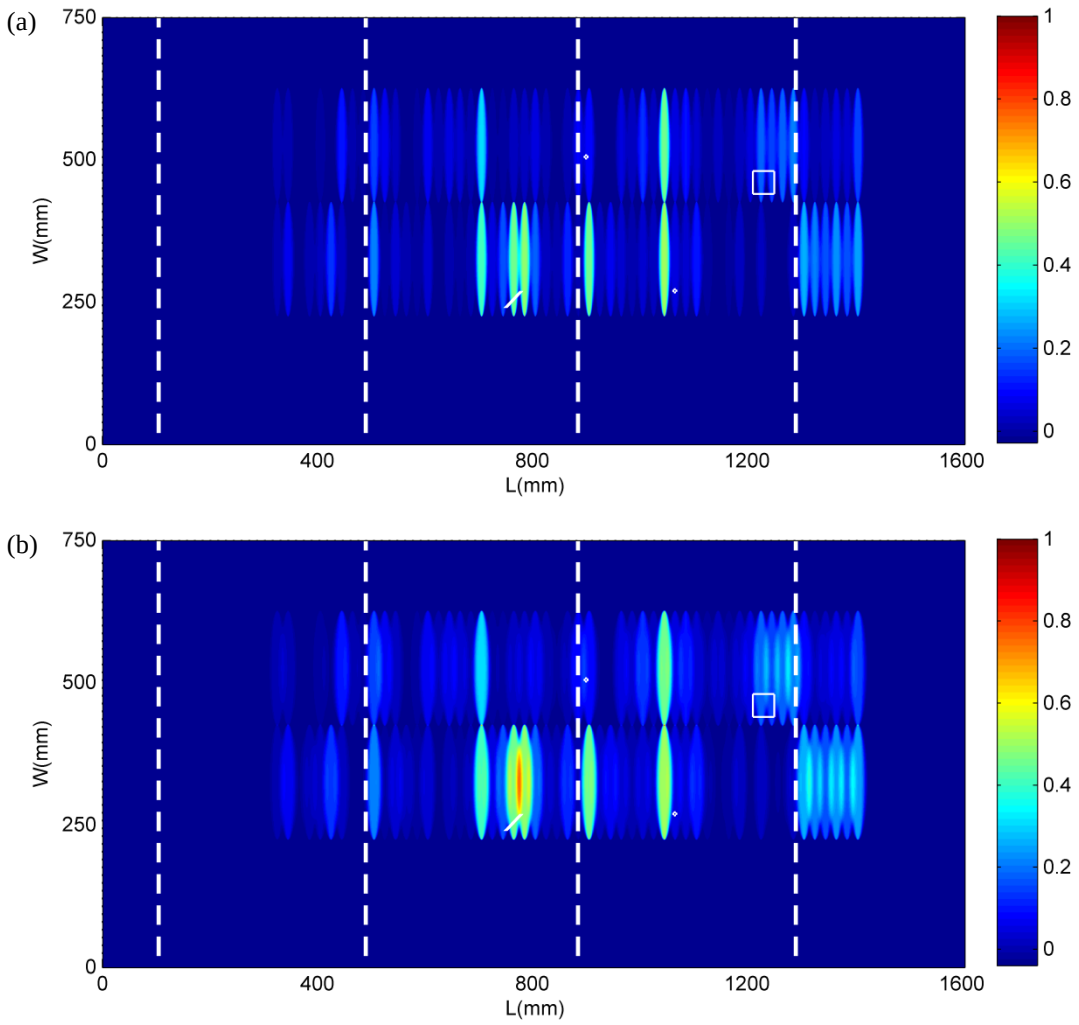

Figure 7.9. Images of the plate constructed using: 1 the first of the ten signals recorded at each scanning point; 2) sensing paths O-1 and O-2; and (a) β=0.005, (b) β=0.010. (The overlapped shapes denote the location of the support and of the defects. The shapes are drawn to scale).

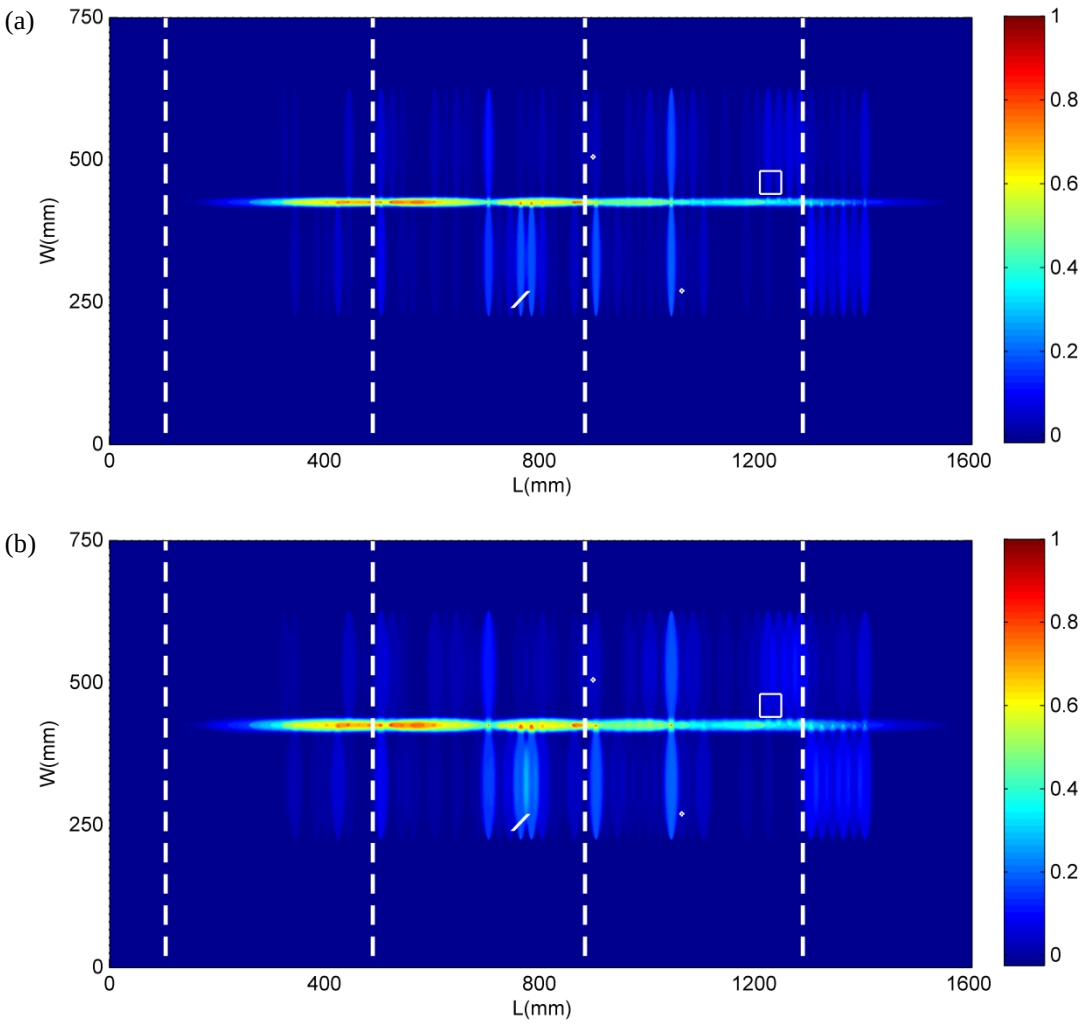

Figure 7.10. Images of the plate constructed using: 1) the first of the ten signals recorded at each scanning point; 2) all four actual sensing paths; and (a) β=0.005, (b) β=0.010. (The overlapped shapes denote the location of the support and of the defects. The shapes are drawn to scale).

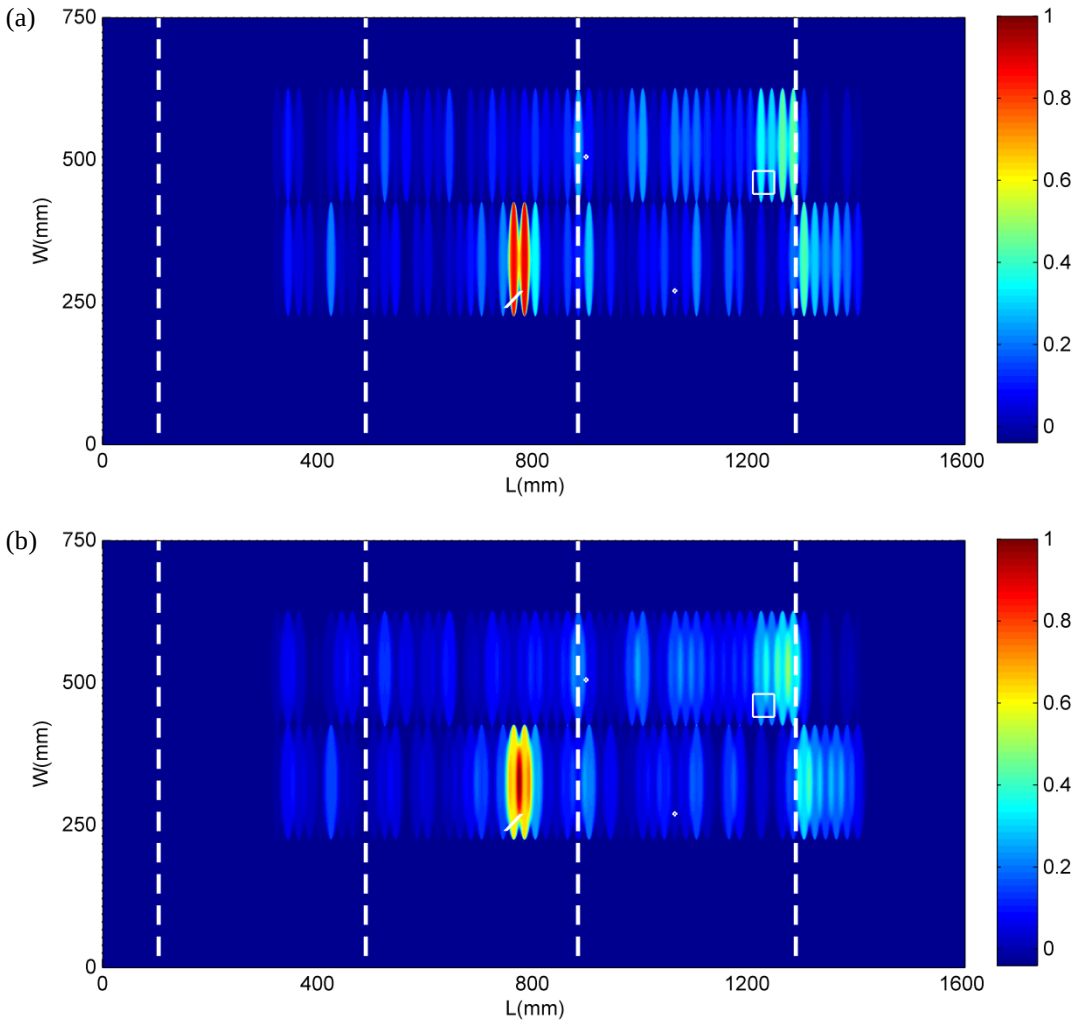

Figure 7.11. Images of the plate constructed using: 1) the ten signals recorded at each scanning point; 2) sensing paths O-1 and O-2; and (a) β=0.005, (b) β=0.010. (The overlapped shapes denote the location of the support and of the defects. The shapes are drawn to scale).

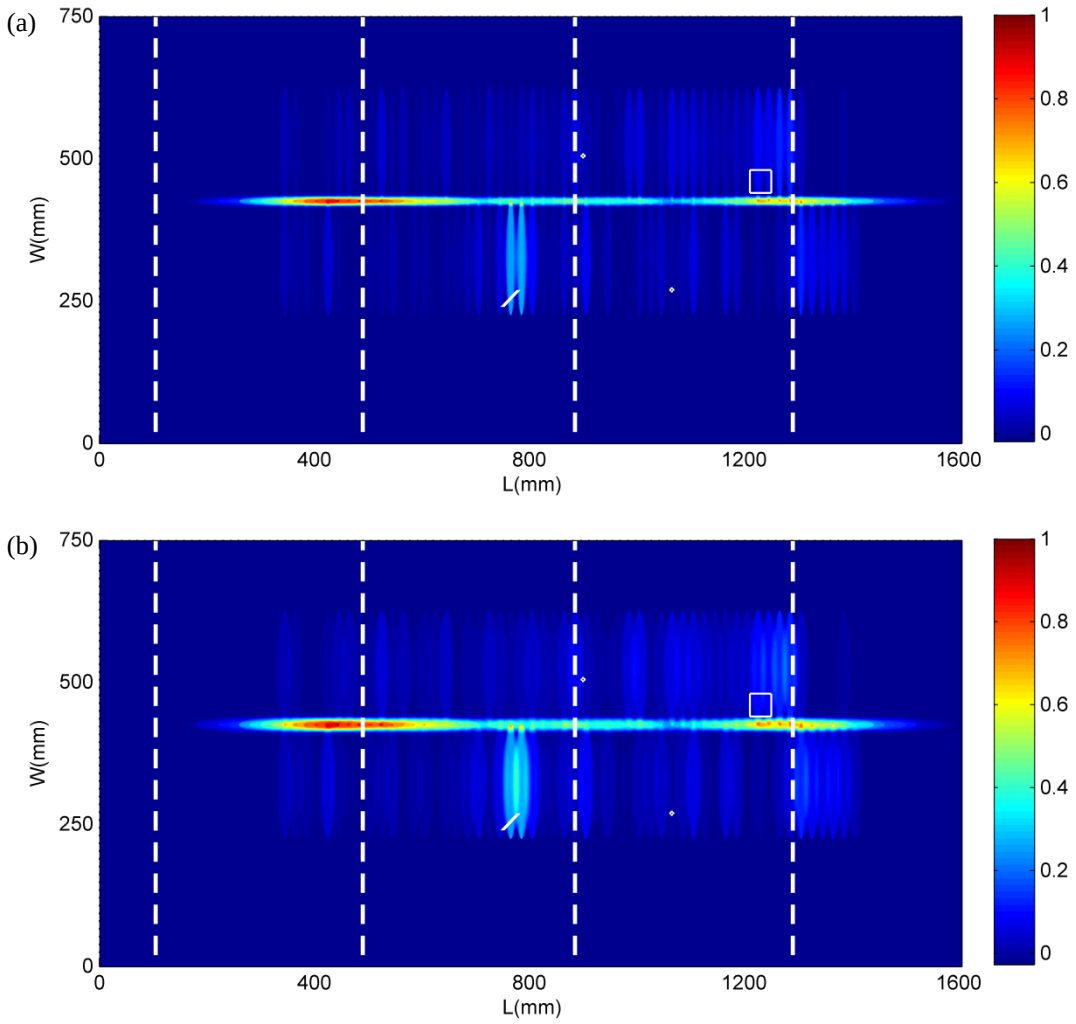

Figure 7.12. Images of the plate constructed using: 1) the ten signals recorded at each scanning point; 2) all four actual sensing paths; and (a) β=0.005, (b) β=0.010. (The overlapped shapes denote the location of the support and of the defects. The shapes are drawn to scale).

In Figs. 7.9-7.12, the construction of the image by means of the damage index was obtained considering the actual sensing paths only. To estimate the damage index in the area of the plate along the oblique directions connecting transducer pairs, we constructed the image of the plate using the actual and the virtual paths listed in Table 7.1. The result is presented in Fig.

7.13 for both β=0.005 and β=0.010 and ten guided wave signals for each transducer. It is clear that the value of damage index in the location of the notch (D1) is very large and also the damage index is significant at the bottom of the square corrosion (D4).

Finally, to investigate the repeatability of the proposed inspection method, we completed three more scans following the same procedure outlined in Section 7.2. The results are presented in Fig. 7.14 which refers to the images constructed using ten measurements per scanning point, sensing paths O-1 and O2, and β=0.010. It is obvious that the results for these three scans are very similar to the ones presented in Fig. 7.11(b). This suggests that the proposed laser-induced GUWs inspection method for immersed waveguides is repeatable.

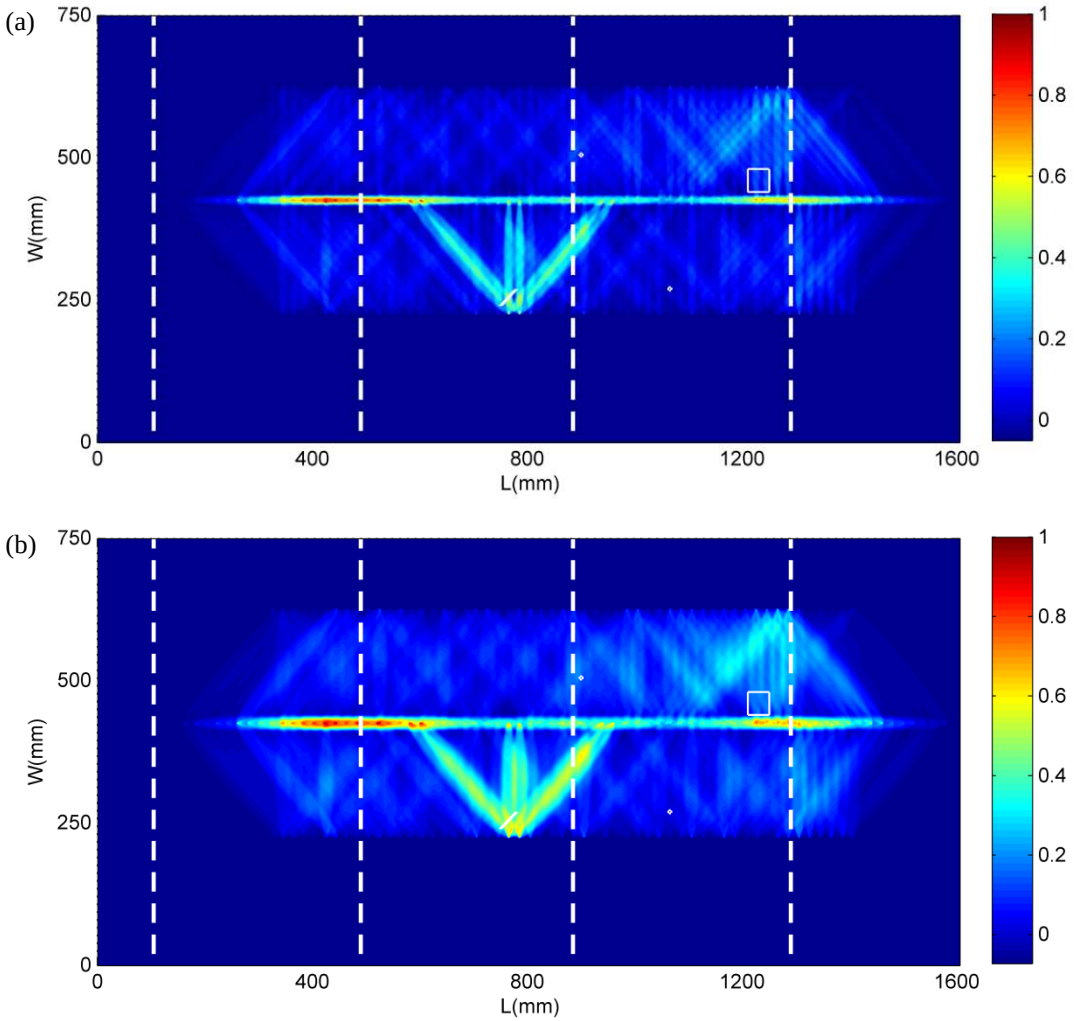

Figure 7.13. Images of the plate constructed using: 1) the ten signals recorded at each scanning point; 2) all four actual and virtual sensing paths; and (a) β=0.005, (b) β=0.010. (The overlapped shapes denote the location of the support and of the defects. The shapes are drawn to scale).

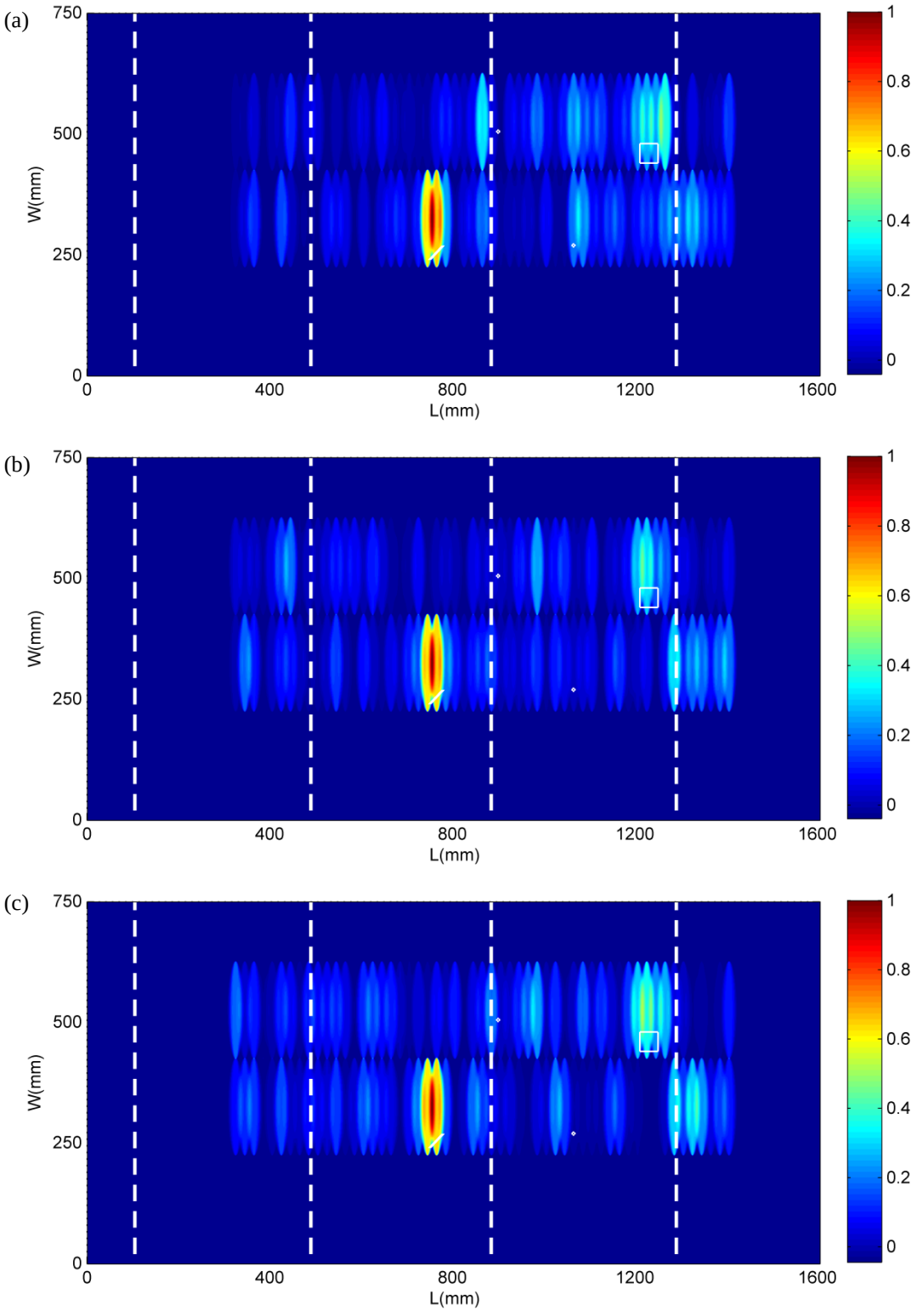

Figure 7.14. Images of the plate constructed using: 1) the ten signals recorded at each scanning point; 2) all four actual and virtual sensing paths; and β=0.010: (a) the second scan, (b) the third scan, and (c) the fourth scan. (The overlapped shapes denote the location of the support and of the defects. The shapes are drawn to scale).

8.0 DAMAGE CLASSIFICATION FOR NONDESTRUCTIVE EVALUATION

In this chapter, we present an experimental study where guided ultrasonic waves were used for the non-contact non-destructive evaluation of an aluminium plate immersed in water. Broadband leaky Lamb waves were generated using a pulsed laser and detected with an array of immersion transducers arranged in a semi-circle. The signals were processed to extract some features from the time, frequency, and joint time-frequency domains. These features were then fed to a supervised learning algorithm based on artificial neural networks to classify the types of defect. We found that the hybrid laser-immersion transducers system and the learning algorithm enable the detection of the defects and their classification with good success rate.

This chapter was extracted from our published paper entitled “Outlier analysis and artificial neural network for the non-contact nondestructive evaluation of immersed plates”.

8.1 INTRODUCTION

The use of guided ultrasonic waves (GUWs) for the NDE of dry structures such as pipes, plates, and rails is constantly increasing. However, little work has been conducted on the use of these waves in wet systems. Na and Kundu (2002) devised a transducer holder to activate flexural cylindrical waves for damage detection in underwater pipes. Mijarez *et al.* (2007) developed a waterproof transmitter and a seawater-activated battery package to monitor the tubular cross-

beam members used in offshore steel structures. Bingham *et al.* (2009) tested a pair of robots crawling along a ship hull and carrying ultrasonic transducers to send and receive guided waves along the hull surface. Sharma and Pathania (2003a,b) investigated the propagation of thermoelastic waves in a plate bordered with inviscid liquids. Sharma and Mukherjee (2015) presented a static non-contact system based on two immersion transducers to generate and detect leaky waves in an immersed plate. Finally, Lee et al. (2014) used a continuous laser and a laser Doppler vibrometry to reconstruct the wave field induced in a plate immersed in water and to compute the velocity-frequency relationship, i.e. the dispersion curves. This non-contact method was also used to demonstrate that the imaging system is capable of damage sizing.

In this chapter, we investigated the ability of a moving non-contact system based on a pulsed laser and immersion ultrasonic transducers (IUTs) to scan an immersed plate using leaky Lamb waves. The waves were generated with short-duration laser pulses, and they were simultaneously detected with an array of five IUTs arranged in a semi-circle. The signals were processed with the Gabor wavelet transform (GWT) to extract some features from the time, frequency, and joint time-frequency domains. The GWT is particularly attractive because it provides the best balance between time and frequency resolution since it uses the smallest possible Heisenberg uncertainty box (Mallat 1999). Moreover, the Gabor wavelet is effective at extracting time-frequency information of broadband signals in plates (Lanza di Scalea et al. 2004, Sale et al. 2011). The features were then fed to a learning algorithm for pattern recognition. The algorithm was an artificial neural network (ANN) used to label four structural conditions. We selected the ANN because it enables the detection and classification of guided waves for the inspection and the health monitoring of dry waveguides such as pipes, rods, beams, and rails (Rizzo et al. 2005, 2007, 2009).

8.2 EXPERIMENTAL SETUP

A Q-switched Nd:YAG pulsed-laser operating at 0.532 μm was used to test a 750 mm × 1605 mm × 2.54 mm aluminum plate immersed in water. A 1 mm diameter laser beam was delivered to the surface of the plate using a mirror and a plano-convex lens with focal length of 100 mm. A tank contained the plate that sat on four polycarbonate supports and surmounted by 65 mm of water. Figure 8.1 shows the setup. Five immersion transducers resonant at 1 MHz were arranged along a semicircle 15 mm above the plate. As traditionally done with conventional wedge transducers, the alignment angle of the detectors was set to maximize the sensitivity to a particular guided mode, in this case the leaky S_0 mode. Owing to Snell's law, $c_p = c_{water}/sin\theta$ where c_p is the phase velocity of the guided wave, c_{water} = 1.5 km/sec is the sound speed in the liquid at room temperature, and θ is the detection angle. In this study θ = 15°.The location of the transducers as well as their distance from the laser-illuminated point is shown in Fig. 8.2. A B-scan system was built in our laboratory to inspect the plate. The system consisted of the laser head and the transducers secured to a moving bench plate. The motion was provided by pulleys and belts driven by a National Instrument PXI unit. A front user interface running under LabVIEW was coded to control the motion of the bench and to select the proper parameters for the generation, detection, and the storage of the ultrasonic waves. The laser irradiated 42 points, hereafter indicated as scanning points. They were linearly spaced by 30 mm and the inspection was conducted five times to evaluate the repeatability of the methodology. To increase the statistical significance of the study, each point was irradiated ten times. This implies that we collected and processed 10 (measurements per scanning point) × 42 (irradiated points on the

plate) × 5 (number of scans) × 5 (number of immersion transducers) = 10500 time waveforms. Figure 8.2 shows the location of the first and the last scanning points, namely P1 and P42.

The following five defects were artificially devised: 1) a 60 mm-long transverse cut; 2) an 80 mm long oblique notch; 3) a 6 mm circular dent; 4) a 10 mm through-thickness hole; 5) a 40×40 mm^2 abraded area to simulate corrosion. The defects are shown in Fig. 8.3a. They were chosen to provide a wide spectrum of structural anomalies. They are also common in the scientific literature as they are representative of defects artificially machined to validate structural health monitoring and NDE techniques for waveguides. The location of the defects on the plate is schematized in Fig. 8.3b, which also marks the position of the scanning points. These points were considered damage-free when the area of the array did not overlap any damage. Based on this assumption 20 out of 42 scanning points were considered damage-free and the ultrasonic waves irradiated from those points were expected to be not affected by the flaw induced in the plate. These points are indicated with the full dots on Fig. 8.3b, whereas the empty circles identify the location of the remaining 22 scanning points.

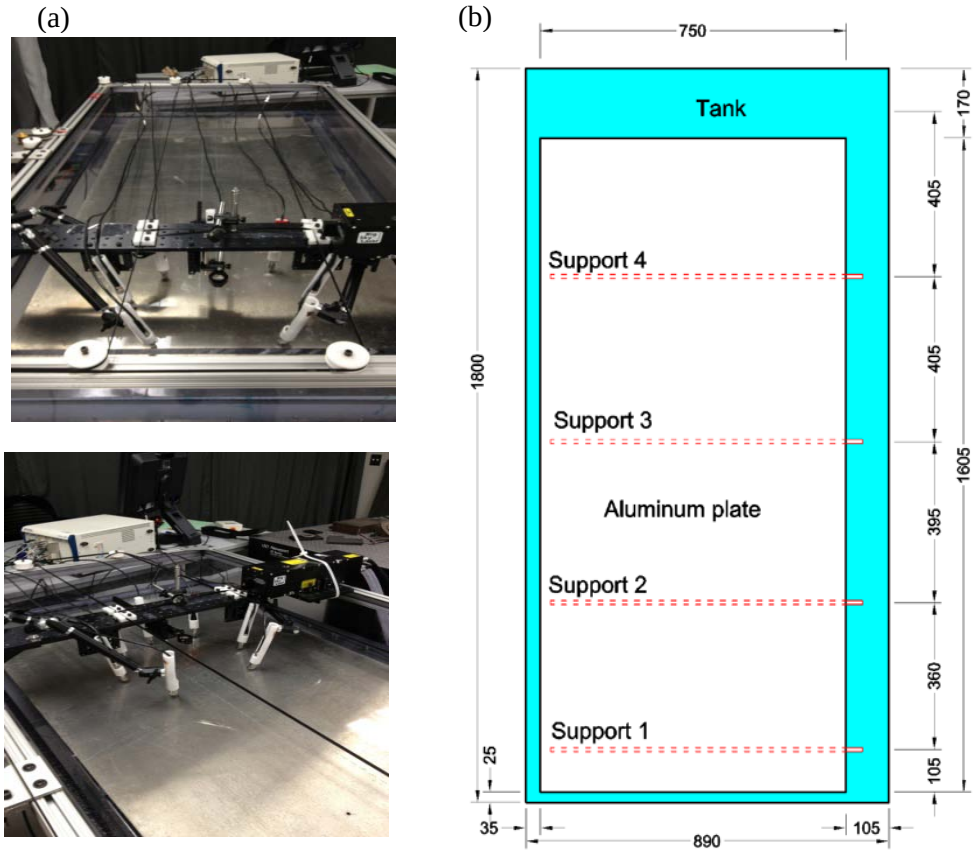

Figure 8.1. (a) Photographs of the experimental setup, and (b) the plan view of the setup. The drawing is on scale and the quotes are in mm.

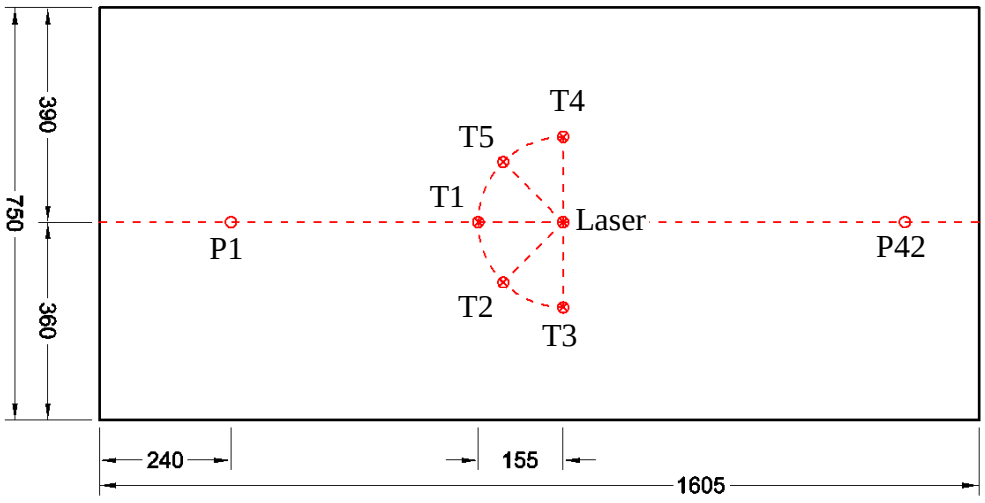

Figure 8.2. Plan view illustrating the position of the transducers (T1-T5). The drawings are on scale and the quotes are in mm.

(a)

(b)

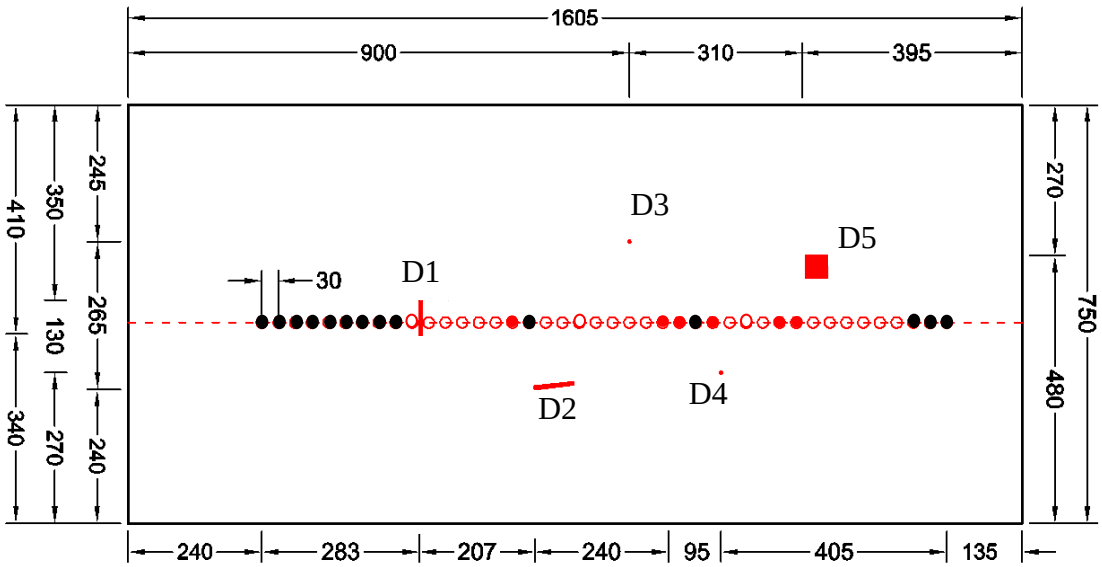

Figure 8.3. (a) Photographs of the artificial defects devised on the plate. D1: 60 mm-long transverse cut. D2: 80-mm long oblique cut. D3: 6 mm in diameter circular dent. D4: 10 mm in diameter through-thickness hole. D5: 40 × 40 mm^2 abraded area. (b) Plan view illustrating the position of the defects as well as scanning points. The full circles identify the points not affected by damage. Among those circles the black circles represent the scanning point used as a baseline data in the outlier analysis.

8.3 SIGNAL PROCESSING

8.3.1 Feature extraction

Figure 8.4 shows the time waveform recorded by each transducer when point 27 was irradiated by the laser during the scan 1. This point was considered defect-free as the area of the array did not overlap with any defect. Three main wave packets are visible: the first packet around 40 μsec is the leaky S_0 mode; the second packet comprised between 50 μsec and 60 μsec is likely the A_1 mode which has a cutoff frequency of 600 kHz; the third wave beyond 80 μsec is the superposition of the quasi-Scholte mode and the bulk wave traveling in water. The A_0 mode is not observed as most of its energy is converted into the quasi-Scholte wave (Cegla et al. 2005). In this study, we analyzed the leaky symmetric mode. As such, any signal processing discussed hereafter was conducted by considering the time window 0–55 μsec only.

Figure 8.5 shows the wavelet transforms of the time-series presented in Fig. 8.4 in the time interval 0–55 μsec. The transform decomposes the original time-domain signal by computing its correlation with a short-duration wave called the mother wavelet that is flexible in time and frequency. The Gabor mother wavelet was used in this study. The transform determines the time of arrival and the frequency content of the propagating modes. The scalograms show the broad frequency content of the leaky S_0 mode and they unveil the dispersion of the symmetric mode that is faster at lower frequencies. From each scalogram, we computed two subplots like the one shown in Fig. 8.6. Figure 8.6a displays the values of the largest wavelet coefficients at each frequency while Fig. 8.6b displays the values of the largest wavelet coefficients at each time.

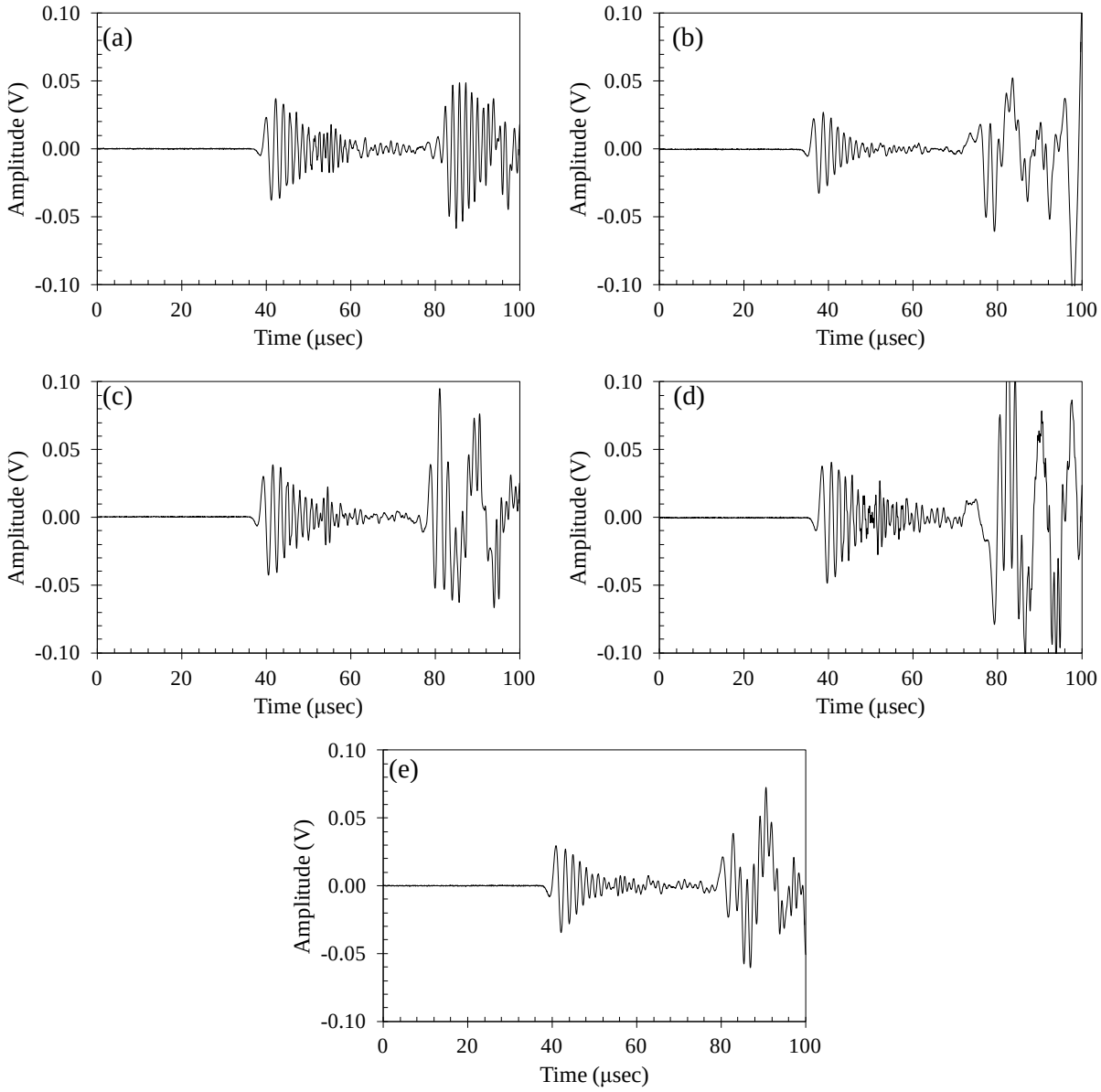

Figure 8.4. Time waveforms generated at the scanning point 27 and sensed by the immersion transducer: (a) T_1, (b) T_2, (c) T_3, (d) T_4, and (e) T_5.

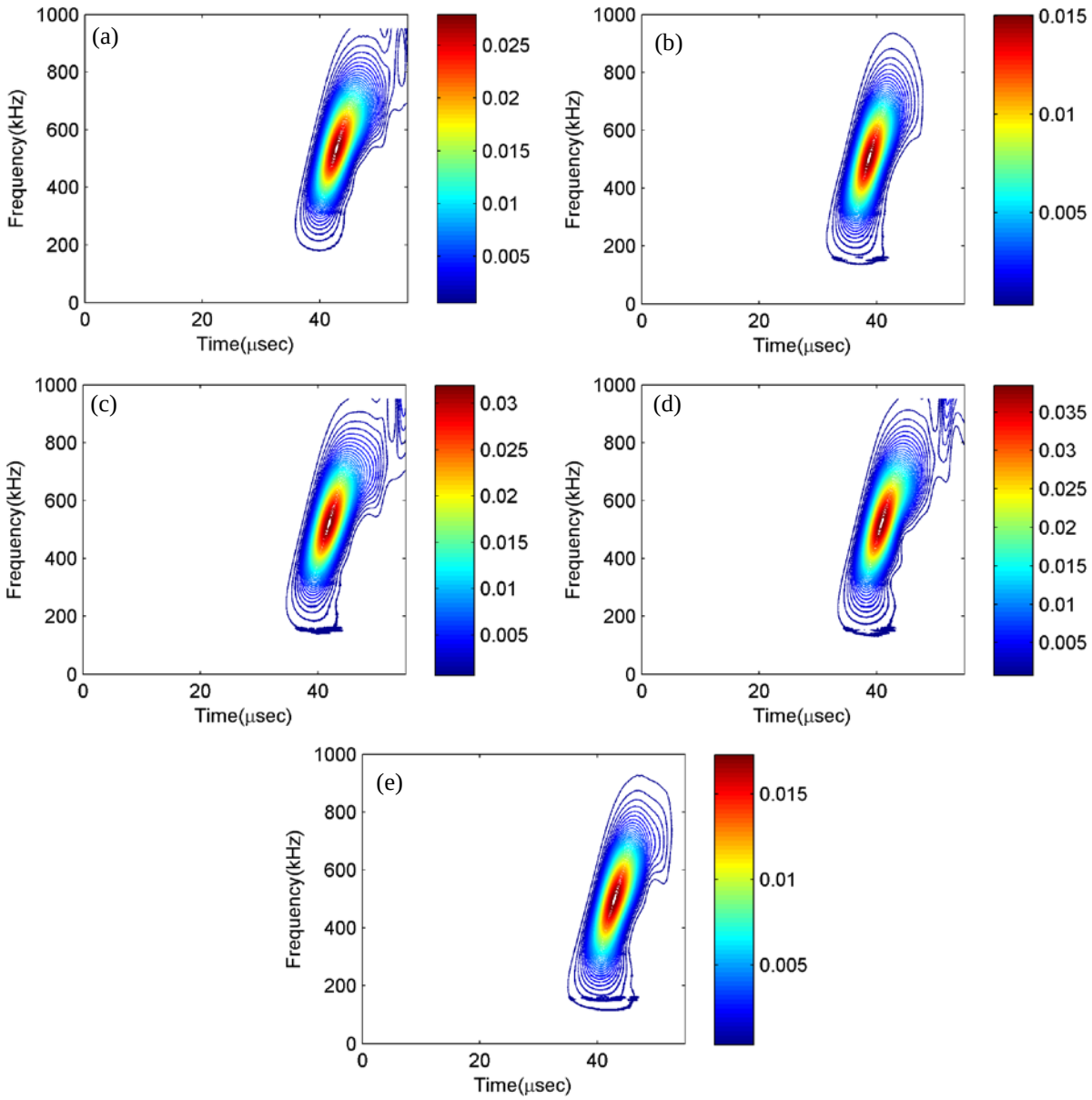

Figure 8.5. Gabor wavelet transform (GWT) scalograms of the time waveforms presented in Fig. 8.4 and relative to the propagation of the leaky S_0 mode.

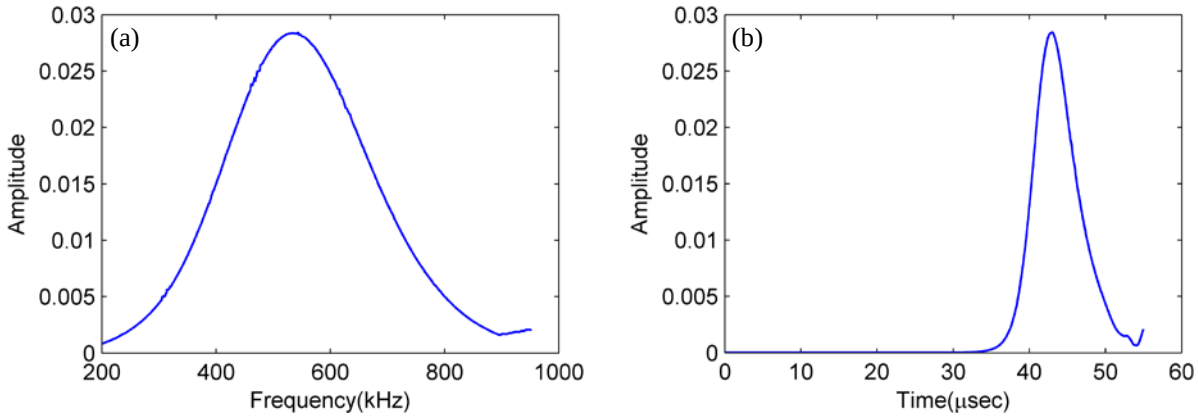

Figure 8.6. Analysis of the scalograms. (a) Plot of the largest wavelet coefficients as a function of the frequency, and (b) plot of the largest wavelet coefficients as a function of the time of arrival. The plots refer to the scalograms presented in Fig. 8.5a, i.e. relative to the time waveforms sensed by the transducer T_1 at the scan point 27.

Leveraging upon previous studies and experience (Rizzo et al. 2005, 2007, 2009), we extracted the eight features listed in Table 8.1. From the time domain, we retained the peak-to-peak amplitude and the root mean square (RMS) which are important information of a signal. From the joint time-frequency analysis, we extracted the scalogram maximum value, the RMS of the curve associated with the largest coefficients in the frequency domain, and the RMS of the curve associated with the largest coefficients in the time domain. In frequency domain, we computed the Fast Fourier Transform (FFT) of the time waveforms to retain the maximum value, the RMS of the bandwidth comprised between 250 and 650 kHz, and the full width half maximum (FWHM) of the same frequency bandwidth. The features can be symbolized as:

$$F_{(i)}^{(k)}, \quad k = 1,2,...,8, \; i = 1,2,...,5 \tag{8.1}$$

where *k* indicates the feature type and the subscript *i* identifies the immersion transducer.

Table 8.1. Features selected in this study.

Feature	Description
1	Scalogram maximum value
2	FFT maximum value
3	RMS of the FFT for the bandwidth comprised between 250 and 650 kHz
4	RMS of the curve associated with the largest coefficients in the frequency domain
5	RMS of the curve associated with the largest coefficients in the time domain
6	Peak-to-peak value of the time window between 0-50 μsec
7	RMS value of the time window between 0-50 μsec
8	FWHM of the FFT for the bandwidth comprised between 250 and 650 kHz

8.3.2 ANN-based method

In order to classify unlabeled signals, we coupled the aforementioned eight features to an ANN able to learn from training samples through iterations. The approach applied here is similar to what done by one of the authors in processing guided waves data associated with dry structures (Rizzo and Lanza di Scalea 2006a,b). A feed-forward back propagation ANN with three layers was used according to the scheme illustrated in Figure 8.7. The input layer received the data vector containing the features, along with the codification of defect types. In this study, we predefined four class labels using a 2-digit (α, β) binary number. The classes (0, 0), (0, 1), and (1, 0) corresponded respectively to the pristine portion of the plate, the transverse cut, and the oblique notch. Owing to their size, the remaining defects were hypothesized to produce the same effect on the guided waves. Thus, they were grouped into the (1, 1) class. The hidden layer of the network processed the data by multiplying the input vectors by weights and adding biases. The results constituted the argument of a transfer function that squashed the output values into a certain range. For the hidden layer ten neurons were used, because the convergence rate was considered acceptable. The hyperbolic tangent sigmoid transfer function:

$$f(x) = \frac{2}{1+e^{-2x}} - 1 \tag{8.2}$$

was employed using the *tansig* function in *MATLAB*® software. This function squashes the output values between –1 and +1. For the input and output layers, we used the *purelin* transfer function which is $f(x)=x$.

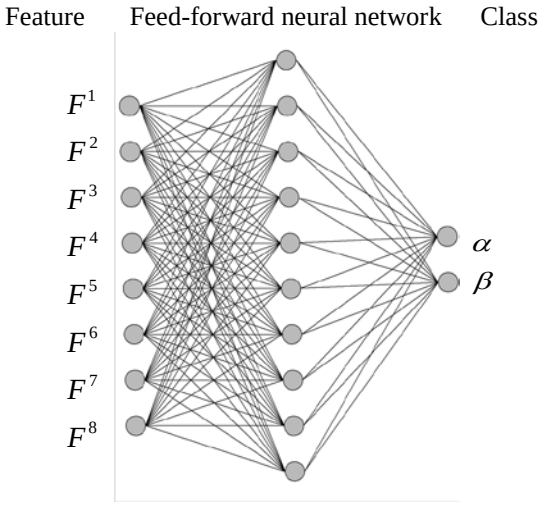

Figure 8.7. Scheme of the neural network used in this study.

To train the network, we used the Levenberg-Marquardt algorithm because of its computational speed (Hagan and Menhaj 1994). The training allowed to determine the weights and biases of each layer. The relationship between the input feature vector **P** and the output vector $\{\alpha\ \beta\}^T$ can be expressed as:

$$\begin{Bmatrix}\alpha\\ \beta\end{Bmatrix}=\mathbf{W}_2\times\left(\text{tansig}\left(\mathbf{W}_1\times\mathbf{P}+\mathbf{b}_1\right)\right)+\mathbf{b}_2 \tag{8.3}$$

where $\mathbf{W}_1$ and $\mathbf{b}_1$ are the weight and bias of hidden layer, respectively, and $\mathbf{W}_2$ and $\mathbf{b}_2$ are the weight and bias of output layer, respectively. The output layer had two nodes, it provided the network outputs, and it compared the outputs with the targets by calculating the mean square error (MSE) as:

$$MSE = \frac{1}{N}\sum_{k=1}^{N}\sum_{j=1}^{m}(y_{kj} - \hat{y}_{kj})^2 \tag{8.4}$$

where N is the number of training samples, m is the number of output nodes, y_{kj} is the desired target, and $\hat{y}_{kj}$ is the network output. If the error was above a certain value, the training process was continued by transmitting the errors backwards from the output layers, and adjusting the weight and biases. If the error was below an established value, the learning process stopped. The training process also stopped when a minimum on the error gradient was reached (Rizzo and Lanza di Scalea 2006a,b).

8.4 RESULTS

The neural network was trained by using 32 scanning points, namely points 1-20 and 31-42, from the first scan. The remaining 178 points were used to test the network. Figure 8.8a shows the success rate of the classifier when the eight features constituted the input vector of the network. The success rate of scan 1 is obviously the highest; this is expected as data from this scan were used to train the network. Interesting the success rates associated with the remaining scan were not identical showing some degree of variability.

The results of labeling the four defect classes are summarized in Tables 8.2 and 8.3. Table 8.2 presents the percentage of data associated to each possible label when the features were used individually: success, false positive, false negative, uncertain, and mislabel. Uncertain data are those outputs that could not be clearly associated to a certain defect class. The column mislabel refers to those classifications where the damage was improperly labeled, i.e. it was assigned to the wrong type of defect. We note that the first damage-sensitive feature provides the

best labeling and it has also the lowest mislabels rate. Table 8.3 presents similar data when the clusters of four features were considered. From this table, we note that the largest success rate and the lowest mislabels are attained by combining the first, second, fourth, and seventh feature. Overall, the results seem to suggest that the use of many features does not improve significantly the success rate of the classifier.

In this study, we also implemented the neural network with two classes, damage and no damage. The success rate results for this analysis are presented in Fig. 8.8b. With respect to Fig. 8.8a, the success rate is very similar.

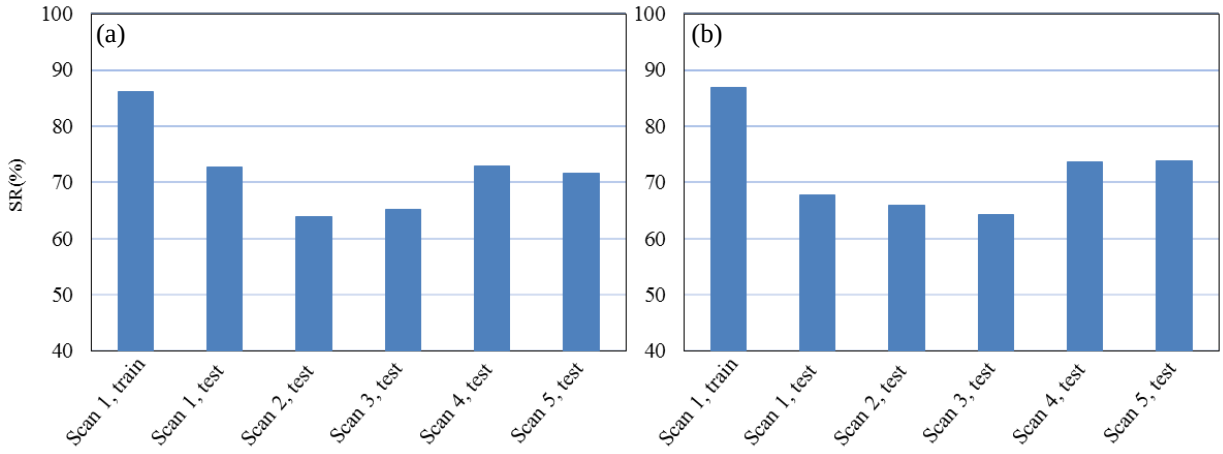

Figure 8.8. Success rate of the ANN when eight features were used together to label: (a) four classes, and (b) two classes.

Table 8.2. Results (%) of the neural network when a single feature was used to label four classes.

Feature	Success	False positive	False negative	Uncertain	Mislabel
1	81.55	0.560	17.30	0.000	0.595
2	78.38	0.476	16.10	0.000	5.048
3	79.31	0.810	16.87	0.143	2.869
4	79.46	0.821	17.33	0.095	2.286
5	77.10	1.012	16.70	0.381	4.810
6	78.36	1.274	16.95	0.274	3.143
7	77.90	1.119	16.87	0.381	3.726
8	78.44	0.024	16.30	0.000	5.238

Table 8.3. Results (%) of the neural network when a combination of four features was used to label four classes.

Features' Combination				Success	False positive	False negative	Uncertain	Mislabel	Features' Combination				Success	False positive	False negative	Uncertain	Mislabel
1	2	3	4	64.55	3.012	10.38	0.119	21.94	2	3	4	5	67.27	2.131	10.12	0.524	19.95
1	2	3	5	63.31	3.702	9.680	0.345	22.96	2	3	4	6	74.33	2.500	11.71	0.060	11.39
1	2	3	6	72.10	2.286	11.69	0.012	13.92	2	3	4	7	70.62	3.131	11.50	0.119	14.63
1	2	3	7	63.36	4.774	9.880	0.405	21.58	2	3	4	8	71.70	3.310	11.04	1.726	12.23
1	2	3	8	72.70	1.048	11.88	0.012	14.36	2	3	5	6	65.79	2.988	9.850	0.048	21.33
1	2	4	5	74.04	1.286	12.62	0.238	11.82	2	3	5	7	70.51	2.786	11.14	0.310	15.25
1	2	4	6	75.57	1.226	12.37	0.286	10.55	2	3	5	8	71.90	2.774	10.94	0.571	13.81
1	2	4	7	76.99	1.560	12.96	0.250	8.240	2	3	6	7	67.31	3.167	10.63	0.060	18.83
1	2	4	8	71.99	1.393	11.81	2.298	12.51	2	3	6	8	71.71	2.774	10.67	1.452	13.39
1	2	5	6	73.90	1.238	12.65	0.393	11.81	2	3	7	8	69.46	3.357	10.62	1.405	15.15
1	2	5	7	71.50	2.500	12.26	0.381	13.36	2	4	5	6	78.20	0.548	13.04	0.060	8.150
1	2	5	8	73.76	1.786	12.61	0.202	11.64	2	4	5	7	74.27	1.500	12.52	0.071	11.63
1	2	6	7	73.15	2.393	12.73	0.643	11.08	2	4	5	8	76.50	0.714	13.18	0.071	9.540
1	2	6	8	74.88	1.714	12.55	2.179	8.680	2	4	6	7	75.44	2.214	12.79	0.345	9.210
1	2	7	8	71.89	1.750	12.02	3.155	11.18	2	4	6	8	73.50	0.857	11.48	4.500	9.670
1	3	4	5	65.40	2.310	11.54	1.571	19.18	2	4	7	8	73.52	1.179	12.42	1.988	10.89
1	3	4	6	70.17	1.250	10.79	0.298	17.50	2	5	6	7	76.40	1.917	13.20	0.012	8.460
1	3	4	7	64.46	2.107	9.580	0.429	23.42	2	5	6	8	74.92	1.702	12.60	1.893	8.890
1	3	4	8	67.00	3.250	9.920	3.345	16.49	2	5	7	8	74.79	1.417	12.58	1.071	10.14
1	3	5	6	69.31	4.024	10.62	0.012	16.04	2	6	7	8	74.01	1.667	12.29	2.214	9.820
1	3	5	7	61.85	3.429	9.630	0.179	24.92	3	4	5	6	67.44	1.476	11.62	0.250	19.21
1	3	5	8	71.29	2.000	9.760	2.679	14.27	3	4	5	7	57.77	4.298	9.510	0.393	28.02
1	3	6	7	62.17	2.405	9.600	0.012	25.82	3	4	5	8	68.82	3.024	10.61	1.869	15.68
1	3	6	8	67.21	3.810	10.73	4.869	13.38	3	4	6	7	59.05	5.048	10.49	0.167	25.25
1	3	7	8	68.99	3.321	9.550	3.500	14.64	3	4	6	8	72.55	2.131	11.58	3.000	10.74
1	4	5	6	79.14	0.595	13.14	0.131	6.990	3	4	7	8	67.96	3.821	10.10	3.583	14.54
1	4	5	7	74.42	2.012	12.68	0.357	10.54	3	5	6	7	62.68	2.512	10.06	0.202	24.55
1	4	5	8	73.56	1.821	12.11	2.393	10.12	3	5	6	8	67.45	3.357	10.79	1.500	16.90
1	4	6	7	77.00	2.024	12.70	0.345	7.930	3	5	7	8	66.82	2.631	10.18	2.357	18.01
1	4	6	8	77.30	0.917	12.38	1.191	8.210	3	6	7	8	63.93	3.762	9.850	4.155	18.31
1	4	7	8	76.50	2.119	12.77	0.500	8.110	4	5	6	7	72.18	1.512	12.49	0.107	13.71
1	5	6	7	71.90	2.536	12.62	0.214	12.73	4	5	6	8	70.14	1.262	12.52	0.333	15.74
1	5	6	8	71.49	1.155	11.99	1.917	13.45	4	5	7	8	68.76	1.976	11.80	3.131	14.33
1	5	7	8	69.65	1.441	11.83	3.619	13.45	4	6	7	8	75.17	2.226	13.27	0.381	8.950
1	6	7	8	71.87	4.107	12.00	2.964	9.060	5	6	7	8	72.74	3.095	12.61	1.524	10.04

9.0 AN IMMERSED PLATE WITH HIDDEN DEFECTS

This chapter presents the results of an experimental study in which guided ultrasonic waves are used for the contactless non-destructive testing of a plate immersed in water. Narrowband leaky Lamb waves are generated using a focused transducer, and are detected with an array of five immersion sensors arranged in a semi-circle. The ultrasonic signals are processed to extract a few damage sensitive features from the time and the frequency domains. These features are then fed to an artificial neural network to identify the presence of hidden defects, i.e. defects devised on the face of the plate not exposed to the probing system.

9.1 INTRODUCTION

Most of the noncontact GUWs-based methods rely on the propagation of the waves along the structure of interest and their leakage into air, where they are detected by air-coupled transducers. A similar approach can be undertaken underwater. In immersed structures the actuation and detection of leaky Lamb waves was demonstrated by Billy et al. (1984) that proposed two inspection schemes to test underwater steel plates of varying thickness (0.5 to 3 mm). In the first scheme a transducer was used in the pulse-echo mode. In the second scheme, a second transducer was positioned at the opposite side of the plate and the backward transmitted ultrasonic signals were recorded. Lamb waves leaking in fluids were also proposed to measure

the properties of composite plates or to extract the dispersion characteristics of the signals (Bar-Cohen and Chimenti 1984, Nayfeh and Chimenti 1998, Banerjee and Kundu 2007, Yu and Tian 2015). Sharma and Mukherjee (2015) used Lamb waves to monitor an immersed plate undergoing accelerated current-impressed corrosion. Two probes were used in a pitch-catch configuration to excite and detect the S_0 and S_1 modes. The former mode is better suited to detect deep notches, while the latter mode is more instrumental at identifying shallow defects. In all the above studies, one or two transducers were used and scan was not performed. The scan of a wet plate was presented by Lee et al. (2014); a Q-switched continuous laser scanned a plate and a laser Doppler vibrometer sensed the ultrasounds. Other studies investigated the propagation of leaky Rayleigh waves (Adler et al. 1984, Bertoni and Tamir 1973, Neubauer 1973) instead of Lamb waves.

In this chapter, we used a focused transducer to generate a toneburst centered at 500 kHz and an array of five IUTs to detect the leaky S_0 mode. A signal processing based on feature extraction and ANN was implemented to detect five artificial hidden defects, i.e. defects devised on a plate's backwall. The novel contribution of the present study with respect to (Bagheri et al. 2014, 2015, Pistone et al. 2013) and with respect to the existing literature lays on the overall methodology, namely: 1) the use of an array of immersion transducers instead of a pair only; 2) the processing of the signals using ANN to classify damage related to an immersed structure; 3) the assembly of a scan system instead of a static probe; 4) the assessment of the setup repeatability; 5) the ambitious detection and classification of hidden defects.

9.2 EXPERIMENTAL SETUP

Figure 9.1 shows the plate tested in this study and the inspection system. The plate, made of aluminum, was 750 mm wide, 1605 mm long, and 2.54 mm thick, and it was immersed in tap water. To avoid sagging, the plate sat on five polycarbonate supports, 13 mm wide. The position of the supports with respect to the plate is schematized in Fig. 10.1b. The actuator consisted of a 12.7 mm focused spherically immersion transducer (Olympus NDT, V303, SU-F), placed 12 mm perpendicularly above the plate. The sensing array consisted of five immersion transducers (Olympus NDT, V303-SU) arranged to form a half-circle as illustrated in Fig. 9.1c. All transducers were resonant at 1 MHz and were secured to a bench plate moved along a straight line by a system of pulleys and belts. This movement was controlled by a National Instruments PXI unit running under LabVIEW. A front user interface was coded to control the parameters for the generation, detection, and storage of the guided waves. A 4 V peak-to-peak (ppk) five cycles, Hann window modulated tone burst with centre frequency equal to 500 kHz was delivered to the actuator. Figure 9.2 shows the wave structure of the first fundamental mode S_0 at 500 kHz for the same plate under dry conditions. It can be seen that the in-plane displacements of the symmetric mode is almost constant across the thickness of the plate whereas the out-of-plane component are largest at the faces of the phases of the aluminum. The leaky waves were detected by the five sensors located 12 mm above the plate and inclined by 15° to maximize the sensitivity to the S_0 mode. The signals were amplified by 60 dB using commercial pre-amplifiers, sampled at 10 MHz with a NI PXI-5105 digitizer, and averaged 100 times to enhance the signal-to-noise ratio.

(a)

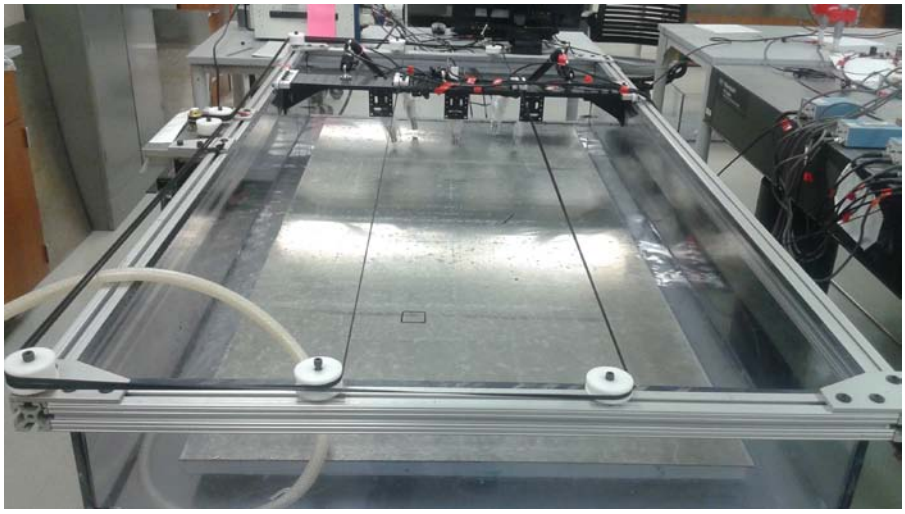

(b)

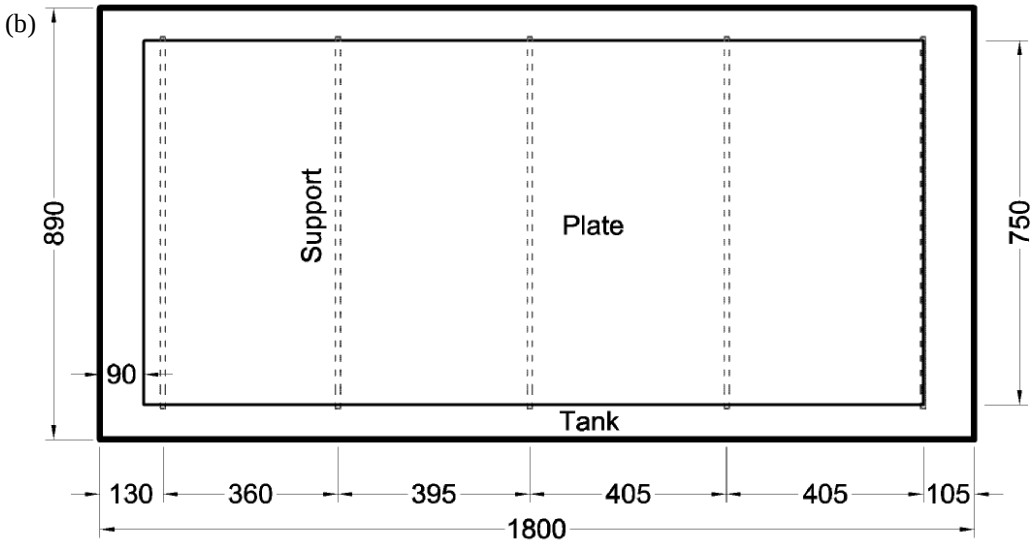

(c)

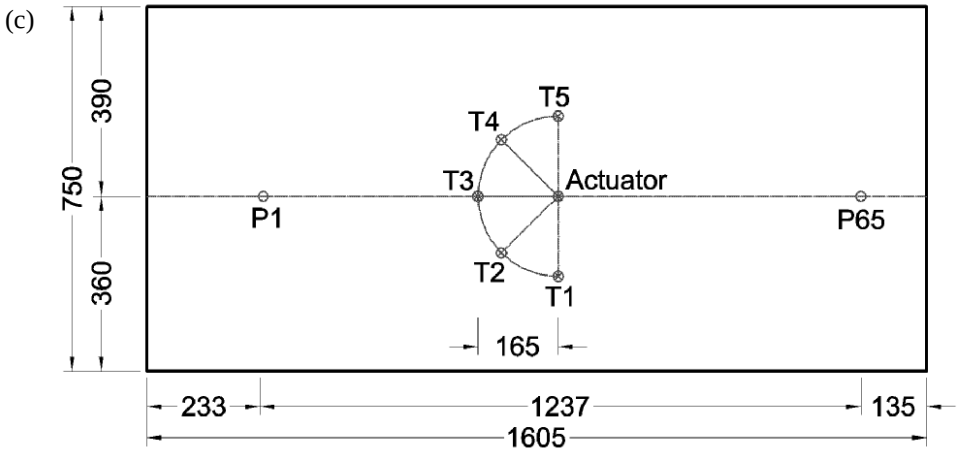

Figure 9.1. Experimental setup: (a) Photo of the overall setup. (b) Plan view of the plate in the tank and of the location of the supports. (b) Plan view of the arrangement of the receivers with respect to the actuator and location of the first and last testing points.

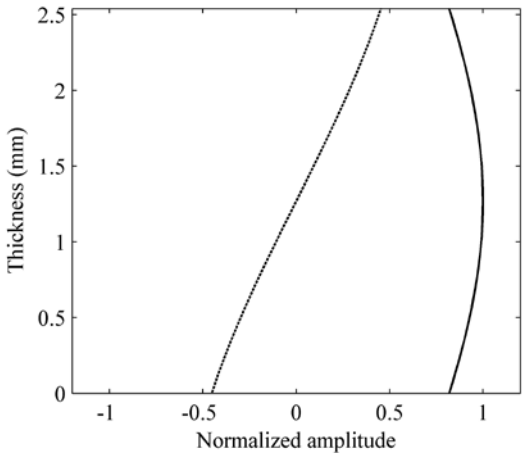

Figure 9.2. Wave structure for 500 kHz on the S_0 mode for the tested plate. The solid and dashed lines represent the in-plane and out-of-plane displacement profiles, respectively.

Five artificial defects were devised. They are shown in Fig. 9.3a and labeled according to the order of the scan direction. The defects were: 1) a 60 mm-long cut perpendicular to the direction of the scan; 2) a 80 mm long oblique notch; 3) a 6 mm dent; 4) a 10 mm through-thickness hole; and 5) a 40 mm × 40 mm abraded area. The latter mimics the presence of corrosion.

To evaluate the ability of the proposed NDE system at detecting hidden defects, the plate was then reversed in order to make the defects invisible to the probe. This was never attempted in our previous studies and was not reported in the cited literature either. Figure 9.3b displays the close-up view photographs of the back side of the plate corresponding to the location of damage. Defects D1 and D2 are barely visible whereas defects D3 and D5 are invisible. The photos in Figs. 9.3a and 10.3b reveal the presence of corrosion pits on both faces of the plate as a result of past exposure to water. Owing to the short duration of the experiment presented in this article, it is safely assumed that the number and the severity of the pits remained constant throughout the experiment.

The test object was inspected at 65 scanning points linearly spaced by 20 mm. The scan was conducted four times to prove the repeatability of the probing system and to increase the testing data for our neural network. This resulted in 65 (testing points) × 5 (receivers) × 4 (scans) = 1300 time waveforms analysed. The relative position of the defects with respect to the scanning points and the plate is schematized in Fig. 9.3c. It is noted here that the location of the supports coincided with the line of sight connecting the actuator to the receivers T1 and T5 at the inspection points 7, 28, and 49. Finally, Table 9.1 lists the points at which the area of the semi-circular array overlapped the defects. The table shows, for example, that only 13 × 4 (scans) = 52 time waveforms were affected by either defects D3, D4, or D5.

(a)

(b)

(c)

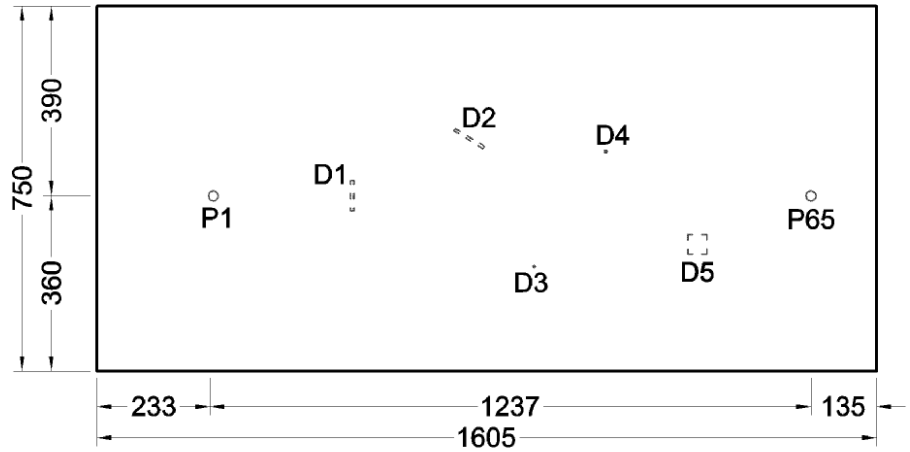

Figure 9.3. (a) Photos of the artificial defects devised on the plate. D1: 60 mm long transverse cut. D2: 80 mm long oblique cut. D3: 6 mm in diameter circular dent. D4: 10 mm in diameter through-thickness hole. D5: 40 mm × 40 mm abraded area. (b) Photos of the reversed are of the plate at the location of the artificial defects. (c) Location of damage. The drawing is on scale and the quotes are in mm.

Table 9.1. Number of damage type for each actuator-sensor path.

Point	T1	T2	T3	T4	T5
1 - 14	0	0	0	0	0
15, 16	0	1	1	1	0
17 - 22	0	0	1	0	0
23, 24	0	0	0	0	0
25 - 28	0	0	0	0	2
29 - 31	0	0	0	0	0
32	0	0	0	2	0
33	3	0	0	2	0
34	3	0	0	0	0
35 - 41	0	0	0	0	0
42	0	0	0	0	4
43 - 46	0	0	0	0	0
47, 48	0	0	0	4	0
49 - 51	5	0	0	0	0
52	0	0	0	0	0
53 - 56	0	5	0	0	0
57 - 65	0	0	0	0	0

9.3 RESULTS

9.3.1 Feature Extraction

The panels on the left of Figure 9.4 show the time waveforms recorded by the five sensors during the first scan at the testing point 5. According to Table 9.1, this point was damage-free. To ease the direct comparison among the ultrasonic traces, the scale of the amplitudes was kept identical. The main packet visible between 50 and 70 μsec is the leaky S_0 mode. The waveforms' amplitudes are similar although the ppk associated with the transducer 4 is about 25% larger than transducers 1 and 2, and about 10% higher than transducers 3 and 5. This is probably due to a slight misalignment of the sensor. We also hypothesize that the wave pattern created by the actuator had some form of directivity, i.e. was not truly omnidirectional. The wave packets tailing the leaky S_0 mode are the leaky A_0 mode, the quasi-Scholte wave

(Bagheri et al. 2014, Pistone and Rizzo 2015) propagating at the solid-liquid interface, and the leaky S_0 mode reflected from the water surface.

The panels on the right column of Fig. 9.4 show instead the time waveforms recorded at the testing point 15 when the damage D1 was along the line of sight between the actuator and the transducer 3, and was expected to affect also T2 and T4. The waveforms' amplitude associated with these transducers, i.e. Figs. 9.4g-9.4i, is visibly smaller than the corresponding amplitudes presented in Figs. 9.4b-9.4d.

In order to process the ultrasonic data we extracted three features relative to the leaky S_0 mode. Therefore, we considered the time gate 50 – 70 μs. The features are symbolized as:

$$F_{(i)}^{(k)} \qquad (k=1, 2, 3;\ i=1, 2, 3, 4, 5) \qquad (9.1)$$

where k indicates the feature type and i identifies the sensor, and they are the signals' ppk and energy, and the maximum amplitude of the signals' Fourier transform (Table 9.2). The energy was computed as the product of the squared signal multiplied the sampling period.

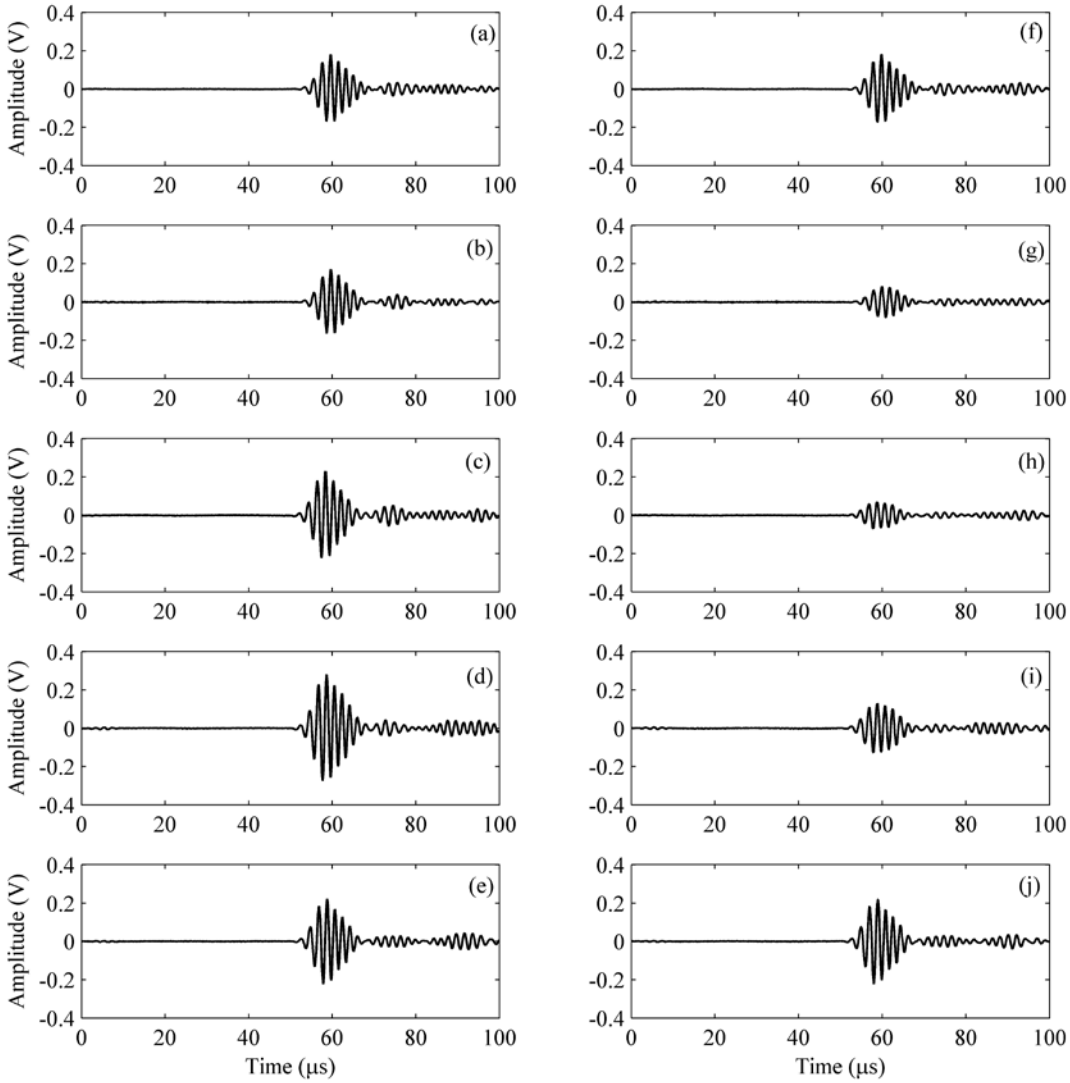

Figure 9.4. Time waveforms measured during the scan 1 by the transducers (a) T1, (b) T2, (c) T3, (d) T4, and (e) T5 at the damage-free testing point 5. Time waveforms measured during the scan 1 by the transducers (f) T1, (g) T2, (h) T3, (i) T4, and (j) T5 at the testing point 15.

Table 9.2. Features selected in this study for damage classification.

Feature	Description
$F^{(1)}$	Peak-to-peak value of the waveform between 50-70 μsec
$F^{(2)}$	Energy of the waveform between 50-70 μsec
$F^{(3)}$	Maximum value of FFT of the waveform between 50-70 μsec

Figure 9.5 shows the first feature as a function of the inspection point from the four scans. To ease the comparison among the five panels, the scale of the ordinate axis is kept the same. The ppk amplitude associated with the first transducer (Fig. 9.5a) is constant with a few exceptions localized at points 7, 21, 28, and 49. The latter point is where the scatter is farther from the average feature value. Table 9.1 indicates that the simulated corrosion was located between the actuation point 49 and the transducer T1. The remaining three scatters are false positives because they flag the presence of damage when in reality it is not. Because these scattered data are consistent throughout the four scans, we believe they were induced by the presence of the base supports located, as was said earlier, at points 7, 28, and 49. We also hypothesize that point 21 might have been affected by the presence of a localized gas bubble or corrosion pit. The largest deviation of the amplitudes is visible in Fig. 9.5c that refers to the transducer T3. As noted in Fig. 9.4h, the transverse notch reduces the ppk amplitude of the wave traveling along the A-T3 path. It is interesting to note that the value of the feature $F_{(3)}^{(1)}$ measured at point 14 is significantly above the average. This occurred because the actuation point was in between the notch and the receiver T3 but very close to the notch. As such the wave packet detected by the sensor was the S_0 mode traveling from the actuator to the receiver combined with the same mode reflected from the damage. The notch partially affected paths A-T2 and A-T4 as shown in Figs. 9.5b and 9.5d. This confirms what listed in Table 9.1 and what

observed in Figs. 9.4g and 9.4i. Overall, it can also be said that the outcomes from the four scans were very repeatable.

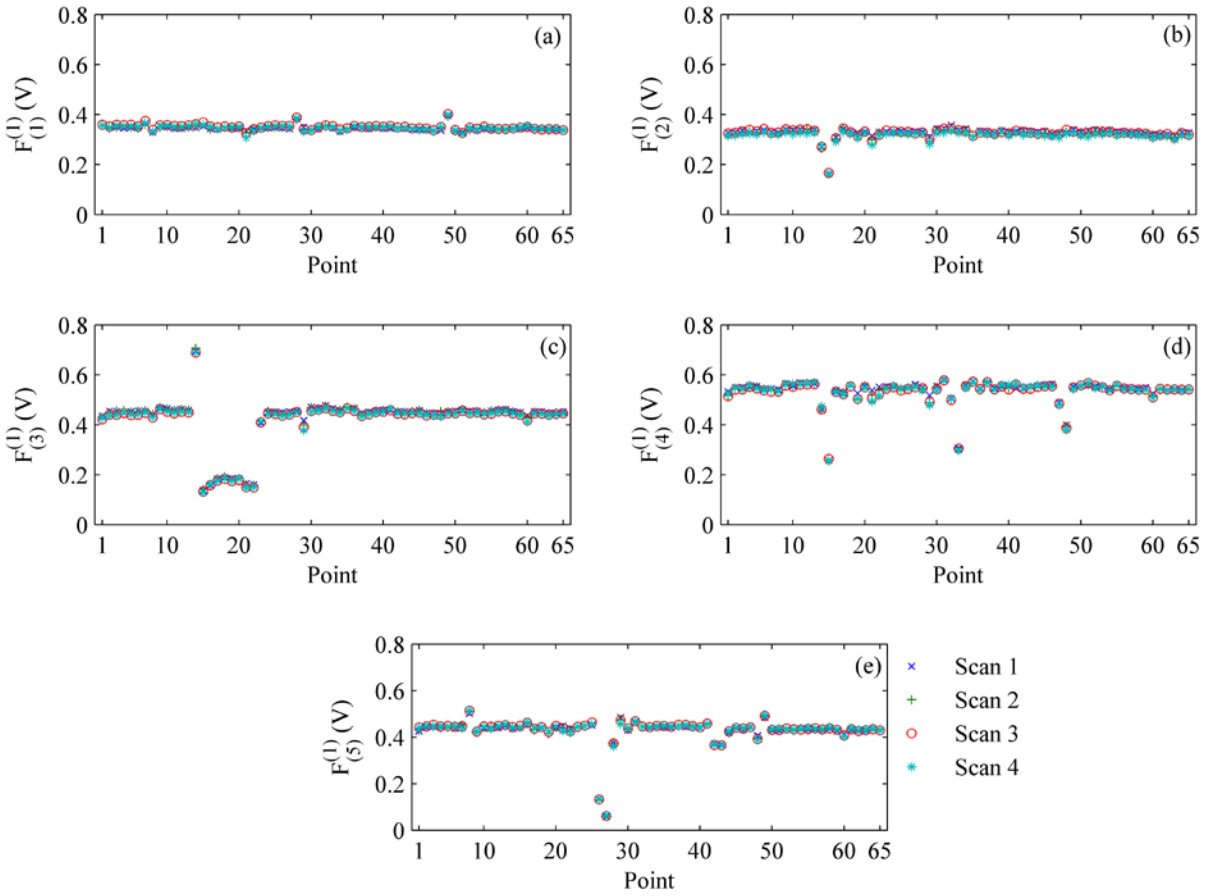

Figure 9.5. Feature $F^{(1)}$ measured at the 65 testing points by the transducers (a) T1, (b) T2, (c) T3, (d) T4, and (e) T5. The results from all four scans are overlapped.

For the sake of completeness, Fig. 9.6 presents the values of the other two features as a function of the inspection point for all four scans. The overall examination of the panels in both Fig. 9.5 and Fig. 9.6 does not flag any evident advantage of one feature over another. In other words, the information retrievable from a panel relative to a specific transducer and feature can be retrieved by the other two corresponding panels. The figures also demonstrate that the test

setup was highly repeatable, i.e. there is no noticeable deterioration of the inspection reliability as the scan number increased.

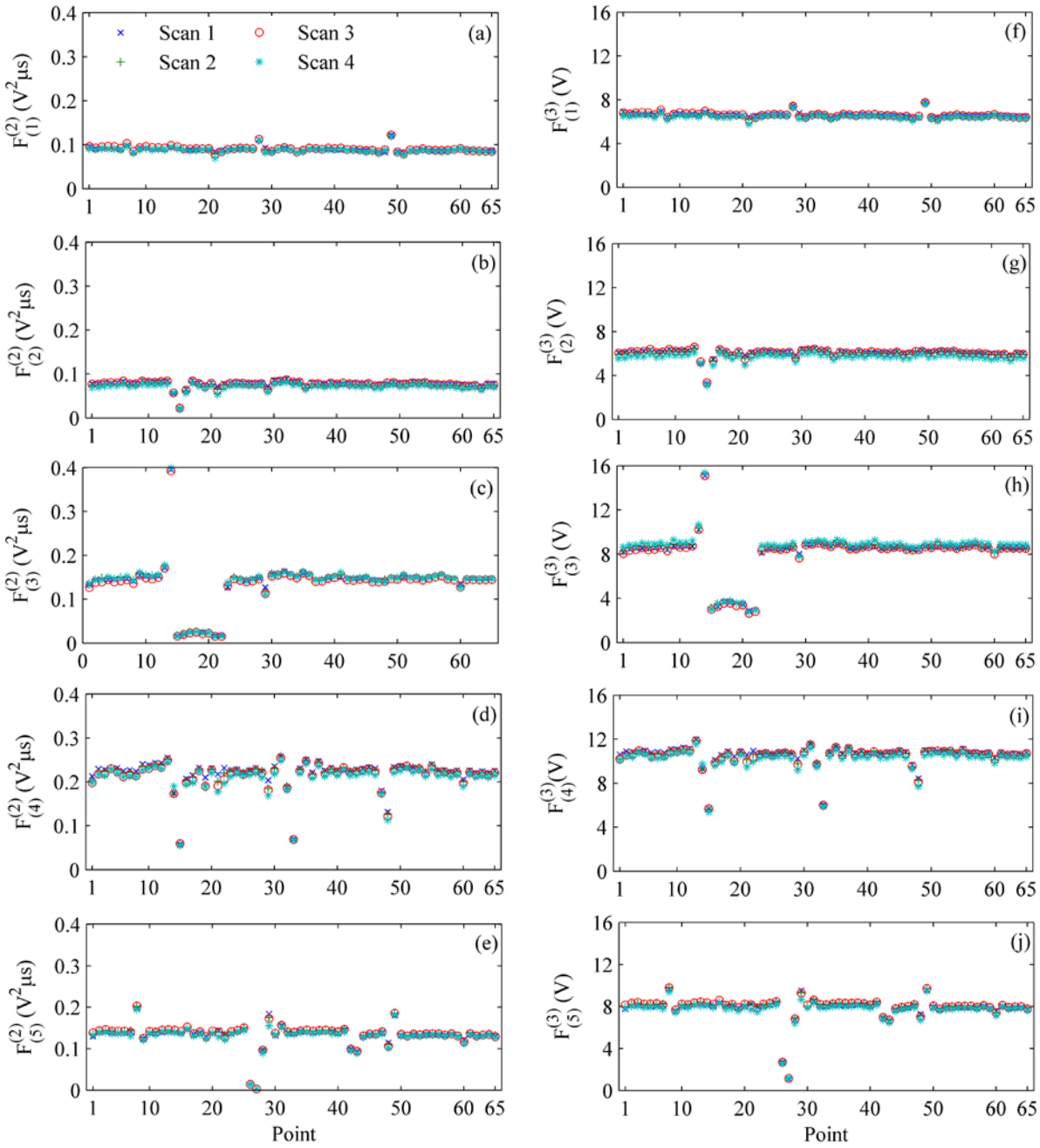

Figure 9.6. Feature $F^{(2)}$ measured at the 65 testing points by the transducers (a) T1, (b) T2, (c) T3, (d) T4, and (e) T5. Feature $F^{(3)}$ measured at the 65 testing points by the transducers (f) T1, (g) T2, (h) T3, (i) T4, and (j) T5. The results from all four scans are overlapped.

9.3.2 Damage classification

The values of the three features were then coupled to an ANN, following an approach similar to what done previously. A feed-forward back propagation network with four layers was implemented according to the scheme illustrated in Fig. 9.7. The input layer received the features' vector from a transducer, along with the true target that contained the codification of the structure condition. Four class labels were coded using two binary digits. The class (0, 0) identified the pristine plate; the class (0, 1) referred to the transverse cut, i.e. damage D1; the class (1, 0) indicated the oblique notch, i.e. damage D2. Finally, the class (1, 1) clustered the remaining defects. This last class hypothesizes that defects D3, D4, and D5 had the same effects on the propagation of the guided waves as a result of their smaller size compared to damages D1 and D2. Two hidden layers processed the data by multiplying the input vectors by weights and adding biases. The results constituted the argument of a transfer function that squashed the output values into a certain range. For the hidden layers, 15 neurons were used, because the convergence rate was considered acceptable. The hyperbolic tangent sigmoid transfer function was employed using the *tansig* function in *MATLAB*® software because it squashes the output values between –1 and +1. For the input and output layers the *purelin* transfer function $f(x)=x$ was adopted.

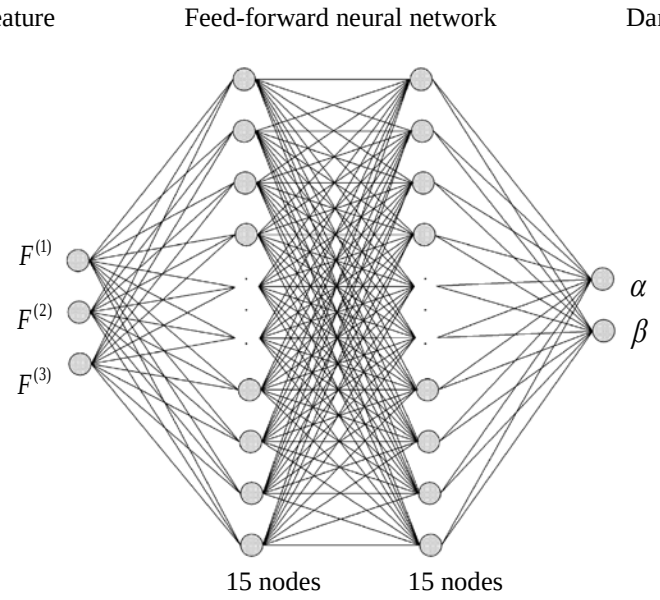

Figure 9.7. Scheme of the neural network used in this study.

The network was trained with the Levenberg-Marquardt algorithm because of its computational speed. The training determined the weights and biases for each layer. The output layer had two output nodes that were compared with the targets through the mean square error (MSE):

$$MSE = \frac{1}{N}\sum_{k=1}^{N}\sum_{j=1}^{m}(y_{kj} - \hat{y}_{kj})^2 \tag{9.2}$$

In Eq. (9.1), N is the number of training samples, m is the number of output nodes, y_{kj} is the desired target, and $\hat{y}_{kj}$ is the network output. If the error was above a certain value, the training process was continued by transmitting the errors backwards from the output layers, and adjusting the weight and biases. If the error was below an established value, the learning process stopped. The training process also stopped when a minimum on the error gradient was reached. In training process, the initial value of weights and biases were fixed in order to get the same

results from the network when fed with the same input data. The Matlab command *rand('state',0)* was used.

The architecture was applied to the data from each individual transducer. Every time, the network was trained using 80% of the experimental data from the first scan, and tested using the remaining data. Specifically, the training samples consisted of 233 data relative to class (0,0), 10 data relative to class (1,0), 6 data relative to class (0,1), and 11 data relative to class (1,1).

The ability to label properly the plate health is presented in Fig. 9.8 that shows the labels relative to the third transducer, i.e. the transducer located along the line of scan. The four panels refer to the four scans. The crosses represent the predicted class whereas the circles represent the true class as determined from Table 9.1. The label *uncertain* identifies those outputs that could not be associated to any class because at least one of the output digits was not close to 0 or 1. Figure 9.8a, which refers to scan 1, presents the best results because most of the data were used for training. Figs. 9.8b and 9.8c show only a very few mislabels and three uncertainties. Figure 9.8d, which refers to the fourth scan, shows several uncertainties: many data from the damage-free class was not assigned any label. Finally, two data belonging to the (1,0) class were labelled as (0,0), i.e. were considered false negatives. The lower success of scan 4 may be attributed to a slight deterioration of the experimental setup due to the increase of gas bubbles in the water or in terms of misalignment of either the actuator or the receiver or both.

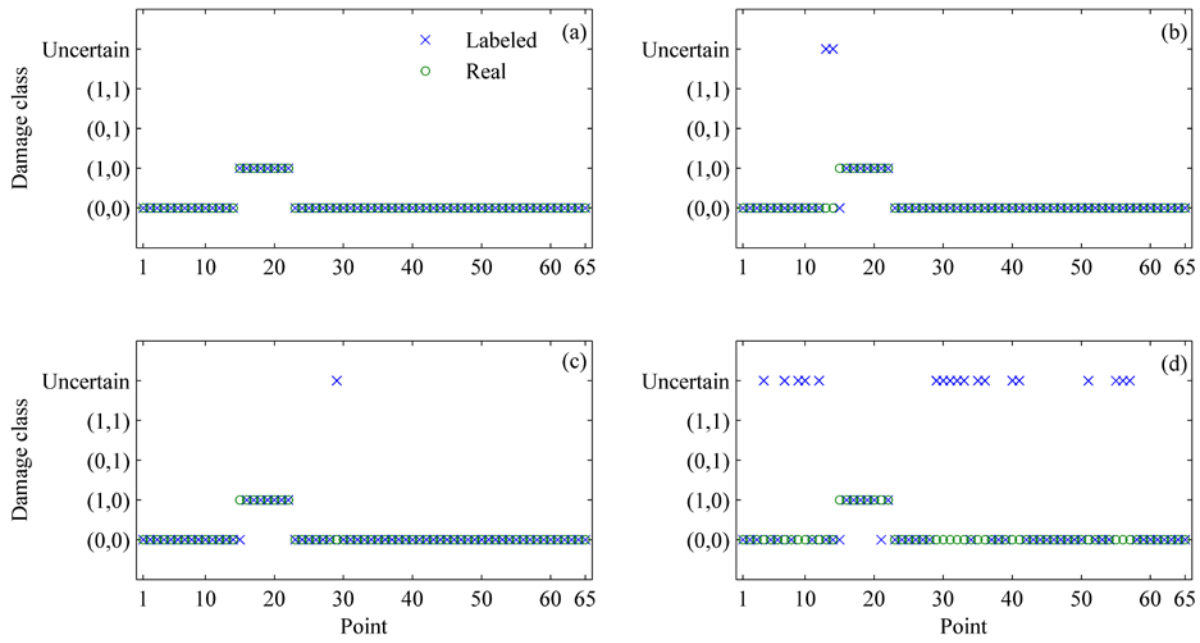

Figure 9.8. True and labeled classes associated with transducers T3 and relative to (a) Scan 1, (b) scan 2, (c) scan 3, and (d) scan 4.

Figure 9.9 shows the same plots but relative to transducer T5, which was expected to be less affected by the presence of damage because the size of the structural anomalies was more challenging. Here, the number of mislabels and uncertainties is similar to those observed in Fig. 9.8.

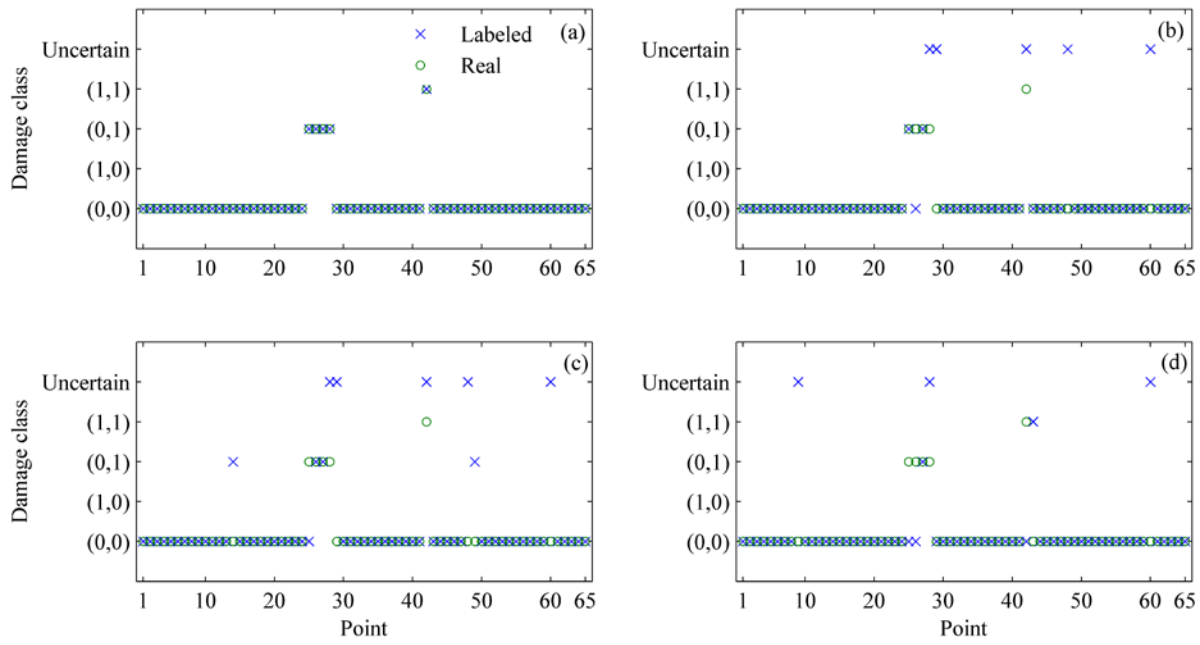

Figure 9.9. True and labeled classes associated with transducers T5 and relative to (a) Scan 1, (b) scan 2, (c) scan 3, and (d) scan 4.

Table 9.3 summarizes the overall results of the network classification. The success rate of scan 1 is obviously the highest because 80% of the data were used for the training. In ~80% of the cases, the network was able to properly identify the condition of the plate during scans 2 and 3. The success slightly declined because, as is said earlier, the last scan probably experienced some variations in the overall setup.

Table 9.3. Results (%) of the neural network for training and test data.

Data	Success	False positive	False negative	Uncertain	Mislabel
Scan 1 (train)	100	0.00	0.00	0.00	0.00
Scan 1 (test)	86.2	1.54	0.00	9.23	3.08
Scan 2 (test)	80.3	1.54	1.23	13.5	3.38
Scan 3 (test)	75.1	2.15	2.15	16.9	3.69
Scan 4 (test)	54.8	0.92	1.23	31.7	11.4

Another way to evaluate the ability of the network to classify the health of the structure is given in Fig. 9.10a that displays the success rate as a function of the class label. Nearly 75% of the data properly labelled the plate as pristine, and very few false positives were flagged. However, the success rate declined with the decrease of the defect size. The reason for such trend is two-fold. First, the classification is rather ambitious because some defects are not visible on the surface and are rather small. Owing to their size, they may not readily fall along any of the actuator-receiver lines of sight. Second, the number of training data associated with the pristine condition is much higher than the other classes, i.e. the class (0,0) overpopulates the training set whereas the other classes are underrepresented. To confirm this hypothesis we run two analyses in which the number of sample data from the classes representing damage was the same and the number of training data from class (0,0) was reduced to 133 and 11, respectively. The results are presented in Figs. 9.10b and 9.10c and it can be seen that the successful classification of the four classes depend on the training data presented to the network. It is interesting to note that the transverse notch was properly labelled 100% of the times when the number of training data relative to its class, (1,0), was identical to the number of training data relative to the pristine case. We did not observe any improvement about the detection of the most subtle defects clustered in the class (1,1). The quantitative results of these two analyses are summarized in Tables 9.4 and 9.5.

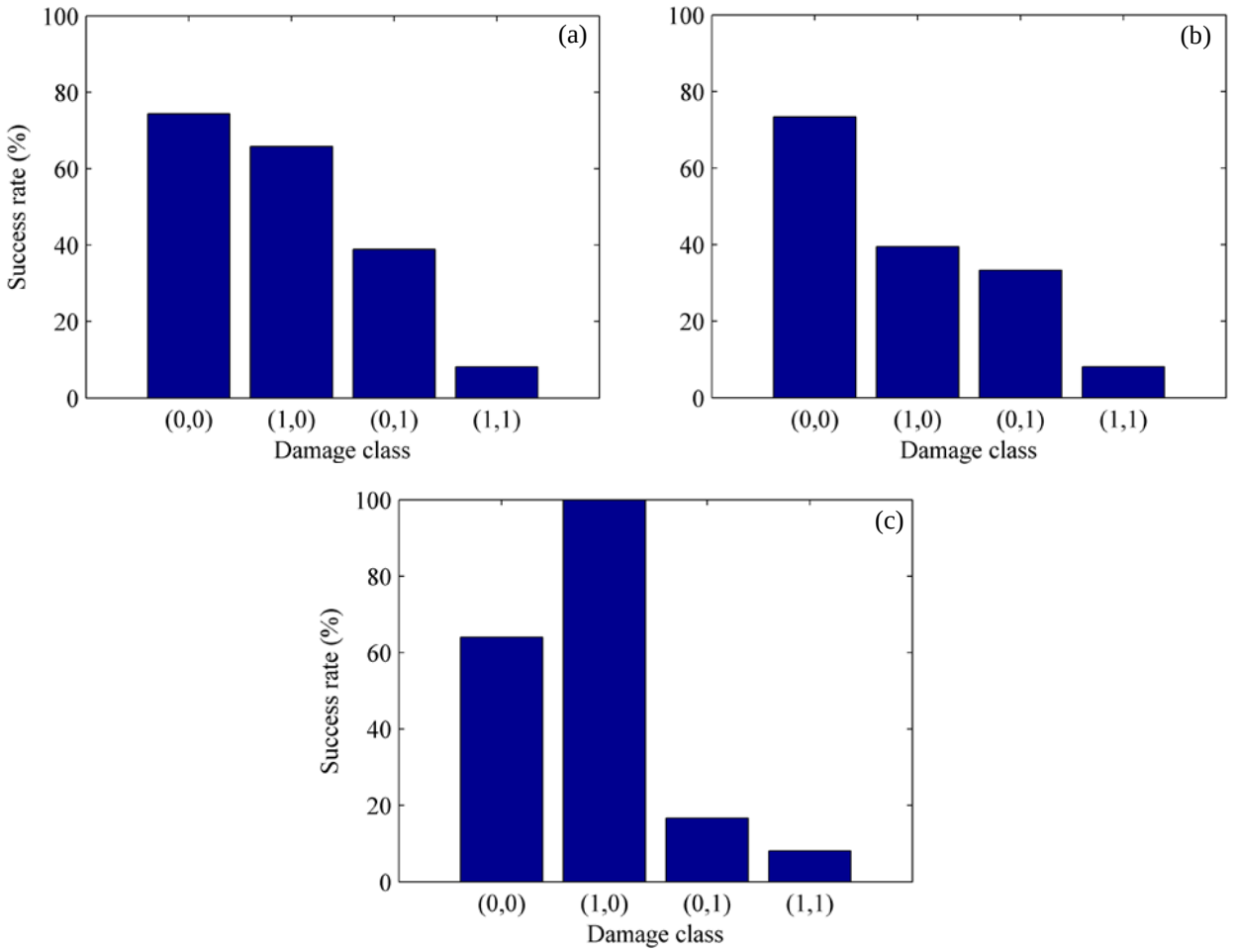

Figure 9.10. Success rate results of all test data for different damage types when the training data contained (a) 80% of samples from scan 1, (b) 50% of samples from scan 1, and (c) 11.7% of samples from scan 1.

Table 9.4. Results (%) of the neural network for the first new analysis.

Data	Success	False positive	False negative	Uncertain	Mislabel
Scan 1 (train)	100	0.00	0.00	0.00	0.00
Scan 1 (test)	80.6	1.82	0.61	14.5	2.42
Scan 2 (test)	77.5	1.54	1.54	16.0	3.38
Scan 3 (test)	68.0	2.46	1.85	22.5	5.23
Scan 4 (test)	57.2	1.85	3.38	30.8	6.77

Table 9.5. Results (%) of the neural network for the second new analysis.

Data	Success	False positive	False negative	Uncertain	Mislabel
Scan 1 (train)	100	0.00	0.00	0.00	0.00
Scan 1 (test)	65.9	2.79	3.14	7.67	20.6
Scan 2 (test)	64.3	2.15	2.77	11.7	19.1
Scan 3 (test)	63.1	3.08	2.77	13.2	17.8
Scan 4 (test)	58.5	4.00	3.69	12.9	20.9

9.4 CONCLUSIONS

In this chapter, an automated damage-detection technique for metallic plates submerged in water is presented. An immersion focused transducer was used to insonify an aluminium plate whereas an array of five transducers, arranged along a semi-circle was used to detect the waves. For each sensor, the signals were processed to extract three features in the time and frequency domain. These features were assembled to constitute the input vector of an artificial neural network to identify and classify four different scenarios, three of which associated with the presence of five structural defects artificially devised on the backwall of the test plate. The results demonstrated that the method is repeatable, robust against background noise, and it is able to classifying properly up to 75% of the overall data points. Obviously, the classification results presented here only refer to the plate under test and to the specific defect examined. The consistent detection of data scatters along the scan line suggested that the effects of the base supports on the ultrasonic signals paired the effects induced by the small artificial defect, namely the dent, the abraded area, and the through thickness hole.

10.0 ULTRASONIC IMAGING OF CYLINDRICAL STRUCTURES

This chapter presents the results of a numerical study where GUWs are processed using a new imaging algorithm for the health monitoring of cylindrical structures. The method utilizes the generation and detection of guided waves from the transducers of two annular arrays located inside a pipe. The fastest mode of the detected signals is processed using the CWT and the Hilbert transform (HT) to extract two damage-sensitive features. The estimation of the features for the healthy condition is formulated in terms of an optimization problem solved with the competitive optimization algorithm (COA). Finally, a probabilistic approach is used to create an image of the pipe to reveal the presence of possible structural anomalies. With respect to most of the GUW-based imaging methods, the proposed approach is baseline-free which means that data from pristine pipes are not necessary. In the study, a commercial finite element code is utilized to mimic the operation of two rings each made of four ultrasonic transducers in contact with the interior wall of a pipe. While one of the transducers acts as transmitter, the other seven act as sensors, and this is repeated for all the elements of the rings. The time waveforms associated with all the possible actuator-sensor pairs are processed using the algorithm proposed here. The findings are compared to the results obtained using a conventional pitch-catch approach.

The chapter is organized as follows. A literature review of the GUW-based methods for damage detection in pipes is presented in Section 10.1, a background on the COA is introduced in Section 10.2. The numerical model is illustrated in Section 10.3 whereas Section 10.4

describes the damage-sensitive features selected in this study, and the ultrasonic imaging approach employed to map the structure. Then, Section 10.5 presents the results of the numerical study. Finally, the dissertation ends with some concluding remarks including a discussion on the generality of finding.

10.1 INTRODUCTION

There exists a rich literature that demonstrates that GUWs are suitable for the NDE and SHM of annular structures (Barshinger et al. 2002, Na and Kundu 2002, Cawley et al. 2003, Kim et al. 2012, Nagy et al. 2014, Dehghan-Niri and Salamone 2014). Some of these works have matured into commercial products as a result of incremental research over a long period of time.

In SHM applications, the use of guided waves is often combined with signal processing to extract damage-sensitive features able to determine the location, severity, and typology of damage. Signal processing may include short-time Fourier transform (Kannan et al. 2007), wavelet analysis (Rizzo et al. 2005, Liu et al. 2012, Ahmad et al. 2009), and Hilbert-Huang transform (HHT), the latter being a combination of the empirical mode decomposition (EMD) and the HT (Cheraghi and Taheri 2007, Esmaeel et al. 2012). Irrespective of the signal processing employed, an accurate diagnostic of the structure to be monitored is achieved by comparing testing data to baseline data that, ideally, include scenarios of the pristine structure operating under all possible environmental conditions. The need for baseline data may be removed by creating an image of the structure of interest from the analysis of the ultrasonic signals transmitted and received by an array of transducers. This is what is done, for example, by synthetic focusing algorithms (Leonard and Hinders 2003, Hayashi and Murase 2005, Deng et al.

2008, Davies and Cawley 2009). In these algorithms, the image of a structure able to support the propagation of guided waves is obtained by maximizing the energy of the wave at a focal point using phased array or synthetic focusing. In the method based on synthetic focusing, the image is reconstructed after post-processing the time-series (Davies and Cawley 2009). Davies et al. (2006) reviewed three common focusing methods for guided wave imaging of plates, namely the common source method (CSM), the synthetic aperture focusing technique (SAFT), and the total focusing method (TFM). In the CSM, all the transducer elements of an array are fired simultaneously to provide the selective excitation of a chosen mode and to reduce coherent noise. Then, the separate reception of the waves by the same transducers on multiple paths allows for the summation of the same mode that was sent or another mode. The SAFT uses the pulse-echo data from each array element in turn. Finally, in the TFM, all possible source-receiver pairs are considered; the elements of one or more arrays are fired in turn and a time waveform is recorded for each firing at all array element positions. Some authors identify the in turn firing of the transducers and the recording at all array element positions as round-robin interrogation (Quaegebeur et al. 2011, Lee et al. 2012). Despite the fact that these algorithms have seen significant developments, their primary disadvantage is the need of a large sensor density in order to obtain a sufficient ray density and ultimately a high image resolution.

To advance the knowledge on the full-matrix TFM approach and reduce the number of transducers in an array, we investigated a new reference-free ultrasonic imaging algorithm for the detection and localization of damages in pipes. The method consists of three main steps: feature extraction, baseline computation, and mapping. Ultrasonic signals are processed using the CWT and the HT to extract two damage-sensitive features that are fed to an optimization procedure that is solved with the COA. The COA serves to establish the baseline dataset that is

then used into a probabilistic approach to map the pipe. Given the success of the COA in damage detection using modal data and other optimization problems (Bagheri et al. 2012, Nicknam and Hosseini 2012, Atashpaz-Gargari and Lucas 2007, Rajabioun et al. 2008), in this study, we coupled the COA to time-series signals associated with the propagation of guided waves in pipes. To the best of the authors' knowledge, the optimization procedure using the COA is applied for the first time to ultrasonic signals whereas the probabilistic approach was applied in (Bagheri et al. 2013) to monitor plates.

In this chapter, we simulated numerically the propagation of guided waves using the commercial finite element code ANSYS. Two rings of transducers were modeled by considering four nodes, equally spaced in the circumferential direction of the mesh. Each node was subjected to a time-dependent force orthogonal to the pipe surface. The ultrasonic signals generated and detected by all the possible transducer (nodes) pairs were processed according to the scheme summarized. We simulated the existence of five different damage scenarios and we found that the algorithm enables the detection of all of them with fair accuracy. We also compared the performance of our signal processing to an imaging approach based on conventional pitch-catch arrangement.

10.2 COMPETITIVE OPTIMIZATION ALGORITHM

The COA is an optimization method that mimics a socio-political process (Atashpaz-Gargari and Lucas 2007). As any optimization algorithm, the objective of the COA is to find the optimal solution, usually the minimum, of the argument $\mathbf{x}$ of a certain function $f(\mathbf{x})$. Figure 10.1 shows the flowchart of the algorithm. The COA begins by establishing the total number of countries

$N_{country}$ that comprises N_{imp} *imperialists* and N_{col} *colonies*, i.e. $N_{country} = N_{imp} + N_{col}$. Each *i*-th country is defined by an array of *n*-variables:

$$Country_i = \left[x_1^i, x_2^i, \ldots, x_n^i \right] \tag{10.1}.$$

and a cost c_i is defined by the objective function ***f(*****x*****)*** as:

$$c_i = f(Country_i) \tag{10.2}.$$

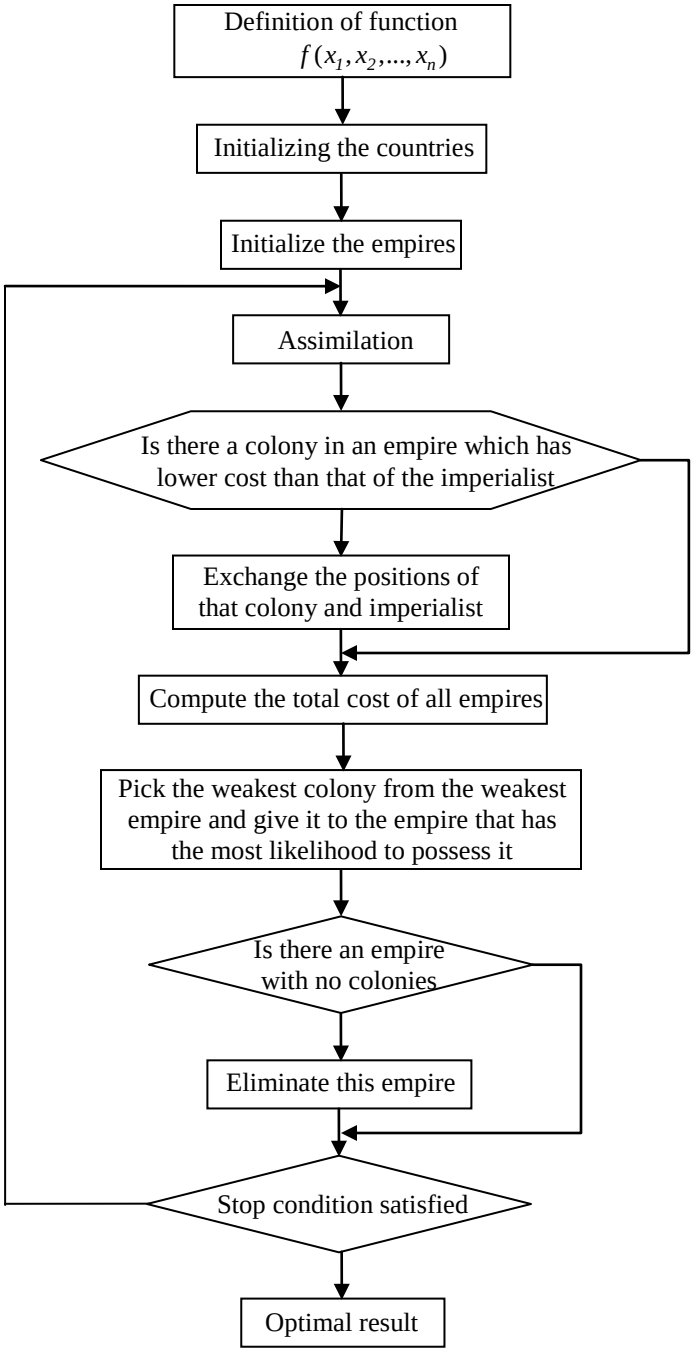

Figure 10.1. Flowchart of the competitive optimization algorithm.

The imperialists represent the most powerful countries and they form the empires that control the colonies. Each colony is assigned to a certain empire based on the imperialist's

power, and the number of colonies *N.C.* belonging to an empire is proportional to the imperialist's normalized power *p*. Mathematically, for the *j*-th imperialist, the normalized cost C_j is:

$$C_j = c_j - \max_i c_i \tag{10.3}$$

The normalized power p_j is defined:

$$p_j = \left| \frac{C_j}{C_T} \right| \tag{10.4}$$

where C_T is the summation of the normalized cost of all imperialists. The number of colonies for the *j*-th imperialist can be computed as:

$$N.C._j = round(p_j N_{col}) \tag{10.5}$$

where *round* indicates the rounding to the nearest integer number (Atashpaz-Gargari and Lucas 2007).

Once the initialization process is complete, the imperialistic countries begin to improve their colonies and attempt to absorb new colonies. This is the assimilation process which is modeled by moving the colonies toward the imperial power along different optimization axes (Atashpaz-Gargari and Lucas 2007). This movement is shown in Fig. 10.2, where a colony moves toward the imperial power by Δl units along the shortest path connecting the colony to the imperialist. Δl is a random variable with uniform distribution and estimated as:

$$\Delta l \sim U(0, \gamma \times l) \tag{10.6}$$

where γ is a positive number greater than one, and l is the distance between the colony and the imperialist. To ensure that many positions are explored in search of the minimal cost, the process of assimilation does not occur through the direct movement of the colonies toward the imperial power. A random path is induced by a random amount of deviation added to the direction of the

movement. This is illustrated by the dashed path in Fig. 10.2b. If during the assimilation process, a colony reaches a position with lower cost than the imperialist, then the imperialist and the colony switch their positions. Then, the algorithm will continue with the imperialist and its colonies in their corresponding new positions.

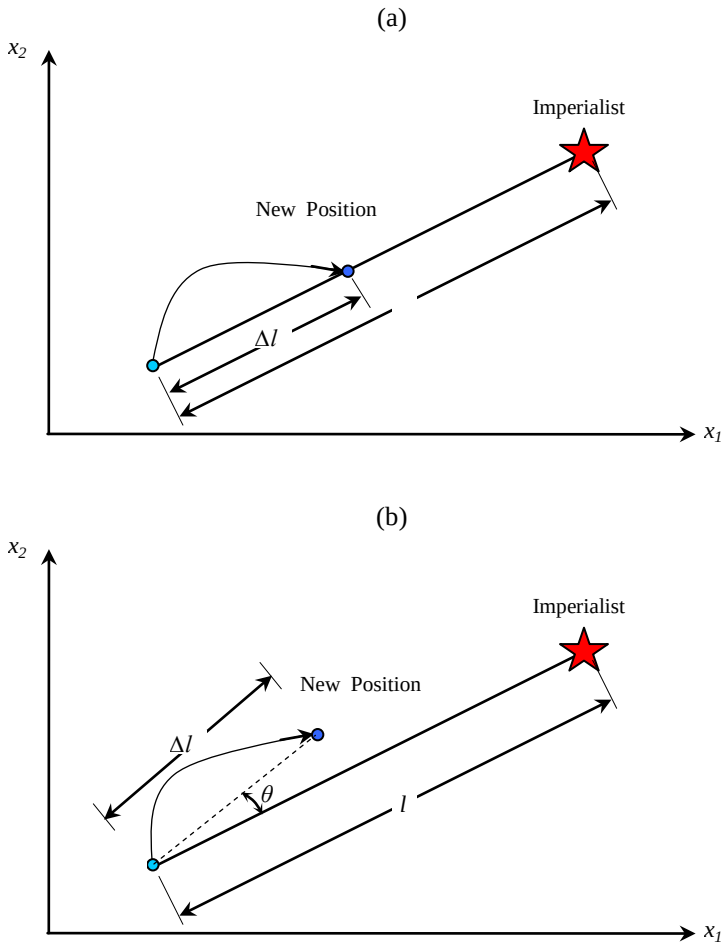

Figure 10.2. Scheme of a colony movement toward its imperialist: (a) without deviation and (b) with deviation.

The total power of an empire depends on both the power of the imperialist country and the power of its colonies. This fact can be modeled by defining the total power of an empire as

the contribution of the power of the imperialistic country plus a fraction of the mean power of its colonies. Therefore, the total cost *T.C.* of an empire *j* is determined by:

$$T.C._j = f\left(imperialist_j\right) + \xi \frac{\sum_{k=1}^{N.C._j} f\left(\text{the } k\text{-th colony of the } j\text{-th empire}\right)}{N.C._j} \tag{10.7}$$

where ξ is a coefficient which represents the effect of colonies' power on the total power. The role of the colonies can be augmented by increasing ξ.

Each empire tries to take possession of the colonies of the other empires. This competition is modeled by picking one or more of the weakest colonies of the weakest empire and by starting a competition among the empires. To start the competition, the normalized total cost *N.T.C.* of an empire *j* is defined as:

$$N.T.C._j = T.C._j - T.C._M \tag{10.8},$$

in which $T.C._M$ is the maximum value of the total costs. Then, the possession probability of the empire *j* is calculated:

$$p_{p_j} = \left| \frac{N.T.C._j}{N.T.C._T} \right| \tag{10.9}$$

where $N.T.C._T$ represents the summation of the normalized total cost of all empires. To divide the colonies among the empires, a vector of the possession probability of the empires ***P*** is defined:

$$\mathbf{P} = [\, p_{p_1}, p_{p_2}, ..., p_{p_{N_{imp}}} \,] \tag{10.10}.$$

Finally, the following vectors **R** and **D** are generated:

$$\mathbf{R} = \left[\, r_1, r_2, ..., r_{N_{imp}} \,\right] \tag{10.11}$$

$$\mathbf{D} = \mathbf{P} - \mathbf{R} \tag{10.12}$$

where the vector **R** is formed by random numbers with uniform distribution comprised between 0 and 1. A certain colony is annexed to an empire whose relevant index in **D** is maximum. The last step of the ICA consists on the elimination of the powerless empires. If one empire only is left then the optimization algorithm is terminated, otherwise the algorithm is started again from the assimilation step.

10.3 NUMERICAL SETUP

The propagation of guided waves in a 40 mild steel pipe was numerically simulated by using a time-transient analysis in ANSYS v.13.0. It is known that the accuracy of the procedure depends upon the temporal and the spatial resolution of the analysis. To achieve good accuracy, both the integration time step and the mesh element size must be in accordance with the maximum frequency of interest (f_{max}) of the dynamic problem. A good rule for the time step resolution Δt is to use a minimum of 20 points per cycle at the highest frequency (Bartoli et al. 2005), i.e.:

$$\Delta t \leq \frac{1}{20 f_{max}} \tag{10.13}$$

For a good spatial resolution 10 nodes per wavelength are required although some researchers (Bartoli et al. 2005, Moser et al. 1999) recommended 20 nodes per wavelength. The latter condition yields to the definition of the maximum element length L_e as:

$$L_e = \frac{\lambda_{min}}{20} \tag{10.14}$$

where λ_{min} is the wavelength corresponding to the highest frequency of the wave mode of interest.

The pipe considered in this study was 600 mm long, 50 mm in external diameter, and 5 mm thick. The following material properties were assumed for the mild steel: density ρ=7932 kg/m^3, Young's modulus E=216.9 GPa, shear modulus G=84.3 GPa, and Poisson's ratio ν=0.2865.

The semi-analytical finite element (SAFE) method (Marzani et al. 2008) was employed to gain insight into the guided waves propagating along the modeled tube. In pipes, three kinds of wave can propagate: longitudinal, torsional, or flexural waves, and they are conventionally labeled as L(0,n), T(0,n), and F(m,n), respectively. The first index m gives the harmonic number of circumferential variation and the second index n is a counter variable. Figure 10.3 shows the dispersion curves of the phase velocity and the group velocity relative to the pipe considered in this study.

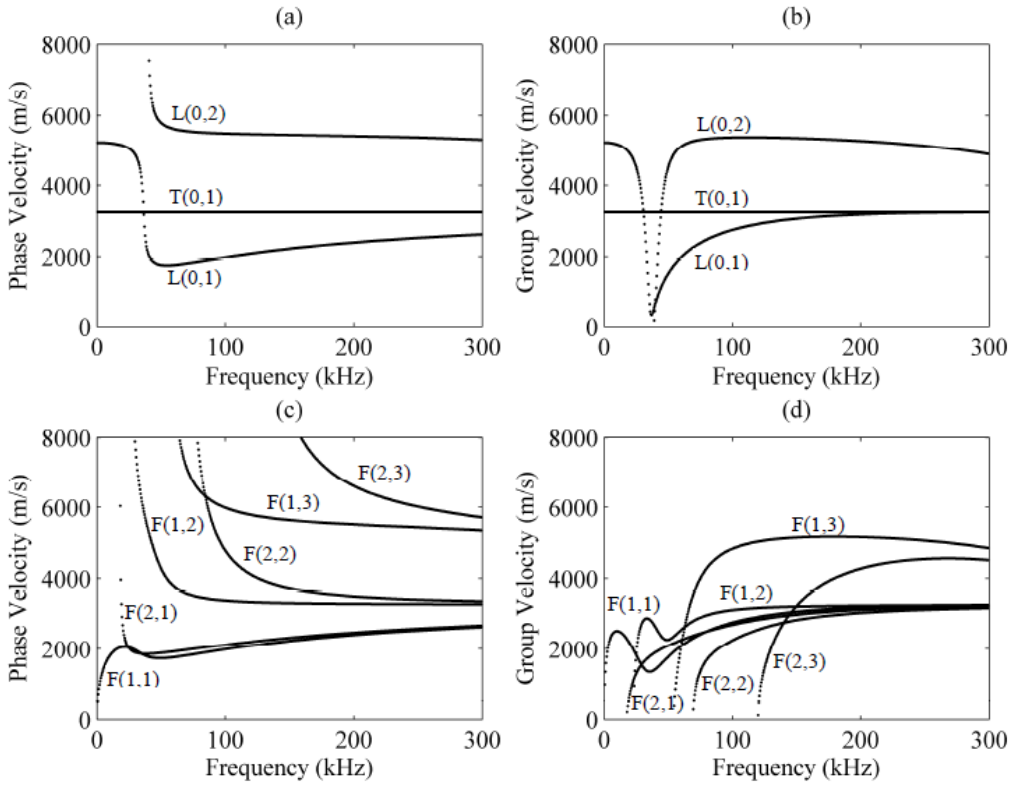

Figure 10.3. Dispersion curves for a 40 mild steel pipe in vacuum: (a) phase velocity for axisymmetric modes, (b) group velocity for axisymmetric modes, (c) phase velocity for non-axisymmetric modes, and (d) group velocity for non-axisymmetric modes.

To test the capability of the proposed SHM system, we simulated five damage scenarios, namely: 1) a through-thickness hole with a diameter of 20.93 mm; 2) a 2 mm thick internal corrosion 10 mm in diameter; 3) a 2 mm thick and 10 mm in diameter external corrosion ; 4) a through-thickness hole with a diameter of 2 mm; 5) a 10 mm diameter 2 mm thick internal corrosion and a through-thickness notch 10 mm long and 1 mm wide. The geometry of the pipe and the first case scenario are presented in Fig. 10.4a. The pipe was discretized according to the scheme shown in Fig. 10.4b using the three-dimensional 8-node “SOLID 185” element with three degrees of freedom per node.

The presence of two rings of transducers was simulated. The rings were 200 mm apart and each ring consisted of four points equally spaced in the circumferential direction. In the model, the position of these eight transducers coincided with eight nodes of the elements. The nodes were located at the inner wall of the pipe in order to simulate the excitation of the waves from the inside. The spatial location of the nodes is illustrated in the insets of Fig. 10.4a.

An unconditionally stable implicit Newmark procedure with a decay factor of 0.005 and integration parameters α=0.252 and δ=0.505 was used to perform the time integration. Small numerical damping was added to avoid undesirable levels of noise that the higher frequencies generate in the structure (Zienkiewicz 1977). In order to satisfy Eq. (10.13) the sampling period Δt was set equal to 0.5 μsec, which corresponds to a sampling frequency of 2 MHz.

(a)

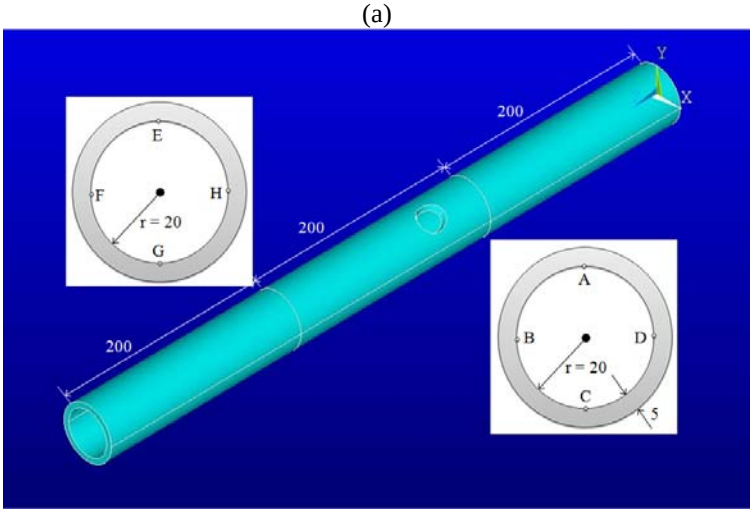

(b)

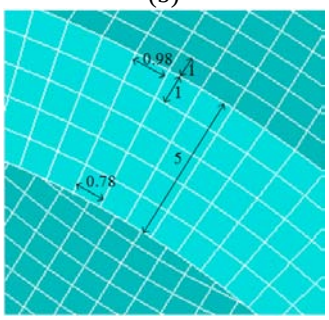

Figure 10.4. (a) The geometry of the pipe and the first damage scenario, and (b) the finite element model of the pipe. Nodes A to D are located 200 mm from the reference system. Nodes E to H are located 400 mm from the reference system. The damage consisting of a through–thickness hole is located 50 mm away from the first ring of transducers. (Dimensions in mm).

Guided waves were excited by imposing a modulated 3-cycle tone burst forcing function perpendicular to the pipe surface (Fig. 10.5a). The corresponding Fourier transform is shown in Fig. 10.5b. The tone burst was centered at 100 kHz and applied at each of the eight nodes discussed before. Based upon Fig. 10.3, at 100 kHz eight different modes may exist. However their generation depends on the actuation mechanism provided by the transducers. For instance, radial excitation allows the generation of flexural modes, while shear excitation perpendicular to the axial direction of the pipe induces torsional modes. The 100 kHz frequency was selected

because it was considered a good trade-off between wavelength and computational effort. The wavelength was small enough, in the order of 35 mm, to be sensitive to the presence of small defects and long enough to maintain the computation-time low. Moreover at 100 kHz only a few modes can exist, making the post-processing analysis easier.

As is said earlier, the simulation was conducted such that while node A was used as the actuator, the remaining seven nodes acted as receivers and the radial displacement was measured. This was serially repeated for all eight transducers. In other words, at each time, one element acted as transmitter to send out the excitation signal and all the remaining transducers served as receivers to pick up the reflection signals. Thus, 56 measurements were taken according to the sensing paths listed in Table 10.1. The paths were clustered in five groups according to the axial or circumferential distance between the actuator and the sensor. The third row in the table represents straight-line paths between a sensor and an actuator, whereas the remaining rows refer to spiral paths around the pipe.

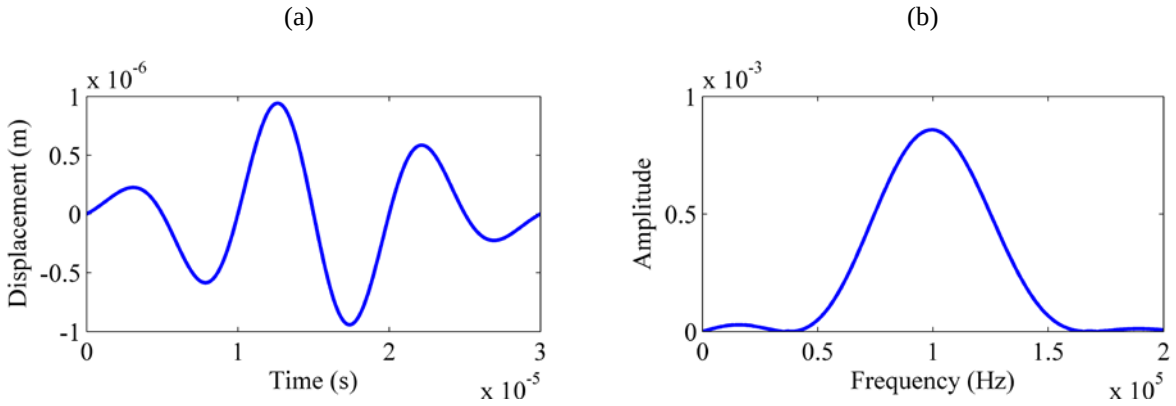

Figure 10.5. (a) 3-cycle tone burst, and (b) the corresponding fast Fourier transform.

Table 10.1. Sensing paths and the geometric distances for each path

Actuator – sensor distance *d*(mm)	Sensing paths	Total number of paths
31.40	AB, AD, BC, CD, EF, EH, FG, GH (and viceversa)	16
62.80	AC, BD, EG, FH (and viceversa)	8
200.0	AE, BF, CG, DH (and viceversa)	8
202.5	AF, AH, BE, BG, CF, CH, DE, DG (and viceversa)	16
209.6	AG, BH, CE, DF (and viceversa)	8

10.4 SIGNAL PROCESSING ALGORITHM

10.4.1 Time-histories

The contour graphs of the Von Mises stress at 30 μsec and 40 μsec, when the 3-cycle tone burst was applied to node A under the first damage scenario, are shown in Fig. 10.6a and 10.6b, respectively. At 30 μsec, the wave reached node C and the hole. The effect of the hole on the amplitude and shape of the lead wavefront as well as the reflections from the hole are visible. Two kinds of ultrasonic wave were measured based upon the relative position of the actuator and the sensor. The first kind is represented by the axisymmetric and non-axisymmetric modes that propagate along the axial direction of the pipe. The second kind was the circumferential guided wave which propagates in the circumferential direction. In this study, we considered the first wave packet detected by the sensor node.

The time-history of the radial displacement at nodes B, C, E, and G for the first damage scenario is presented in Fig. 10.7. The mode's amplitude measured at node C was larger than that measured at node B due to the constructive interference of the waves that depart symmetrically from the source and travel in the circumferential direction. Figure 10.8 shows the corresponding CWT scalograms of the time-histories showed in Fig. 10.7. The out-of-plane axis of the

scalogram indicates the wavelet coefficient of the nodal displacement. The Hilbert spectrum of the time-histories presented in Fig. 10.7 are displayed in Fig. 10.9. The HT is the convolution of the signal with $1/t$ where t represents the time. Using the original signal and the HT results, we are able to compute the amplitude and the frequency at a given time (see Huang et al. 1998) and to plot the Hilbert spectrum. In Fig. 10.9, as expected, the main energy is located around 100 kHz.

(a)

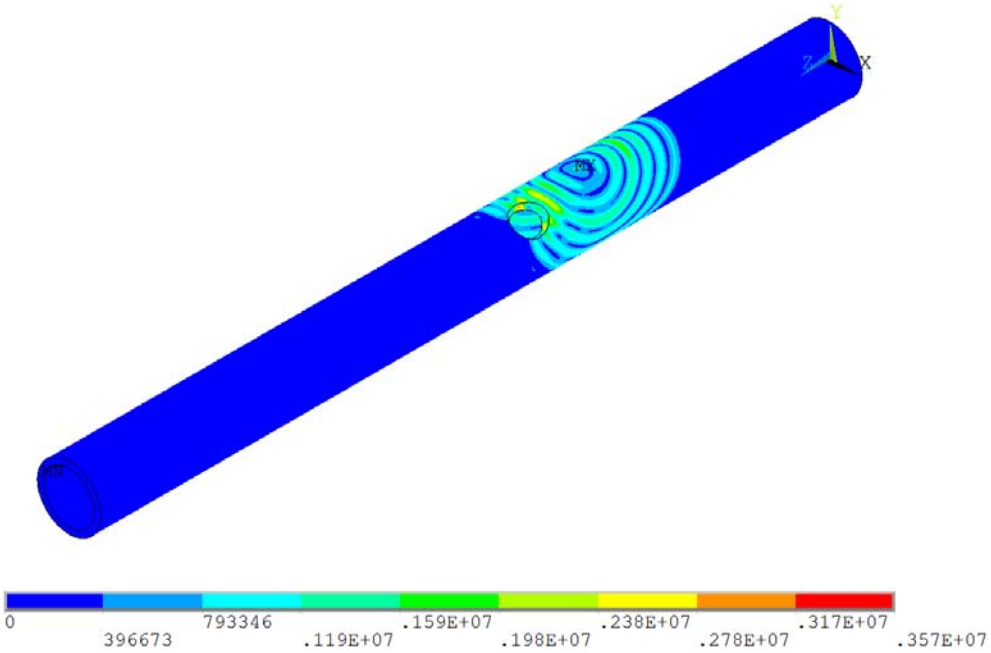

(b)

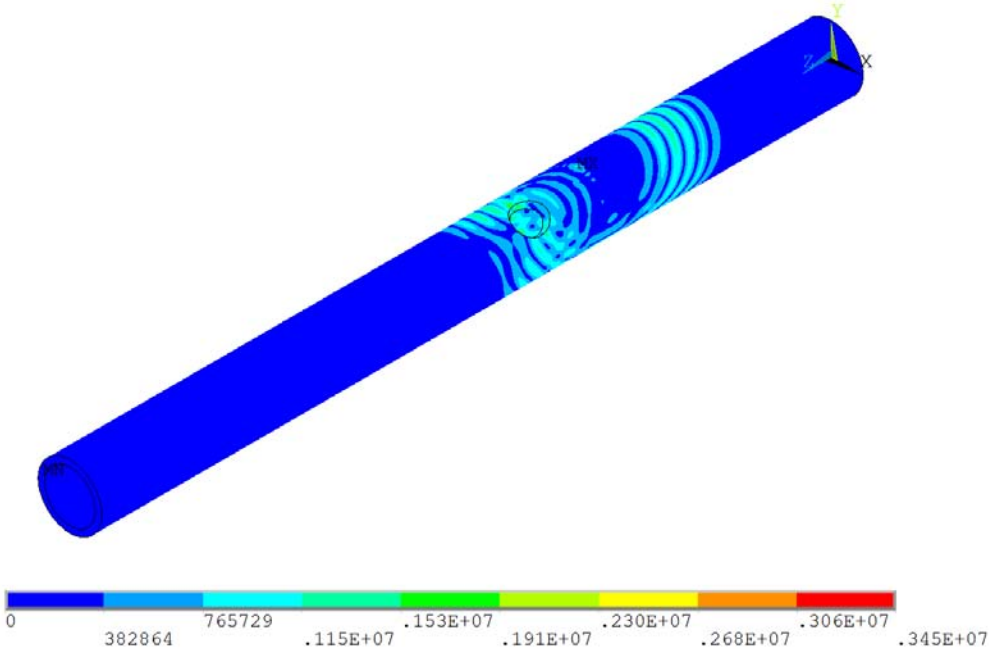

Figure 10.6. Plot of Von Mises stress for the first damage type when the tone burst was applied at node A for measured time: (a) 30 μsec and (b) 40 μsec (Units expressed in N/m^2).

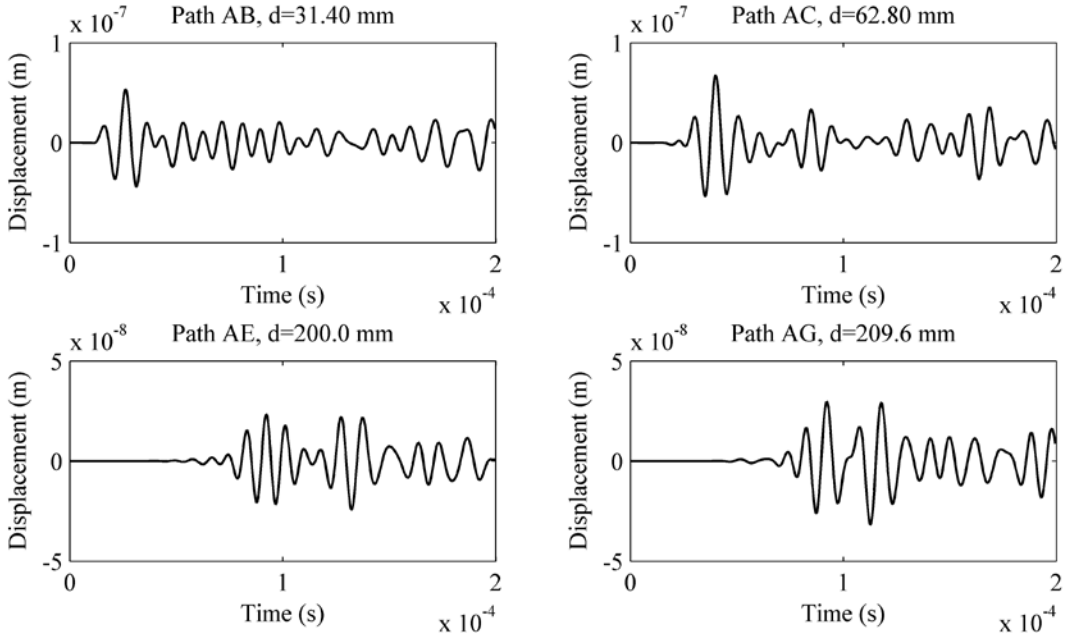

Figure 10.7. The time-history of radial displacements for the first defect type at nodes B, C, E, and G when the 3-cycle tone burst was applied at node A.

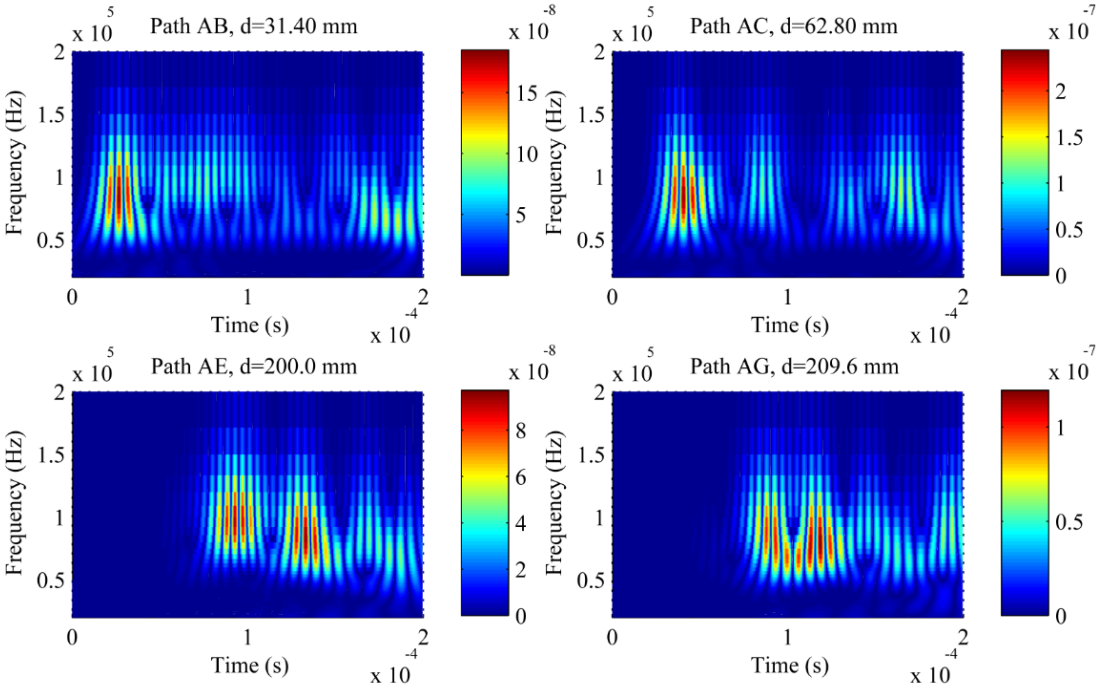

Figure 10.8. Wavelet scalograms associated with the time-histories shown in Figure 10.7.

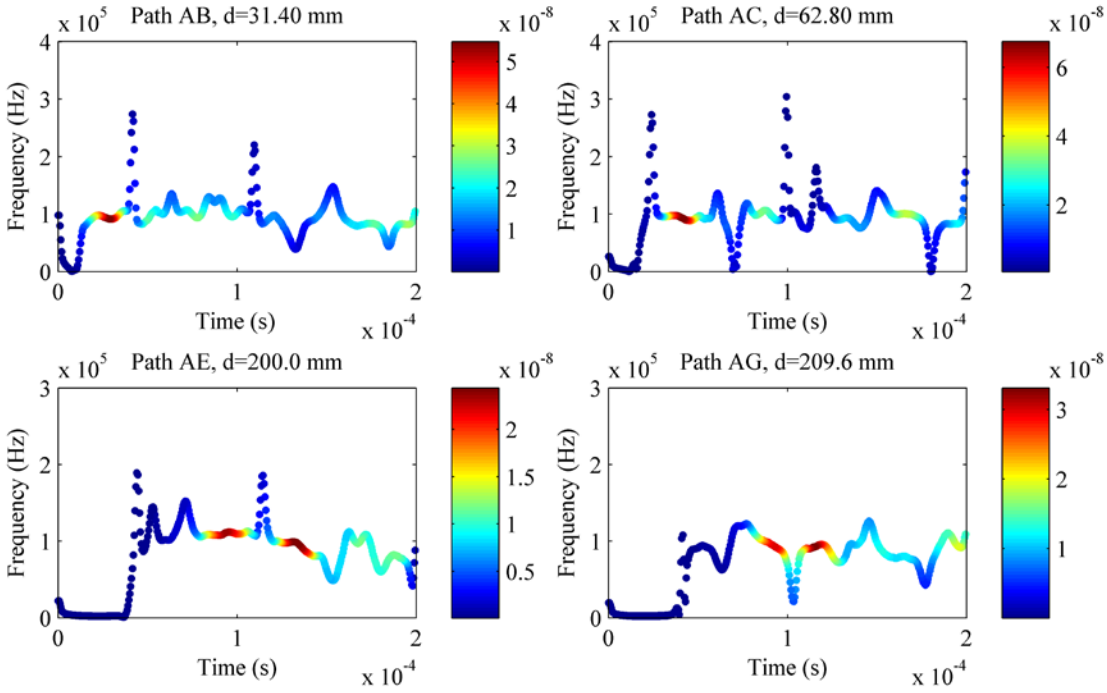

Figure 10.9. Hilbert spectra associated with the time-histories presented in Figure 10.7.

10.4.2 Feature extraction

The signals were processed with the CWT and the HT to extract a few features from the time and the joint time-frequency domains. The CWT is particularly attractive because it provides the best balance between time and frequency resolution since it uses the smallest possible Heisenberg uncertainty box (Mallat 1999). The HT provides useful information about the envelope of the signal (Huang et al. 1998).

From the scalogram of the first wave packet, the wavelet energy spectrum can be written as:

$$\mathbf{E}_j^i(t,f) = \left|\mathbf{W}_j^i(t,f)\right|^2 \qquad i = 1, 2, \ldots, 5 \quad j = 1, 2, \ldots, m(i) \tag{10.15}$$

where **E** and **W** are the wavelet energy spectrum and the scalogram of the time history, respectively. The index *i* identifies the *i*-th sensing path length according to the groups defined in Table 10.1. The count variable *m* is equal to 8 when *i* is equal to 2, 3, and 5, whereas it is equal to 16 when *i* is equal to 1 and 4 and it represents the number of wave paths having the same distance, i.e. the number shown in the third column of Table 10.1. From the wavelet energy spectrum the following feature is built:

$$F_j^i = \sum_t \sum_f \mathbf{E}_j^i(t, f) \qquad i = 1, 2, \ldots, 5 \;\; j = 1, 2, \ldots, m(i) \tag{10.16}$$

where *F* is the defined feature using the CWT.

A second feature was extracted from the Hilbert transform of the time signals, and it is defined as:

$$H_j^i = \sum_t \left| y_j^i(t) \right|^2 \qquad i = 1, 2, \ldots, 5 \;\; j = 1, 2, \ldots, m(i) \tag{10.17}$$

where *H* is the feature using the HT, and *y(t)* is the HT of the guided wave signal.

10.4.3 Features for healthy status

Wave propagation properties in pipes are complicate. This is due to the presence of at least three modes at any given frequency and to mode conversion that occurs in presence of certain types of defects. Thus, establishing which time waveforms are related to the healthy portion of the pipe can be difficult. The mere use of the signal amplitude may not be feasible, since certain waves may be the result of constructive interference. Conversely, other time waveforms may have small amplitude as a result of destructive interference rather than of the existence of a defect. Finally, different amplitudes may be the effect of different sensitivities of the transducers used in the arrays.

In this study, the COA was applied to identify the values of the features associated with the healthy status of the pipe. The proposed approach does not require the availability of a pristine pipe, but it assumes that only some portion of the structure along at least one line of sight between a transducer pair is damage-free. Thus, the method can be considered pseudo baseline free.

For the CWT-feature *F*, the following relationship associated with the *i*-th sensing path associated with the *j*-th guided wave signal can be defined:

$$e_j^i F_j^i - F_h^i = 0 \tag{10.18}$$

where *e* is a coefficient and the subscript *h* indicates the value of the feature associated with a wave path that is not affected by the presence of the defect, i.e. a *healthy* path. The goal of the COA is to find those parameters *e* and F_h that minimize an objective function. Expanding Eq. (10.18) to all the guided waves related to the same *i*-th path distance, we obtain:

$$\begin{bmatrix} e_1^i & 0 & & \\ 0 & e_2^i & & \\ & & \ddots & 0 \\ & & 0 & e_m^i \end{bmatrix} \begin{Bmatrix} F_1^i \\ F_2^i \\ \vdots \\ F_m^i \end{Bmatrix} - F_h{}^i \begin{Bmatrix} 1 \\ 1 \\ \vdots \\ 1 \end{Bmatrix} = 0 \tag{10.19}$$

which can be re-written in a short matrix form as:

$$\mathbf{e}^i \mathbf{F}^i - F_h{}^i \mathbf{I} = 0 \tag{10.20}$$

where $\mathbf{e}^i$ is a diagonal matrix, and **I** is an identity vector. An objective function is then expressed in terms of the Euclidean length:

$$f(e_1^i, e_2^i, ..., e_m^i, F_h^i) = \left\| \mathbf{e}^i \mathbf{F}^i - F_h{}^i \mathbf{I} \right\|^2 \tag{10.21}$$

In order to minimize the objective function *f()*, the COA was applied to determine the parameters *e* and the feature' value F_h associated with a healthy pipe. In order to find a suitable value for

these parameters, we need to consider a constraint for them. Because, we are interested in finding a solution that has a physical meaning in our problem. Under the conventional assumption that the features associated with the damaged pipe diverge from the baseline, we impose that baseline data are comprised between the minimum and the maximum value of the feature. As such the arguments of the objective function are constrained within a specific domain, and the optimization algorithm searches the global minimum point within this domain. These constraints are represented by:

$$\min \mathbf{F}^i \le F_h^i \le \max \mathbf{F}^i \tag{10.22a},$$

$$\frac{\min \mathbf{F}^i}{\max \mathbf{F}^i} \le e_j^i \le \frac{\max \mathbf{F}^i}{\min \mathbf{F}^i} \tag{10.22b}.$$

In the optimization process, when we generate the initial solutions for the problem, we consider the mentioned constraints for each parameter. Moreover, in modifying the solutions to reach to the final solution, we have to follow the same role.

It should be mentioned that there are a few connections between some variables and terms in Sections 10.2 and 10.4.3. In this section, e_1, e_2, …, e_m, and F_h are variables of the presented problem, so, using Eq. (10.1) a country is defined as [e_1, e_2, …, e_m, F_h] which represents that a country contains of variables of the problem. For starting to find the optimum solution, an initial value is assigned to each vector or country which means that a country represents an initial solution for the problem. By evaluating the objective function, Eq. (10.21), using each county or vector, we get the value of cost, Eq. (10.2). The power of each country is the normalized value of cost, Eq. (10.4), and represents its nearness to the global or local minimum point of the objective function. Also, imperialists represents solutions that are close to a minimum point, whereas colonies represents solutions that are far from a minimum point. The aim of considering assimilation process is to search all parts of the solution domain in order to

reach to the global minimum point which represents for the values of variables e_1, e_2, …, e_m, and F_h.

Similar to the objective function calculated from the CWT, the objective function associated with the feature based on the Hilbert transform was defined as:

$$f(e_1^i, e_2^i, ..., e_m^i, H_h^i) = \left\| \mathbf{e}^i \mathbf{H}^i - H_h{}^i \mathbf{I} \right\|^2 \tag{10.23}$$

and subjected to the constraints:

$$\min \mathbf{H}^i \le H_h^i \le \max \mathbf{H}^i \tag{10.24a},$$

$$\frac{\min \mathbf{H}^i}{\max \mathbf{H}^i} \le e_j^i \le \frac{\max \mathbf{H}^i}{\min \mathbf{H}^i} \tag{10.24b}.$$

The rules adopted to establish these constraints were similar to those presented in Eq. (10.22).

10.4.4 Probabilistic method

Once the features associated with the healthy pipe were determined, a damage index $DI_{i,j}$ was calculated for each j-th guided wave signal along the i-th sensing path length. The index was defined as:

$$DI_{i,j} = \left| \frac{F_j^i - F_h{}^i}{F_h{}^i} \right| \tag{10.25a}$$

$$DI_{i,j} = \left| \frac{H_j^i - H_h{}^i}{H_h{}^i} \right| \tag{10.25b}.$$

They can determine the presence of damage along a given sensing path, but not for other points. To probe neighborhood portions of the pipe, these indexes were multiplied by a probability distribution function to compute the damage index in other portions. The value of this function is equal to 1 for every point located on the path, and it decreases with the increase of the

distance from the path. More details in this regards will be discussed later. By iterating the mentioned process to all the possible pairs of transducers, we obtained the damage index for each point of the pipe. Analytically, we divided the pipe into a uniform 1 mm×1 mm pixel, and the probability $P(x, y)$ that damage occurred at a grid node position (x, y) was defined as:

$$P(x,y) = \sum_{i=1}^{5} \sum_{j=1}^{m} DI_{i,j} W_{i,j}\left[r_{i,j}(x,y)\right] \tag{10.26}$$

where $W_{i,j}[r_{i,j}(x, y)]$ is the probabilistic weight for the j-th guided wave signal at the i-th sensing path at (x, y), and $r_{i,j}(x, y)$ is the relative distance of the node (x, y) to the actuator and to the sensor associated with the j-th guided wave signal at the i-th sensing path, i.e.:

$$r_{i,j}(x,y) = \frac{d^s_{i,j}(x,y) + d^a_{i,j}(x,y)}{d_{i,j}} - 1 \tag{10.27}.$$

In Eq. (10.27), $d_{i,j}$ is the length of the actuator-sensor line of sight, $d^a_{i,j}(x, y)$ and $d^s_{i,j}(x, y)$ are the node-actuator and the node-sensor distance, respectively. The relative distance is zero for a line between an actuator and a sensor. The selected probabilistic weight is the Gaussian function:

$$W_{i,j}\left[r_{i,j}(x,y)\right] = \exp\left[-\left(\frac{r_{i,j}(x,y)}{\beta}\right)^2\right] \tag{10.28}$$

where β is a constant coefficient which determines the size of the monitoring area. The probabilistic weight is a number comprised between 0 and 1. A weight equal to 1 indicates a point located on the line of sight between an actuator and a sensor, whereas a null weight is assigned to a point far from the sensing path. The coefficient β can be determined by a trial and error method, and depends on the circumferential distance between two neighboring transducers in the same ring. As shown in Fig. 10.10, which presents the probabilistic weight W relative to transducers pair BF and associated with three values of β, namely β =0.02, β =0.05, and β =0.1,

a small coefficient reduces the zone of influence of the transducer pair. This means that flaws nearby the transducers might go undetected. Conversely, a large β expands the zone of influence of the probabilistic weight causing, however, unwanted overlap among different transducer pairs. Fig. 10.10 suggests that for β =0.05 and β =0.1, there are some overlaps between path BF and path AE and also between path BF and path CG. In the study presented in this dissertation, we used β =0.02, which allowed for covering the entire monitoring area of the tube. This coefficient proved to be a good trade-off between sensitivity to damage and broad coverage area.

Finally, the damage index *DI* at a given node *(x, y)* of the grid was defined as:

$$DI(x,y) = \frac{P(x,y) - \mu_D}{\sigma_D} \tag{10.29}$$

where μ_D and σ_D are the mean and standard deviation value of *P(x,y)*, respectively. The index of Eq. (10.29) was normalized to the maximum value of the *DI*, and a threshold was applied such that all the values below the threshold were set to zero. The normalization was made in order to select a unique threshold value for all the kinds of damages considered in the study. In this dissertation, the threshold was arbitrarily set to 0.7. It is expected that a threshold close to 0 may generate false positives, whereas a threshold close to 1 may produce false negatives.

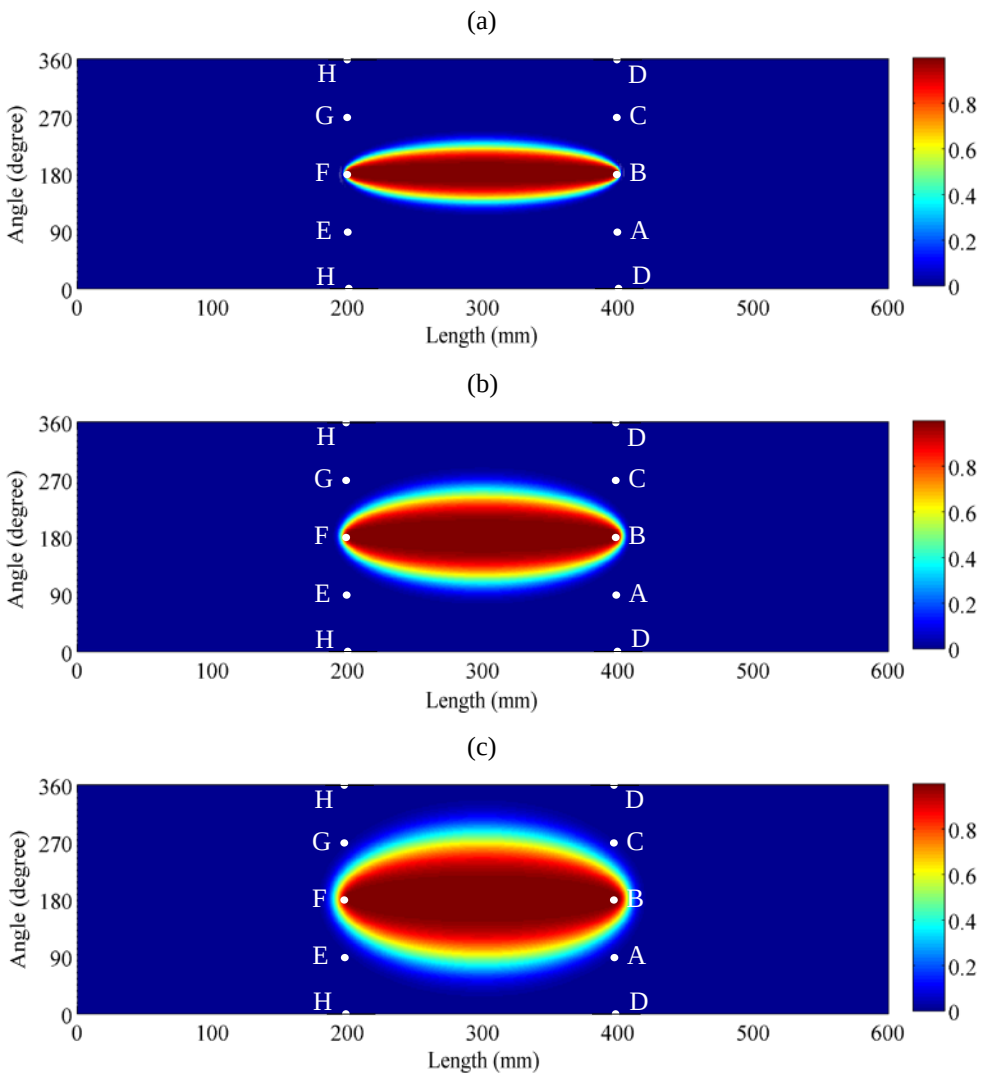

Figure 10.10. Map of the unwrapped pipe using different probabilistic weights for path BF: (a) β=0.02, (b) β=0.05, and (c) β=0.10.

10.5 RESULTS

10.5.1 Pristine pipe

In order to prove that the proposed methodology is baseline-free, we present first the results of the finite element simulation on the pristine pipe. Figure 10.11 shows the values F_j^i as defined in Eq. (10.16), and relative to the CWT-based features. Each inset is relative to a specific actuator-sensor distance and within the same inset the values associated with all actuator-sensor pairs are presented. It can be clearly seen that the values of the histograms are constant for each inset. As a result of the absence of structural anomalies along the path that connects each pair of transducers. In order to formulate a strategy for the computation of the damage index defined in Eq. (10.29), the constant F_h^i (i = 1, 2,…,5), that is representative of a healthy path, were determined for each actuator-sensor distance. These values were extracted from the five histograms presented in Fig. 10.11, and they are presented in Fig. 10.12. The amplitudes F_h^i were calculated by simply averaging the values F_j^i; since the values F_j^i for each set were similar the application of the COA was not necessary. Once the features F_h^i were determined, Eq. (10.25a) was applied and the probabilistic method discussed in Section 10.4.4 begun. Figure 10.13 shows the view of the unwrapped pristine pipe when the probabilistic method was applied, and the damage index as defined in Eq. (10.29) was computed. For this scenario, we did not apply any threshold. The image of the pipe does not show any structural flaw. The computational approach and the result depict an ideal situation where all the transducers have the same sensitivity. In reality this may not be the case and the measured signals for each same-distance path may be different. However, the use of a threshold in the damage detection algorithm can overcome this

issue. Finally, we will evaluate in Section 10.5.4 any effect of noise which is present in any experimental setting.

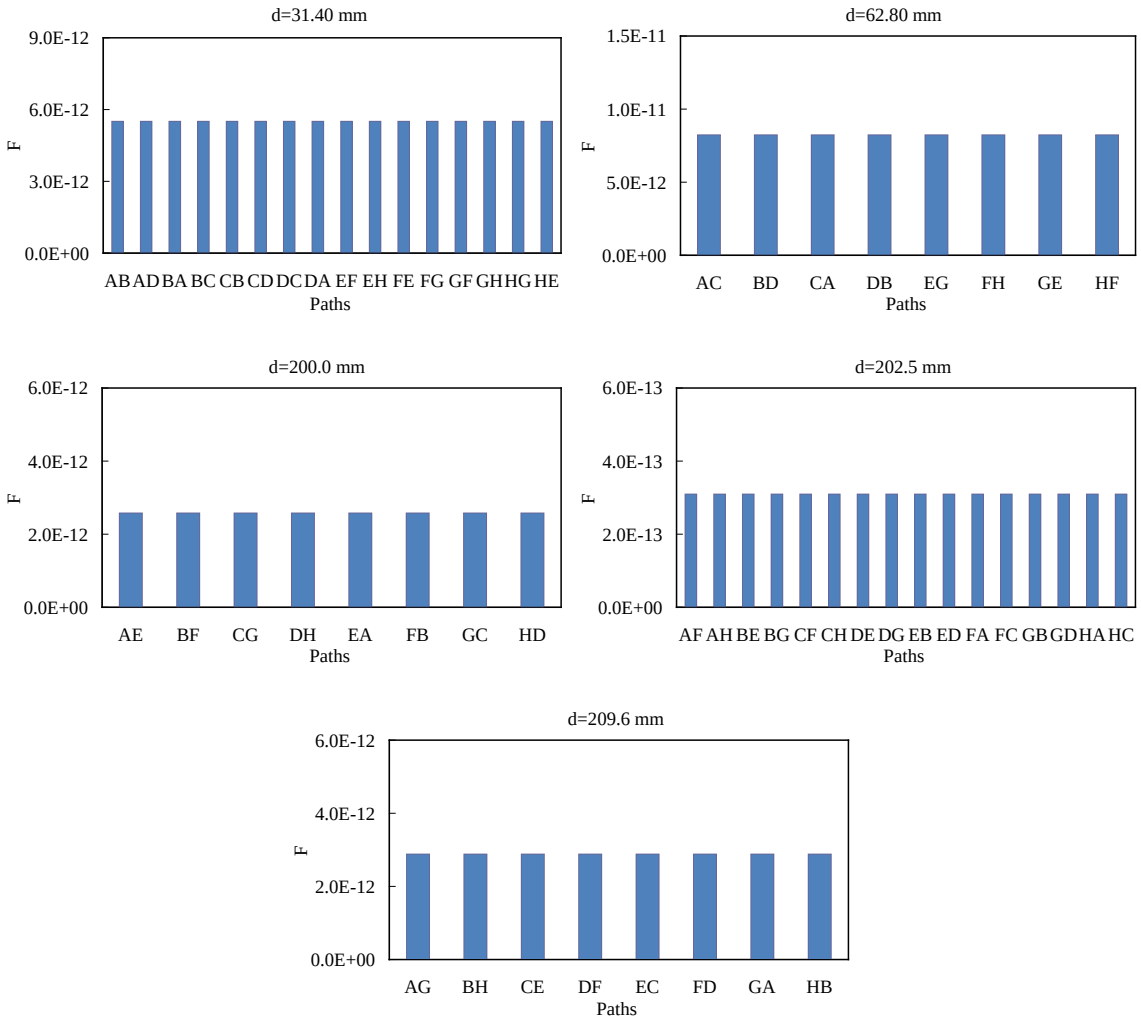

Figure 10.11. Analysis of the undamaged pipe. Values of the CWT-based feature *F* for each sensing path. The data are grouped according to the actuator-sensing distance *d*.

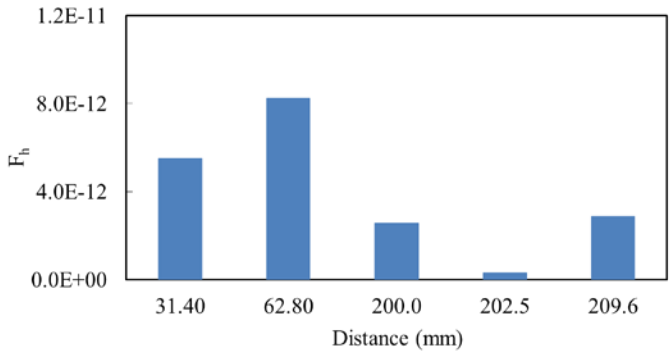

Figure 10.12. CWT-based features for healthy condition in the undamaged pipe.

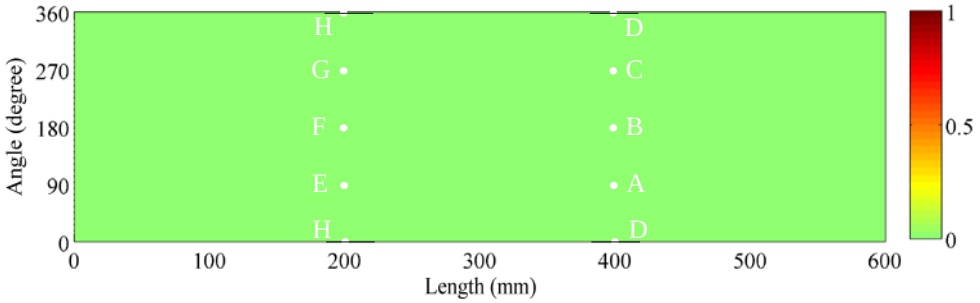

Figure 10.13. Analysis of the undamaged pipe. Unwrapped plate view of the map of the damage index on the pipe using the CWT-based feature.

10.5.2 Case scenario 1

The results associated with the first damage scenario are presented next. Similar to Fig. 10.11, Fig. 10.14 shows the values of the CWT-based features relative to the damaged pipe. In this scenario, the histograms are not constant which suggests that some wave paths were affected by the hole. In general, owing to the complex pattern of wave propagation in pipes, the least feature's value is not necessarily associated with a damaged condition, neither the tallest histogram identifies a healthy status. Moreover, in practical applications the transducers in the arrays may not have the same sensitivity, due to differences in manufacturing or bonding. Figure

10.15 presents the features (H_j^i) associated with the HT-based features. The meaning and the interpretation of the five insets are identical to those discussed for Fig. 10.14. Overall, it can be said that the information provided by the HT-based feature is similar to that provided by the CWT-feature and the difference between the two features is quantitative only. Both Figs. 10.14 and 10.15 were however unable to suggest which value of the histogram is associated with a pristine path. In order to determine the constants F_h^i and H_h^i (i = 1, 2, …, 5) to be inserted in Eqs. (10.25a) and (10.25b), respectively, the COA was used. The following parameters were set: population of countries=50; population of imperialist=5; maximum number of iterations=1000. The selection of these parameters was based on trial and error and their values generally depend on the number of variables of the objective function. A good rule of thumb is to choose 1 imperialist every 10 countries. Figure 10.16 shows the values of the CWT- and HT-based features associated with the undamaged path as a function of the travel distance. These values identify pristine conditions encountered by the guided waves as they travel the damaged pipe. By comparing the CWT-based feature's results displayed in Figs. 10.14 and 10.16, it can be seen that F_h is near to the value of F in paths with d equals to 31.4 and 62.8 *mm*, because there is no defects in these paths. In the remaining paths, F_h is between the minimum and maximum value of F, and it can be fund that the presence of damage causes to increase or decrease the amplitude of the guided waves which is related to the complexity of a pipe. For the HT-based feature, the same descriptions are valid.

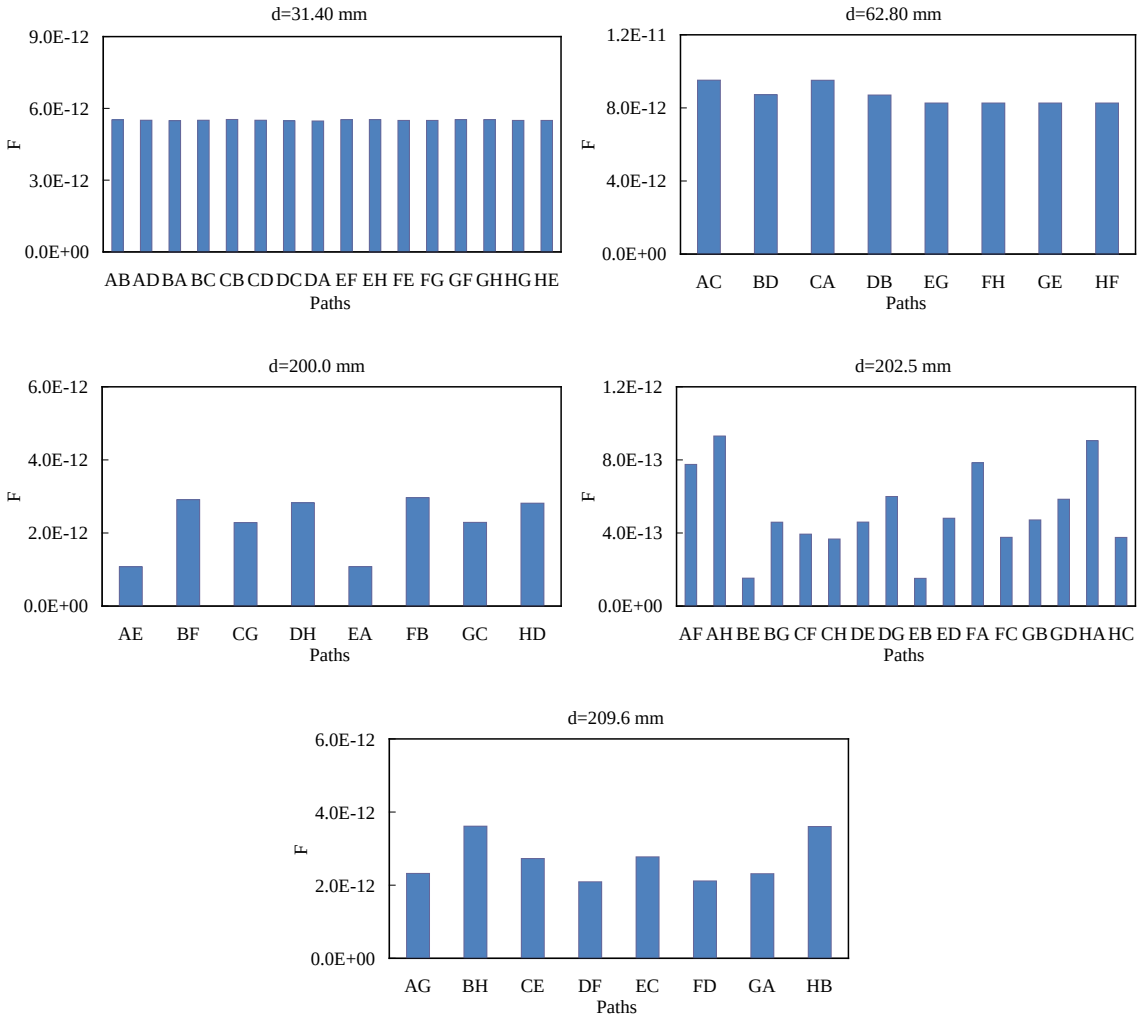

Figure 10.14. Analysis of the damaged pipe in the first scenario. Values of the CWT-based feature F for each sensing path. The data are grouped according to the actuator-sensing distance *d*.

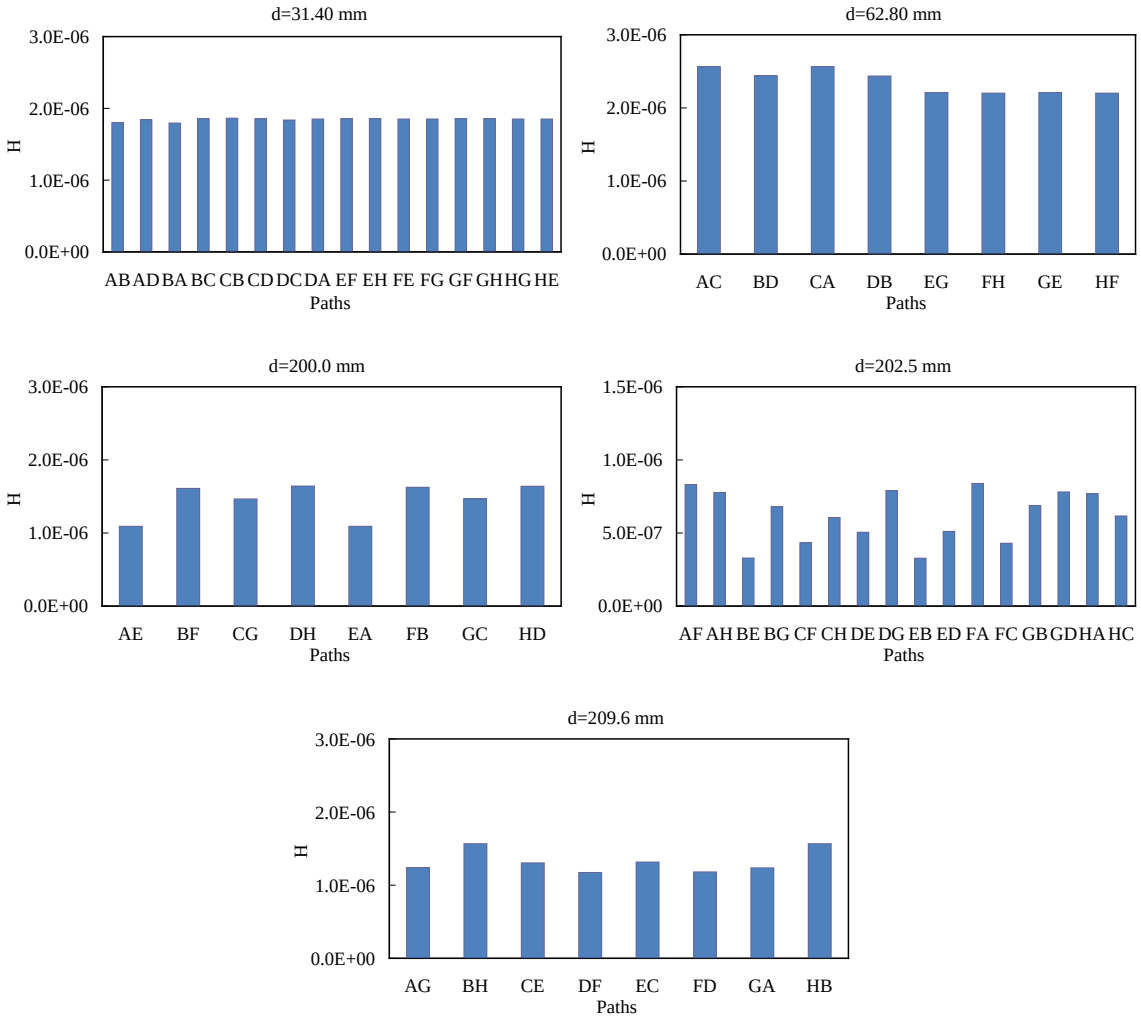

Figure 10.15. Analysis of the damaged pipe in the first scenario. Values of the HT-based feature *H* for each sensing path. The data are grouped according to the actuator-sensing distance *d*.

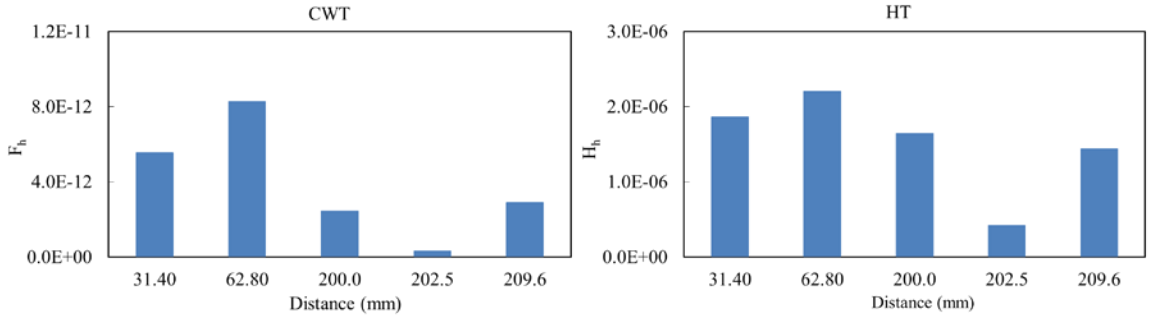

Figure 10.16. Analysis of the damaged pipe in the first scenario: results of the COA, features' values associated with healthy paths.

The results presented in Figs. 10.14 and 10.15 indicate the presence of some damage but are unable to show which values determine the size and the location. Thus, we applied the probabilistic method described in Section 10.4.4. Figures 10.17a provides the image of the pipe for the first damage case when the CWT-based feature was considered. The contour plot shows the amplitude of the damage index as defined in Eq. (10.29). The white circle superimposed to the image represents the true position of the hole. Owing to the threshold set in this study, the contour plot goes from 0.7 to 1 whereas all the *DI* below 0.7 were set to zero. The aim for considering a threshold 0.7 for the damage index is related to detect severe defects in the monitoring area of the pipe. Figure 10.17b shows the value of the damage index as calculated using the HT-based feature, i.e. by using the damage index defined in Eq. (10.25b). As we did not use any data generated in the simulation of the pristine pipe, the results presented in Fig. 10.17 show that the approach is baseline-free.

To evaluate the role of the coefficient β on the imaging reconstruction process, Figs. 10.18a and 10.18b are presented. They show the damage index associated with the CWT-based feature when β=0.05 and β=0.10 are used, respectively. The location of the true defect is overlapped with a circle. As the coefficient β increases the area relative to higher values of the damage index becomes larger, thus degrading the accuracy of the image.

To emphasize the advantage of the COA at locating and sizing damage, we applied the probabilistic method using the features F_h^i and H_h^i (i = 1, 2, …, 5) obtained by simply averaging the histograms shown in Fig. 10.14 and 10.15, rather than using the COA. The resulting images are presented in Fig. 10.19. The comparison of Fig. 10.19 with Fig. 10.17, clearly demonstrate that the image obtained with the use of COA outperforms the image presented in Fig. 10.19.

(a)

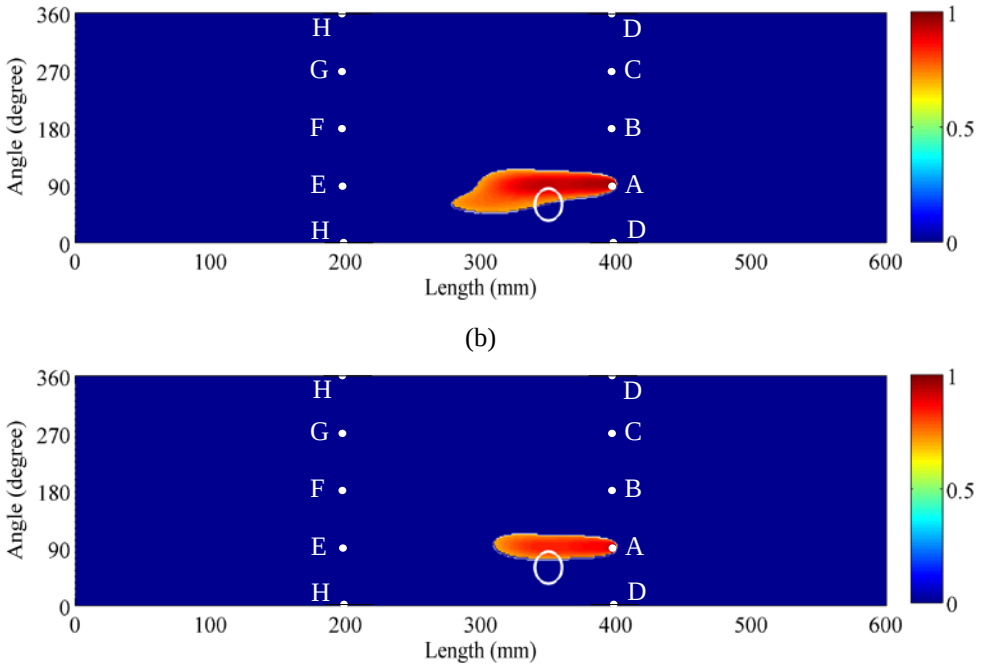

Figure 10.17. Mapping of the damage index for the first scenario. Results associated with (a) the CWT-based feature and (b) the Hilbert-based feature.

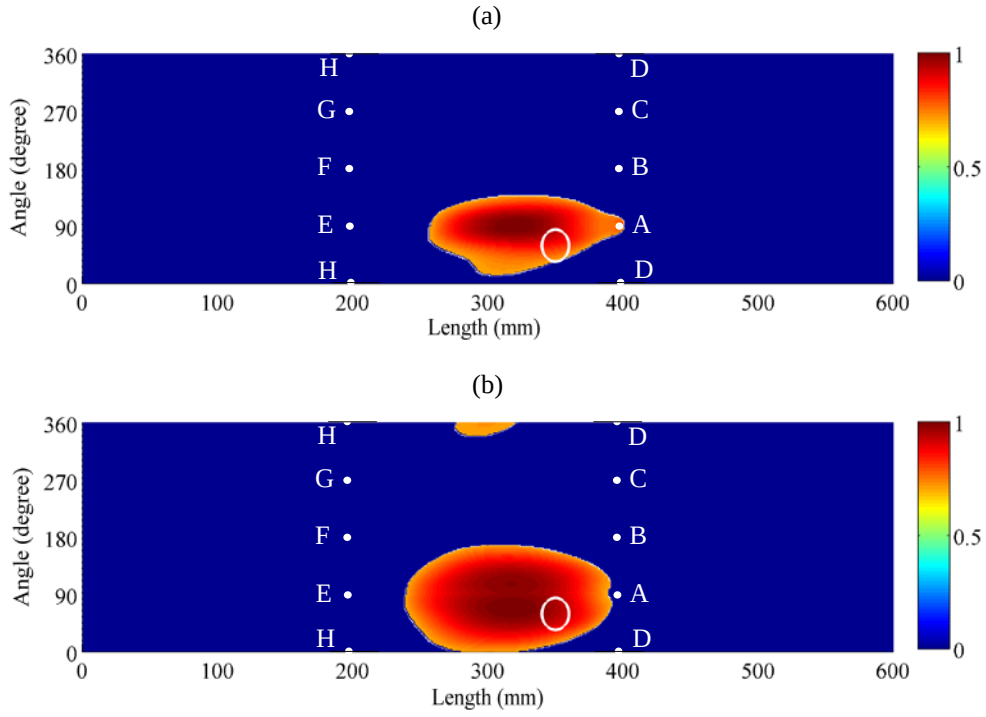

Figure 10.18. Mapping of the damage index for the first scenario using the CWT-based feature for: (a) β=0.05 and (b) β=0.10.

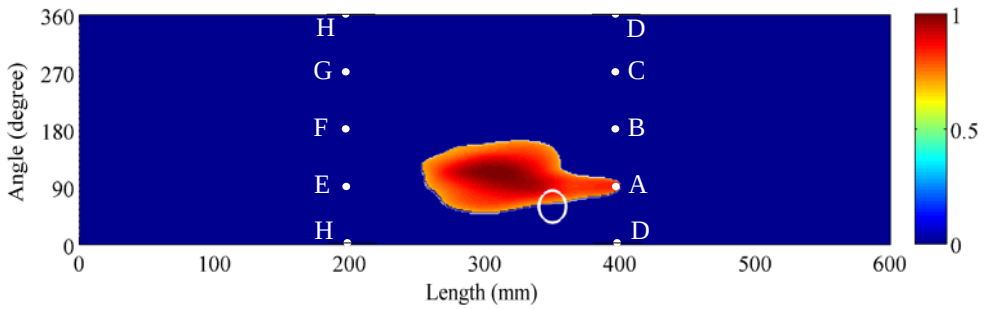

Figure 10.19. Mapping of the damage index on the pipe without the usage of the COA. Results associated with the CWT-based feature.

10.5.3 Other case scenarios

The damage index computed under the internal and external corrosion is shown in Figs. 10.20 and 10.21, respectively. The true position of the corroded areas is superimposed and it is within the area having the large damage index values. The results from both CWT- and HT- based feature are nearly identical. The pipe mapping associated with the fourth damage scenario, i.e. in the presence of a small through-thickness hole is illustrated in Fig. 10.22a. Despite the hole's diameter was much smaller than the signal's wavelength, the proposed algorithm enables the detection of small features. Finally, Fig. 10.22b shows the image of the pipe under the presence of two defects simultaneously. The presence of the small notch was determined but we could not locate the corrosion precisely.

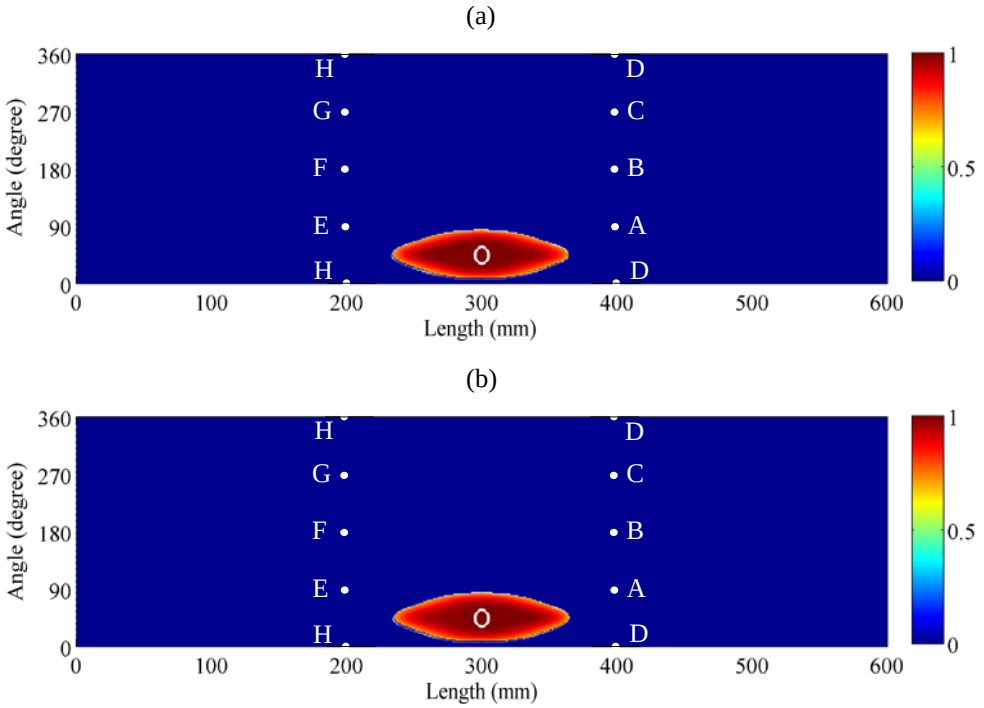

Figure 10.20. Mapping of the damage index for the second scenario. Results associated with (a) the CWT-based feature and (b) the Hilbert-based feature.

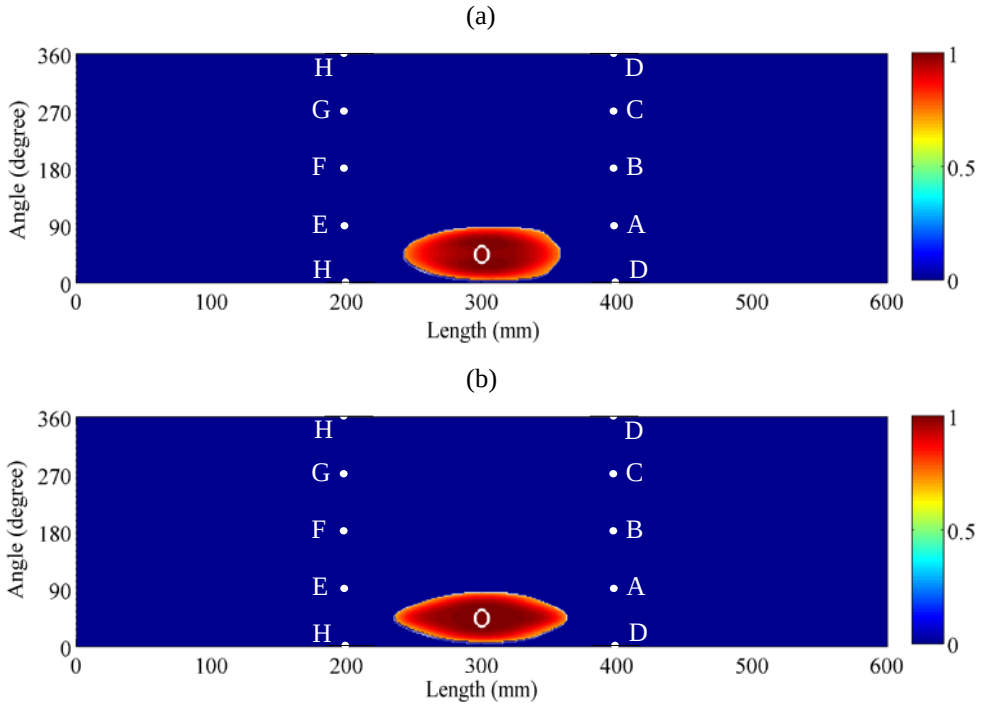

Figure 10.21. Mapping of the damage index for the third scenario. Results associated with (a) the CWT-based feature and (b) the Hilbert-based feature.

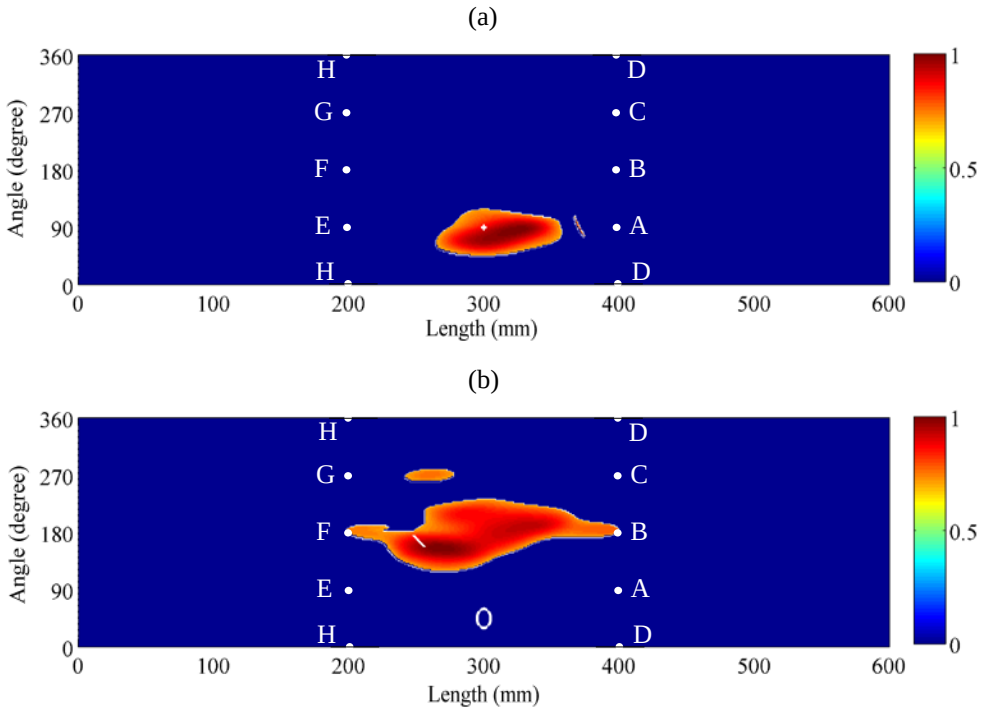

Figure 10.22. Mapping of the damage index for: (a) the fourth scenario and (b) the fifth scenario. Results associated with the CWT-based feature and (b) the Hilbert-based feature.

10.5.4 Effect of noise

Real monitoring systems always contain noise which may affect the ability to detect damage. To test the robustness of the proposed method against noise, white Gaussian noise was added to the original numerical signals using the MATLAB command *awgn* which is a function of the signal, the signal-to-noise ratio (SNR), and the power of the signal. We found that if we use 15 dB for the SNR, we can have a noisy signal that looks like a measured signal. Figure 10.23a displays a comparison between the original and noisy signals at node E when the 3-cycle tone burst was applied at node A. It can be seen that the effect of noise is significant at low value of displacement.

The map of the pipe subjected to the third damage scenario is shown in Fig. 10.23b. It presents the damage index computed using the HT-based feature corrupted with noise when the SNR is equal to ~15 dB. When compared to Fig. 10.21b, Fig. 10.23b shows some differences but are not significant. Similar conclusions can be drawn for the other damage scenarios which, for the sake of space, are not presented here. Therefore, it can be concluded that the presented approach is robust against some random noise in ultrasonic signals.

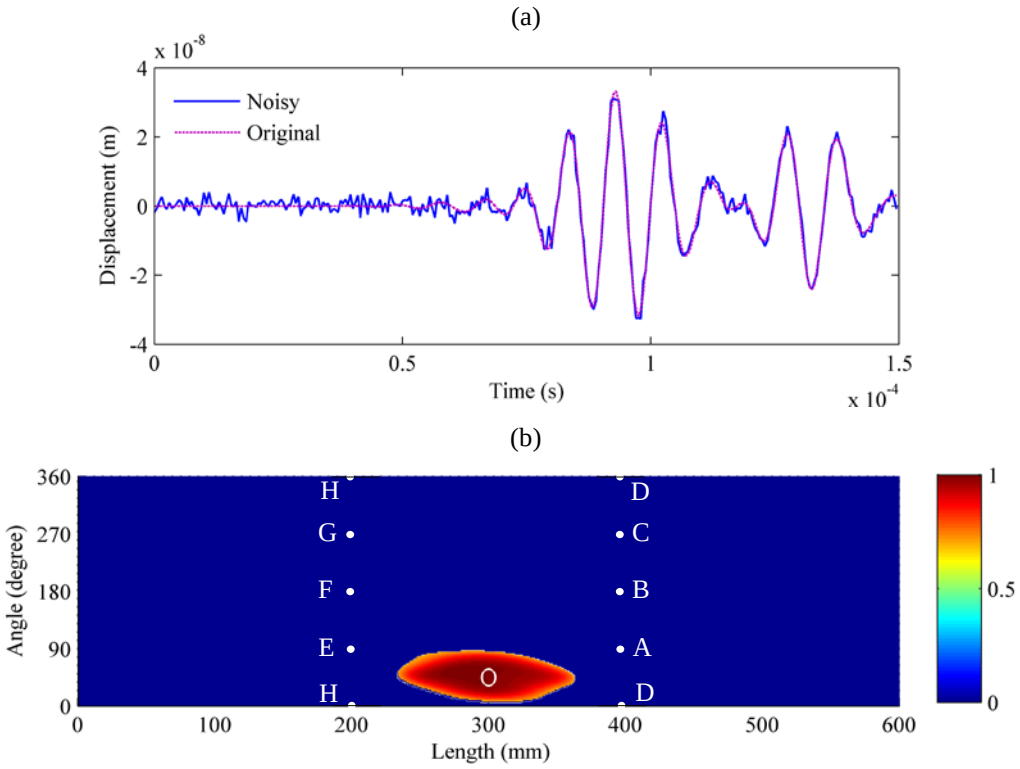

Figure 10.23. (a) Comparing the original and noisy ultrasonic signals for the third defect type at node E when the 3-cycle tone burst was applied at node A. (b) Mapping of the damage index for the third scenario with noise in ultrasonic signals the Hilbert-based feature.

10.5.5 Pitch-catch configuration: straight lines only

Finally, we considered the signals associated with the straight-line paths only, i.e. the lines of sight AE, BF, CG, and DH. This approach simulates those academic studies (Deng et al. 2008, Barshinger et al. 2002) that do not exploit the spiral sensing paths around the pipe and do consider instead the signal transmitted and received by the pair of transducers located along a line-of-sight. The results associated with such simulation are presented in Fig. 10.24 which refers to the first two damage scenarios. In the first damage case (Fig. 10.24a), we can determine the presence of damage but not its exact location, whereas the image relative to the second scenario (Fig. 10.24b) suggests that the defects are not localized on a single path but between two paths.

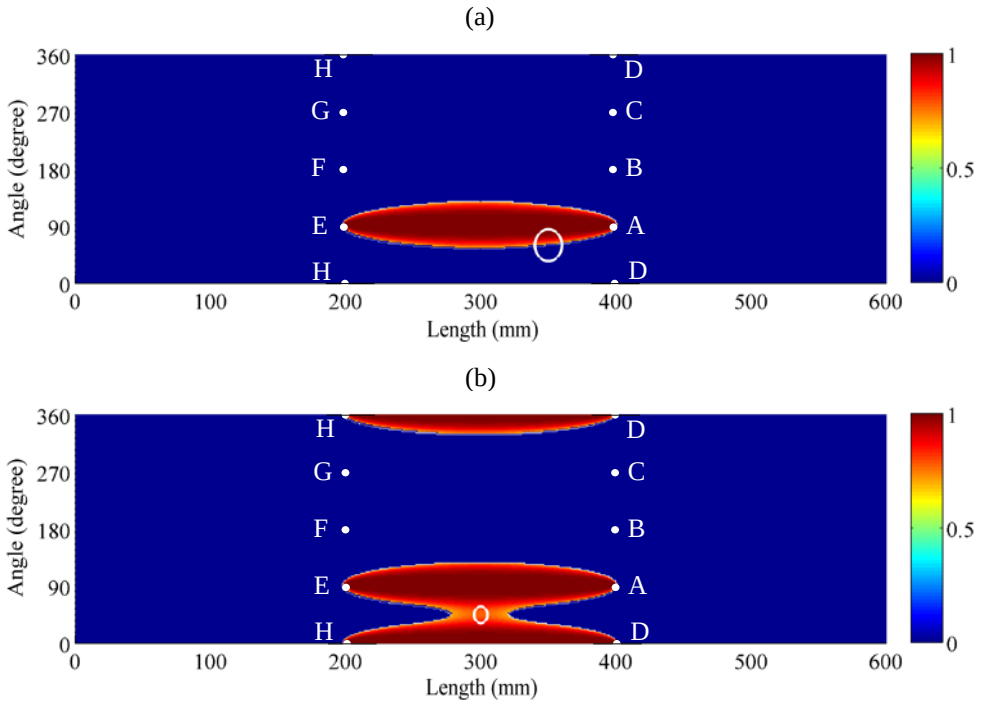

Figure 10.24. Mapping the damage index using a pitch-catch configuration. (a) The first damage scenario, and (b) the second damage scenario.

10.6 CONCLUSIONS

This chapter presents a baseline-free approach for the SHM of pipes using guided ultrasonic waves and signal processing. The waves are assumed to be generated and detected by two rings of ultrasonic transducers spaced apart along the axial direction of the pipes. The waves propagating along the axial and circumferential directions are processed using the CWT and the HT in order to extract two damage-sensitive features. Then, an optimization framework was used to identify those features' values associated with the wave paths not affected by damage. These features constituted the baseline dataset. Once the baseline was determined a probabilistic approach was used to estimate a damage index to map the structure of interest. With respect to most SHM methods based on guided waves, the proposed approach does not require data from a pristine structure.

We found that the images denote the presence of the defects. This was possible because some of the actuator-sensor paths were not affected by damage and the COA was able to identify the baseline dataset properly. This implies that the proposed health monitoring scheme is baseline free provided the material is isotropic, i.e. the attenuation is not dependent on the direction of propagation, which is true for common pipes and the sensitivity of the probing devices is very similar. To test the algorithm against noise, the recorded time waveforms were corrupted with noise and the images of the pipe with and without added noise were compared. The results demonstrated that irrespective of the presence of noise, the damage index based on the probabilistic approach was able to localize the damage. Overall, both the wavelet-based and the Hilbert-based features performed equally well and one methodology only could have been used without compromising the quality and the quantity of the results.

As the use of COA and the probabilistic method proposed here is novel, future studies may take one or more of the following directions. Validate the proposed methodology experimentally or compare it to the ultrasonic tomography method proposed by others such as Leonard and Hinders (2003). Consider damage located at many different locations, e.g. closer to the actuators/receivers. Test the robustness of the proposed method against the presence of broadband signals and smaller holes. Test the method on other waveguides, or evaluating any difference related to a position of the arrays. In fact, in this study, the transducers were considered to be attached to the interior wall. However, this solution may result not feasible unless the probing mechanism is movable such as in-line PIGS. Therefore any differences in terms of the sensitivity to the presence of damage between interior or exterior transducers should be investigated.

11.0 CONCLUSIONS AND RECOMMENDATIONS FOR FUTURE WORK

In this chapter, we present the principal findings and recommendations for future works relative to the main chapters of this document.

Chapter 3. When a slender beam is probed by a single straight chain, a single reflected wave is visible, whereas the vibration-induced solitary wave is formed by a few pulses. Under this configuration, the amplitude of the reflected solitary waves decreases monotonically by 7% when the beam goes from Euler stress to yielding stress. Across the same stress range the time of arrival of the vibration-induced solitary wave decrease by almost 95% whereas the time of arrival of the reflected wave vary by less than 1%. The amplitude of the vibration-induced wave does not exhibit a regular trend due to the presence of multiple peaks in the wave cluster. Nonetheless, the largest and the smallest value of the VSW/ISW ratio differ by 75%. Finally, the speed of the reflected solitary wave decreases monotonically by nearly 2% when the beam goes from compression to tension. This latter variation is much higher than any variation observed in acoustoelasticity in which the speed of linear waves in a bulk medium or a waveguide depends upon the applied stress. These finding are summarized in the second column of Table 11.1. The quantitative data refers to the features computed from the sensing site farer from the beam.

Table 11.1 also reports the findings associated with the same or other features and relative to the numerical analysis of the two straight chains and of the single and double L-shaped chains.

When the beam is probed by two single straight chains, a single reflected pulse and two pulses of the vibration induces waves VSW is observed in the first chain whereas a single transmitted wave and a cluster of pulses associated with the local oscillation of the beam are seen. These findings were obtained by considering the last particle of the second chain free to move. When this particle was restrained the results were slightly different and more variability of the selected features was observed. The third column of Table 11.1 summarizes some quantitative results associated with the features measured at the sensing sites closer to the beam.

When the slender beam is probed by a single L-shaped chain, the single pulse generated by the striker is fragmented into two pulses: the incident wave and a second pulse that is generated at the elbow. Then, a single reflected wave is visible. Prior to the arrival of the vibration induced solitary wave a cluster of pulses is visible and they are generated by the local oscillations of a few particles adjacent to the beam. The cluster of the vibration-induced solitary wave is constituted by several peaks. Overall the numerical force profiles present more pulses with respect to the straight chain case. The fourth column of Table 11.1 summarizes some quantitative results associated with the features measured at the sensing site farer from the beam.

When the slender beam is probed by two L-shaped chain, the force profiles are more complex, with the presence of cluster of peaks due to local oscillations of the particles near to the beam and due to the vibration of the beam. The fifth column of Table 11.1 summarizes some quantitative results associated with the features measured at the sensing sites closer to the beam.

Table 11.1. Summary of some of the features extracted from the four HNSW-based transducers

	Variation across axial stress ranging from Euler stress to yield stress.			
Feature	**Single straight chain**	**Two straight chains**[1]	**Single L-shaped chain**	**Two L-shaped chains**
RSW/ISW	7% monotonic decrease		6% monotonic decrease	2% monotonic decrease
VSW/ISW	75% non – monotonic fluctuation	95% non – monotonic fluctuation[2]		
TOF RSW	<1% monotonic increase	<1% monotonic increase	<0.4% monotonic increase	<0.1% monotonic increase
TOF VSW	~95% monotonic decrease	~85% monotonic decrease		1.5% non – monotonic fluctuation
Veloc. RSW	<2% monotonic decrease			
TSW/RSW	N/A	~2% monotonic decrease		
SVSW/TSW	N/A	~12% monotonic decrease		
TSW/ISW	N/A	~2% monotonic decrease		~4% monotonic increase
TOF TSW		~10% monotonic decrease		~0.3% monotonic decrease
TOF SVSW		~2% monotonic decrease		
RMS			60% nearly monotonic increase	17% nearly monotonic increase[3]
Energy			90% nearly monotonic increase	45% nearly monotonic increase[4]
VSW/TSW				10% monotonic decrease

For future work, simulating real railroad tracks in contact with a granular system is suggested with considering the effect of sleepers, fastenings, and ballast on the model of the structure. For this purpose, it would be more appropriate model the rail with the finite element method instead of the continuous beam theory.

[1] We report on this table the case of the last particle of the second chain free to move. See section 3.2.1.2 for the analysis of the case with the last particle of the second chain restrained.

[2] Please note that when two chains where used the wave induced by the vibration of the beam and propagating along the first chain was indicated as FVSW.

[3] It refers to the force profile measured in the first chain at the sensing site closest to the beam.

[4] It refers to the force profile measured in the first chain at the sensing site closest to the beam.

Chapter 4. We examined straight chains composed by particles of different materials and diameters. A total of 77 different chains was considered. The features of the amplitude ratio and the time of flight associated with the reflected wave and the vibration-induced solitary pulses were considered. The effect of the particle diameter and the material type on the sensitivity to the variation of the axial stress was examined. The results did not exhibit a regular trend, i.e. we did not find that for example the largest and heaviest particles provide the largest sensitivity.

For example, by considering the amplitude of the reflected wave we found that a chain made of magnesium particles, the lightest material considered in this analysis, provide the largest sensitivity when the sphere are 35 mm in diameter; conversely, particles are made of tungsten, the heaviest material considered in our analysis, the largest variation is observed when the sphere are 15 mm in diameter. This is because larger particles will carry out too much acoustic energy which will not be reflected but it will be transformed into beam vibration.

Overall it seems that if the product of the particle diameter multiplied its density is too high or too low, the sensitivity of the reflected solitary waves to the variation of axial stress decreases, both in terms of the amplitude and time of arrival.

We then fixed again the geometric and mechanical properties of the granular medium and considered the small effect that temperature has in the Young's modulus of the beam. We found that this effect is minimal on the solitary wave based features.

We simulated the scenario of a slender beam having different neutral temperatures. We used the pattern recognition classifier of the artificial neural network to associate an input vector formed by a set of few solitary wave-based features to the true neutral temperature. We found that the combination of certain features was able to identify the neutral temperature with a margin of error of less than 0.5 °C.

Finally, the same four chain configurations discussed above where considered to examine a rail-like beam, i.e. a 20 meters long beam having the cross section area and the least moment of inertia of an AREMA 141 rail. Considering this rail-like beam fixed at both ends we determined that the Euler stress is close to 15 MPa. However, field experience showed that real rails buckle at much higher stresses, due to the presence of ties, tie plates, and ballast. We found that the configuration with two straight chains provide the largest sensitivity to the variation of axial stress; in particular the amplitude of the transmitted wave across the web shows a variation of 5% in the range of stress considered here. Moreover, the time of flight of the transmitted and the vibration induced solitary waves vary by 1%. Again, these numbers are higher than any number associated with the acoustoelastic phenomenon. Also, the configuration with the L-shaped transducers shows some degree of sensitivity although not as large as for the straight chain case.

For future study, improving the model of the rail and run the same parametric analysis presented in this chapter but applied to rail sections in order to find the optimal design of the chain of particles that provides the largest sensitivity is suggested.

Chapter 5. In this chapter, we presented the results of a series of four rounds of experiments that aimed at validating the numerical predictions described in Chapter 3. The same beam, the same loading machine, and the same testing protocol were used for the four rounds of experiments. In all the experiments we pre-loaded the beam up to 20% of its yielding load and then held the ends by setting the loading machine in a displacement control. Then, the beam was heated until the nominal stress was about 55% of the beam's Euler stress. For each experiment the beam was heated twice, i.e. the heating ramp was monitored twice using the solitary-wave based transducer. The beam was probed at discrete temperature steps and for each step 15 measurements were taken in order to investigate the statistical significance of the experiments.

The figures of the axial stress as a function of the temperature demonstrate that the setup was highly repeatable. By averaging the interpolating data, we found that the average stress rate was 1.773 ± 0.096 MPa/°C, i.e. the standard deviation of the stress rate was 5.4%.

Overall the experimental results confirmed most of the numerical predictions. The time waveforms relative to the single L-shaped transducer showed smaller pulses due to the presence of attenuation and acoustic leakage across the guide's elbow. This implied that the numerical features overestimated the experimental values. The standard deviation associated with each temperature step was in most case satisfactory. For some features, the standard deviation has the same order of magnitude of the predicted variation of that feature with respect to stress. The arrival time of the cluster associated with the vibration-induced solitary waves provides the largest sensitivity to stress, whereas the largest amplitude within the same cluster did not show any regular trend with respect to the temperature. As some of the selected features denoted a monotonic variation with respect to stress, we were able to extrapolate a few parabolic relationships between the wave's feature and stress. These relationships allows for the univocal determination of the neutral temperature and the estimation of the axial stress.

The analysis of two L-shaped transducers provided similar evidences. Here, however more features can be extracted due to the presence of a second chain. Moreover, the experiment confirmed that the use of two transducers is easier to accomplish as the presence of the two granular systems makes easy to maintain contact between the transducers and the beam to be inspected. We confirmed experimentally that the relative variation of the wave speed with respect to stress is significantly higher of what can be observed in acoustoelasticity.

The analysis of the single straight chain showed that the time waveforms are less noisy than the corresponding waveforms associated with the L-shaped transducers. This eases the

identification of the pulses. However, with the exception of the arrival of the VSW and the energy associated with the oscillation of the particles adjacent to the beam, the other features do not vary significantly when compared to the standard deviation of the experimental data. As for the L-shaped case, a parabolic relationship between the arrival time of the VSW and the axial stress was extrapolated.

Similar conclusions can be driven from the analysis of the two straight chains. For the straight chains, both cases, the relative variation of the solitary wave speed is well above few percent but the data demonstrate a lack of repeatability that warrants more investigation.

Chapter 6. This chapter presented a reference-free approach for structural health monitoring of plate-like structures by means of guided ultrasonic waves and signal processing. The waves were generated by an array of transducers able to generate and detect the propagation of the first anti-symmetric mode. The approach included the extraction of damage-sensitive features from the signals processed by means of the continuous wavelet transform and the empirical mode decomposition. The signals from all the possible combinations of the array's actuator-sensor pairs were considered. The features are examined to assess the presence of damage and then used in a probabilistic approach to estimate a discontinuity index that maps the structure under consideration.

In this study, the monitoring system is modeled using a finite element model. A square aluminum plate is considered and the propagation of the ultrasound is generated by imposing a time-varying force profile perpendicular to ten nodes of the model. Damage was simulated in terms of an isolated through-the-thickness notch. The features extracted from the wavelet transform and the mode decomposition were able to identify the presence of the defect. This was possible because some of the actuator-sensor paths were not affected by damage and the

amplitude associated with the sensing path having same distance was identified. This implies that the proposed health monitoring scheme is baseline free provided the material is isotropic, i.e. the attenuation and the dispersion is not dependent on the direction of propagation, and the sensitivity of the probing devices is very similar. To test the algorithm against noise, the recorded time waveforms were corrupted with noise and the images of the plate with and without added noise were compared. The results demonstrate that irrespective of the presence of noise, the discontinuity index based on a probabilistic approach is able to localize the damage.

As the method has been tested under the condition that part of the array was not affected by damage, future numerical (and experimental) studies should consider a multi-damaged scenario such that all the sensing paths are affected by one or more structural anomalies.

Chapter 7. This chapter presented a probabilistic-based method for detecting defects in underwater waveguides. The method employs laser pulses to generate broadband guided waves and non-contact immersion transducers to detect the propagation of the leaky S_0 mode. To localize defects, a pseudo reference-free imaging algorithm based on wavelet transform and probabilistic analysis is proposed. The experiments show that notches as small as few mm in length can be detected as well as areas with simulated corrosion. With respect to the existing GUW-based methods for plates, the imaging approach presented in this chapter does not require the measurement from a pristine structure, it is truly non-contact, and it requires a smaller number of transducers.

Future work may consider a different planar distribution of the transducers, more complicated structural configurations, and different features for the creation of the damage index.

Chapter 8. In this chapter, a NDE technique for immersed metallic plates was presented. The technique is based on the noncontact generation and detection of GUWs. The waves are generated by a pulsed laser and are detected by an array of IUTs.

The propagation of the leaky first symmetric mode along an aluminum plate subjected to a few representative defects was characterized in the time, frequency, and joint time-frequency domain. A set of eight features were extracted from these domains to create a vector of damage indexes that was then fed to an ANN. The neural network instead allows the classification of the type of damage, since there is the availability of data from the structure with known types and levels of damage. Overall, we found that the ANN provides better results at detecting the presence of damage and we also found that the number of features selected is not critical to enhance the success rate. Actually, the highest success rate was achieved in the case of single feature.

The success rate of the algorithms may be increased by either extracting different features and/or by modifying the architecture of the network. Future studies may consider different arrangements of the transducers within the array, may test longer, wider, and thicker plates, and assess the feasibility of the proposed approach in presence of fouling.

Chapter 9. In this chapter, an automated damage-detection technique for metallic plates submerged in water is presented. The technique is based on the noncontact generation and detection of ultrasounds in water and the processing of the leaky S_0 mode. An immersion focused transducer was used to insonify an aluminium plate whereas an array of five transducers, arranged along a semi-circle was used to detect the waves. For each sensor, the signals were processed to extract three features in the time and frequency domain. These features were assembled to constitute the input vector of an artificial neural network to identify and classify

four different scenarios, three of which associated with the presence of five structural defects artificially devised on the backwall of the test plate.

The results demonstrated that the method is repeatable, robust against background noise, and it is able to classifying properly up to 75% of the overall data points. Obviously, the classification results presented here only refer to the plate under test and to the specific defect examined. The consistent detection of data scatters along the scan line suggested that the effects of the base supports on the ultrasonic signals paired the effects induced by the small artificial defect, namely the dent, the abraded area, and the through thickness hole. The use of the immersion transducer as the actuation system is a simpler and an economical solution with respect to pulsed laser we used in previous studies. The defect classification performance could also be improved by selecting a larger number of signal features, by optimizing the number of neurons of the neural network, or by arranging the spatial direction of the detectors differently.

Chapter 10. This chapter presented a baseline-free approach for the SHM of pipes using guided ultrasonic waves and signal processing. The waves were assumed to be generated and detected by two rings of ultrasonic transducers spaced apart along the axial direction of the pipes. The waves propagating along the axial and circumferential directions are processed using the CWT and the HT in order to extract two damage-sensitive features. Then, an optimization framework was used to identify those features' values associated with the wave paths not affected by damage. These features constituted the baseline dataset. Once the baseline was determined a probabilistic approach was used to estimate a damage index to map the structure of interest.

The proposed monitoring scheme was validated numerically using a commercial finite element code. A mild steel pipe was modeled and the propagation of the ultrasound was

generated by imposing a time-varying force profile perpendicular to eight nodes of the mesh. These nodes were distributed over two rings placed 200 mm apart and the four nodes of each ring were equally spaced along the circumferential direction. Three kinds of damage, namely through-the-thickness hole, corrosion, and notch were modeled and combined to give rise to five different damage scenarios.

The SHM approach proposed in this chapter is expected to be equally valid when applied to larger pipes as well as any other structures that support the propagation of GUWs. For larger pipes, we expect that the number of transducers needs to be increased in order to offer the same image quality and resolution, and to avoid blind spots where damage may be missed. Nonetheless, the amount of transducers to be used is expected to be lesser than the number of transducers adopted in the systems presented in the literature. Similarly, for other structures, the number of transducers will be dependent on the area to be covered. Finally, the frequency to be used for the excitation signals will depend on the dispersive nature of the waveguide and the possibility to isolate single mode.

With respect to the existing GUW-based imaging methods for pipes, the proposed SHM approach is baseline free and it is based on the simultaneous use of a transmitter and a receiver that are not necessarily located along a straight line of sight. The method is also suitable for parallel computing and it seems to perform well even if a small number of sensors is used. Some limitations that however need to be verified seem to be: lower performance when multiple damages are present and low accuracy at determining the exact shape of the defect.

Future studies can also validate the proposed methodology experimentally, whereas numerical and experimental studies should evaluate the robustness of the proposed method against the presence of broadband signals, smaller holes or other waveguides.

PUBLICATIONS STEMMED FROM THIS WORK

Peer-reviewed journal paper

1. **A. Bagheri**, and P. Rizzo, "Guided ultrasonic wave testing of an immersed plate with hidden defects", *Optical Engineering*, 2015, under review.
2. **A. Bagheri**, E. La Malfa Ribolla, P. Rizzo, and L. Al-Nazer, "On the coupling dynamics of thermally stressed beams and granular chains", *Archive of Applied Mechanics*, 2015, under review.
3. **A. Bagheri**, P. Rizzo, and K. Li, "An optimization-based algorithm for ultrasonic imaging of cylindrical structures", *Mechanical Systems and Signal Processing*, 2015, first revision submitted.
4. **A. Bagheri**, E. La Malfa Ribolla, P. Rizzo, L. Al-Nazer, and G. Giambanco, "On the use of L-shaped granular chains for the assessment of thermal stress in slender structures", *Experimental Mechanics*, 2015, 55(3), 543-558.
5. **A. Bagheri**, P. Rizzo, and L. Al-Nazer, "On the optimization of granular medium to infer the axial stress in slender structures", *Mechanics of Advanced Materials and Structures*, 2015, DOI:10.1080/15376494.2015.1039679.
6. **A. Bagheri**, E. Pistone, and P. Rizzo, "Outlier analysis and artificial neural network for the non-contact nondestructive evaluation of immersed plates", *Research in Nondestructive Evaluation*, 2015, DOI:10.1080/09349847.2015.1022677.
7. **A. Bagheri**, P. Rizzo, and L. Al-Nazer, "Determination of the neutral temperature of slender beams by means of nonlinear solitary waves", *ASCE Journal of Engineering Mechanics*, 2014, 04014163.
8. **A. Bagheri**, E. Pistone, and P. Rizzo, "Guided ultrasonic wave imaging for immersed plates based on wavelet transform and probabilistic analysis", *Research in Nondestructive Evaluation*, 2014; 25(2), 63-81.
9. **A. Bagheri**, K. Li, and P. Rizzo, "Reference-free damage detection by means of wavelet transform and empirical mode decomposition applied to Lamb waves", *Journal of Intelligent Material Systems and Structures*, 2013; 24(2), 194-208.

Conference Paper

1. A. Bagheri, E. Pistone, and P. Rizzo, "On the processing of leaky guided ultrasonic waves for the noncontact inspection of underwater structures", 24th ASNT Research Symposium, Anaheim, USA, 2015.
2. A. Bagheri, E. La Malfa Ribolla, P. Rizzo, and L. Al-Nazer, "Granular chains for the assessment of thermal stress in slender structures", In 2015 SPIE Smart Structures/NDE, San Diego, USA, 2015.
3. A. Bagheri, E. La Malfa Ribolla, P. Rizzo, and L. Al-Nazer, "Solitary waves for the assessment of thermal stress and neutral temperature in slender structures", The 94th TRB Annual Meeting, Washington DC, USA, 2015.
4. A. Bagheri, P. Rizzo, and L. Al-Nazer, "Solitary waves to infer axial stress in slender structures: a numerical model", IMAC XXXIII A Conference and Exposition on Structural Dynamics, Orlando, USA, 2015.
5. P. Rizzo, A. Bagheri, and K. Li, "Guided ultrasonic waves for the nondestructive evaluation imaging of pipes", Proceedings of ASCE's Shale Energy Engineering Conference, Pittsburgh, USA, 2014, pp. 151-158.
6. A. Bagheri, P. Rizzo, E. Pistone, "On the processing of leaky guided waves propagating in immersed plates", In SPIE Smart Structures and Materials+Nondestructive Evaluation and Health Monitoring, San Diego, USA, 2014, 90640W.
7. E. Pistone, A. Bagheri, K. Li, and P. Rizzo, "Signal processing for the inspection of immersed structures", Proc. SPIE 8695, Health Monitoring of Structural and Biological Systems 2013, San Diego, USA, 2013, 86951A.
8. E. Pistone, A. Bagheri, and P. Rizzo, "Signal processing for the smart inspection of underwater plates", Proceedings of 6th ECCOMAS Conference on Smart Structures and Materials, SMART2013, Politecnico di Torino, Italy, 2013.
9. E. Pistone, A. Bagheri, K. Li, and P. Rizzo, "Advancements on the inspection of underwater plates by means of guided waves", The 9th International Workshop on Structural Health Monitoring, Stanford University, USA, 2013.

List of other publications generated at Pitt

1. K. Li, **A. Bagheri**, and P. Rizzo, "A parametric study on the optimization of metamaterials for energy harvesting applications", *Smart Materials and Structures,* 2015, under review.
2. **A. Bagheri**, and P. Rizzo, "Determination of the serviceability of tennis balls using nonlinear solitary waves", *Sports Engineering*, 2015, under review.
3. **A. Bagheri**, A. Zare Hosseinzadeh, G. Ghodrati Amiri, and P. Rizzo "Time domain damage localization and quantification in seismically excited structures using a limited number of sensors", *Journal of Vibration and Control*, 2014, second revision submitted.
4. **A. Bagheri**, D. Persano Adorno, P. Rizzo, R. Barraco, and L. Bellomonte, "Empirical mode decomposition and neural network for the classification of electroretinographic data", *Medical & Biological Engineering & Computing*, 2014; 52:619–628.

BIBLIOGRAPHY

Adler, L., de Billy, M., & Quentin, G. J. (1982). Excitation of ultrasonic Rayleigh leaky waves at liquid-solid interface for general angle incidence. Journal of Applied Physics, 53(12), 8756-8758.

Ahmad, R., Banerjee, S., & Kundu, T. (2009). Pipe wall damage detection in buried pipes using guided waves. Journal of Pressure Vessel Technology, 131(1), 011501.

Alleyne, D. N., & Cawley, P. (1996). The excitation of Lamb waves in pipes using dry-coupled piezoelectric transducers. Journal of Nondestructive Evaluation, 15(1), 11-20.

Alleyne, D., & Cawley, P. (1991). A two-dimensional Fourier transform method for the measurement of propagating multimode signals. The Journal of the Acoustical Society of America, 89(3), 1159-1168.

Anton, S. R., Inman, D. J., & Park, G. (2009). Reference-free damage detection using instantaneous baseline measurements. AIAA journal, 47(8), 1952-1964.

Atashpaz-Gargari, E., & Lucas, C. (2007, September). Imperialist competitive algorithm: an algorithm for optimization inspired by imperialistic competition. InEvolutionary computation, 2007. CEC 2007. IEEE Congress on (pp. 4661-4667). IEEE.

Bagheri, A., La Malfa Ribolla, E., Rizzo, P., Al-Nazer, L., & Giambanco, G. (2015). On the use of L-shaped granular chains for the assessment of thermal stress in slender structures. Experimental Mechanics, 2015, 55(3), 543-558.

Bagheri, A., Li, K., & Rizzo, P. (2013). Reference-free damage detection by means of wavelet transform and empirical mode decomposition applied to Lamb waves. Journal of Intelligent Material Systems and Structures, 24(2), 194-208.

Bagheri, A., Pistone, E., & Rizzo, P. (2014). Guided ultrasonic wave imaging for immersed plates based on wavelet transform and probabilistic analysis. Research in Nondestructive Evaluation, 25(2), 63-81.

Bagheri, A., Pistone, E., & Rizzo, P. (2015). Outlier Analysis and Artificial Neural Network for the Non-contact Nondestructive Evaluation of Immersed Plates. Research in Nondestructive Evaluation, DOI: 10.1080/09349847.2015.1022677.

Bagheri, A., Razeghi, H. R., & Amiri, G. G. (2012). Detection and estimation of damage in structures using imperialist competitive algorithm. Shock and Vibration, 19(3), 405-419.

Bagheri, A., Razeghi, H.R., & Ghodrati Amiri, G. (2012). Detection and estimation of damage in structures using imperialist competitive algorithm. Shock and Vibration, 19(3), 405-419.

Bagheri, A., Rizzo, P., & Al-Nazer, L. (2014). Determination of the neutral temperature of slender beams by means of nonlinear solitary waves. ASCE Journal of Engineering Mechanics, 04014163.

Bagheri, A., Rizzo, P., & Al-Nazer, L. (2015). On the optimization of granular medium to infer the axial stress in slender structures", Mechanics of Advanced Materials and Structures, DOI:10.1080/15376494.2015.1039679.

Banerjee, S., & Kundu, T. (2007). Ultrasonic field modeling in plates immersed in fluid. International Journal of Solids and Structures, 44(18), 6013-6029.

Bar-Cohen, Y., & Chimenti, D. E. (1984). Leaky Lamb waves in fiber-reinforced composite plates. Review of Progress in Quantitative Nondestructive Evaluation. 3, 1043-1049.

Barshinger, J., Rose, J. L., & Avioli, M. J. (2002). Guided wave resonance tuning for pipe inspection, ASME Journal of Pressure Vessel Technology, 124, 303-310.

Bartoli, I., Lanza di Scalea, F., Fateh, M., & Viola, E. (2005). Modeling guided wave propagation with application to the long-range defect detection in railroad tracks. NDT&E International, 38, 325-334.

Begambre, O., & Laier, J.E. (2009). A hybrid particle swarm optimization-simplex algorithm (PSOS) for structural damage identification. Advances in Engineering Software, 40(9), 883–891.

Berhanu, B., Rizzo, P., & Ochs, M. (2013). Highly nonlinear solitary waves for the assessment of dental implant mobility. Journal of Applied Mechanics, 80(1), 011028.

Bertoni, H. L., & Tamir, T. (1973). Unified theory of Rayleigh-angle phenomena for acoustic beams at liquid-solid interfaces. Applied Physics, 2(4), 157-172.

Billy, M., Adler, L., & Quentin, G. (1984). Measurements of backscattered leaky Lamb waves in plates. The Journal of the Acoustical Society of America, 75(3), 998-1001.

Boechler, N., Theocharis, G., & Daraio, C. (2011). Bifurcation-based acoustic switching and rectification. Nature materials, 10(9), 665-668.

Cai, L., Rizzo, P., & Al-Nazer, L. (2013a). On the coupling mechanism between nonlinear solitary waves and slender beams. International Journal of Solids and Structures, 50(25), 4173-4183.

Cai, L., Yang, J., Rizzo, P., Ni, X., & Daraio, C. (2013b). Propagation of highly nonlinear solitary waves in a curved granular chain. Granular Matter, 15(3), 357-366.

Carretero-González, R., Khatri, D., Porter, M. A., Kevrekidis, P. G., & Daraio, C. (2009). Dissipative solitary waves in granular crystals. Physical review letters, 102(2), 024102.

Cawley, P., Lowe, M. J. S., Alleyne, D. N., Pavlakovic, B., & Wilcox, P. (2003). Practical long range guided wave inspection-applications to pipes and rail. Materials Evaluation, 61(1), 66-74.

Cegla, F. B., Cawley, P., & Lowe, M. J. S. (2005). Material property measurement using the quasi-Scholte mode-A waveguide sensor. The Journal of the Acoustical Society of America, 117(3), 1098-1107.

Chen, J., & Young, B. (2006). Stress–strain curves for stainless steel at elevated temperatures. Engineering Structures, 28(2), 229-239.

Chen, J., Su, Z., & Cheng, L. (2010). Identification of corrosion damage in submerged structures using fundamental anti-symmetric Lamb waves. Smart Materials and Structures, 19(1), 015004.

Cheraghi, N., & Taheri, F. (2007). A damage index for structural health monitoring based on the empirical mode decomposition. Journal of Mechanics of Materials and Structures, 2(1), 43-61.

Cheraghi, N., Zou, G. P., & Taheri, F. (2005). Piezoelectric-Based Degradation Assessment of a Pipe Using Fourier and Wavelet Analyses. Computer-Aided Civil and Infrastructure Engineering, 20(5), 369-382.

Clarke, T., & Cawley, P. (2011). Enhancing the defect localization capability of a guided wave SHM system applied to a complex structure. Structural Health Monitoring, 10(3), 247-259.

Clarke, T., Cawley, P., Wilcox, P. D., & Croxford, A. J. (2009). Evaluation of the damage detection capability of a sparse-array guided-wave SHM system applied to a complex structure under varying thermal conditions. Ultrasonics, Ferroelectrics, and Frequency Control, IEEE Transactions on, 56(12), 2666-2678.

Coste, C., & Gilles, B. (1999). On the validity of Hertz contact law for granular material acoustics. The European Physical Journal B-Condensed Matter and Complex Systems, 7(1), 155-168.

Coste, C., Falcon, E., & Fauve, S. (1997). Solitary waves in a chain of beads under Hertz contact. Physical Review E, 56(5), 6104.

Daraio, C., Nesterenko, V. F., Herbold, E. B., & Jin, S. (2005). Strongly nonlinear waves in a chain of Teflon beads. Physical Review E, 72(1), 016603.

Daraio, C., Nesterenko, V. F., Herbold, E. B., & Jin, S. (2006a). Energy trapping and shock disintegration in a composite granular medium. Physical Review Letters, 96(5), 058002.

Daraio, C., Nesterenko, V. F., Herbold, E. B., & Jin, S. (2006b). Tunability of solitary wave properties in one-dimensional strongly nonlinear phononic crystals. Physical Review E, 73(2), 026610.

Daubechies, I. (1992). Ten lectures on wavelets. CBMS-NSF Conference Series in applied Mathematics, Montpelier, Vermont.

Davies, J., & Cawley, P. (2009). The application of synthetic focusing for imaging crack-like defects in pipelines using guided waves. Ultrasonics, Ferroelectrics, and Frequency Control, IEEE Transactions on, 56(4), 759-771.

Davies, J., Simonetti, F., Lowe, M., & Cawley, P. (2006). Review of synthetically focused guided wave imaging techniques with application to defect sizing. In Quantitative Nondestructive Evaluation (Vol. 820, No. 1, pp. 142-149). AIP Publishing.

De Marchi, L., Marzani, A., Speciale, N., & Viola, E. (2010). Prediction of pulse dispersion in tapered waveguides. NDT & E International, 43(3), 265-271.

Dehghan-Niri, E., & Salamone, S. (2015). A multi-helical ultrasonic imaging approach for the structural health monitoring of cylindrical structures. Structural Health Monitoring, 14(1), 73-85.

Demma, A., Cawley, P., Lowe, M., & Roosenbrand, A. G. (2003). The reflection of the fundamental torsional mode from cracks and notches in pipes. The Journal of the Acoustical Society of America, 114(2), 611-625.

Deng, F., Wu, B., & He, C. (2008). A time-reversal defect-identifying method for guided wave inspection in pipes. Journal of Pressure Vessel Technology, 130(2), 021503.

Diamanti, K., Hodgkinson, J. M., & Soutis, C. (2004). Detection of low-velocity impact damage in composite plates using Lamb waves. Structural Health Monitoring, 3(1), 33-41.

Discalea, F. L., Matt, H., Bartoli, I., Coccia, S., Park, G., & Farrar, C. (2007). Health monitoring of UAV wing skin-to-spar joints using guided waves and macro fiber composite transducers. Journal of intelligent material systems and structures, 18(4), 373-388.

EC3 (2001). Eurocode 3: Design of steel structures – Part 1.2: General rules –Structural fire design. Brussels: European Committee for Standardization. DD ENV 1993-1-2:2001, CEN.

EN 10088-1 (1995). Stainless steels-Part 1: List of stainless steels. Brussels: European Committee for Standardization, EN 10088-1:1995E, CEN.

EN 1993-1-2 (2005). Eurocode 3: Design of steel structures - Part 1-2: General rules -Structural fire design

Esmaeel, R. A., Briand, J., & Taheri, F. (2012). Computational simulation and experimental verification of a new vibration-based structural health monitoring approach using piezoelectric sensors. Structural Health Monitoring, 11(2), 237-250.

Federal Railroad Administration: http://safetydata.fra.dot.gov/OfficeofSafety/publicsite/Query/inccaus.aspx

Fraternali, F., Porter, M. A., & Daraio, C. (2009). Optimal design of composite granular protectors. Mechanics of Advanced Materials and Structures, 17(1), 1-19.

Gaul, L., Hurlebaus, S., & Jacobs, L. J. (2001). Localization of a "synthetic" acoustic emission source on the surface of a fatigue specimen. Journal of Research in Nondestructive Evaluation, 13(2), 105-117.

Ghee Koh, C., Ming See, L., & Balendra, T. (1995). Damage detection of buildings: numerical and experimental studies. Journal of Structural Engineering, 121(8), 1155-1160.

Ghodrati, A., Seyed, R., & Bagheri, A. (2011). Damage detection in plates based on pattern search and genetic algorithms. Smart Structures and Systems, 7(2), 117-132.

Giridhara, G., Rathod, V. T., Naik, S., Mahapatra, D. R., & Gopalakrishnan, S. (2010). Rapid localization of damage using a circular sensor array and Lamb wave based triangulation. Mechanical Systems and Signal Processing, 24(8), 2929-2946.

Giurgiutiu, V. (2005). Tuned Lamb wave excitation and detection with piezoelectric wafer active sensors for structural health monitoring. Journal of intelligent material systems and structures, 16(4), 291-305.

Giurgiutiu, V., & Bao, J. (2004). Embedded-ultrasonics structural radar for in situ structural health monitoring of thin-wall structures. Structural Health Monitoring, 3(2), 121-140.

Grabowska, J., Palacz, M., & Krawczuk, M. (2008). Damage identification by wavelet analysis. Mechanical systems and signal processing, 22(7), 1623-1635.

Gu, H., & Wang, M. L. (2009). A monolithic interdigitated PVDF transducer for Lamb wave inspection. Structural Health Monitoring, 8(2), 137-148.

Hagan, M. T., & Menhaj, M. B. (1994). Training feedforward networks with the Marquardt algorithm. Neural Networks, IEEE Transactions on, 5(6), 989-993.

Hall, J. S., & Michaels, J. E. (2010). Minimum variance ultrasonic imaging applied to an in situ sparse guided wave array. Ultrasonics, Ferroelectrics, and Frequency Control, IEEE Transactions on, 57(10), 2311-2323.

Hascoët, E., & Herrmann, H. J. (2000). Shocks in non-loaded bead chains with impurities. The European Physical Journal B-Condensed Matter and Complex Systems, 14(1), 183-190.

Hay, T. R., Royer, R. L., Gao, H., Zhao, X., & Rose, J. L. (2006). A comparison of embedded sensor Lamb wave ultrasonic tomography approaches for material loss detection. Smart materials and structures, 15(4), 946.

Hayashi, T., & Murase, M. (2005). Defect imaging with guided waves in a pipe.The Journal of the Acoustical Society of America, 117(4), 2134-2140.

Higuti, R. T., Martinez-Graullera, O., Martin, C. J., Octavio, A., Elvira, L., & De Espinosa, F. M. (2010). Damage characterization using guided-wave linear arrays and image compounding techniques. Ultrasonics, Ferroelectrics, and Frequency Control, IEEE Transactions on, 57(9), 1985-1995.

Holmes, C., Drinkwater, B. W., & Wilcox, P. D. (2005). Post-processing of the full matrix of ultrasonic transmit–receive array data for non-destructive evaluation. NDT & E International, 38(8), 701-711.

Hong, J., & Xu, A. (2002). Nondestructive identification of impurities in granular medium. Applied physics letters, 81(25), 4868-4870.

Hou, J., Leonard, K. R., & Hinders, M. K. (2004). Automatic multi-mode Lamb wave arrival time extraction for improved tomographic reconstruction. Inverse Problems, 20(6), 1873.

Huang N.E. et al. (1998). The empirical mode decomposition and the Hilbert spectrum for nonlinear and non-stationary time series analysis. Proceedings of the Royal Society A, 454: 903-995.

Hunter, A. J., Drinkwater, B. W., & Wilcox, P. D. (2008). The wavenumber algorithm for full-matrix imaging using an ultrasonic array. Ultrasonics, Ferroelectrics, and Frequency Control, IEEE Transactions on, 55(11), 2450-2462.

Inoue, H., Kishimoto, K., & Shibuya, T. (1996). Experimental wavelet analysis of flexural waves in beams. Experimental Mechanics, 36(3), 212-217.

Ip, K. H., Peter, W. T., & Tam, H. Y. (2004). Extraction of patch-induced Lamb waves using a wavelet transform. Smart materials and Structures, 13(4), 861.

Jafarkhani, R., & Masri, S. F. (2011). Finite element model updating using evolutionary strategy for damage detection. Computer-Aided Civil and Infrastructure Engineering, 26(3), 207-224.

Job, S., Melo, F., Sokolow, A., & Sen, S. (2005). How Hertzian solitary waves interact with boundaries in a 1D granular medium. Physical review letters, 94(17), 178002.

Job, S., Melo, F., Sokolow, A., & Sen, S. (2007). Solitary wave trains in granular chains: experiments, theory and simulations. Granular Matter, 10(1), 13-20.

Kaewunruen, S., & Remennikov, A. M. (2006). Non-destructive testing (NDT): a tool for dynamic health monitoring of railway track structures. Materials Australia, 14-16.

Kaewunruen, S., & Remennikov, A. M. (2007). Field trials for dynamic characteristics of railway track and its components using impact excitation technique. NDT & E International, 40(7), 510-519.

Kannan, E., Maxfield, B. W., & Balasubramaniam, K. (2007). SHM of pipes using torsional waves generated by in situ magnetostrictive tapes. Smart Materials and Structures, 16(6), 2505.

Kažys, R., Tumšys, O., & Pagodinas, D. (2008). Ultrasonic detection of defects in strongly attenuating structures using the Hilbert–Huang transform.NDT & E International, 41(6), 457-466.

Khatri, D., Daraio, C., & Rizzo, P. (2008). Highly nonlinear waves' sensor technology for highway infrastructures. In The 15th International Symposium on: Smart Structures and Materials & Nondestructive Evaluation and Health Monitoring (pp. 69340U-69340U).

Kim, H. W., Lee, H. J., & Kim, Y. Y. (2012). Health monitoring of axially-cracked pipes by using helically propagating shear-horizontal waves. NDT & E International, 46, 115-121.

Kim, M. K., Kim, E. J., An, Y. K., Park, H. W., & Sohn, H. (2011). Reference-free impedance-based crack detection in plates. Journal of Sound and Vibration, 330(24), 5949-5962.

Kim, Y. Y., Park, C. I., Cho, S. H., & Han, S. W. (2005). Torsional wave experiments with a new magnetostrictive transducer configuration. The Journal of the Acoustical Society of America, 117(6), 3459-3468.

Kishimoto, K., Inoue, H., Hamada, M., & Shibuya, T. (1995). Time frequency analysis of dispersive waves by means of wavelet transform. Journal of Applied Mechanics, 62(4), 841-846.

Landau, L, & Lifshitz, E. (1986). Theory of Elasticity. 3rd Edition. Pergamon.

Lanza di Scalea, F., Rizzo, P., & Marzani, A. (2004). Propagation of ultrasonic guided waves in lap-shear adhesive joints: Case of incident a Lamb wave. The Journal of the Acoustical Society of America, 115, 146-156.

Lanza di Scalea, F., Rizzo, P., & Seible, F. (2003). Stress measurement and defect detection in steel strands by guided stress waves. Journal of materials in civil engineering, 15(3), 219-227.

Lazaridi, A. N., & Nesterenko, V. F. (1985). Observation of a new type of solitary waves in a one-dimensional granular medium. Journal of Applied Mechanics and Technical Physics, 26(3), 405-408.

Lee, C., & Park, S. (2011). Damage classification of pipelines under water flow operation using multi-mode actuated sensing technology. Smart Materials and Structures, 20(11), 115002.

Lee, H., Yang, J. & Sohn, H. (2012). Baseline-free pipeline monitoring using optical fiber-guided laser ultrasonics. Structural Health Monitoring, 11(6), 684–695.

Lee, J. R., Jang, J. K., & Kong, C. W. (2014). Fully Noncontact Wave Propagation Imaging in an Immersed Metallic Plate with a Crack. Shock and Vibration, ID: 895693.

Lee, S. J., Gandhi, N., Hall, J. S., Michaels, J. E., Xu, B., Michaels, T. E., & Ruzzene, M. (2012). Baseline-free guided wave imaging via adaptive source removal. Structural Health Monitoring, 11(4), 472-481.

Leo, M., Looney, D., D'Orazio, T., & Mandic, D. P. (2012). Identification of defective areas in composite materials by bivariate EMD analysis of ultrasound. Instrumentation and Measurement, IEEE Transactions on, 61(1), 221-232.

Leonard, K. R., & Hinders, M. K. (2003). Guided wave helical ultrasonic tomography of pipes. The Journal of the Acoustical Society of America, 114(2), 767-774.

Li, F., Yu, L., & Yang, J. (2013). Solitary wave-based strain measurements in one-dimensional granular crystals. Journal of Physics D: Applied Physics, 46(15), 155106.

Li, F., Zhao, L., Tian, Z., Yu, L., & Yang, J. (2013). Visualization of solitary waves via laser Doppler vibrometry for heavy impurity identification in a granular chain. Smart Materials and Structures, 22(3), 035016.

Liu, Y., Li, Z., & Gong, K. (2012). Detection of a radial crack in annular structures using guided circumferential waves and continuous wavelet transform. Mechanical Systems and Signal Processing, 30, 157-167.

Lowe, M. J., Alleyne, D. N., & Cawley, P. (1998). Defect detection in pipes using guided waves. Ultrasonics, 36(1), 147-154.

Lu, Y., Oruklu, E., & Saniie, J. (2008). Application of Hilbert-Huang transform for ultrasonic nondestructive evaluation. In Ultrasonics Symposium, 2008. IUS 2008. IEEE (pp. 1499-1502). IEEE.

Lu, Y., Ye L, & Wang D. (2009). Time-domain analyses and correlations of Lamb wave signals for damage detection in a composite panel of multiple stiffeners. Journal of Composite Materials, 43, 3211-3230.

Mallat, S. (1999). A wavelet tour of signal processing. Second edition. London, Academic press.

Marzani, A., Viola, E., Bartoli, I., Di Scalea, F. L., & Rizzo, P. (2008). A semi-analytical finite element formulation for modeling stress wave propagation in axisymmetric damped waveguides. Journal of Sound and Vibration, 318(3), 488-505.

Marzani, A., Viola, E., Bartoli, I., Lanza di Scalea, F. & Rizzo, P. (2008). A semi-analytical finite element formulation for modeling stress wave propagation in axisymmetric damped waveguides. Journal of Sound and Vibration, 318(3), 488–505.

Miao, X., Wang, D., Ye, L., Lu, Y., Li, F., & Meng G. (2011). Identification of dual notches based on time-reversal lamb waves and a damage diagnostic imaging algorithm. Journal of Intelligent Material Systems and Structures, 22(17), 1983–1992.

Michaels, J. E. (2008). Detection, localization and characterization of damage in plates with an in situ array of spatially distributed ultrasonic sensors. Smart Materials and Structures, 17(3), 035035.

Michaels, J. E., & Michaels, T. E. (2007). Guided wave signal processing and image fusion for in situ damage localization in plates. Wave Motion, 44(6), 482-492.

Mijarez, R., Gaydecki, P., & Burdekin, M. (2007). Flood member detection for real-time structural health monitoring of sub-sea structures of offshore steel oilrigs. Smart Materials and Structures, 16(5), 1857.

Moilanen, P., Nicholson, P. H. F., Kilappa, V., Cheng, S., & Timonen, J. (2006). Measuring guided waves in long bones: Modeling and experiments in free and immersed plates. Ultrasound in medicine & biology, 32(5), 709-719.

Moser, F., Jacobs, L. J., & Qu, J. (1999). Modeling elastic wave propagation in waveguides with the finite element method. NDT & E International, 32(4), 225-234.

Moustafa, A., & Salamone, S. (2012). Fractal dimension–based Lamb wave tomography algorithm for damage detection in plate-like structures. Journal of Intelligent Material Systems and Structures, 23(11), 1269-1276.

Na, W. B., & Kundu, T. (2002). Underwater pipeline inspection using guided waves. Journal of pressure vessel technology, 124(2), 196-200.

Na, W.B., Kundu, T. & Ehsani, M. R. (2003). Lamb waves for detecting delamination between steel bars and concrete. Computer-Aided Civil and Infrastructure Engineering, 18(1), 58-63.

Nagy, P. B., Simonetti, F., & Instanes, G. (2014). Corrosion and erosion monitoring in plates and pipes using constant group velocity Lamb wave inspection. Ultrasonics, 54(7), 1832-1841.

Nayfeh, A. H., & Chimenti, D. E. (1988). Propagation of guided waves in fluid-coupled plates of fiber-reinforced composite. The Journal of the Acoustical Society of America, 83(5), 1736-1743.

Nesterenko, V. (2001). Dynamics of Heterogeneous Materials. Springer.

Nesterenko, V. F. (1983). Propagation of nonlinear compression pulses in granular media. Journal of Applied Mechanics and Technical Physics, 24(5), 733-743.

Nesterenko, V. F., Daraio, C., Herbold, E. B., & Jin, S. (2005). Anomalous wave reflection at the interface of two strongly nonlinear granular media. Physical review letters, 95(15), 158702.

Nesterenko, V. F., Lazaridi, A. N., & Sibiryakov, E. B. (1995). The decay of soliton at the contact of two "acoustic vacuums". Journal of applied mechanics and technical physics, 36(2), 166-168.

Neubauer, W. G. (1973). Ultrasonic reflection of a bounded beam at Rayleigh and critical angles for a plane liquid-solid interface. Journal of Applied Physics, 44(1), 48-55.

Ni, X., & Rizzo, P. (2012a). Highly nonlinear solitary waves for the inspection of adhesive joints. Experimental mechanics, 52(9), 1493-1501.

Ni, X., & Rizzo, P. (2012b). Use of Highly Nonlinear Solitary Waves in Nondestructive Testing. Materials evaluation, 70(5), 561-569.

Ni, X., Cai, L., & Rizzo, P. (2013). A comparative study on three different transducers for the measurement of nonlinear solitary waves. Sensors, 13(1), 1231-1246.

Ni, X., Rizzo, P., & Daraio, C. (2011a). Actuators for the generation of highly nonlinear solitary waves. Review of Scientific Instruments, 82(3), 034902.

Ni, X., Rizzo, P., & Daraio, C. (2011b). Laser-based excitation of nonlinear solitary waves in a chain of particles. Physical Review E, 84(2), 026601.

Ni, X., Rizzo, P., Yang, J., Katri, D., & Daraio, C. (2012). Monitoring the hydration of cement using highly nonlinear solitary waves. NDT & E International, 52, 76-85.

Nicknam, A., & Hosseini, M. H. (2012). Structural damage localization and evaluation based on modal data via a new evolutionary algorithm. Archive of Applied Mechanics, 82(2), 191-203.

Niri, E. D., & Salamone, S. (2012). A probabilistic framework for acoustic emission source localization in plate-like structures. Smart Materials and Structures, 21(3), 035009.

Paget, C. A., Grondel, S., Levin, K., & Delebarre, C. (2003). Damage assessment in composites by Lamb waves and wavelet coefficients. Smart Materials and Structures, 12(3), 393.

Park, H. W., Sohn, H., Law, K. H., & Farrar, C. R. (2007). Time reversal active sensing for health monitoring of a composite plate. Journal of Sound and Vibration, 302(1), 50-66.

Park, S., Lee, C., & Sohn, H. (2010). Reference-free crack detection using transfer impedances. Journal of Sound and Vibration, 329(12), 2337-2348.

Pavlakovic, B. N. (1998). Leaky guided ultrasonic waves in NDT (Doctoral dissertation, Imperial College London).

Perera, R. & Torres, R. (2006). Structural damage detection via modal data with Genetic algorithms. Journal of Structural Engineering ASCE, 132(9), 1491-1501.

Pistone, E., & Rizzo, P. (2015). On the use of an array of ultrasonic immersion transducers for the nondestructive testing of immersed plates. Nondestructive Testing and Evaluation, 30(1), 26-38.

Pistone, E., Li, K., & Rizzo, P. (2013). Noncontact monitoring of immersed plates by means of laser-induced ultrasounds. Structural Health Monitoring, 12(5-6), 549-565.

Portzgen, N., Gisolf, D., & Blacquiere, G. (2007). Inverse wave field extrapolation: a different NDI approach to imaging defects. Ultrasonics, Ferroelectrics, and Frequency Control, IEEE Transactions on, 54(1), 118-127.

Qiang, W., & Shenfang, Y. (2009). Baseline-free imaging method based on new PZT sensor arrangements. Journal of Intelligent Material Systems and Structures, 20(14), 1663-1673.

Quaegebeur, N., Masson, P., Langlois-Demers, D., & Micheau, P. (2011). Dispersion-based imaging for structural health monitoring using sparse and compact arrays. Smart Materials and Structures, 20(2), 025005.

Raghavan, A., & Cesnik, C. E. (2007). Review of guided-wave structural health monitoring. Shock and Vibration Digest, 39(2), 91-116.

Rajabioun, R., Atashpaz-Gargari, E. & Lucas, C. (2008). Colonial competitive algorithm as a tool for Nash equilibrium point achievement, Lecture Notes in Computer Science, 5073, 680-695.

Rizzo, P. & Lanza di Scalea, F. (2007). Wavelet-based unsupervised and supervised learning algorithms for ultrasonic structural monitoring of waveguides. In: Reece, P.L. (ed.), Progress in Smart Materials and Structures Research, 227-290, NOVA Science Publishers, New York.

Rizzo, P., & Lanza di Scalea, F. (2006). Feature extraction for defect detection in strands by guided ultrasonic waves. Structural Health Monitoring, 5(3), 297-308.

Rizzo, P., & Lanza di Scalea, F. (2006). Wavelet-based feature extraction for automatic defect classification in strands by ultrasonic structural monitoring. Smart Structures and Systems, 2(3), 253-274.

Rizzo, P., & Lanza di Scalea, F. (2003). Effect of frequency on the acoustoelastic response of steel bars. Experimental Techniques, 27(6), 40-43.

Rizzo, P., & Lanza di Scalea, F. (2004) Monitoring in cable stays via guided wave magnetostrictive ultrasonics. Materials Evaluation. 62, 1057–1065.

Rizzo, P., & Lanza di Scalea, F. (2004). Wave propagation in multi-wire strands by wavelet-based laser ultrasound. Experimental Mechanics, 44(4), 407-415.

Rizzo, P., & Lanza di Scalea, F. (2005). Ultrasonic inspection of multi-wire steel strands with the aid of the wavelet transform. Smart Materials and Structures, 14, 685–695.

Rizzo, P., Bartoli, I., Marzani, A. & Lanza di Scalea, F. (2005). Defect classification in pipes by neural networks using multiple guided ultrasonic wave features extracted after wavelet processing. ASME Journal of Pressure Vessel Technology, 127, 294 -303.

Rizzo, P., Cammarata, M., Dutta, D., Sohn, H., & Harries, K. (2009). An unsupervised learning algorithm for fatigue crack detection in waveguides. Smart Materials and Structures, 18(2), 1-11.

Rizzo, P., Marzani, A., & Bruck, J. (2010). Ultrasonic guided waves for nondestructive evaluation/structural health monitoring of trusses. Measurement Science and Technology, 21(4), 045701.

Rizzo, P., Sorrivi, E., di Scalea, F. L., & Viola, E. (2007). Wavelet-based outlier analysis for guided wave structural monitoring: application to multi-wire strands. Journal of Sound and Vibration, 307(1), 52-68.

Robertson, C. Adelaide advertise, (2012). Website: http://www.telegraph.co.uk/news/picturegalleries/worldnews/4360255/Heatwave-inMelbourne-plays-havoc-with-the-Australian-Open.html.

Sakumoto, Y., Nakazato, T., & Matsuzaki, A. (1996). High-temperature properties of stainless steel for building structures. Journal of Structural Engineering, 122(4), 399-406.

Sale, M., Rizzo, P., and Marzani, A. (2011). Semi-analytical formulation for the guided waves-based reconstruction of elastic moduli. Mechanical System and Signal Processing, 25, 2241-2256.

Sen, S., Manciu, M., & Wright, J. D. (1998). Solitonlike pulses in perturbed and driven Hertzian chains and their possible applications in detecting buried impurities. Physical Review E, 57(2), 2386.

Sharma, J.N. & Pathania, V. (2003a). Thermoelastic waves in a plate bordered with layers of inviscid liquid. Journal of Thermal Stresses, 26, 149-166.

Sharma, J.N. & Pathania, V. (2003b). Generalized thermoelastic Lamb waves in a plate bordered with layers of inviscid liquid. Journal of Sound and Vibration, 268, 897-916.

Sharma, S., & Mukherjee, A. (2015). Ultrasonic guided waves for monitoring corrosion in submerged plates. Structural Control and Health Monitoring, 22(1), 19-35.

Shelke, A., Uddin, A., & Yang, J. (2014). Impact identification in sandwich structures using solitary wave-supporting granular crystal sensors. AIAA Journal, 52(10), 2283-2290.

Shin, H.J. & Rose, J.L. (1998). Guided wave tuning principles for defect detection in tubing. Journal of Nondestructive Evaluation, 17(1), 27-36.

Sohn, H., Kim, S. D., & Harries, K. (2008). Reference-free damage classification based on cluster analysis. Computer-Aided Civil and Infrastructure Engineering, 23(5), 324-338.

Sohn, H., Park, H. W., Law, K. H., & Farrar, C. R. (2007). Combination of a time reversal process and a consecutiv outlier analysis for baseline-free damage diagnosis. Journal of Intelligent Material Systems and Structures, 18(4), 335-346.

Staszewski, W. J., Pierce, S. G., Worden, K., Philp, W. R., Tomlinson, G. R., & Culshaw, B. (1997). Wavelet signal processing for enhanced Lamb-wave defect detection in composite plates using optical fiber detection. Optical Engineering, 36(7), 1877-1888.

Su, Z., Wang, X., Chen, Z., Ye, L., & Wang, D. (2006). A built-in active sensor network for health monitoring of composite structures. Smart Materials and Structures, 15(6), 1939.

Su, Z., Wang, X., Cheng, L., Yu, L., & Chen, Z. (2009). On selection of data fusion schemes for structural damage evaluation. Structural Health Monitoring, 8(3), 223-241.

Szelengowicz, I., Kevrekidis, P. G., & Daraio, C. (2012). Wave propagation in square granular crystals with spherical interstitial intruders. Physical Review E, 86(6), 061306.

Taha, M. R., Noureldin, A., Lucero, J. L., & Baca, T. J. (2006). Wavelet transform for structural health monitoring: a compendium of uses and features. Structural Health Monitoring, 5(3), 267-295.

Tedesco, J. W., McDougal, W. G., & Ross, C. A. (1999). Structural dynamics: theory and applications. Addison Wesley Longman.

Tichler, A. M., Gómez, L. R., Upadhyaya, N., Campman, X., Nesterenko, V. F., & Vitelli, V. (2013). Transmission and reflection of strongly nonlinear solitary waves at granular interfaces. Physical review letters, 111(4), 048001.

Todoroki, A., Takeuchi, Y., Shimamura, Y., Iwasaki, A., & Sugiya, T. (2004). Fracture monitoring system of sewer pipe with composite fracture sensors via the Internet. Structural Health Monitoring, 3(1), 5-17.

Tua, P. S., Quek, S. T., & Wang, Q. (2005). Detection of cracks in cylindrical pipes and plates using piezo-actuated Lamb waves. Smart materials and structures, 14(6), 1325.

U.S. Environmental Protection Agency. Addressing the challenge through innovation, http://www.epa.gov/nrmrl/pubs/600f07015/600f07015.pdf.

Valle, C., Niethammer, M., Qu, J. & Jacobs, L.J. (2001). Crack characterization using guided circumferential waves. Journal of the Acoustical Society of America, 110(3), 1282-1290.

Velichko, A., & Wilcox, P. D. (2010). An analytical comparison of ultrasonic array imaging algorithms. The Journal of the Acoustical Society of America, 127(4), 2377-2384.

Vortok International & AEA Technology. Verse® Technical Information Pack. AEA Technology.

Wang D., Ye L. & Lu Y. (2009). A probabilistic diagnostic algorithm for identification of multiple notches using digital damage fingerprints (DDFs). Journal of Intelligent Material Systems and Structures, 20, 1439-1450.

Wang, C. H., Rose, J. T., & Chang, F. K. (2004). A synthetic time-reversal imaging method for structural health monitoring. Smart materials and structures, 13(2), 415.

Wang, D., Ye, L., Lu, Y., & Li, F. (2010a). A damage diagnostic imaging algorithm based on the quantitative comparison of Lamb wave signals. Smart materials and structures, 19(6), 065008.

Wang, D., Ye, L., Su, Z., Lu, Y., Li, F., & Meng, G. (2010b). Probabilistic damage identification based on correlation analysis using guided wave signals in aluminum plates. Structural Health Monitoring, 9(2), 133-144.

Wei, L., Pei-wen, Q., Qi, Z., & Guang, Y. (2006). Ultrasonic defect detection of a petroleum pipeline in a viscoelastic medium. Russian Journal of Nondestructive Testing, 42(10), 692-699.

Xu, C. G., Xu, B. Q., & Xu, G. D. (2011). Laser-induced thermoelastic Leaky Lamb waves at the fluid–solid interface. Applied Physics A, 105(2), 379-386.

Xu, H., Xu, C., & Zhou, S. (2010, June). A new ultrasonic guided wave signal processing method for UNDE of laminated composite material. In Mechanic Automation and Control Engineering (MACE), 2010 International Conference on (pp. 2542-2545). IEEE.

Xu, J., Xiong, H., & Wu, X. (2011, September). Signal processing for the guided wave test based on the empirical mode decomposition. In Electrical and Control Engineering (ICECE), 2011 International Conference on (pp. 375-378). IEEE.

Yadav, S. K., Banerjee, S., & Kundu, T. (2012). On sequencing the feature extraction techniques for online damage characterization. Journal of Intelligent Material Systems and Structures, 1045389X12463466.

Yan, F., Royer, R. L., & Rose, J. L. (2010). Ultrasonic guided wave imaging techniques in structural health monitoring. Journal of Intelligent Material Systems and Structures, 21(3), 377-384.

Yang, J., Dunatunga, S., & Daraio, C. (2012a). Amplitude-dependent attenuation of compressive waves in curved granular crystals constrained by elastic guides. Acta Mechanica, 223(3), 549-562.

Yang, J., Gonzalez, M., Kim, E., Agbasi, C., & Sutton, M. (2014). Attenuation of Solitary Waves and Localization of Breathers in 1D Granular Crystals Visualized via High Speed Photography. Experimental Mechanics, 54(6), 1043-1057.

Yang, J., Sangiorgio, S. N., Borkowski, S. L., Silvestro, C., De Nardo, L., Daraio, C., & Ebramzadeh, E. (2012b). Site-specific quantification of bone quality using highly nonlinear solitary waves. Journal of Biomechanical Engineering, 134(10), 101001.

Yang, J., Silvestro, C., Khatri, D., De Nardo, L., & Daraio, C. (2011). Interaction of highly nonlinear solitary waves with linear elastic media. Physical Review E,83(4), 046606.

Yang, J., Silvestro, C., Sangiorgio, S. N., Borkowski, S. L., Ebramzadeh, E., De Nardo, L., & Daraio, C. (2012c). Nondestructive evaluation of orthopaedic implant stability in THA using highly nonlinear solitary waves. Smart Materials and Structures, 21(1), 012002.

Yu, L., & Tian, Z. (2015). Case study of guided wave propagation in a one-side water-immersed steel plate. Case Studies in Nondestructive Testing and Evaluation, 3, 1-8.

Zhang, R. R., Ma, S., Safak, E., & Hartzell, S. (2003). Hilbert-Huang transform analysis of dynamic and earthquake motion recordings. Journal of Engineering Mechanics, 129(8), 861-875.

Zhao, X., Gao, H., Zhang, G., Ayhan, B., Yan, F., Kwan, C., & Rose, J. L. (2007a). Active health monitoring of an aircraft wing with embedded piezoelectric sensor/actuator network: I. Defect detection, localization and growth monitoring. Smart materials and structures, 16(4), 1208.

Zhao, X., Qian, T., Mei, G., Kwan, C., Zane, R., Walsh, C., ... & Popovic, Z. (2007b). Active health monitoring of an aircraft wing with an embedded piezoelectric sensor/actuator network: II. Wireless approaches. Smart materials and structures, 16(4), 1218.

Zhou, C., Su, Z., & Cheng, L. (2011). Probability-based diagnostic imaging using hybrid features extracted from ultrasonic Lamb wave signals. Smart Materials and Structures, 20(12), 125005.

Zienkiewicz, O.C. (1977). The finite element method. McGraw-Hill, London.